DEPARTAMENTO DE ASTROFISICA

Universidad de La Laguna

Discovery and characterization of substellar companions in stellar clusters using Karhunen-Loève Image Processing of HST data

Memoria que presenta
D. Giovanni Maria Strampelli
para optar al grado de
Doctor en Ciencias Físicas.

INSTITUTO Đ ASTROFISICA Đ CANARIAS
enero de 2021

Examination date: January, 2021
Thesis supervisor: Antonio Aparicio
Thesis supervisor: Massimo Robberto
Thesis supervisor: Laurent Pueyo

ISBN: xx-xxx-xxxx-x
Depósito legal: TF-xxxx/2002
Some of the figures included in this document have been already published in *The Astrophysical Journal*.
Some of the material included in this document has been already published in *The Astrophysical Journal*.

To Maria Libera, Giuseppe, Maria Luisa and Vittorio,
without whom the stars would always lay out of my reach.
Ad astra per aspera!

All that is gold does not glitter,
Not all those who wander are lost;
The old that is strong does not wither,
Deep roots are not reached by the frost.

From the ashes a fire shall be woken,
A light from the shadows shall spring;
Renewed shall be blade that was broken,
The crownless again shall be king.

J.R.R. Tolkien, The Fellowship of the Ring

Acknowledgments

A special thanks go to Maria Libera, my wife, for her patience and support. Every time I felt lost in the pursuit of my goal, she represented my safe haven, the cornerstone around which everything else became possible. I want to thanks also my parents, Giuseppe and Maria Luisa Strampelli, and my brother Vittorio, and acknowledge the sacrifice they endure to allow me to leave my country and come abroad to pursue my dream.

I want to give thanks to Professor Antonio Aparicio, Dr. Massimo Robberto, and Dr. Laurent Pueyo for all their supervision over these years. Working closely with each of them every day taught me a lot about the spirit of this job and all the piratical aspects and strategies one needs to employ to truly succeed in this field. I'm also truly grateful to Professor Gianpaolo Piotto to be the bridge between me and Professor Antonio Aparicio during the very early time of this project, when all of this was just an embryo in the minds of my soon-to-be supervisors and mine. I want to thank Dr. Jonathan Aguilar for his support and his useful insight during the time we shared together as both Ph.D. students. Knowing I wasn't alone in this endeavor truly helped me face most of the harder days.

I would also like to recognize the amazing work done by Dr. Gaspard Duchen and Dr. Carlo Manara as referee of this work, engaging me in meaningfully and challenging comments during the whole period we worked together to bring this thesis to a new level of excellence. Moreover, I want to say thanks to Dr. Armin Rest and Dr. Annalisa Calamida. Without them, I would never have come to the U.S.A. in the first place, and none of this would ever be possible. I also want to thanks the University of La Laguna and the Institute of Astronomy of the Canary Island, as well as the Space Telescope Science Institute and the Johns Hopkins University for allowing this beautiful project to evolve and succeed.

Finally, I want to say thanks to all my friends who helped me along the way sustaining me and motivating me until the very end.

Resumen

Las estrellas se forman en regiones del espacio donde se acumulan cantidades suficientes de materia, alcanzando densidades lo suficientemente elevadas como para superar eventualmente todos los posibles agentes capaces de prevenir el colapso gravitacional, como la presión térmica y radiativa, el campo magnético y la turbulencia. El colapso gravitacional suele ser de naturaleza jerárquica, lo que frecuentemente conduce a la fragmentación en una amplia gama de tamaños. Desde las entidades de mayor escala que contienen miles de estrellas hasta los sistemas múltiples y binarios, siempre hay cierto grado de agrupaciones cuando se trata de la formación de estrellas (Hopkins 2013; Vázquez-Semadeni et al. 2019). Desde el trabajo inicial de Larson (1972), en el que el autor propuso que todos los sistemas estelares nacieron como múltiples y la siguiente evolución dinámica crearía la mezcla de los sistemas simples, dobles y múltiples que observamos en el campo, se han dado muchos pasos hacia adelante en la comprensión de la formación de estrellas. Gracias al gran avance en la sensibilidad y resolución de las técnicas de observación modernas, se ha vuelto cada vez más claro que la mayoría de las estrellas nacen en sistemas múltiples cuyos componentes luego sufrirían una interacción dinámica que conduce a la expulsión de unos componentes a órbitas distantes o de escape (Reipurth et al. 2001; Reipurth et al. 2010), endureciendo las binarias restantes y reduciendo la fracción de multiplicidad para el cúmulo (MF), es decir, la proporción de sistemas no únicos en una muestra dada (Goodwin et al. 2007).

Si bien se necesitan análisis aún más detallados para comprender mejor y restringir las propiedades clave de las protoestrellas recién nacidas y la formación de estrellas en general, la binariedad y la multiplicidad son ampliamente aceptadas en general como uno de los principales canales para la formación estelar, con la inevitable implicación de que la evolución dinámica es una parte esencial de la evolución estelar temprana (Reipurth et al. 2014). Los estudios de sistemas binarios y múltiples durante la fase protoestelar y posteriormente durante la fase

de estrella presecuencia principal (PMS), son de hecho fundamentales porque ofrecen el escenario perfecto para observar y analizar los resultados de la fragmentación de las nubes moleculares dando una visión significativa de la física de los procesos en curso durante estas fases. Además, las estrellas binarias, por ser pares coetáneos nacidos en el mismo entorno y con la misma metalicidad pero con masas diferentes, representan el laboratorio perfecto donde se pueden inspeccionar las propiedades clave de la evolución estelar desde las primeras fases de la formación estelar hasta la fenomenología más violenta que puede caracterizar los momentos finales de su vida. En sistemas jóvenes, conocer la temperatura efectiva y la luminosidad absoluta de un par puede restringir los modelos teóricos desarrollados para predecir isócronas y trayectorias evolutivas en los diagramas de H-R durante la fase PMS (Gennaro et al. 2012; Stassun et al. 2014). Por otro lado, ignorar la presencia de las binarias representa una molestia que puede afectar el análisis estadístico de los propios diagramas de H-R (Jerabkova et al. 2019).

Para abordar este problema (y muchos otros) relacionados con las primeras fases de las formaciones estelares, se han realizado muchas encuestas a lo largo del tiempo. Para las fuentes de Clase 0/I, generalmente se prefieren las observaciones de infrarrojos (Haisch et al. 2004; Duchêne et al. 2007; Connelley et al. 2008a; Connelley et al. 2008b), submilimitros (Chen et al. 2008; Chen et al. 2009; Maury et al. 2010; Enoch et al. 2011; Tobin et al. 2013; Tobin et al. 2018; Hsieh et al. 2020) o de radio continuo (Rodríguez et al. 2003; Reipurth et al. 2002; Reipurth et al. 2004; Tobin et al. 2019) .Las estrellas PMS (T-Tauri Star (TTS) o fuentes de Clase I/II) se han estudiado en una amplia gama de entornos diferentes: cúmulo estelar denso (por ejemplo, el cúmulo de la nebulosa de Orión Orion Nebula Cluster (ONC) así como IC 348 en la nube de Perseo; Petr et al. 1998; Luhman et al. 2005; Köhler et al. 2006; Reipurth et al. 2007; Duchêne et al. 2018; Strampelli et al. 2020b; Strampelli et al. 2020c), las jóvenes asociaciones OB (por ejemplo, la Scorpion-Centaurus; Brown & Verschueren 1997); Shatsky & Tokovinin 2002; Kouwenhoven et al. 2007), las asociaciones T (por ejemplo, las regiones de formación estelar Tauro-Auriga; Kraus et al. 2008; Kraus et al. 2011). Los estudios de múltiples longitudes de ondas de las regiones cercanas de formación estelar, así como la interferometría speckle, la óptica adaptativa, el enmascaramiento de la apertura y las imágenes Hubble Space Telescope (HST) High-Contrast Imaging (HCI) (o imágenes directas) son sólo unas de las diferentes técnicas aplicadas para realizar estas encuestas de multiplicidad.

Centrándose en este último aspecto, la HCI comprende un amplio grupo de técnicas utilizadas para adquirir imágenes directas de estrellas y otros cuerpos muy cercanos a sus estrellas anfitrionas (es decir, capturar fotones directamente

de la fuente en lugar de inferir su presencia a partir de características reveladoras del sistema observado). Esta técnica puede ser sensible a compañeras tan cercanas como las a unas pocas o unos pocos cientos de UA cuyas masas van desde la masa planetaria hasta las estrellas enanas marrones y las de baja masa. El principal desafío de observación en las técnicas de HCI es que los objetos potencialmente resueltos pueden estar ocultos bajo las alas extendidas de la función de dispersión de punto (PSF) de la estrella primaria. Aunque la primaria se puede suprimir a través de algún tipo de hardware de supresión (por ejemplo, una parte física de un telescopio que elimina selectivamente la luz de la estrella anfitriona bloqueando su camino óptico al tiempo que retiene todos los fotones restantes), los intentos actuales, desde el suelo con la Óptica Adaptativa (OA) o desde el espacio, están limitados por la presencia dominante de puntos brillantes cuasiestáticos que enmascaran por completo la débil señal que nos interesa ((Schneider & Silverstone 2003; Biller et al. 2004; Marois et al. 2005; Masciadri et al. 2005)) y que se deben principalmente a imperfecciones en la óptica. Soummer et al. (2012) propuso un enfoque novedoso para realizar la sustracción de PSF mediante el análisis de componentes principales (PCA). Cuando se ensambla una biblioteca adecuada de PSF de referencia, se lleva a cabo el PCA y se usa un análisis de procesamiento de imágenes de Karhunen-Loeve (KLIP) de estas referencias para crear una base ortogonal de imágenes propias sobre las cuales se proyecta la imagen científica. El objetivo principal de la sustracción de PSF es entonces, reconstruir la PSF de un objetivo aislado usando el conjunto de imágenes de referencia y sustraerlo de la imagen del objetivo obteniendo la señal astronómica candidata. En teoría, debido a que la PSF es un proceso aleatorio continuo del estado del sistema instrumento-telescopio en el momento en que se adquirieron los datos, se necesitarían un número infinito de referencias para reconstruirla. En la práctica, el propósito es encontrar la mejor estimación de la PSF dado el conocimiento limitado proporcionado por las referencias disponibles.

El enfoque principal de esta tesis consiste en el desarrollo y aplicación de una canalización capaz de recuperar compañeras débiles incrustadas en la función de dispersión del punto estelar anfitrión en las imágenes HST ACS/WFC3-IR. Para lograr este propósito, el método propuesto por ? para realizar la sustracción de la función de dispersión de puntos (PSF) usando el PCA servirá como la piedra básica a partir de la cual se construirá todo el proyecto. Hasta la fecha, tres artículos son el resultado de este proyecto:

- Strampelli et al. (2020a): presenta *Stra*KLIP, la canalización desarrollada gracias a la colaboración entre la Universidad de La Laguna (España), el

Space Telescope Science Institute (EE.UU.) y la Johns Hopkins University (EE.UU.), para detectar y caracterizar señales astronómicas cercanas débiles alrededor de primarias brillantes aprovechando el algoritmo KLIP recién introducido.

- Strampelli et al. (2020b): presenta una primera aplicación científica de *Stra*KLIP en los datos HST/WFC3-IR sobre el Cúmulo de la Nebulosa de Orión (ONC) en el filtro F130N y F139M.

- Strampelli et al. (2020c): se centra en los datos HST/ACS visibles del propio ONC, presentando una nueva fotometría PSF para el cúmulo y una segunda aplicación de la propia canalización *Stra*KLIP.

Una de las características clave de *Stra*KLIP es que está diseñada para funcionar con conjuntos de observaciones de imágenes de campo amplio no diseñadas específicamente para el análisis HCI. Desde este punto de vista, representa una nueva herramienta que se puede aplicar a prácticamente cualquier gran conjunto de datos de imágenes, ya sea desde el espacio (HST, JWST, WFIRST-Nancy Grace Roman Telescope) o desde el suelo (por ejemplo, LSST-Observatorio Vera Rubín).

En Strampelli et al. (2020c), la nueva fotometría ACS se ha combinado con el precedente catálogo WFC3-IR de Robberto et al. (2020), enlazando dos programas HST Treasury (GO-10246 y GO-13826, P.I. M. Robberto) en un catálogo único de las fuentes para el ONC, que abarca un amplia gama de filtros desde las bandas visibles hasta los infrarrojos (es decir, filtros F435W, F555W, F658N, F775W, F850LP, F130N y F139M). Gracias a esta amplia variedad de filtros disponibles, se ha adoptado un enfoque bayesiano con la estrategia de la Markov Chain Monte Carlo (MCMC) para estimar tres parámetros fundamentales a través del sistema de Distribución de energía espectral (SED): masa, edad y extinción. Se han probado tres diferentes funciones de masa inicial (FMI) (Kroupa, y Chabrier para estrellas individuales y sistemas estelares) y dos diferentes leyes de enrojecimiento ($R_V = 3.1 y 5$). En general, observamos que cambiar la FMI, así como cambiar las leyes de enrojecimiento, no tiene un impacto fuerte en las distribuciones de los parámetros resultantes, aunque $R_V = 5$ parece producir distribuciones más superficiales en comparación con $R_V = 3.1$ tanto en la masa como en los parámetros A_V. Como valores representativos para este cúmulo encontramos: una masa mediana entre 0.15 - 0.21 Mc, una extinción mediana Av entre 1.64 - 2.42 magnitudes y una edad mediana entre 1.6 - 1.8 Myr.

En particular, un análisis más profundo de la distribución de edades de las estrellas en el cúmulo reveló la presencia de al menos dos poblaciones diferentes

con una edad promedio de ~ 0.85 y 1.6 Myr, apoyando firmemente la idea de que la formación de estrellas en el ONC no fue solo un proceso continuo diluido durante un período prolongado de tiempo, sino que se describe mejor mediante al menos dos episodios discretos y subsecuentes de formación estelar en un rango de ~ 3 Myr.

Aprovechando el filtro F658N disponible en el catálogo, se han estimado la luminosidad de acreción (L_{acc}) y la tasa de acreción de masa ($\dot{M}_{acc}$) para una muestra de ~ 700 fuentes de cúmulos auténticas, lo que proporciona uno de los catálogos más amplios de tasas de acreción de masa en la ONC hasta la fecha. La relación $\dot{M}_{acc}$ - $M_\star$ presenta dos regímenes diferentes. Por un lado, observamos que las estrellas más masivas ($M_\star > 0.3 M_\odot$) muestran una relación lineal bastante superficial que coincide con la predicha en el contexto de los discos de acreción irradiados centralmente alrededor de estrellas de masa solar con una capa de acreción activa (Mohanty et al. (2005); Hartmann et al. 2006). Por otro lado, las estrellas de menor masa ($M_\star \lesssim 0.3 M_\odot$) se pueden dividir a su vez en dos poblaciones diferentes. Si extendemos la línea que se ajusta a las estrellas de mayor masa, vemos que coincide muy bien con una población de objetos de baja masa con altas tasas de acreción. Por otro lado, hay una segunda rama que sale en $M_\star \sim 0.3 M_\odot$, que muestra una relación más pronunciada entre $\dot{M}_{acc}$ y $M_\star$. Estas dos poblaciones de baja masa también muestran diferencias en la edad: una parece más joven con una mayor tasa de acreción, la otra más evolucionada con una menor tasa de acreción de masa. Una disminución de la tasa de acreción de masa frente a la edad no es sorprendente, pero en este caso sugiere la coexistencia en la ONC de dos poblaciones jóvenes diferentes. Además, un análisis de la extinción de estos objetos sugiere que las fuentes más antiguas se encuentran típicamente en regiones menos incrustadas, es decir, más evolucionadas habiendo estado expuestas durante más tiempo al flujo ionizante de las estrellas OB.

La binariedad ha sido uno de los enfoques principales de ambos artículos (Strampelli et al. 2020b; Strampelli et al. 2020c). Como resultado del primer análisis, se han detectado 39 pares de candidatos cúmulos cerrados, con separación de 0.16" - 0.77" y una masa primaria $(M_p) = 0.015 - 1.27 M_\odot$ y una masa complementaria $(M_c) = 0.004 - 0.54 M_\odot$. De estos 39 sistemas binarios, 21 son detecciones candidatas realmente nuevas. Como resultado del segundo análisis, en cambio, solo se detectan 15 binarios a través de la canalización *Stra*KLIP, que abarcan un rango de separación de $0.12'' - 0.34''$ y $M_p = 0.032 - 1.38 M_\odot$ y $M_c = 0.006 - 1.00 M_\odot$. De esta muestra, 5 son detecciones realmente nuevas. 12 de las anteriores binarias WFC3-IR KLIP se confirman a través de este nuevo análisis ACS KLIP.

Combinando ambos programas de tesorería del ONC, se ha compilado un

nuevo catálogo de 119 binarias, que abarca un rango de $M_p = 0.015 - 1.93 M_{odot}$, $M_c = 0.004 - 1 M_{\odot}$ y separaciones $0.12'' - 1.95''$. Este catálogo comprende binarias identificadas por Strampelli et al. 2020b en datos WFC3-IR (obtenidos de KLIP o del catálogo Robberto et al. 2020) y binarias presentes en Strampelli et al. 2020c en datos ACS (a su vez obtenidos de KLIP o del catálogo Robberto et al. 2013). Como resultado, una vez que se consideran los argumentos de completitud y alineación al azar, se establece un nuevo valor de la fracción de multiplicidad para el cúmulo: MF ONC $= 13\% \pm 1\%$. En comparación con otras regiones de formación estelar, el MF ONC es ~ 2 veces más pequeño que, por ejemplo, Tauro, mientras que es aún compatible con el valor observado en el campo en un rango similar de masas y separaciones. Además, se ha encontrado una distribución general pesada en el fondo de la relación de masa (q) para las binarias en el cúmulo, muy cercana al valor observado para las binarias de campo en un rango similar de masas y separaciones. La distribución de separación binaria muestra dos grupos claramente distintos de binarios distinguibles por su respectiva separación: cercana (separación $\lesssim 0.6''$) y amplia (separación $> 0.6''$). Además, un análisis de la distribución de binarias anchas sobre las cercanas en función de la distancia desde el centro del cúmulo, revela una clara señal de evolución dinámica en su pasado. En general, estos resultados apuntan al hecho de que las binarias del ONC pueden representar una buena plantilla para la población típica de binarias de campo, lo que respalda la hipótesis de que la ONC puede considerarse como la región de formación estelar cercana más típica de la Vía Láctea.

Abstract

Stars form in regions of space where sufficient quantities of matters accumulates, reaching densities high enough to eventually overcome all possible agents able to prevent gravitational collapse, such as thermal and radiative pressure, magnetic field and turbulence. The gravitational collapse is usually hierarchical in nature, often leading to fragmentation over a wide range of sizes. From the largest-scale entities containing thousands of stars to multiple and binary systems, there is always some degree of groupings when star formation is involved (Hopkins 2013; Vázquez-Semadeni et al. 2019). Since the early work of Larson (1972), where the author proposed that all stellar systems were born as multiple ones and the following dynamical evolution would create the mixture of single, double and multiple systems we observe in the field, many steps forward have been made in the understanding of star formation. Thanks to major advancement in sensitivity and resolution of modern observing techniques, it has become increasingly clear that the majority of stars are indeed born in multiple systems whose components will then undergo dynamical interaction leading to ejection of some components either into distant orbits or escape (Reipurth et al. 2001; Reipurth et al. 2010), hardening the remaining binaries and reducing the overall Multiplicity Fraction (MF), i.e. the ratio of non-single system in a given sample (Goodwin et al. 2007).

While more detailed analysis are always needed in order to better understand and constrain key properties of newborn protostars and star formation in general, binarity and multiplicity in general are widely accepted as one of the principal channel for star formation, with the inevitable implication that dynamical evolution is an essential part of early stellar evolution (Reipurth et al. 2014). Studies of binaries and multiple systems during the protostellar phase and later during the Pre-Main Sequence (PMS) phase are indeed fundamental because they offer the perfect stage to observe and analyze the results of fragmentation of molecular clouds, giving meaningful insight in the physics of the

processes at play during these phases. Moreover, binary stars, because are coeval pairs born in the same environment and with the same metallicity but with different masses, represent the perfect laboratory where to inspect key properties of stellar evolution, from the early phases of star formation to the most violent phenomenology that may characterize the final moments of their life. In young systems, knowing the effective temperature and absolute luminosity of a pair can constrain theoretical models developed to predict isochrones and evolutionary tracks on the H-R diagrams during the PMS phase (Gennaro et al. 2012; Stassun et al. 2014). Ignoring the presence of binaries, on the other hand, represents a nuisance that may affect the statistical analysis of the same H-R diagrams (Jerabkova et al. 2019).

To address this (and many others) problems related to the very early stages of star formations, plenty of surveys have bee perform over time. For Class 0/I sources, infrared (Haisch et al. 2004; Duchêne et al. 2007; Connelley et al. 2008a; Connelley et al. 2008b), submillimiter (Chen et al. 2008; Chen et al. 2009; Maury et al. 2010; Enoch et al. 2011; Tobin et al. 2013; Tobin et al. 2018; Hsieh et al. 2020) or radio continuum observations (Rodríguez et al. 2003; Reipurth et al. 2002; Reipurth et al. 2004; Tobin et al. 2019) are generally preferred. PMS stars (T-Tauri Star (TTS) or Class I/II sources) have been studied over a broad range of different environment: dense stellar cluster (e.g. the Orion Nebula Cluster (ONC) as well as IC 348 in the Perseus cloud; Petr et al. 1998; Luhman et al. 2005; Köhler et al. 2006; Reipurth et al. 2007; Duchêne et al. 2018; Strampelli et al. 2020b; Strampelli et al. 2020c), young OB associations (e.g. the Scorpion-Centaurus; Brown & Verschueren 1997); Shatsky & Tokovinin 2002; Kouwenhoven et al. 2007), T associations (e.g. the Taurus-Auriga star forming regions; Kraus et al. 2008; Kraus et al. 2011). Multi-wavelength surveys of nearby star-forming regions, as well as speckle interferometry, adaptive optics, aperture masking and Hubble Space Telescope (HST) High-Contrast Imaging (HCI) (or direct imaging) are just some of the different techniques applied to perform these multiplicity surveys.

Focusing on the latter, HCI comprises a wide group of techniques used to acquire direct image of stars and other bodies very close to their host stars (i.e., capturing photons directly from the source rather than inferring its presence from telltale features of the observed system). This technique can be sensitive to companions as close as a few to few hundred AU whose masses span from planetary mass to brown dwarfs and low mass stars. The main observational challenge in HCI techniques is that objects potentially resolved may be hidden under the extended PSF wings of the primary star. Even though the primary can be suppressed through some sort of suppression hardware (for example a physical part of a telescope that selectively remove the light of the host star blocking its

optical path while retaining all the remaining photons), current attempts, both from the ground with Adaptive Optics (AO) and from space, are limited by a dominating presence of bright quasi-static speckles that completely mask out the faint signal that we are interested in (Schneider & Silverstone 2003; Biller et al. 2004; Marois et al. 2005; Masciadri et al. 2005) that are caused mainly by imperfections in the optics. Soummer et al. (2012) proposed a novel approach to perform PSF subtraction using Principal Component Analysis (PCA). When a suitable library of reference PSF is assembled, the PCA is carried out and a Karhunen-Loéve Image Processing (KLIP) analysis of these references is used to create an orthogonal basis of eigenimages, on which the science image is then projected. The primary goal of PSF subtraction is then, to reconstruct the PSF of an isolated target using the set of reference images and to subtract it from the target image obtaining the candidate astronomical signal. In theory, because the PSF is a continuous random process of the state of the instrument-telescope system at the time the data was acquired, an infinite number of references would be needed to reconstruct it. In practice, the aim is to find the best estimate of the PSF given the limited knowledge provided by the references at hand.

The main focus of this thesis consists in the development and application of a pipeline able to recover faint companions embedded in the host star point spread function in *HST* ACS/WFC3-IR images. To achieve this goal, the method proposed by Soummer et al. (2012) to perform Point Spread Function (PSF) subtraction using PCA will serve as the basic stone from which the whole project is built.

Three papers so far have been the outcome of this project:

- Strampelli et al. (2020a): introduce *Stra*KLIP, the pipeline developed thanks to the collaboration of between the University of La Laguna (Spain), the Space Telescope Science Institute (USA) and the Johns Hopkins University (USA), to detect and characterize faint close-in astronomical signals around bright primaries taking advantage of the KLIP algorithm just introduced.

- Strampelli et al. (2020b): present a first scientific application of *Stra*KLIP on *HST*/WFC3-IR data on the Orion Nebula Cluster (ONC) in filter F130N and F139M.

- Strampelli et al. (2020c): focus on *HST*/ACS visible data of the same ONC, presenting a new PSF photometry for the cluster and a second application of the *Stra*KLIP pipeline itself.

One of the key characteristics of *Stra*KLIP is that it is designed to work with sets of wide-field imaging observations not specifically tailored for HCI analysis. From this point of view, it represents a new tools that can be applied to virtually any large image dataset, either from space (HST, JWST, WFIRST-Nancy GraceRoman Telescope) or from the ground (e.g. LSST-Vera Rubin Observatory).

In Strampelli et al. (2020c), the new ACS photometry has been combined with the precedent WFC3-IR catalog from Robberto et al. (2020), linking together two *HST* Treasury programs (GO-10246 and GO-13826, P.I. M. Robberto) in one unique catalog of sources for the ONC, spanning a wide range of filters from visible bands to infrared (i.e. filters F435W, F555W, F658N, F775W, F850LP, F130N and F139M). Thanks to this wide variety of filters available, a Bayesian approach with Markov Chain Monte Carlo (MCMC) strategy have been adopted to estimate three fundamental parameters through Spectral Energy Distribution (SED) fitting: mass, age and extinction. Three different Initial Mass Function (IMF): Kroupa (Kroupa 2001), Chabrier single and system (Chabrier 2003) and two different reddening laws ($R_v = 3.1$ and 5) have been tested. Overall, we observe that changing the IMF, as well as changing the reddening laws, does not strongly impact the outcoming parameter distributions, even though $R_v = 5$ seems to produce more shallow distributions compared to $R_v = 3.1$ in both the mass and A_V parameters. As representative values for this cluster we find: a median mass between $0.15 - 0.21$ $M_\odot$, a median extinction A_V between $1.64 - 2.42$ magnitudes and a median age between $1.6 - 1.8$ Myr.

In particular, a more in depth analysis of the age distribution for stars in the cluster unveiled the presence of at least two different populations with an average age of $\sim$ 0.85 and 1.6 Myr, strongly supporting the idea that star formation in the ONC was neither just one singular event or a process diluted over a prolonged period of time, but instead is best described by at least two discrete and sequential episodes of star formation over the first few Myr (Beccari et al. 2017).

Taking advantage of the available F658N filter in the survey, accretion luminosity (L_{acc}) and mass accretion rate ($\dot{M}_{acc}$) have been estimated for a sample of $\sim$ 700 bonafide cluster sources, providing one of the most extend catalog of mass accretion rates in the ONC up to-date. The $\dot{M}_{acc}-M_\star$ relationship exhibit two different regimes. On one side, we observe that more massive stars ($M_\star > 0.3$ $M_\odot$) display a rather shallow linear relation that agrees with that predicted in the context of centrally irradiated accretion disks around solar-mass stars with an active accretion layer (Mohanty et al. (2005); Hartmann et al. 2006). On the other, lower mass stars ($M_\star \lesssim 0.3$ $M_\odot$) can be in turn divided in two different populations as well. If we extend the line fitting the higher

mass stars, we see that it nicely matches a population of low mass objects with high accretion rates. There is, on the other hand, a second branch, departing at $M_\star \sim 0.3\ M_\odot$, displaying a steeper relation between $\dot{M}_{acc}$ and $M_\star$. These two low mass populations also display differences in age: one appear younger with higher accretion rate, the other more evolved with a lower mass accretion rate. A decay of the mass accretion rate vs. age is not surprising, but in this case it suggests the coexistance in the ONC of two different young populations. Moreover, an analysis of the extinction of these objects suggest that the older sources typically lie in regions less embedded, i.e. more evolved having been exposed for longer time to the ionizing flux from the OB stars.

Binarity has been one of the main focus of both papers (Strampelli et al. 2020b; Strampelli et al. 2020c). As a result from the first analysis, 39 close-in cluster candidates pairs have been detected, with separation $0.16'' - 0.77''$ and primary mass (M_p) $= 0.015 - 1.27\ M_\odot$ and companion mass (M_c) $= 0.004 - 0.54\ M_\odot$. Of these 39 binary systems, 21 are truly new candidate detections. From the second analysis, instead, only 15 binaries are detected through the *Stra*KLIP pipeline, spanning a range of separation $0.12'' - 0.34''$ and $M_p = 0.032 - 1.38\ M_\odot$ and $M_c = 0.006 - 1.00\ M_\odot$. Of this sample, 5 are truly new detections. 12 of the previously WFC3-IR KLIP binaries are confirmed through this new ACS KLIP analysis.

Combining together both ONC Treasury programs, a new catalog of 119 binaries has been compiled, spanning a range of separations $0.12 - 1.95''$. This catalog comprehend binaries identified by Strampelli et al. 2020b on WFC3-IR data (obtained either from KLIP or from Robberto et al. 2020 catalog) and binaries present in Strampelli et al. 2020c on ACS data (again, obtained either from KLIP or from Robberto et al. 2013 catalog). As a result, once completeness and chance alignment arguments are considered, a new value of the multiplicity fraction for the cluster is establish in the range of $M_p = 0.015 - 1.6\ M_\odot$, $M_c = 0.004 - 1\ M_\odot$: $MF_{ONC} = 13\% \pm 1\%$. Compared to other star-forming regions, the MF_{ONC} is ~ 2 times smaller than e.g. Taurus, while it is still compatible with the value observed in the field over similar range of masses and separations. Also, an overall bottom-heavy mass ratio (q) distribution is found for the binaries in the cluster, very close to the value observed for field binaries in similar range of masses and separations. The binary separation distribution shows two clearly distinct groups of binaries distinguishable by their respective separation: *close* (separation $\lesssim 0.6''$) and a *wide* (separation $> 0.6''$). Moreover, an analysis of the distribution of *wide* over *close* binaries as a function of the distance from the center of the cluster, reveal clear sign of dynamical evolution in its past. Overall, these results hint to the fact that the ONC binaries may represent a good template for the typical population of field binaries, supporting

the hypothesis that the ONC may be regarded as a most typical nearby star-forming region in the Milky Way.

Contents

List of Figures

List of Tables

Acronyms

$\dot{M}_{acc}$ mass accretion rate. xvi, xvii, 53, 133

$L_\star$ star luminosity. 133

L_{acc} accretion luminosity. xvi, 53, 133

$M_\odot$ solar mass. xvi, xvii, xxi, xxii, xxiv, 2, 8, 9, 12, 13, 15, 16, 17, 24, 25, 31, 32, 37, 38, 52, 53, 132, 133, 134

$M_\star$ star mass. xvi, xvii, 53, 133

M_c companion mass. xvii, 9, 52, 53, 132, 134

M_p primary mass. xvii, 9, 52, 53, 132, 134

q mass ratio. xvii, 9, 30, 33, 34, 35, 52, 132, 134

ACS Advance Camera for Surveys. xv, xvi, xvii, 6, 40, 51, 52, 131, 132, 133, 134, 135

ADI Angular Differential Imaging. 42, 43

AO Adaptive Optics. xv, 42

AU Astronomical Unit. xiv, xxi, xxii, 4, 9, 15, 16, 17, 18, 20, 21, 22, 23, 24, 26, 27, 41, 52, 53

AWS Amazon Web Services. 133

BBP Birth Binary Population. 37, 38, 39

BD Brown Dwarf. xxiii, 25, 31, 36

CF Companion Fraction. 25, 26, 27, 28, 29

HCI High-Contrast Imaging. xiv, xvi, 41, 51, 132

HF Higher-order Fraction. 26

HST Hubble Space Telescope. xiv, xv, xvi, xxiv, 6, 40, 47, 48, 51, 52, 131, 132, 133

IBP Initial Binary Population. 30, 35, 37, 38

IMF Initial Mass Function. xvi, xxiii, 30, 31, 32, 38, 39, 52, 133

IR Infrared. xv, xvi, xvii, 4, 6, 40, 51, 52, 53, 131, 132, 134, 135

JHU Johns Hopkins University. xv, 51, 131

KLIP Karhunen-Loéve Image Processing. xv, xvii, xxiv, 43, 47, 48, 49, 51, 134

LOCI Locally Optimized Combination of Images. 43, 47, 48, 49

MCMC Markov Chain Monte Carlo. xvi, 52, 132

MF Multiplicity Fraction. xiii, xvii, 25, 26, 27, 28, 29, 53, 132, 134

MS Main-Sequence. xxii, xxiii, 2, 24, 27, 28, 31, 32, 33, 34, 35

MW Milky Way. 31, 52

ONC Orion Nebula Cluster. xiv, xv, xvi, xvii, xviii, 27, 39, 51, 52, 53, 132, 133, 135

PCA Principal Component Analysis. xv, 44

PMS Pre-Main Sequence. xiii, xiv, 2, 3, 21, 23, 27, 34, 39

PSF Point Spread Function. xiv, xv, xxiv, 40, 41, 42, 43, 44, 45, 46, 47, 48, 49, 52, 131, 132, 134

RDI Reference Differential Imaging. 42, 43

SED Spectral Energy Distribution. xvi, 4, 52, 132

SNR Signal to Noise Ratio. 47, 131

STScI Space Telescope Science Institute. xv, 51, 131

TTS T-Tauri Star. xiv, 3, 4, 34, 39

ULL University of La Laguna. xv, 51, 131

VLM Very Low-Mass. xxii, 25, 28, 35, 36

WFC3 Wide Field Camera 3. xv, xvi, xvii, 6, 40, 51, 52, 53, 131, 132, 134, 135

YSO Young Stellar Object. 4

1

Introduction

Stars are the primary tracers of the structure and dynamical evolution of the universe. Generation after generation, they govern the chemical evolution of barionic matter, providing the conditions that ultimately allow life to appear, evolve, and look back at the universe itself. So it is paramount in astrophysics to understand and properly characterize the steps that bring a star to form.

The idea that stars are born from gravitational condensation of diffuse matter in space is very old, indeed almost as old as the concept of universal gravitational attraction, having been suggested by Newton in 1692. In his first letter to Bentley, as quoted by Jeans (1929), Newton said *"It seems to me, that if the matter of our sun and planets, and all the matter of the universe, were evenly scattered throughout all the heavens, and every particle had an innate gravity towards all the rest, and the whole space throughout which this matter was scattered, was finite, the matter on the outside of this space would by its gravity tend towards all the matter on the inside, and by consequence fall down into the middle of the whole space, and there compose one great spherical mass. But if the matter were evenly disposed throughout an infinite space, it could never convene into one mass; but some of it would convene into one mass and some into another, so as to make an infinite number of great masses, scattered great distances from one to another throughout all that infinite space. And thus might the sun and fixed stars be formed, supposing the matter were of a lucid nature."*

It is only in the past half century that firm evidence has become available that stars form from self-gravitating clumps of diffuse interstellar matter, and it is only in recent decades that a general star formation scenario has been established and grounded on quantitative basis, building on pioneering work

by e.g. Jeans (stability of gaseous clouds, 1902), Hayashi (PMS evolutionary tracks, 1961), Larson (numerical model of collapsing star, 1969). Historically, the great majority of the models of star formation have aimed at building a scenario for the formation of single, isolated stars.

While modelling single star formation is not a trivial problem, it still addresses the most simple case. Following the invention of the telescope (the companion of Mizar, ζ Ursae Majoris, was discovered by Galileo in 1617!), it was soon realized that many stars have companions. Mitchell 1676, pointed out the abundance of double stars. Binary stars have represented first a curiosity, then a tool to determine the main stellar parameters. We now understand the key role they play in shaping cosmic evolution. They originate a variety of dramatic astrophysical phenomena, like Type Ia supernovae used to measure the history of the expansion rate of the universe or the kilonovae, mergers of neutron stars that may produce the majority of elements heavier than Iron.

In the last few decades, however, a new picture has emerged claiming that the standard scenario should aim at explaining the formation of gravitationally bound multiple systems, i.e. binary or multiple stars, rather than singe objects. These developments are grounded on several studies showing that young stars frequently have a higher multiplicity than Main-Sequence (MS) stars in the solar neighborhood (Duchêne 1999; Mathieu et al. 2000). This has led several authors to suggest that most stars are born in multiple systems that are dynamically destroyed during their early lifetime (Simon et al. 1993; Kroupa 1995; Patience et al. 1998).

Before illustrating these last developments, we will start by briefly summarizing the canonical scenario as described by Shu et al. (1987). We will underline later the main factors that have been invoked to explain to the formation of multiple systems.

Observations at mm and sub-mm frequencies suggest that the star formation process begins within *giant molecular clouds*, large structures with mass of the order 10^6 $M_\odot$ and size of several tens of parsecs. Giant molecular clouds are aggregates of *clumps*, smaller units with masses $M_{cl} \sim 10^3 - 10^4$ $M_\odot$ and sizes $R_{cl} \sim 2 - 2.5$ pc. Clumps contain subregions of high gas density, called *cores* (e.g., Myers & Benson 1983), with masses of the order of 1 $M_\odot$ and dimensions ~ 0.1 pc. Cores can be regarded as the precursors of individual stars, or gravitationally bound multiple systems.

Clumps are gravitationally bound and near mechanical equilibrium, supported as a whole against gravitational collapse by the presence of magnetic fields, rotation, and supersonic turbulence. Shu et al. (1987) suggest that magnetic fields represent the primary source of support, given that turbulence

quickly dissipates. More recent studies however, have questioned this conclusion, as we will see later.

With this premises, the star formation process can be summarized in six major phases:

I. Isothermal clouds may be stable, in the sense that an increase e.g. of the external pressure on the cloud can provoke a global compression and thus an increase in temperature and internal pressure to balances the external one. There is a limit, however, beyond which the cloud becomes gravitationally unstable, usually referred to as the critical mass (Jeans mass), of a cloud of certain temperature, size and composition, above which small perturbations rapidly grow.

II. The star formation process begins when a cloud, because e.g. of a density perturbation, "passes the brink of instability" (Shu et al. 1987). At this point the dynamical collapse begins, rapidly increasing the central density toward stellar values. This eventually leads to the prompt formation of a central protostar in hydrostatic equilibrium embedded within an infalling envelope of dust and gas. Generally, the structure will not be spherically symmetric and because of its net angular momentum a disk may develop out of the envelope material. Initially the protostar will accrete material from the infalling envelope, but soon it will start accreting also from its surrounding disk (Shu et al. 1987).

III. Disk accretion, paired with the strong magnetic fields of the rotating protostar, is generally accompanied by mass loss in the polar directions, creating an observable bipolar flow that may carve a cavity into the surrounding residual envelope up to the circumstellar environment (Frank et al 2014). Infall eventually stops because the envelope material runs out, possibly with the contribution of the outflows dissipating the envelopes. As the system evolves, accretion occurs preferentially through the disk (Hartmann et al. 2016).

IV. With the dissipation of the envolelope, and the decrease of accretion of material via direct infall, the young central star (along with its surrounding nebular disk) becomes visible at visible and near-infrared wavelengths as a bona-fide PMS star (TTS stars).

V. Over timescales of the order of a few Myr, also the circumstellar disk finally disappears, possibly leaving behind a cohort of planets (Alexander et al. 2014).

From an observational point of view, the dense, cold gas of prestellar or protostellar cores (Myers & Benson 1983) is generally studied using mm to sub-mm emission. Together with a typical velocity dispersion ~ 0.5 km s^{-1}, they show signatures of infall but lack any indication of a central point source that may have already been formed (Andre et al. 2000; André et al. 2009). The presence of a deeply embedded infrared sources is the general signature of a protostar. In a classic study of the Ophiucus star forming region, Lada & Wilking 1984 found that the IR-sources could be divided in morphological classes based on the shape of their SED. The resulting morphological classes (shown in Figure 1.1) can be grouped in four distinct entity: Class 0, I, II, and III sources (Class 0 sources were actually introduced later by Andre et al. 1993).

A Class 0 object can be regarded as the result of the initial contraction process. It represents the youngest accreting protostar. In this stage most of the mass of the system is still in the surrounding dense envelope opaque at visible and near-IR radiation. As the protostar evolves in a Class I Young Stellar Object (YSO) (Lada 1987), the envelope dissipates and the protostars becomes visible at short wavelenghts (TTS star). These objects are identifiable by a SED broader the black body curve past $\sim 2\,\mu m$, an indication of the existence, besides the stellar photosphere, of circumstellar material of lower temperature. Class I sources are in fact surrounded by disks with radii of $100 - 1000$ AU and still present an infalling, extended envelope. Once the cirumstellar envelopes are fully cleared, the new source is labeled as Class II. These are typically visible sources, although the presence of a disk seen nearly edge-on can occasionally play a role blocking the observer line of sight to the central object. These sources also posses a broader than an isothermal black body SED, but the flux is flat or decreasing past $2\,\mu m$. The SED of Class III sources finally can be modeled as a nearly isothermal, reddened black body with small or negligible IR excess and therefore represents the last phase before the source reaches the main sequence.

The need of explaining the formation of multiple systems, basically ignored in the standard scenario we have summarized (sort of "heliocentric bias", Kratter 2011), was recognized very early in astronomy. Kuiper (1935) first argued that determining empirically the multiplicity frequency and distribution of key orbital parameters of binary systems would prove to be highly valuable to establish a theoretical framework for their formation. The frequency and properties of multiple systems, how they depend on the mass of the primary and on the environment in which they form, must contain the imprint of the physical process which the systems, and the stellar population in general, went through at the epoch of formation. A better understanding of these properties provides benchmarks for formation scenarios that must depart from the one established

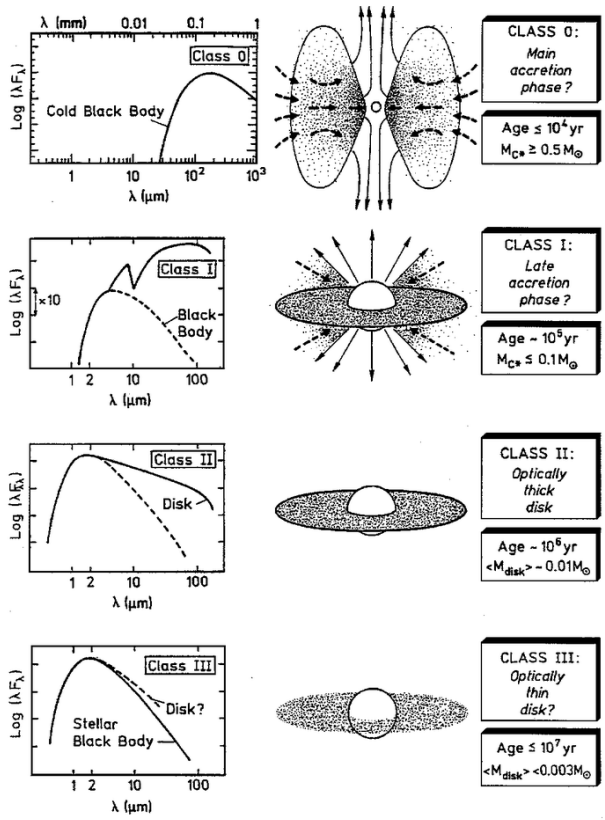

FIGURE 1.1— Classification of young stellar objects based on the spectral energy distribution (left) and schematic diagrams of each stage (right). From:Palla 1996.

for single stars.

This is an area of intense theoretical research and in the last twenty years many steps forward have been made since the reviews of Mathieu (1994) and Tohline (2002). The main physical mechanisms can be roughly divided into three categories (1) core mediated processes, (2) disk mediated processes, and

(3) few-body dynamical processes in young clusters, (Kratter 2011), their dominance following some sort of timeline. Each category can embrace a variety of scenarios depending e.g. on the importance attributed to turbulence, rotation and magnetic support.

We will return to some of these details in Chapter 2, after having provided a brief summary of the fundamental parameters and equations of star formation (§2.1 to §2.3) and of the impact that the characterization of multiple systems has on the theory of star formation (§2.4 to §2.7), focusing on the latest multiplicity surveys. This chapter will set the stage and motivations for the research program presented in the following chapters. After introducing the observational strategies and techniques that have been adopted to detect multiple system with direct imaging observations (§2.8), in §3 we will introduce the three projects that represent the core product of the research program and that have been recently presented in the format of refereed paper (one published, two under review at the time of this writing). For convenience, they will be reproduced in the following chapters. The first one focuses on the *Stra*KLIP pipeline that has developed to perform PSF subtraction (§4). The second and the third are based on data taken with the best imaging cameras currently available, namely *HST* WFC3-IR and ACS onboard the Hubble Space Telescope, and deal with the detection and characterization of the substellar and planetary-mass companions in the Orion Nebula cluster, respectively presented in §5 and §6. The conclusions of this program will be provided in the closing chapter §7.

2

Part 1: Origin of stars

2.1 Basic physical parameters

In order to characterize the processes that bring the collapse of a protostellar gas cloud to the formation of a single or multiple system, we need to introduce the main physical parameters at play during this process. The following discussion will follow Tohline (2002) review on the "origin of binary stars".

The mean mass density of a protostellar cloud can be defined as:

$$\overline{\rho}_{cl} \equiv \frac{3M_{cl}}{4\pi R_{cl}^3} \tag{2.1}$$

where M_{cl} and R_{cl} are the mass and radius of the cloud, respectively. The corresponding number density is defined as:

$$n = \frac{\overline{\rho}_{cl}}{\mu m_p} \tag{2.2}$$

where m_p is the mass of a proton and μ is the mean molecular weight.

Under slow (reversible) adiabatic compression, the temperature of the cloud will depend on the efficiency of radiative cooling. If the density is low, photons can escape and the cloud will be approximately isothermal. Viceversa, the loss of energy will be negligible and the temperature of the protostellar cloud (T_{cl}) will follow the polytropic relation:

$$T_{cl} \propto \overline{\rho}_{cl}^{\gamma-1} \tag{2.3}$$

where γ is the effective adiabatic exponent of the gas, e.g. $\gamma \simeq 7/5$ for H_2 (that become rotationally excited and emits efficiently only above $T_{cl} \sim 300$K) and, at

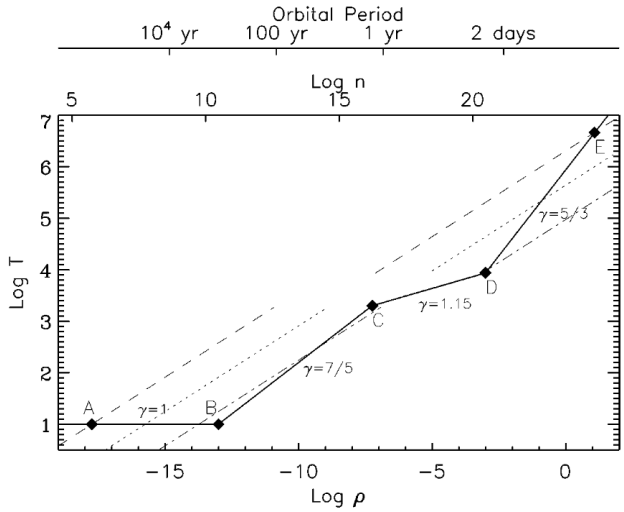

FIGURE 2.1— The solid curves shows the evolutionary trajectory of the central region of a protostellar gas cloud in the temperature-density plane. The density is shown both in g cm^{-3} (bottom horizontal axis) and in cm^{-3} (top horizontal axis); the temperature is given in degrees Kelvin. Also shown at the top of figure the corresponding orbital period of a binary. As reference, lines of constant M_{eq}, as defined by Equation 2.16, have been drawn at values of 1 $M_\odot$ (dashed), 10^{-1} $M_\odot$ (dotted), and 10^{-2} $M_\odot$ (dash-dot); the vertical gap between temperatures of 2,000 K and 10,000 K signifies that the molecular gas is being dissociated and ionized; hence, μ changes from 2 (lower section of each line) to 1/2 (upper section of each line). From: Tohline (1982)

temperatures high enough that H_2 is dissociated, $\gamma = 5/3$ for neutral hydrogen, HI.

Figure 2.1 shows the enormous range of temperatures and, especially, densities a stellar-mass core has to traverse while contracting from molecular cloud conditions toward a structure hot and dense enough to ignite hydrogen. The different segments of this curve have been labeled with the value of the effective adiabatic exponent γ that governs the polytropic relation given in eq. 2.3. One can immediately recognize two nearly isothermal phases and two adiabatic ones, regulated by molecular and atomic cooling. We will come back many times to this plot during the following discussion.

When discussing binary systems, a few key parameters need to be introduced:

- the system mass $m_{syst} = M_p + M_c$ and mass ratio $(q) = \frac{M_c}{M_p} \leq 1$;
- the period P of the system

$$P = \left[\frac{4\pi^2 a^3}{Gm}\right]^{1/2} \tag{2.4}$$

  where a its semi-major axis and G the gravitational constant. This expression holds for both circular and elliptical orbits.

- the eccentricity $e = \frac{r_{apo} - r_{peri}}{r_{apo} + r_{peri}}$ where r_{apo} and r_{peri} are the apo- and pericentric distances of the secondary-star.

When P is expressed in year, a in AU and m_{syst} in $M_\odot$, these three properties are easily related through Kepler's Third law:

$$\frac{a_{AU}^3}{P_{yr}^2} = M_p + M_c \tag{2.5}$$

Discussing the formation scenario of binary systems, there are three key time scales that must also be kept in mind:

- The free-fall time (i.e. the characteristic time that would take a core to collapse under its own gravity if no other forces were present to oppose the collapse:

$$\tau_{ff} = \left[\frac{3\pi}{32 G \overline{\rho}_{cl}}\right]^{1/2} \tag{2.6}$$

  where G is the universal gravitational constant. This formula derives from the Virial Theorem, discussed in Sec.2.2.

- The sound-crossing time, i.e. the time for a sound wave to travel a distance, r, inside a medium:

$$\tau_s = \frac{r}{c_s} \tag{2.7}$$

  where $c_s = \left[\gamma \frac{\mathcal{R} T_c}{\mu}\right]^{1/2}$ is the isothermal sound speed, $\mathcal{R}$ is the perfect gas constant and T_{cl} is the temparature of the core.

- The rotational period of the core:

$$\tau_{rot} = \frac{2\pi}{\omega} \tag{2.8}$$

where ω is the mean angular velocity of the core.

2.2 Virial Theorem and Jeans Mass

The virial theorem (e.g. Hansen & Kawaler 1994) expresses the condition of equilibrium for a protostellar gas cloud as:

$$2(E_{therm} + E_{rot}) + E_{grav} = 0 \tag{2.9}$$

where E_{therm}, E_{rot} and E_{grav} are the thermal, rotational and gravitational energy of the cloud defined as:

$$E_{therm} \sim \frac{3\mathcal{R}}{2\mu} M_c T_c \tag{2.10}$$

$$E_{rot} = \frac{1}{2} I\omega \sim \frac{1}{5} M_c R_c^2 \omega^2 \tag{2.11}$$

$$E_{grav} \sim \frac{-3GM_c^2}{5R_c} \tag{2.12}$$

where $I \simeq \frac{2}{5} M_c R_c^2$ is the configuration's principal momentum of inertia. If we divide eq. 2.9 by $|E_{grav}|$, we can define:

$$\alpha \equiv \frac{E_{therm}}{|E_{grav}|} \sim \frac{5}{2} \frac{\mathcal{R}}{\mu} T_c \frac{R_c}{GM_c} \tag{2.13}$$

and

$$\beta \equiv \frac{E_{rot}}{|E_{grav}|} = \frac{1}{3} \frac{R_c^3 \omega^2}{GM_c} \tag{2.14}$$

and the virial equilibrium condition can be rewritten as:

$$\alpha + \beta = \frac{1}{2} \tag{2.15}$$

Eq. 2.15 states that if the sum of thermal and rotational energy does not balance gravitational energy, i.e. $\alpha + \beta < \frac{1}{2}$, then the gas cloud collapses under its own gravity. If rotation is negligible ($\beta << 1/2$) then equilibrium requires

$\alpha \simeq 1/2$. This condition of equilibrium can be expresses as a relation between mass, temperature and radius (or temperature and mean mass density):

$$M_j \sim 5\frac{\mathcal{R}}{\mu}T_c\frac{R_c}{G} \sim 5.5\left[\frac{\mathcal{R}T_c}{\mu G}\right]^{3/2}\overline{\rho}_{cl}^{-1/2} \tag{2.16}$$

This critical mass value, corresponding to the thermal vs. gravitational equilibrium of a cloud of given temperature, radius, and chemical composition is called "Jeans Mass". If the cloud has a mass larger than the Jeans mass, the gravitational energy dominates over thermal energy and the cloud will contract; the reduction of radius (or increase of mean mass density) further reduces the Jeans mass; the process is thus dynamically unstable, i.e. the cloud collapses.

The same equations can be solved for the maximum radius that a cloud of given mass, temperature and chemical composition can have to maintain equilibrium between gravitational and thermal energy:

$$R_J = \lambda_j \sim \sqrt{\frac{\mathcal{R}T_cR_c^3}{\mu G M_c}} \sim \sqrt{\frac{\mathcal{R}T_c}{\mu G}}\overline{\rho}^{-1/2} \tag{2.17}$$

where we have introduced the Jeans's length λ_J, since this critical radius also represents the wavelength of the shorter "global" perturbation that may trigger instability (Jeans 1902). Perturbations of shorter wavelength are "local" and propagate through the cloud as sound waves allowing pressure to maintain hydrostatic equilibrium.

A collapsing cloud has $\alpha + \beta < \frac{1}{2}$, viceversa an expanding cloud. Equilibrium requires $\alpha + \beta = \frac{1}{2}$ or, neglecting rotation, $\alpha = \frac{1}{2}$. However, due to the dependence of the temperature on the density, a second condition must be satisfied on the thermodynamic status of the gas. Assuming the mass of the cloud M and the angular momentum J are conserved during the process, then:

$$\alpha \propto TR \propto \overline{\rho}_{cl}^{\gamma-4/3} \tag{2.18}$$

and

$$\beta \propto R^{-1} \propto \overline{\rho}_{cl}^{1/3} \tag{2.19}$$

Eq. 2.18 clearly shows the primary role of γ in the star formation process. An adiabatic index $\gamma < 4/3$ means that as ρ increases during a contraction ($\alpha < \frac{1}{2}$), the energy ratio α further decreases, i.e. the cloud is unstable. Stability requires $\alpha = \frac{1}{2}$ and $\gamma > 4/3$. During the initial isothermal phase, $T = \rho^{\gamma-1}$ =const, thus $\gamma = 1 < 4/3$: if $\alpha < \frac{1}{2}$ an isothermal cloud can collapse. A change of the mean molecular weight due to molecular dissociation (at low temperatures) or

atomic ionization (at higher temperatures) causes a change of γ. In the case of molecular gas, values $\gamma \simeq 7/5$ are obtained when the gas temperature is high enough to excite the roto-vibrational level of H_2. Fully ionized gas has $\gamma = 5/3$. Both values are larger than $4/3$, indicating that during these phases the tendency will be to increase α, i.e. the collapse will slow down.

2.3 Formation of a single protostar

2.3.1 Protostellar Collapse

The processes that may trigger the gravitational collapse are not fully understood (Larson 2003), but two main scenarios have been identified: a) collapse begins with a marginally stable clump of gas in which a density fluctuation allows gravity to dominates over thermal pressure and cause a runaway collapse (Hayashi et al. 1986); b) a prestellar core initially magnetically supported condenses gradually by ambipolar diffusion. As the neutral gas contracts slowly across the field lines, the core becomes increasingly centrally condensed and increasingly supported by thermal pressure, eventually reaching the configuration of singular isothermal sphere with no magnetic support, an unstable configuration (Shu et al. 1987).

Regardless of the triggering mechanism, the first phase of collapse happens in a core extremely rarefied and in nearly isothermal conditions. Simulations show that a low density $\sim 1\ M_\odot$ core is optically thin to its own radiation (i.e. it cools efficiently due to thermal emission by dust grains, maintaining isothermal conditions). Simulations also show that the collapse of an isothermal core is highly non-uniform and results in the runaway growth of a central, density peak. As the inner layers of the core increase their density, their free-fall time decreases (see eq. 2.6) while their outer edge provides an outward pressure gradient that slows down the collapse of the outer layers. The collapse of the inner regions produces a rarefaction wave that propagates inward at the sound speed (see eq. 2.7). With the inner regions collapsing faster than the less dense outer regions, a central density peak is generated while the rest of the collapsing core assumes a characteristic $\rho \propto r^{-2}$ density profile for an isothermal medium, or more in general $\rho \propto r^{-2/(2-\gamma)}$ for a polytropic medium with $P \propto \rho^\gamma$. Calculations indicate that the central density peak contains only a very small fraction of the mass of a collapsing core. In order to form a star at the center of a spherically collapsing core almost all of its final mass must be acquired through accretion from the infalling envelope.

At some point the density of the central density peak becomes large enough, about $\rho_{crit} \sim 10^{-13}$ g/cm^3 for a $\sim 1\ M_\odot$ core (point B in Fig. 2.1) that the optical depth prevents radiation from escaping. Retaining its own thermal

energy, the temperature at the center rises above its initial value of $T \sim 10$ K. At densities above 10^{-12} g/cm^3 the gas is completely in adiabatic regime with $\gamma \simeq 7/5$ (Larson 1972; Tohline 1982; Masunaga & Inutsuka 2000). As the density continues to rise, pressure increases faster than gravity and the collapse decelerates, essentially coming to a halt when the central density reaches about 2×10^{-10} g/cm^{-3}. The central density peak reaches hydrostatic equilibrium conditions and continues to grow accreting material through an accretion shock formed at its surface.

The life-time of this first hydrostatic core is much shorter than the previous adiabatic contraction phase. When $\sim 0.1\ M_\odot$ has accumulated in the core, the temperature reaches $T \sim 1000$ K and at this temperature dust evaporates depressing this cooling channel ("opacity gap"). Also, above this temperature collisions have enough kinetic energy to provide the 4.5 eV binding energy needed for H_2 dissociation, eliminating this other cooling channel. On the other hand, the transforming of thermal energy in chemical energy tends to stabilize the temperature. The competition between these heating and cooling mechanisms can be studied through numerical simulations, that show that the temperature remains nearly constant, i.e. $T \sim \rho^{0.15}$. Since $\gamma \simeq 1.15 < 4/3$, the inner part of the first core resumes collapsing ("*second collapse*") transitioning from point C to D in Fig. 2.1.

At $T > 3,000$ K the hydrogen starts ionizing, becoming fully ionized at T$\sim 10,000$ K. Since free electrons can absorb and scatter photons of any wavelengths, the gas becomes again optically thick and the core becomes again fully supported against gravitational energy by thermal pressure with $\gamma = 5/3$. Note that at low masses the support is provided by electron degeneracy pressure, but also in this case $\gamma = 5/3$. A contracting second hydrostatic core of ionized hydrogen develops (transition from point D to E in Fig. 2.1). This second hydrostatic core is a true protostar (Tohline 1982). If $M \gtrsim 0.075\ M_\odot$, it will contract along the Hayashi track to reach Hydrogen burning and the main sequence, otherwise it will continue to slowly cool down as a degenerate object and fade away as a brown dwarf.

To summarize, a 1 $M_\odot$ spherical core can achieve virial equilibrium in only two places along the evolutionary track shown in Fig. 2.1: in A ($\overline{\rho}_{cl} \sim 1.8\ 10^{-18}$ gcm^{-3}, T$\sim$ 10 K), or in E ($\overline{\rho}_{cl} \sim 12$gcm^{-3} and T$\sim$ 5 10^6 K), with the only stable configuration found at point E since $\gamma = 5/3 > 4/3$. Thus, once the Jeans instability is reached in A, the dynamical collapse proceeds in a free-fall like timescale until a star-like configuration is reached, with almost 19 orders of magnitudes density increase!

2.3.2 Rotating cores

In principle, rotation can provide the balance against gravity in the core, and in particular even when $\alpha << \frac{1}{2}$ one can still have $\beta \simeq \frac{1}{2}$. In this case, from the virial theorem it follows that the core's mean angular velocity needed to sustain equilibrium must be close to its maximum possible value (i.e. $\omega \simeq \omega_{max} \simeq [2G\pi\overline{\rho}_{cl}]^{1/2}$) and thus the core's rotational period will be:

$$\tau_{rot} = \frac{2\pi}{\omega} \simeq 4.6\tau_{ff} \tag{2.20}$$

When rotation is introduced, the free-fall collapse can be prevented at much lower densities, with a tendency to stability because the contribution of β always increases as the core contracts (see eq. 2.19). During contraction there will be a tendency for the core as a whole to drop α to very small values while $\beta = 1/2 - \alpha$ rises to a value $\simeq 1/2$. Hence, even during the initial isothermal phase of core's contraction, virial equilibrium can be achieved. Still, approaching the virial equilibrium condition $\alpha + \beta = \frac{1}{2}$ is not enough to guarantee stability against future collapse. [Ledoux (1945) analyzed the stability of a nearly spherical rotating system finding that the original stability condition $\gamma > 4/3$ for a non-rotating core now becomes:

$$\gamma > \gamma_{crit} \simeq \frac{2(2-5\beta)}{3(1-2\beta)} \tag{2.21}$$

When $\beta \to 0$, then $\gamma_{crit} = 4/3$ consistent with the case of non rotating cores. When $\beta \neq 0$, then $\gamma_{crit} \lesssim 4/3$. Eq. 2.21 shows that a rotating, isothermal ($\gamma_{crit} = 1$) sphere, cannot be stable against further collapse unless $\beta > 1/4$. Departing from spherical symmetry has minor effect on this value, i.e. rotationally flattened, axisymmetric, isothermal gas cores are stable against dynamical collapse (or expansion) ony if $\beta \gtrsim 0.25 - 0.3$ (Hayashi et al. 1982; Tohline 1984; Hachisu & Eriguchi 1985).

2.4 Formation of binary and multiple systems

Thanks to major advances in our physical understanding of the fragmentation process, the collapse and fragmentation of molecular cloud cores (Boss & Bodenheimer 1979) is generally regarded as the most likely mechanism behind the formation of the majority of multiple systems (see, e.g. Shu et al. 1987; McKee and Ostriker 2007; Reipurth et al. 2014), a mechanism well supported by different simulations (Bodenheimer et al. 2000; Tohline 2002; Goodwin et al. 2007; Hansen et al. 2012). Before discussing the main fragmentation modes, generally classified depending on the time when the fragmentation happens during

the different collapse phases of the core, we briefly illustrate the historic *capture* mechanism that recently has been evoked to explain the existence of the most exotic binary stars.

2.4.1 Capture

Clump/filament fragmentation occurring before the collapse of the individual cores can result in single cores that through random encounters may become gravitationally bounded ("capture"), with separations of $\sim 10^3 - 10^4$ AU (Kauffmann et al. 2008; Launhardt et al. 2010). Such encounters should be rare and require the dissipation of significant amounts of energy, possibly transferred to a third body ("three-body capture") ejected with substantial kinetic energy. In the case of close encounters, the deformation of the stellar structure caused by tidal interactions can also dissipate energy and produce a binary, but very favorable initial conditions are needed to produce a bound system. As a consequence, this process (that would only produce very tight binaries) may only play some role in the densest environments. A version of this process where the tidal interaction involves circumstellar disks may extend the range of interaction, but overall capture mechanisms do not seem capable of explaining the formation of most binaries. The situation can be entirely different if the binary pairs, or multiple systems, are already formed (Fujii et al. 2012). In this case the capture/ejection process may become much more efficient and may lead to the formation of bound massive stars in massive ($\sim 10^5 - 10^6$ $M_\odot$) dense clusters ($\rho \sim 10 - 100$ $M_\odot \mathrm{pc}^{-1}$,Fujii & Portegies Zwart 2013). These systems are the possible precursors of the pairs of collapsed objects (black holes and neutron stars) that through their mergers have originated the spectacular gravitational waves event recently detected with LIGO/VIRGO (Smartt et al.(2017)).

2.4.2 Core Fragmentation

Fragmentation can take place either during or just after the core's isothermal collapse phase ("prompt fragmentation", Boss 1986). Fragmentation occurs because initial density perturbations that are gravitationally unstable will rapidly grow in amplitude (the free-fall time depends on the density as $t \propto \rho^{-1/2}$, as shown by Eq. 2.6) producing fragments with typical separation $\sim 10^2 - 10^3$ AU (Tohline 2002). Another way to describe this process is to look at the Jeans mass: we have seen that the Jeans mass depends on $T^{3/2}\rho^{-1/2}$. Contracting cores increase both their temperature and density, but as long as the $rho^{-1/2}$ grows more rapidly than $T^{3/2}$ (the isothermal case), the Jeans mass will decrease, enabling local density fluctuations of smaller mass to collapse breaking the core into multiple subcores. The fragmentation process may repeat sequen-

tially as long as the local conditions, e.g. temperature and chemical composition (or equivalently the isothermal sound speed $c_s = \sqrt{\mathcal{R}T/\mu}$) allow the fragments to radiate away the PdV energy gained with their isothermal compression. However, as shown in Figure 2.1, at some point (B) the density of the subcores will become so high that radiation will not be efficiently transported outside. At that point the adiabatic index increases, and the Jeans mass cannot decrease any further: hierarchical fragmentation stops. This *opacity limited fragmentation* limit sets the minimum mass of a protostar, about 10^{-2} $M_\odot$.

Detailed analyses of this process have been largely carried out through numerical simulations, but some of the main characteristics can be illustrated by analogy with the case of single isolated stars. A collapsing rotating cloud, highly unstable ($\alpha << 1/2$) evolves through a homologous sequence of flatter and flatter pressure-free oblate ellipsoid configurations, until the cloud becomes very flat, decelerating and eventually becoming supported in the equatorial plane by its angular momentum ($\beta \simeq 1$). A slowly rotating core may enter the adiabatic phase before the collapse begins to slow down, split in fragments with separation of $\sim 3 - 300$ AU (Machida et al. 2005a; Machida et al. 2008).

Viceversa, if the rotating cloud is marginally supported ($\alpha \lesssim 1/2$ initially) it will develop a central condensation that will collapse ahead of the rest of the cloud reaching an equilibrium configuration ($\alpha + \beta \simeq 1/2$) and possibly stop contracting depending on the values of γ and β, while the outer regions will still be contracting and accreting over their much longer time-scales. Simulations show that these nonhomologous collapses do not generally lead to fragmentation (Tohline 2002).

In any case, the inner part of a rotating core reaching hydrostatic equilibrium will contain just a small fraction of the cloud's initial mass. It will be surrounded by a an accretion disk that will add material with high specific angular momentum. It has been proposed that the increase of rotational vs. gravitational energy (β ratio) will cause the core to deform into an elongated pear-shaped surface that will become more and more elongated, breaking eventually into two separated masses: this process, the classic "fission" theory of binary formation, that has now been largely discredited on the basis of dynamical (stability) and physical (viscous dissipation) considerations.

2.4.3 Disk fragmentation

Star-disk interactions, or a self-gravitating disk itself may generate instabilities resulting in nonaxysimmetric long-wavelength structures (e.g. two-armed spiral arms) that may fragment in clumps containing a sizeable fraction of the disk mass (Kratter & Lodato 2016). Close encounters between stars can also trigger

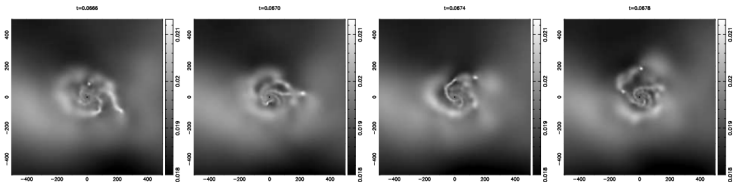

FIGURE 2.2— Evolution of a CAR in a turbulent molecular core. The sides of the boxes are 1000 AU. The timescale runs from 66.6 to 67.8 kyr in step of 400 yrs. The gray color bar shows the value of the density in each plot. From: Goodwin et al. (2004)

instabilities in circumstellar discs which in turn can lead to the fragmentation of otherwise stable discs (Bonnell 1994). Since these encounters have to occur mainly during the Class 0 phase, when the disk mass is still a major component in the total mass of the system, this constrain put a serious limit on the time at disposal for this interaction to be effective, about 10^5 yr.

Figure 2.2 shows the formation of a fragment in a mildly-turbulent, rotating 5.4 $M_\odot$ core, a simulation based on observations of the isolated core L1544 (Goodwin et al. 2004). Fragmentation happens in a 'disk-like' feature in the circumstellar accretion region (CAR). Fragmentation can occur when two conditions are met. First, the density in the spiral waves becomes high enough that their typical width becomes smaller than the Jeans length (the critical size below which a small perturbation becomes unstable to gravitational collapse). Second, the collapse time must be small enough compared to the local rotation period that the density enhancement may escape being diluted by differential rotation. In these simulations, fragmentation occurs for some regions that exceed $\sim 10 - 12\ g\,cm^{-3}$ in density (corresponding to a Jeans length of ~ 20 AU) beyond $\sim 50 - 100$ AU from the central star.

While disk instability remains a very active field of research, being also related to the key problem of planet formation, there is still general agreement that prompt fragmentation is the preferred mechanism for the formation of binary stars due to the fact that a well-defined massive disk comparable to the central source is very hard to form early on when the central source is still very low in mass and the disk itself is a much "fluffier" structure (Boss 1988).

2.4.4 Close binary formation

Very close binaries with separations of the order of a few AU represent the main theoretical challenge. Observationally they can hardly be spatially resolved

and thus are classified as "spectroscopic binaries" since their orbital motion can be more easily measured with radial velocity techniques. Spectroscopic binaries generally posses semi-major axis measurable in units of stellar radii, rarely exceeding a few AU. This close separation cannot be the outcome of a "classical" formation process, but it is probably the product of a spiral-in process through the viscous circumstellar medium during the protostellar phase of the system (Gorti & Bhatt 1996; Stahler 2010; Korntreff et al. 2012), and/or in the framework of the capture scenario, with the hardening mechanism associated to the ejection of companion star during a close encounter. The formation of close binaries and compact triples can be also traced to disc fragmentation followed by accretion-driven inward migration. The prevalence of triple and higher order multiple systems among close binaries is not casual, but probably derive from the fact that high accretion create massive stars who in turn have a large fraction of close in binaries and hierarchical systems (Tokovinin 2020) As discussed by (Stahler 2010), the ultimate product of this process can be an early merger if the sustained infall of matter from the envelope feeds orbital decay. Recently, Bally et al. 2020 analyzed the proper motion of three stars ejected from Orion's OMC1 cloud core finding that Src I is suspected to be either a very tight binary (with a separation of the order of a few AU) or protostellar merger remnant, product of dynamical interactions happened ~ 550 yr ago.

2.4.5 The role of turbulence

So far we have largely neglected the role of turbulence, but the width of the emission lines detected in molecular clouds is usually too large for thermal broadening, an indication that the gas is in a status of supersonic turbulence. Turbulence removes ordered kinetic energy from the largest scales to smaller scales, down to microscopic levels. In a turbulent flow there is a scaling relation between the velocity dispersion and the typical size of the region: moving to smaller scales, different points have smaller velocity differences. Therefore, under a certain "sonic" scale turbulence is subsonic, pressure becomes important and an hydrostatic treatment becomes appropriate. But over large scales supersonic turbulence cannot be ignored, and hydrostatic equilibrium is just an approximation (de Jong et al. 1980; Shu et al. 1987; Mouschovias 1991).

Supersonic turbulence, with Mach numbers $M \simeq 5 - 20$ (Zuckerman & Palmer 1974), drives shock waves that produce local density enhancements, become Jeans unstable and induce fragmentation and further collapse (**?**; Delgado-Donate et al. 2004; Delgado-Donate et al. 2004). In fact, supersonic turbulence has been invoked to generate the seeds of initial higher density from which a protostellar core can grow (Ballesteros-Paredes et al. 2007 and reference therein).

These density peaks involve only a small fraction of the total mass, making supersonic turbulence a key mechanism to determine the number and type of stars forming in a molecular cloud, i.e. the star formation efficiency and the initial mass function (see Section 2.6.4).

To quantify the level of turbulence we can define (in a similar way to eq. 2.13 and 2.14):

$$\delta = \frac{E_{turb}}{|E_{grav}|} \tag{2.22}$$

where E_{turb} is the kinetic energy related to turbulent motions. Simulations of turbulent core ranges for 'slightly turbulent', where $\delta = 0 - 0.25$ to 'highly turbulent' where $\delta = 1$. Simulations show that even very low turbulence level (where $\delta \sim 0.025$) are sufficient for cores to fragment. The number of emerging fragments seems to be relate to the level of turbulence adopted (Goodwin et al. 2004; Bate 2000b).

2.4.6 The role of magnetic fields

Because fragmentation is expected at densities $\sim 10^{-13}\ gcm^{-3}$ (see Section 2.3.1 and point B in Fig. 2.1) at which point the magnetic field is supposed to be still decoupled from the gas due to extremely low fractional ionization (Tohline 2002), magnetic fields are not generally considered to play a key role in the fragmentation of a molecular cloud. However, the simulations by Machida et al. 2005a; Machida et al. 2005b on the effect of magnetic fields on fragmentation find that $\sim 50\%$ of rotating, magnetized clouds can fragment if either the rotation is relatively high or the magnetic field strength is particularly low. Other simulations of magnetized rotating clouds support this view, showing that the fragmentation tends to be suppressed if magnetic fields are significant (Hosking & Whitworth 2004; Machida et al. 2005b; Price & Bate 2007). On the other hand, Boss (2002), Boss (2004) find that the opposite is true, so the debate is still open.

2.5 Early dynamical evolution of multiple system

Since the early work of Larson (1972), where the author proposed that all stars where born as multiple systems and the following dynamical evolution would create the mixture of single, double and multiples observed in the field, many studies have been carried out to determine the formation rate of multiple systems. Thanks to the constant progress in sensitivity and resolution of modern observing technique, it has become increasingly clear that the majority of stars are indeed born in multiple systems whose component undergo dynamical interaction leading to ejection of some components either into distant orbits or

escape (Reipurth et al. 2001; Reipurth et al. 2010). This dynamical evolution will reduce the overall multiplicity fraction (i.e. the ratio of non-single system in a given sample, see Section 2.6.1), hardening at the same time the surviving binaries (Goodwin et al. 2007).

Several papers (Chen et al. 2013; Duchêne & Kraus 2013; Reipurth et al. 2014) have shown that, in the case of visual binaries, the number of multiple systems appears to decrease since the very early stage of star formation from Class 0 to II and to field stars, a clear indication that very early dynamical evolution is in place. This may be consistent with the scenario proposed by Connelley et al. (2008a), Connelley et al. (2008b) where a large number of companions with separations $>\sim$ 1000 AU is ejected during the Class 0 phase but remain gravitationally bound due to the much more significant mass of the Class I envelope. As the envelope dissipate, these wide companions become unbound and their frequency at large separation declines. This implies that Class I protostars are not dynamically pristine, but have experienced dynamical evolution even before becoming visible as Class I objects, with implications on our capability of reconstructing the cluster evolution from dynamical studies. Sadavoy & Stahler (2017) studied the relationship between young, embedded binaries and their parent core in the Perseus Molecular Cloud finding that the majority of embedded binary are found toward the center of their parent core. Binaries with separation larger than $\sim$ 500 AU show a tendency to be aligned with the long aces of their parent core. On the contrary, tighter binaries show no preference at all. The authors tested their observations versus different evolutionary models, finding that the best way to explain their observation is to assume that all stars formed as wide binaries, and these binaries either brake-up or shrink into tighter binary.

Figure 2.3 shows the companion fraction vs separation and the binary fraction vs the spectral index (a proxy for the age, tracing the amount of circumstellar material) for a sample of 189 Class I sources investigated by Connelley et al. (2008a), Connelley et al. (2008b) (among which the authors detected a total of 89 companions). Even though different definitions of spectral index have been used in the literature, the authors adopted the convention set by Lada & Kylafis (1991), where the spectral index $\alpha = -dlog\,\nu F_\nu / dlog\,\nu$. In this convention, Class 0 and I YSOs have a positive spectral index, whereas Class II and III objects have a negative spectral index from $\sim 10\,\mu m$ to $\sim 100\,\mu m$. The right panel of the figure in particular, shows a decline of the binary function for wide binaries when plotted against the spectral index, supporting the scenario in which multiple systems dynamically interact and eventually break up producing the field distribution of singles, binaries, and higher-order multiples. Intriguingly, Connelley et al. (2009) studied a sample of 47 protostars

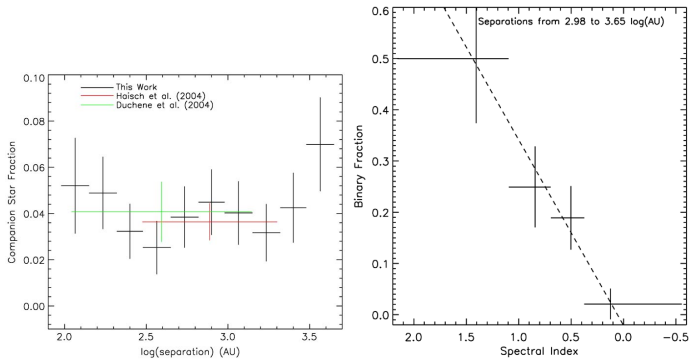

FIGURE 2.3— Left: Separation distribution function of embedded protostellar binaries. Right: Population of wide companions (separations larger than 1000 AU) is found to disappear with decreasing spectral index α (age proxy). From: Connelley et al. (2008a) and Connelley et al. (2008b)

finding that every target with a close-in companion also has a second young star within a projected separation of $\sim$ 25000 AU, pointing to the possibility of a loose ternary system. Similar trends are also observed in Taurus for Class II/III sources as well (Joncour et al. 2017).

From a theoretical point of view, the most refined hydrodynamical simulations of star cluster formation from the collapse and fragmentation of turbulent molecular clouds predict a high number (N $\simeq 5-10$) of fragments per core (Delgado-Donate et al. 2004; Goodwin et al. 2004; Goodwin et al. 2004) unless radiative feedback from newly formed protostars is taken into account, which halts the production of new fragments in dense molecular core (Bate 2009). Since dynamical decay tends to dilute the multiplicity fraction faster when multiple system of higher order are involved (Goodwin & Kroupa 2005), high order multiplicity would pollute the PMS stellar population with a majority of single stars which is not what we observe. One concludes that given the observed values of multiplicities the vast majority of stars form as binaries, while non-hierarchical higher order multiples, although present, do not represent a predominant outcome (Kroupa 2011).

In general, the separation distribution function (i.e. the distribution of separation between primary and companions in a samples of multiples systems) is another important tracer of dynamical evolution. In the simple case of binary systems, even though the separation distribution function, in particular

for solar-mass type star (De Rosa et al. 2014; Ward-Duong et al. 2015), has a peak around 30 AU (Duquennoy & Mayor 1991; Raghavan et al. 2010), while at large separations can be approximated as $\propto 1/a$ as originally proposed by Opik in 1924, binaries are found with a very broad range of separations from spectroscopic to wide common proper-motion binaries with separation ~ 1 parsec (Reipurth 2017). This huge range of separation, can be a real challenge for any star formation theory unless some sort of dynamical evolution is invoked.

2.5.1 Triple system's dynamic

When multiples bodies are randomly placed within a volume, the majority of the system's configurations will be non-hierarchical (i.e. the third body is closer than ~ 10 times the separation of the other two bodies). Such configurations are highly unstable, and will on a timescale of around 100 crossing times decay into a hierarchical configuration, through the ejection of the third body, either into a distant orbit or into an escape (Anosova 1986; Sterzik & Durisen 1998; Umbreit et al. 2005; Reipurth et al. 2010).

The majority of triple system are found in a hierarchical structure (see for example Tokovinin 2018; Tokovinin 2020b; Tokovinin 2020c and references therein). However, triple systems do not generally form directly in a hierarchical system, in particular triple systems coming from a single formation mechanism such as fragmentation for example, but instead in a highly unstable non-hierarchical configuration (Reipurth 2017). In this chaotic environment, the motion of the three components occasionally leads them in a very close volume of space where the three components may exchange energy and momentum (Valtonen & Karttune 2006). In the majority of the cases, the outcome of these triple close-in encounters is the ejection of the least massive member on either a very wide orbit or escape, leaving the two remaining bodies bound in a binary system (van Albada 1968; Anosova 1986). During the transition from a non-hierarchical to a hierarchical system, the inner binary will shrinks in order to provide the energy the system needs to eject an outer component on a distant or an escape orbit. Another possible outcome of such interactions is that one body rapidly occupy the dense center of the cloud where it will quickly grows while banishing the two other components of the triple system to the outskirts of the core (Reipurth & Mikkola 2015).

Numerical simulations from Reipurth & Mikkola 2015 (see Figure 2.4), show that a triple non-hierarchical system embedded in a cloud core (with identical starting stellar seed) will evolve through dynamical interactions while accreting from the cloud itself. In both cases a close-in pair is formed from the dynamical evolution of the triple system, one ejecting the third component on an escape

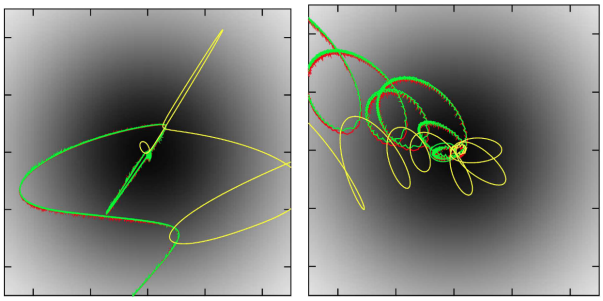

FIGURE 2.4— Triple system dynamical evolution. The two numerical simulations show the dynamical evolution of a triple systems while moving through a dense cloud core modelled as a Plummer core. In both simulations two of the stars form a close pairs. In the left panel the the third component become an unbound single star in the end, while in the right panel a bound triple system is formed. The width of each panel is 10,000 AU. From: Reipurth & Mikkola 2015

route (left), while the other will keep it on wide external orbit, and a bound triple system is formed (right). In general, the final masses of each component of the system highly depending on the overall evolution during this phase. Figure 2.5 instead (from Reipurth et al. 2010) shows the dynamical outcome of one hundred N-body simulations of unstable triple systems embedded in dense cloud cores. As expected, many companions are ejected into unbound orbits and quickly escape (red), but others are ejected with insufficient momentum to climb out of the potential well of the cloud core and associated binary (blue). These loosely bound companions reach distances of many thousands of AU before falling back and eventually being ejected into escapes as the cloud cores gradually disappear. These simulations show that as a consequence of this ejection process, the inner system shrink due to the loss of energy required to eject the outer companion (energy that will come from the binding energy of the remaining binary) and at the same time they will frequently get a highly eccentric orbit. The observable result of this ejection process is shown in Figure 2.6, where the multiplicity frequency and the companion frequency clearly declines through the protostellar PMS because of the breakup of small multiple systems (Chen et al. 2013).

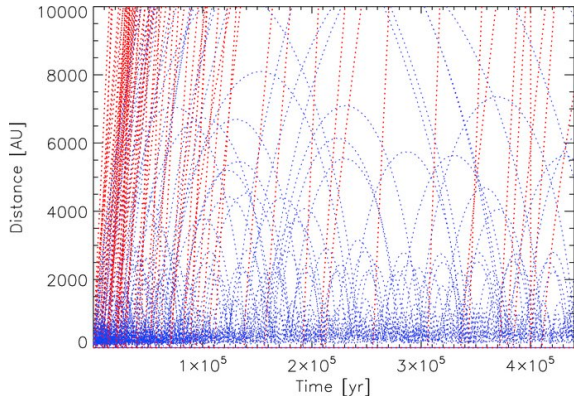

FIGURE 2.5— One hundred simulations showing the dynamical evolution of a triple system of three 0.5 $M_\odot$ stars with initial mean separations of 100 AU embedded in a 3 $M_\odot$ cloud core. Among the numerous ejections seen in the plot, those leading to an escape are plotted in red, while bound systems are blue. From: (Reipurth et al. 2010)

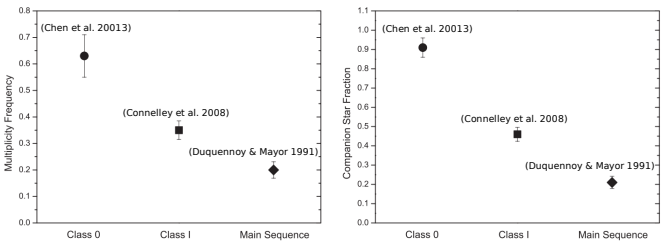

FIGURE 2.6— Left: Observed multiplicity frequencies with separations from 50 AU to 5000 AU for Class 0 protostars (Chen et al. 2013), Class I young stellar objects (Connelley et al. 2008a; Connelley et al. 2008b), and MS stars (Duquennoy & Mayor 1991). Right: same as left for companion star fractions. From: (Chen et al. 2013)

2.5.2 Origin of Low Mass

Even though the formation of a single star from the collapse of a molecular cloud as always been the standard view of the origin of single stars, the high multiplicity of protostars has made clear that this can not be regarded any more as the primary channel and it should not be automatically assumed that single

low-mass star in star-forming region represent cases of single and isolated star formation events (Reipurth et al. 2014). The origin of Very Low-Mass (VLM) ($M \lesssim 0.1\ M_{\odot}$) and Brown Dwarf (BD) has been debated for a long time. The general consensus seems to converge over on three formation hypothesis:

- from a cloud core whose mass is very small (Padoan & Nordlund 2004);
- from a seed that has been removed from the infall zone due to a dynamical ejection (Reipurth et al. 2001; Basu & Vorobyov 2012)
- from a cloud core that undergoes photoevapoaration due to the formation of nearby OB star (Whitworth & Zinnecker 2004)

In other words, the formation of single stars (compared to multiples), rather than proceeding through similar but independent channels, may be strongly interconnected. For example, N-body simulation with accretion processes suggest that the majority of BD ejections are non-violent events, but rather the result of an unstable triple system that disassociated, typically leaving a VLM binary and an isolated BD drifting apart at low velocity. Typically this process happens in the first 100 Myr of evolution of the system (Reipurth & Mikkola 2015).

Summarizing, when we observe a isolated stars it can be a product of one of the following three channel:

- it may be born in isolation;
- it may be born in a multiple system and then be ejected during an early dynamical evolution phase;
- it may be the product of a stellar merger due to a spiral-in process during the protostellar phase;

2.6 Statistics of multiple systems

2.6.1 Stellar multiplicity

The most immediately quantifiable parameter of binary populations are the Multiplicity Fraction (MF) and the Companion Fraction (CF), the difference between the two being the frequency of higher-order multiple systems. If we define f_n the fraction of system containing n stars (Batten 1973), than we can write the multiplicity fraction as MF $= 1 - f_1 = f_2 + f_3 + f_4 + ...$, or:

$$MF = \frac{B + T + Q}{S + B + T + Q} \tag{2.23}$$

Mass	MF	CF
M$\lesssim 0.1$	$22^{+6\%}_{-4\%}$	$22^{+6\%}_{-4\%}$
$0.1 \lesssim$M$\lesssim 0.5$	$26 \pm 3\%$	$33 \pm 5\%$
$0.7 \lesssim$M$\lesssim 1.3$	$44 \pm 2\%$	$62 \pm 3\%$
$1.3 \lesssim$M$\lesssim 5$	$\gtrsim 50\%$	$100 \pm 10\%$

TABLE 2.1— Multiplicity and companion fraction binned by mass intervals for main sequence stars. From: Duchêne & Kraus 2013.

where S, B, T and Q are the number of single, binary, triple and quadruple, etc., providing the fraction of non-single system in a given sample. The Higher-order Fraction (HF) of multiples can also be simply expressed as $HF = 1 - f_1 - f_2 = f_3 + f_4 + ...$

The CF $= f_2 + 2f_3 + 3f_4 + ...$ instead quantifies the average number of stellar companion per system and is expressed as:

$$CF = \frac{B + 2T + 3Q}{S + B + T + Q} \tag{2.24}$$

Measures of MF are less sensitive to the actual detection of *all* the sub-component of a given system compared to the CF[1], and this is the reason why MF is used more frequently to compare theory to observations.

In principle, a description of multiplicity statistics should be multi-parametric, taking into account the joint distributions of the main orbital parameters (mass ratio, period or semi-major axis, and eccentricity, see Sec.2.6.2) at all hierarchical levels. But even in the simple case of a binary system, these distributions are poorly constrained, and the number of variables and complexity increases quickly when dealing with higher order systems. For this reason, the multiplicity is usually characterized to a first order by the fractions f_n and their combinations such as MF, CF, and HF. Table 2.1 from Duchêne & Kraus 2013 summarize the general trend of MF and MC as a function of increasing primary mass for main sequence stars. Overall, the multiplicity in main sequence stars is a steep and monotonic function of the mass. In the following of this section, the main results regarding multiplicity will be review in more detail.

2.6.1.1 Multiplicity in Embedded protostars

Chen et al. (2013) performed a major survey of Class 0 multiple systems in the projected separation range of $50-5000$ AU. They derive a multiplicity frequency

[1] unlike MF, CF may exceed unity when all the objects in the survey are multiple systems or when the number of components in the higher order multiple system greatly exceed the number of single systems.

MF $= 0.64 \pm 0.08$ and a companion frequency CF $= 0.91 \pm 0.05$. Since their survey is complete only up to a separation $\sim$ 1800 AU, these results can be interpreted as a lower limit. An earlier stuydy by Haisch et al. (2004) probed the range of separation $\sim 300 - 2000$ AU, finding a companion frequency CF $= 0.18 \pm 0.04$ for the more evolved Class I sources. Also in a similar separation range, $110 - 1400$ AU, Duchêne et al. (2004) obtained CF $= 0.27 \pm 0.06$ while using adaptive optics to probe a range reaching smaller separations, i.e. $14 - 1400$ AU, Duchêne et al. (2007) find CF $= 0.47 \pm 0.08$, with an overabundance of close-in companions.

2.6.1.2 Multiplicity in Pre-Main Sequence stars

PMS stars in nearby T associations (like the Taurus-Auriga or the Chamaeleon star-forming regions) appear to have an average CF roughly twice the value among solar-type MS stars. In Taurus, for example, Kraus et al. (2008) and Kraus et al. (2011) find $\mathrm{CF}_{0.7-2.5\,M_\odot} \simeq 0.64^{+0.11}_{-0.09}$ and $\mathrm{CF}_{0.27-0.7\,M_\odot} \simeq 0.79^{+0.12}_{-0.11}$ over a $3 - 5000$ AU separation, where we have explicitely indicated the mass range of the primaries. Together with these high companion frequencies, the authors find that $\sim 1/4 - 1/3$ of all systems are singles, still a relatively large fraction. This suggests the prevalence of higher order multiples in Taurus. On the other hand, surveys of young and denser star forming regions such as the ONC (Petr et al. 1998; Köhler et al. 2006; Reipurth et al. 2007) and NGC 2024 (Beck et al. 2003) in the Orion complex, as well IC-348 in the Perseus cloud (Luhman et al. 2005) show a much smaller Companion Frequency. Reipurth et al. (2007), in particular, finds in the ONC CF $^{Class\,II/II} \sim 0.088 \pm 0.011$ for projected separations in the range $67.5 - 675$ AU. This is a factor ~ 2.5 smaller than what found in Taurus over similar range of separations. On a smaller range of separations ($10 - 60$ AU), results from Duchêne et al. (2018) for the ONC seems to be more consistent with that observed in other star-forming regions and twice as high as among field stars.

2.6.1.3 Multiplicity in Main Sequence stars

Moving to Main Sequence systems, their multiplicity has been the object of many studies over the years. Raghavan et al. (2010) find CF $^{MS}_{0.7-1.3\,M_\odot} = 0.62 \pm 0.03$ and MF $^{MS}_{0.7-1.3\,M_\odot} = 0.44 \pm 0.02$, suggesting that the majority of MS stars in the field are single but with a ratio almost close to 50/50. Moreover, taking advantage of their larger sample, they also report a marginally higher multiplicity rate among the super-solar dwarf compared to sub-solar i.e. MF $^{MS}_{1-1.3\,M_\odot} = 0.50 \pm 0.04$ vs. MF $^{MS}_{0.7-1\,M_\odot} = 0.41 \pm 0.03$, while for the companion frequency the difference is larger, with CF $^{MS}_{1-1.3\,M_\odot} = 0.75 \pm 0.05$ vs. CF

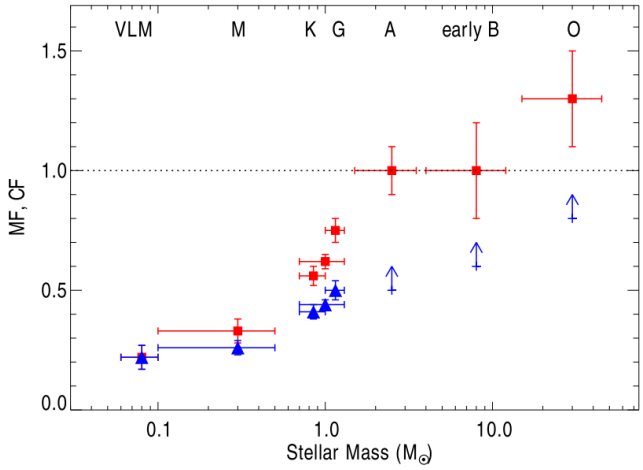

FIGURE 2.7— Companion (red squares) and multiplicity (blue triangles) fraction, function of the primary mass for MS stars and field VLM objects. The horizontal error bars represent the approximate mass range for each population. From: Duchêne & Kraus (2013)

$^{MS}_{0.7-1\,M_\odot} = 0.56 \pm 0.04$: higher order systems are more frequent at larger masses. By comparison, low-mass MS stars tend to show lower multiplicity and companion frequency, i.e. MF $^{MS}_{0.1-0.5\,M_\odot} = 0.26 \pm 0.03$ and CF $^{MS}_{0.1-0.5\,M_\odot} = 0.33 \pm 0.05$ (Delfosse et al. 2004; Dieterich et al. 2012). Moving to even lower mass, the ratios remain low with MF $^{MS}_{\lesssim 0.1 M_\odot} \simeq 0.20 - 0.25$ (Duchêne & Kraus 2013) consistent with the binary fraction $f_{2(\lesssim 0.1 M_\odot)} = 0.22^{+0.06}_{-0.04}$ reported by Allen 2007 for ultracool dwarf companions. In contrast to low- and very low-mass stars, Duchêne & Kraus (2013) determine for intermediate-mass stars a multiplicity function of MF $^{MS}_{1.5-5\,M_\odot} \geq 0.50$. The authors remark that this value is just a lower limit due to incompleteness of the surveys considered in their study that prevents a more robust estimation of the frequency of higher-order multiple systems. Kouwenhoven et al. (2007b) in the same mass-range found a CF $^{MS}_{1.5-5\,M_\odot} \geq 1.00 \pm 0.10$.

In general, there is widespread consensus that the frequency of multiple systems increases with stellar mass (Lada 2006; Duchêne & Kraus 2013). As shown in Fig. 2.7, the Multiplicity Frequency of MS stars is a steep, monotonic

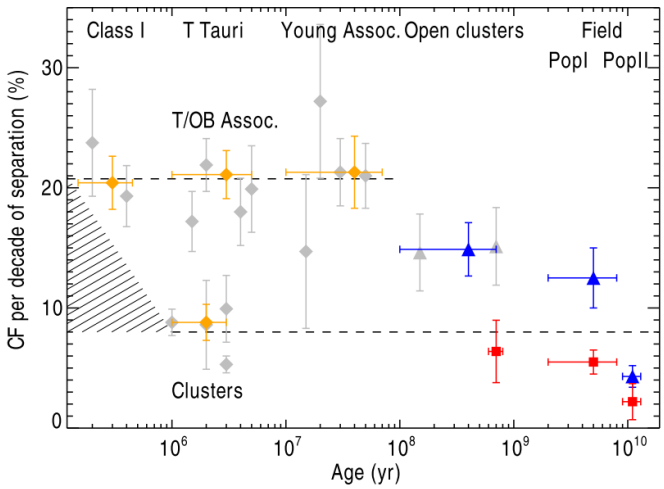

FIGURE 2.8— Frequency of visual companions per decade of projected separation vs. age for solar-type (blue triangles), low-mass (red squares) and overall populations of young stars (orange diamonds). Results from individual surveys are indicated as gray symbols (see Duchêne & Kraus 2013 for more details). The dashed lines represent constant frequencies describing qualitatively the predicted behavior of low-density associations (top line) and dense clusters (bottom line). The hashed region represent the range of possible behaviors for stellar clusters in the embedded phases. From: Duchêne & Kraus (2013)

function of stellar mass. The dependencies of MF and CF on primary mass are qualitatively similar, with CF showing a steeper slope resulting primarily from the fact that MF has an intrinsic upper bound at 1.00.

The frequency of visual companions is shown in Fig. 2.8 and highlights two parallel trends. First, stellar multiplicity seems to be 'frozen' on timescales < 50 Myr for star-forming regions and young associations. Second, there is no striking difference between young open cluster on one side and Population I field stars on the other. The marked multiplicity deficit among Population II stars suggests either a metallicity dependence in binary formation or ejection on a timescale of several Gyr (Duchêne & Kraus 2013).

2.6.2 Initial Binary Population

As we have seen in the previous section, a statistical description of multiplicity should be multi-parametric in order to account for the joint probability distributions of the main system parameters like mass ratio, period, and eccentricity. Specifically, one can describe an Initial Binary Population (IBP) introducing four fundamental distribution functions:

- the distribtution of mass, i.e. the Initial Mass Function (IMF) $\xi(m)$;
- the distribution of periods P (or semi-major axis): $df = f_P(lP)dlP$ (where $lP = log_{10}(P)$);
- the distribution of mass ratio $q = \mathrm{M}_{comp}/\mathrm{M}_{prim} \leq 1$: $df = f_q(q)dq$;
- the distribution of eccentricities e: $df = f_e(e)de$

In other words, an IBP describes the initial properties of binaries in a star clusters according to the particular distributions of their parameters we just enunciated. The concept of IBP is convenient because a full numerical solution to the problem of cloud collapse and star or binary formation is not jet viable (Kroupa 2011). Even though the current theories are not completely able to predict binary properties of a stellar population, the adoption of an IBP may allow the synthesis of stellar binary populations, building on the standard procedure of adopting an IMF. The real challenge is to theoretically justify the adopted IBP, which may be affected by the physical process happening inside dense star forming region through stellar-dynamical evolution.

In the following sections we will briefly describe the four distributions.

2.6.3 Initial Mass Function

The stellar IMF represent the distribution of initial mass of a complete ensemble of stars which formed together. Because stars do not form all at once at the same time, a truly IMF does not really exist. When we observe a stellar population, some of more massive stars may have already evolved out of the main sequence and/or ejected from the system, stellar mergers may have happened while low-mass stars may be still accreting and building up their initial mass. So the true IMF can be regarded as a mathematical device to model stellar populations, i.e the ideal 'parent' distribution function of the masses of stars formed in a star formation event. The initial number of stars dN in a bin of mass $m, m + dm$ can be defined as:

$$dN = \xi(m)dm \tag{2.25}$$

where $\xi(m)$ represent the stellar IMF. The existence of a universal form for the IMF (within statistical scatters) has been historically favored by observations after correcting for stellar and dynamical evaluations and unknown multiple systems. Several forms have been suggested starting with the original work of Salpeter (1955) who first derived, for masses $0.4 - 10\ M_\odot$

$$\xi(m) \propto m^{-2.3}\,. \tag{2.26}$$

Kroupa 2001 has proposed a two-parts power law:

$$\xi(m) \propto m^{-\alpha_i}\,,\ i = 1, 2 \tag{2.27}$$

where

$$\alpha_1 = 1.3 \pm 0.3\,,\ 0.08 \lesssim m/M_\odot \lesssim 0.5 \tag{2.28}$$

$$\alpha_2 = 2.3 \pm 0.5\,,\ 0.5 \lesssim m/M_\odot \lesssim m_{max} \tag{2.29}$$

and $m_{max} \lesssim 150\ M_\odot$ depends on the stellar mass of the embedded cluster.

Assessing if and how the IMF changes between different regions ("universality") has been a major research topic in the last few decades. Massey (2003) found $\alpha_3 = 2.3 \pm 0.1$ for $m \gtrsim 10\ M_\odot$ in many OB associations ans star cluster in the Milky Way (MW) and in the Large and Small Magellanic Clouds. Performing an analysis of OB stars counts in the MW disk, Scalo (1986) found a steeper index $\alpha_{MW\,disk} \simeq 2.7$ for $m \gtrsim 1\ M_\odot$. Similar results have been obtained from Tinsley (1980) and Reid et al. (2002) who found $2.5 \lesssim \alpha_{MW\,disk} \lesssim 2.8$. A power-law distribution cannot proceed indefinitely, and a peak is reached between 0.4 $M_\odot$ and the hydrogen burning limit $m_H \simeq 0.072\ M_\odot$, as there is substantial evidence that the IMF flattens to decrease in the substellar regime. For BDs an index $\alpha_0 \simeq 0.3 \pm 0.5$ has been reported by (Martín et al. 2000; Chabrier 2003; Thies & Kroupa 2007).

One of the major obstacles to determine the IMF is that stellar masses cannot be measured directly from observations, but normally can only be inferred by transforming luminosity to mass through theoretical stellar evolutionary models. Because of the uncertainties involved in the process, reliably results have been achieved mainly for MS stars, i.e. on populations that may be less representative of the original cluster.

To mitigate this factor of uncertainty, for a group of main sequence stars one can introduce an "initial luminosity function" as a proxy for the IMF $\xi(m)$ through the relation:

$$\xi(m) = \frac{dN}{dM_\lambda}\frac{dM_\lambda}{dm}. \tag{2.30}$$

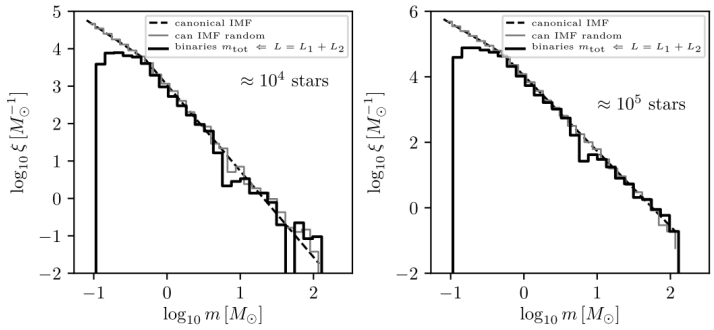

FIGURE 2.9— Effect of unresolved binaries on the IMF estimated from observations for two different clusters. The canonical IMF is the dashed line, whereas the distribution of stars drawn randomly from the stellar IMF is shown as a solid gray line. Assuming all stars are in unresolved binaries, the measured IMF is shown as the thick solid histogram assuming. Unresolved binaries can significantly affect the low mass end of the IMF if not accounted for appropriately producing an artificial turn-over of the distribution, while they have a negligible effect on the high-mass end of the IMF. From: Kroupa & Jerabkova (2018)

where M_x is the absolute magnitude of a star of mass m in a pass-band filter indicated by λ and $\Psi_\lambda = \frac{dN}{dM_\lambda}$ is the stellar luminosity function. When counting the number of MS stars as a function of luminosity, one must take into account that $\sim 50\%$ of them are binaries (with some being higher order; Goodwin et al. 2007; Duchêne & Kraus 2013; see also next Section. 2.6.1). Therefore, when drawing the IMF from the luminosity function Ψ_λ, one has to pay particular attention to not underestimate the number of stars in binary systems, in particular for low-mass star systems. Understanding the binary population is therefore paramount in avoiding bias that can otherwise lead to flawed dynamical histories for the population under study: errors at the low mass end at the IMF result in wrong predictions by synthetic models of old populations. Indeed, an observer could derive different IMFs in two populations which in reality only differs in their binary populations.

Figure 2.9 shows how unresolved binaries affect the derived IMF for two population of $\sim 10^4$ and 10^5 stars. The system mass is calculated from the combined luminosity of the system, leading to the 'system IMF' who is is virtually identical to the IMF for $m \gtrsim 1\ M_\odot$, but it lacks in reality in low mass stars. So the importance of detecting and resolving binary system becomes even more important when we realize that only the 'system IMF' can be obtained from the

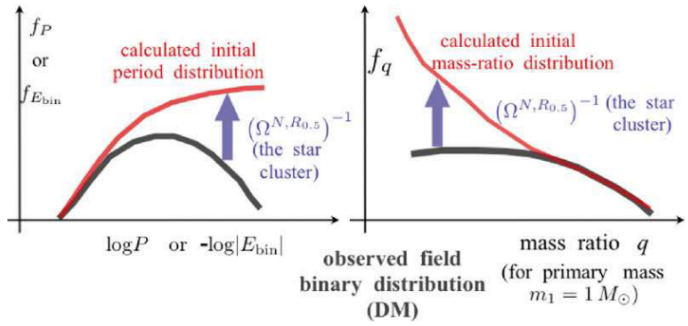

FIGURE 2.10— Schematic visualization of how the initial period distribution (left panel) or mass-ratio distribution (right panel) are back computed (blue arrow) through the application of the stellar-dynamical operator $\Omega^{N,R_{0.5}}$. The black thick line represent the observed Galactic-field main sequence period (left panel) and the MS mass ratio (right panel) from Duquennoy & Mayor (1991). From: Kroupa (2011)

observations.

2.6.4 Period Distribution

The orbital periods, P, follow a power-law distribution usually expressed as $f_p(P) \propto P^{\alpha}$, with the particular case $\alpha = -1$ (a logarithmically flat distribution known as "Opik's law", (Öpik 1914)) being frequently favored. This distributions has been measured in both star-forming regions and in samples of late-type stars in the Galactic field. Other authors (Duquennoy & Mayor 1991; Fischer & Marcy 1992) have suggested a log-normal period (lP) distribution function for G- and M-dwarf in the Galactic-field:

$$f_P(lP) = f_{tot}\left(\frac{1}{\sigma_{lP}\sqrt{2\pi}}\right) e^{\left[-\frac{1}{2}\frac{(lP-\overline{lP}^2)}{\sigma^2_{lp}}\right]} \tag{2.31}$$

with $\overline{lP} \simeq 4.8$, $\sigma_{lP} \simeq 2.3$ and $\int_{all\,lP} f_{lp}(lP)dlP = f_{tot} \simeq 0.5$ K-dwarf appear to have similar distribution.

2.6.5 Mass-ratio distribution

The mass ratio of multiple system q can be estimated from the observed flux ratio when spectroscopic observations are not sufficient and is frequently char-

acterized by a power law distribution, $f_q(q) \propto q^{\gamma}$.

2.6.5.1 Mass-ratio distribution in Pre-Main Sequence Stars

Due to the shallow mass-luminosity relation for PMS stars, $L_2/L_1 \propto (M_2/M_1)^{1.6}$ instead of the 3.5 exponent appropriate for the MS (Zinnecker et al. 1992), imaging surveys of binary systems easily reach $q \sim 0.1$, However, uncertainties in PMS evolutionary models as well as the possibility of circumstellar dust emission and differential extinction smooth out and/or bias the real mass ratio distributions, particularly for the surveys relaying on photometry to estimate mass. For this reason spectroscopic follow-up campaigns are needed to derive accurate q ratios (e.g., White & Ghez 2001 or Hartigan & Kenyon 2003). One finds that TTS solar-type binaries display a mass-ratio distribution roughly flat, with a power law's exponent $\gamma^{Class\ II/III}_{0.25-2.5M_{\odot}} = 0.2 \pm 0.2$ (Kraus et al. 2011) albeit with a marginally significant trend with stellar mass. Moving to lower mass binaries, however, Kraus & Hillenbrand (2012) found $\gamma^{Class\ II/III}_{0.07-0.12\ M_{\odot}} \sim 1$, i.e. low mass binaries tend to have similar mass. It is uncertain if this trend continues through the substellar regime, but there is definitely a small fraction of objects that seem to host binary companions that are much less massive than the primary, and may also have unusually wide orbital radii (e.g., Luhman et al. 2009). At the other extreme, intermediate-mass binaries have a small but significant preference for low-q systems (Kouwenhoven et al. 2007). Kouwenhoven et al. (2007b), in the young and nearby OB association Scorpius OB2 derived for intermediate-mass stars a $\gamma^{ScoOB2} \simeq -0.4$.

2.6.5.2 Mass-ratio distribution in Main Sequence Stars

Duquennoy & Mayor (1991) find a single peak among solar-type MS stars in the galactic field around $q \sim 0.3$. Raghavan et al. (2010), with a higher completeness survey, establish that this distribution is instead flat Duchêne & Kraus (2013) fitted a power-law to Raghavan et al. (2010) sample finding $\gamma^{MS}_{0.7-1.3\ M_{\odot}} = 0.28 \pm 0.05$. Moreover, they find that splitting the sample at the median orbital period, short-period binaries are characterized by a strong peak at $q \sim 1$ and a slowly declining $f_q(q)$ function towards low mass ratios, while long-period binaries have a single peak around $q \sim 0.3$, similar to Duquennoy & Mayor (1991). In particular, they estimate $\gamma^{MS,logP\leq 5.5}_{0.7-1.3\ M_{\odot}} = 1.16 \pm 0.16$ and $\gamma^{MS,logP>5.5}_{0.7-1.3M_{\odot}} = -0.01 \pm 0.03$.

Concerning low-mass stars, Duchêne & Kraus (2013) fitted the RECONS[2] sample finding $\gamma^{MS,a\leq 5AU}_{0.1-0.5\ M_{\odot}} = 2.7 \pm 1.6$ and $\gamma^{MS,a>5AU}_{0.1-0.5\ M_{\odot}} = -0.3 \pm 0.3$. The main

[2] REsearch Consortium On Nearby Stars, http://www.recons.org/

problem with substellar objects is that estimated masses strongly depend on the assumed age of the objects, and therefore are not as precise as for hydrogen-burning stars. However, for substellar pairs the uncertainty plays similarly to both components, so that the absolute uncertainties in q are substantially smaller than on the single masses estimate. The mass ratio distribution for VLM stars is heavily skewed toward $q \sim 1$ with an estimated $\gamma_{M \leq 0.1\,M_\odot} = 4.2 \pm 1.0$ (see Duchêne & Kraus 2013).

The mass-ratio for SBs is found either be relative shallow with a $\gamma = -0.3 \pm 0.2$ (Carquillat & Prieur 2007), or can be described by a Gaussian distribution centered at $q \sim 0.4$ (Vuissoz & Debernardi 2004). Among VBs, the VAST survey suggests a mass ratio distribution $\gamma \sim -0.6$.

2.6.6 Eccentricity Distribution

Eccentricity, e, is an important parameter to probe the dynamical evolution of a system due to the fact that after achieving a hierarchical configuration, the shrinking of the orbit of the inner binary can lead to high eccentricity (Reipurth et al. 2014); on the other hand, short period binaries can circularize their orbits as a result of tidal dissipation (Koch & Hrivnak 1981).

There are other orbital parameters that define the orientation of the orbital plane relative to our viewing geometry and are therefore not as astrophysically compelling. The orientation of orbital planes is random not only with respect to our line of sight, but it also appear to be unrelated to the stellar rotation spin vector (e.g. Hale 1994; Popovic et al. 2004). Moreover, multiple systems only have a modest preference for internal coplanarity (e.g. Sterzik & Tokovinin 2002). The great majority of multiple systems observed so far are *hierarchical*, i.e. the ratio of separations between their inner an outer components is large enough to ensure long-term dynamical stability. If they are also stable, their stellar motion can be described by perturbed Keplerian orbits.

2.7 From primordial to the field binary population

To build this bridge between the IBP and the observed distributions of binaries (i.e. between the intial - or *primordial* - and actual distribution of parameter: f_{lp}, f_q, f_e) that will reconcile pre- and main sequence observation, we need to correct them for all the dynamical process acting in the birth-cluster of stars as these evolve towards the Galactic-field (see Fig. 2.10 for a graphical explanation). Fig. 2.11 present the evolution of the binary fraction f (the ratio of binaries system in a given sample - see Section 2.6.1) as a function of the mass of the primary m, showing a decrease of the binary fraction for old MS Galactic field stars (marker on the plot). On the other hand, we know from previous

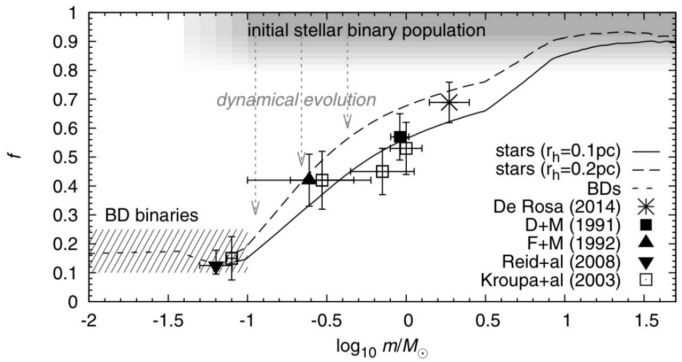

FIGURE 2.11— Binary fraction f as a function of the mass of the primary m. For old main sequence Galactic field stars, f decrease with m. However, young stars (see Section 2.6.1) posses a binary fraction ~ 1 regardless of the mass of the primary (shaded gray region called "initial stellar binary population" - see next Section. 2.6.2). The difference between young stars and BDs with $f \sim 0.15$ implies that BDs forms with stars, but follow a different distribution function (Marks et al. 2015). The old main sequence field binary properties can be well reproduced if all star form as binaries in embedded clusters with half-mass radii r_h (Thies et al 2015), in which the binary systems dynamically evolve and dissolve over time (Marks et al. 2012; Belloni et al. 2018). From: Thies et al (2015)

arguments that most of the stars should have form as multiple systems, so that the f should be very high at *birth* (represented by the shaded area on the top of the figure). Thies et al (2015) provided an updated analytical model of stellar and substellar binarity finding that the resulting binary fraction and the dynamically evolved companion mass-ratio distribution are in good agreement with observational data on stellar and VLM binaries in the Galactic field, in clusters and in dynamically unprocessed groups of stars if all stars originally form as binaries in embedded clusters.

The 'Heggie-Hills Law' (Heggie 1975; Hills 1975), according to which wide (soft) binaries gets wider and tight (hard) binaries gets tighter brings to the result that wider binaries are disrupted preferentially than binaries with small mass-ratio. This tightening of binaries also imply ejection and stellar merger (see section 2.5.1). The boundary between soft/hard binaries depend on the velocity dispersion in the birth population. This dynamical disruption of binaries can be characterized through the 'stellar-dynamical operator' $\Omega^{M_{ecl},R_{0.5}}$ (where M_{ecl} is the mass of the embedded cluster with half-mass radius $R_{0.5}$). When we want to

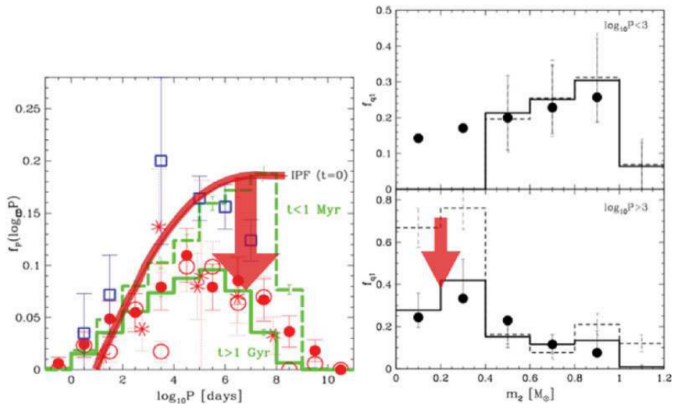

FIGURE 2.12— Visual representation of the transformation of the birth binary population properties to the final distributions after the $\Omega^{M_{ec},R_{0.5}}$ operator acted on them. **Left panel:** the birth period function (birth PF - thick red line) is eigenevolved to the initial PF (dashed green histogram). Then the $\Omega^{M_{ec},R_{0.5}}$ operator is allowed to act on the initial PF producing the final PF (solid green histogram). The solid dots, open circles, stars and open squares are G-, K-, M-dwarfs and pre-main sequence system respectively. **Right panel:** transformation of the initial mass-ratio distribution for primaries $m \sim 1\ M_{\odot}$ (dashed histogram) to the final mass-ratio distribution after the population emerges from its star cluster (solid black histogram). From: Kroupa (2008)

represent it as a function of the number N of star in the cluster, we will refer to it as $\Omega^{N,R_{0.5}}$. The mass-ratio, eccentricity and period evolution induced through pre-main sequence eigenevolution, can be calculated and are fully detailed in Kroupa (2008). By pre-main sequence eigenevolution is intended the sum of all dissipative physical processes that transfer mass, energy and angular momentum between the companions when they are still very young and accreting.

The two-stage transformation from the Birth Binary Population (BBP) f_P, f_q, f_e to the final observed distribution can than be expressed as:

$$\mathcal{D}_{outcome}(lP, e, q : m_1) = \Omega^{M_{ec},R_{0.5}}\left[\mathcal{D}_{in}(lP, e, q : m_1)\right] \tag{2.32}$$

or

$$\mathcal{D}_{outcome}(lP, e, q : m_1) = \Omega^{M_{ec},R_{0.5}}\left[\Omega_{eigenevol}\left[\mathcal{D}_{birth}(lP, e, q : m_1)\right]\right] \tag{2.33}$$

where $\mathcal{D}_{in}(lP, e, q : m_1) = \Omega_{eigenevol}\left[\mathcal{D}_{birth}(lP, e, q : m_1)\right]$ represent in this formulation the IBP and $\mathcal{D}_{birth}(lP, e, q : m_1) = f_P(lP)f_e(e)f_q(q)$ is the BBP

taking the three birth parameter lP_b, e_b, q_b to be separable (not correlated). The difference between the BBP and the IBP lies in the pre-main sequence eigenevolution (or in other words, the initial population is derived from a birth population through initial processes that act too quickly to be treated by an N-body integration). The operator $\Omega_{eigenevol}$ is accountable for generating the correlations between period, eccentricity and mass ratio. A formulation that is quite successful in reproducing the overall observable correlations between lP, e, q for short period binaries ($P \simeq 10^3 d$) based on pre-main sequence tidal-circularization theory as been introduced by Kroupa (1995). The 'stellar-dynamical operator' $\Omega^{M_{ec},R_{0.5}}$ is provided by Nbody star-cluster simulations and can be regarded as the transformation of the number of binaries in different different binding-eneregy bins such that the reduction of soft binaries is largest and the shrinking of hard binary is increased. Kroupa (2008) provided a definition for the BBP as:

1. random pairing from the canonical IMF (eq. 2.27) for $0.08 \lesssim m/M_{sun} \lesssim 2$;
2. thermal eccentricity distribution $f_e(e) = 2e$;
3. the period distribution function follow

$$f_{P,birth} = \eta \frac{lP - lP_{min}}{\delta + (lP - lp_{min})^2}, \tag{2.34}$$

where $\eta = 2.5$, $\delta = 45$, $lP_{min} = 1$ and $\int_{lP_{min}}^{lP_{max}} dlP = 1$ such that the birth binary fraction is unity (lP_{max}=8.43).

Passing the above birth distributions through eigenevolution and then letting the $\Omega^{M_{ecl},R_{0.5}}$ act on it will lead to the Galactic field population observed. This process is grafically shown in Figures 2.12 where the action of the $\Omega^{M_{ecl},R_{0.5}}$ operator is represented by the red arrows. The top left panel of the figure shows how the birth period function (thick red line; eq. 2.34 with $\eta = 2.5$,$\delta = 45$ and $lP = 1$) is eigenevolved to the initial period function (dashed green histogram $\eta \sim 3.5$,$\delta \sim 100$ and $lP = 0$). After the eigenevolution have taken place, the $\Omega^{M_{ec},R_{0.5}}$ operator is allow to act on the initial period function producing the final distribution (solid green histogram). The solid dots, open circles, stars and open squares are G-, K-, M-dwarfs and pre-main sequence system respectively. The top right panel of the same figure shows the transformation of the initial mass-ratio distribution for primaries $m \sim 1\ M_\odot$ (dashed histogram) to the final mass-ratio distribution after the population emerges from its star cluster (solid black histogram). The upper panel shows how the short-period binaries ($lP < 3$) are actually not affected by the $\Omega^{M_{ec},R_{0.5}}$ operator while

the long-period are. Note that the birth mass-ratio distribution, which results from random pairing from the IMF (see point 1 in precedent BBP enunciation; Woitas et al. 2001), is given by the dashed histogram in the lower panel, while eigenevolution transforms this distribution to the dashed histogram shown in the upper panel. The bottom panels show comparison between the *overall*-initial mass-ratio distribution and the final mass-ratio distribution (right) and the eccentricities for short/long period binaries (left).

The general consensus that have emerged so far about the origin of stellar populations is that stars forms accordingly to a universal IMF and mostly in binary systems and in very dense clusters that expel their residual gas and rapidly evolve in T- or OB-associations. If massive enough, the dense embedded clusters may reach masses of the order of globular cluster's through intense star-burst while rapidly expanding. Some open questions still remains: why the star-formation product is so universal (given the constraints we shown earlier), and how massive stars are distributed in binaries for example.

2.8 Observation and characterization of multiple systems

From an observational point of view, as we review earlier in section 2.6.1, there are still big discrepancies between the observed properties of multiple systems and the predicted one from theory.

Studies of binaries and multiple systems during the protostellar stage and later during the PMS phase are important because they offer the perfect stage to observe and study the results of fragmentation of molecular clouds, giving fundamental insight at the the physics of the processes at play during these stages. The problem is though, in particular for the case of protostars, that these objects are generally still deeply embedded, so such observations are heavily hampered by extinctions that can exceed $A_V \sim 100$ mag. This is the reason why, in the case of Class 0/I sources, infrared (eg. Haisch et al. 2004; Duchêne et al. 2007; Connelley et al. 2008a; Connelley et al. 2008b), submillimiter (eg. Chen et al. 2008; Chen et al. 2009; Maury et al. 2010; Enoch et al. 2011; Tobin et al. 2013) or centimeter wavelength observations (eg. Rodríguez et al. 2003; Reipurth et al. 2002; Reipurth et al. 2004) are generally preferred for this kind of studies. Surveys of PMS stars (TTS or Class II/II sources) have been performed over time across a broad range of environments: dense stellar clusters (e.g. the ONC as well as IC 348 in the Perseus cloud; Petr et al. 1998; Köhler et al. 2006; Reipurth et al. 2007; Luhman et al. 2005), young OB associations (e.g. the Scorpion-Centaurus; (Brown & Verschueren 1997); Shatsky & Tokovinin 2002; Kouwenhoven et al. 2007)), T associations

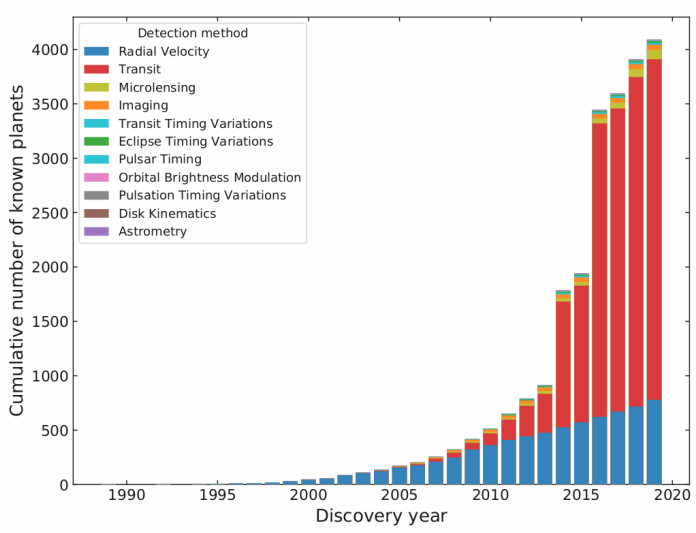

FIGURE 2.13— The cumulative number of exoplanet discovered over time. Radial velocity and transit detections provide the majority of detections. Evident also the huge contribution of the Kepler mission, which began releasing data in 2010. The direct imaging contributions to these detections are wide-separation objects which are classified as planets based only on the inferred mass. Data courtesy of the NASA Exoplanet Archive[4]

(e.g. the Taurus-Auriga star forming regions (Kraus et al. 2008; Kraus et al. 2011)). Multi-wavelengths surveys of nearby star-forming regions, as well as speckle interferometry, adaptive optics, aperture masking and *HST* high contrast imaging (or direct imaging) are just some of the different technique applied to obtain these multiplicity surveys. Because the focus of this thesis is the development and application of a pipeline able to recover faint companions embedded in the primary PSF in *HST* ACS/WFC3-IR images, in the rest of this Chapter we will just focus on the latter subject.

2.8.1 Detection of astronomical sources in high-contrast imaging

[4] https://exoplanetarchive.ipac.caltech.edu/index.html

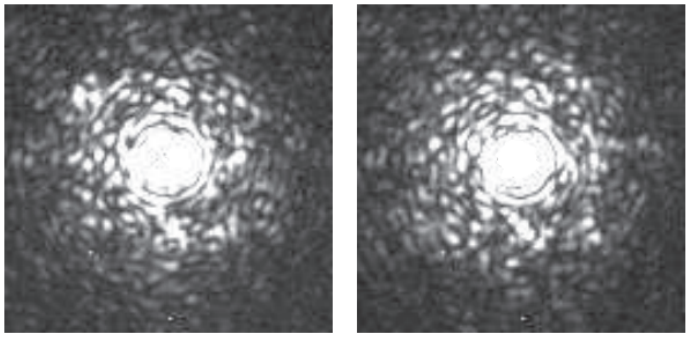

FIGURE 2.14— Direct images of the bright star HD 137704 (magnitude V=5.47) obtained with the Adaptive Optics system at the Palomar Hale telescope. The core of the image has been saturated to illustrate the speckles. From: Soummer et al. 2007.

High-Contrast Imaging (HCI) is a general term for a wide group of techniques used to acquire direct image of stars and other bodies very close to their host stars (i.e., capturing photons directly from the source rather than inferring its presence from telltale feature of the observed system) and can be sensitive to companions as close as a few to few hundred AU whose masses span from planetary mass to brown dwarfs and low mass stars. In view of these qualities, HCI plays an important role, covering the gap between the study of exoplanets and stellar astrophysics, naturally providing insight to fundamental questions such: formation, distribution and characterization of the detected sources.

Decades have passed since the first discovery of an exoplanet in the 1990s and since then, the field has seen an exponential increase in both their detection and technique devised to find and characterize them. Up to date, eleven different technique have been developed (each one with it's own perks and quirks) and the number of exoplanets discovered with each technique are briefly summarized in Figure 2.13. Using HCI techniques to detect close in companions, exoplanets, circumstellar disks, or other structures around stars, the main observational challenge is that objects potentially resolved may be hidden under the PSF wings of the primary (Oppenheimer & Hinkley 2009). The major obstacle to direct detection of candidates companions is the overwhelming luminosity of the host star. Even though the primary can be suppressed through some sort of suppression hardware (i.e. a chronograph), current attempts, both from

the ground with Adaptive Optics (AO) and from space, are limited by a dominating presence of bright quasi-static speckles (Schneider & Silverstone 2003; Biller et al. 2004; Marois et al. 2005; Masciadri et al. 2005). In the case of AO ground-based observations, the residual uncorrected aberrations produce random intensity fluctuations of the background. which appear as speckles in the field. When non-coronaghraphic direct high quality images are used, these speckles mostly appears at the positions of the diffraction rings of the star (Soummer et al. 2007). Figure 2.14 shows two high quality PSF obtained with the AO system at Palomar where this phenomenon, also known as "speckle pinning" (Bloemhof et al. 2001), is clearly visible. These pinned speckle are caused by antisymmetric perturbation of the perfect PSF, and cannot be smaller than λ/D (Perrin et al. 2003). In the absence of static aberrations, speckle pinning happens at the top of the Airy rings. In the presence of static aberrations and even with a perfect coronagraph, residual speckle pinning exists at the position of the maxima of the coronagraphic PSF corresponding to the propagated static aberrations through the coronagraph (Soummer et al. 2007).

Hinkley et al. (2007) studied the residual speckle lifetimes, evidencing two types of speckles: one short-term speckles with a few seconds lifetime and another, quasi-static speckles, with a lifetime of a few hundred seconds. As pointed out by Soummer et al. (2007), even though there is no reason to believe the universality of these specifics values, quasi-static speckles are produced by deformation of the optics (both thermal and mechanical) and the timescale for these slow variation aberrations are typical in the range of tens of minutes.

Once a coronagraph has removed the speckle pinning contribution, the dynamic range at which a companion may be detected can be improved further by use of speckle reduction techniques (speckle nulling) or speckle subtraction: for example multi-wavelength approach, Reference Differential Imaging (RDI) or Angular Differential Imaging (ADI).

Even though speckles remain fixed in space for a given filter, they will generally be observed in different locations in other passbands (Marois et al. 2000; Sparks & Ford 2002; Biller et al. 2004; Marois et al. 2005; Hinkley et al. 2007). This key feature allow a faint companion — characterized by a fixed position in all filters — to be selected out from the speckle noise. Thus, multi-wavelength observations will greatly improve the companion detection efficiency.

In general, when the regime where we are dominated by the speckles is reached, it is possible to subtract them using reference PSF images A reference PSF image is any image whose subtraction from the target image is able to reduce the signal from the speckles while preserving the signal of the astronomical source we are looking for. Since there is always some level of uncertainties in the estimate of a true PSF due to photon statistics, it can be highly advantageous

to build the PSF model out of multiple reference stars.

In the case of RDI, the library of reference PSF images is built using observations of calibration stars that act as true references. The model PSF is then subtracted from the target image. References and target images should be acquired maintaining the same instrument configuration, in the same part of the sky, and as close in time as possible. This helps reducing changes in the PSF due to variations resulting from e.g. the unstable thermal environment in a low-earth orbit environment, or instrument flexures and variable atmospheric conditions on the ground (Marois et al. 2005). To reduce the impact of using a particular realization of the reference PSF on the subtraction residuals, it is advantageous to combine multiple PSF images.

In the case of ADI instead, the model PSF is built from a sequence of images acquired with an altitude/azimuth telescope while the instrument field derotator is switched off. This keeps the instrument and telescope optics aligned and allows the field of view to rotate with respect to the instrument. Because the position of the speckles depends solely on the orientation of the telescope, over a series of exposures the speckles will remain in fixed positions compared to the reference frame of the telescope while a companion will rotate along with the sky. For each image, a reference PSF is constructed from other appropriately selected images of the same sequence and subtracted to remove quasi-static PSF structure. All residual images are then rotated to align the field and then combined (Marois et al. 2006).

Once a library of noise realizations has been built according to one or more of these strategies, PSF subtraction can be performed according to one of the many algorithm already developed. In the rest of this Chapter we will focus on two common algorithms, the Locally Optimized Combination of Images (LOCI) and the Karhunen-Loéve Image Processing (KLIP) algorithms, with a greater effort on the latter because it is the adopted technique to perform PSF subtraction in this project.

2.8.2 Locally Optimized Combination of Images algorithm (LOCI)

Lafrenière et al. (2007) proposed a method to subtract speckles form a single target image starting from an ensemble of N reference PSF images. The heart of the algorithm consist in splitting the target image into subsections (i.e. a small portion of it) and to compute, for each subsection independently, a "locally optimized combination of images" (i.e. a linear combination of the reference images) whose subtraction from the target image will minimize the noise. By optimizing the weights given to the N available reference PSF images according to the residual noise obtained, this approach produces a representation of the

target PSF image that is better than any predefined combination of the reference PSF images. This technique take advantage of the fact that the correlation between the target image and the reference PSF images generally varies with the position within the target image, so it aims at optimizing the coefficients of the linear combination for subsections of the target image.

2.8.3 The Karhunen-Loève Image Processing algorithm (KLIP)

More recently, Soummer et al. (2012) proposed a new method to achieve PSF subtraction using Principal Component Analysis (PCA). In a more general context, PCA is a mathematical algorithm that reduces the dimensionality of the data while retaining most of the variation in the data set and it is been extensively used in astronomy (e.g. Connolly et al. 1995; Cowan et al. 2009). It accomplishes this reduction by identifying directions, called principal components, along which the variation in the data is maximal. PCA was invented by Pearson (1901) as an analogue of the principal axis theorem in mechanics (i.e. it provides a constructive procedure to find the perpendicular principal axis associated with an ellipsoid or hyperboloid). It was also later independently developed by Hotelling (1936). Depending on the field of application, it is also named the discrete Karhunen–Loève transform (KLT) in signal processing, the Hotelling transform in multivariate quality control, proper orthogonal decomposition (POD), singular value decomposition (SVD), eigenvalue decomposition (EVD). PCA can be achieved by eigenvalue decomposition of a data covariance matrix, usually after a normalization step of the initial data has be performed (i.e. mean centering – subtracting each data value from its variable's measured mean so that its empirical mean is zero).

When a suitable library of reference PSFs is assembled, the PCA is carried out and a Karhunen-Loève transformation of these references is used to create an orthogonal basis of eignimages, on which the science image is then projected. Following Soummer et al. (2012) notation, an astronomical observation can be expressed as:

$$T(n) = I_{\psi_0} + \epsilon A(n) \tag{2.35}$$

or in other words an isolated PSF (I_{ψ_0}) with ($\epsilon = 1$) or without ($\epsilon = 0$) a faint astronomical signal $A(n)$. The scalar quantity $\psi = \psi(t, \lambda, \theta, \phi, T_{exp}, m_{star})$ is representative of the state of the instrument-telescope system at the time the data was acquired. The pixel mapping functions p and q maps the pixel index n ($n \in [1, N]$) over the overall image (with a total of N pixels).

The PSF intensity can be expressed as:

$$I_\psi(n) = I(p[n], q[n], \psi) \tag{2.36}$$

while a set of reference images can be expressed as:

$$\{R_k(n) = I_{\psi_k}(n)\}_{k=1,...,K} \tag{2.37}$$

where these references have been pre-selected so that they do not contain any spurious astronomical signal in the search region S of the PSF (with a dimension of N_S pixels). Moreover, the observations have been carried out at neighboring states of the telescope/instrument system, such as $|\psi_i - \psi_j| < \delta$ for all $i, j \in [0, K]$ and δ is a small quantity that can be fine tuned using the correlation between images as proxy.

The primary goal of PSF subtraction is to reconstruct $I_{\psi_0}(n)$ using the set of reference images and to subtract it from the target image obtaining the final astronomical signal $\epsilon A(n) = T - I_{\psi_0}(n)$. In theory, because $I_\psi(n)$ is a continuous random process of ψ, an infinite number of references would be needed to reconstruct it. In practice, what we seek is to find the best estimate $\hat{I}_{\psi_0}(n)$ of $I_{\psi_0}(n)$ using the limited knowledge provided by the K references. Assuming each reference in the library as unique, the ensemble $\{I_{\psi_k}\}_{k=1,...,K}$ spans $\boldsymbol{I}_K$, a K-dimensional sub-space of $\mathbf{R}^{N_S}$, which posses an infinity of orthonormal bases $\{Z_k\}_{k=1,...,K}$.

This problem of finding the best estimate of $\hat{I}_{\psi_0}(n)$ can be rephrased as:

What is the best set of basis $\{Z_k(n)\}_{k=1,..,K}$ most likely to minimize the distance between a random realization of $I_\psi(n)$ and $\boldsymbol{I}_K$? Or

$$\min_{\{Z_k\}} \left\{ E_\psi \left[\sum_{n=1}^{N_S} \left(I_\psi - \sum_{k=1}^{K} < I_\psi, Z_k >_S Z_k(n) \right)^2 \right] \right\} \tag{2.38}$$

where $E_\psi[\cdot]$ represent the expected value over the telescope realizations while $< \cdot, \cdot >_S$ is the inner product over S. If we assume that all the images are of zero means over S, than the optimal basis set $\{Z_k\}_{k=1,...,K}$ can be obtained from the Karhunen-Loève transformation of the $\{I_\psi\}$ (Karhunen 1947; Loève 1948):

$$Z_k^{KL}(n) = \frac{1}{\sqrt{\Lambda_k}} \sum_{p=1}^{K} c_k(\psi_p) R_p(n) \tag{2.39}$$

where the vector $C_k = [c_k(\psi_1), ..., c_k(\psi_k)]$ are the eigenvector of the K-dimensional covariance matrix E_{RR} of the $R_k(n)$ references over S and $\{\Lambda\}_{k=1,...,K}$ are its eigenvalues.

As stated before we would need an infinite number of modes K to obtain the best estimate of $\hat{I}_{\psi_0}(n)$. To avoid this, we can truncate the Karhunen-Loève transformation, choosing a finite number of modes $K_{klip} < K$ to keep in the estimate of $\hat{I}_{\psi_0}(n)$:

$$\hat{I}_{\psi_0}(n) = \sum_{k=1}^{K_{klip}} < T, Z_k^{KL} >_S Z_k^{KL}(n) \tag{2.40}$$

Once $\hat{I}_{\psi_0}(n)$ has been properly assessed, we can calculate the final image $F(n) = T(n) - \hat{I}_{\psi_0}(n)$ as :

$$\begin{aligned} F(n) = \left(I_{\psi_0}(n) - \sum_{k=1}^{K_{klip}} < I_{\psi_0}, Z_k^{KL} >_S Z_k^{KL}(n) \right) + \\ + \epsilon \left(A(n) - \sum_{k=1}^{K_{klip}} < A, Z_k^{KL} >_S Z_k^{KL}(n) \right) \end{aligned} \tag{2.41}$$

From eq. 2.41, we can obtain an expression for the signal of the candidate source as:

$$S = \sum_{A(n) \neq 0} \left(A(n) - \sum_{k=1}^{K_{klip}} < A, Z_k^{KL} >_S Z_k^{KL}(n) \right) \tag{2.42}$$

For $k << K$, $< A, Z_k^{KL} >_S \simeq 0$ because the morphology of the astronomical signal cannot be reproduced by a PSF realization due to the fact that the PSF of a faint planet is localized over a few pixels and so almost orthogonal to the main modes of the telescope's PSF realizations. Figure 2.15 shows how the throughput based on eq. 2.42 varies depending on the shape of the astronomical signal. The first curve (point source) represent a planet located at 1.5 arcsec from the target star. As we said, because the planet's signal is mostly orthogonal to the main KL modes, the throughput is high. On the other hand, more extended sources as HD 181327 disk and wider disk model (the other two curves) shows a reduced throughput.

Similarly, the variance in the search zone S after the PSF has been subtracted can be obtained from eq. 2.41 and is given by:

$$\begin{aligned} \sigma_S^2 = ||I_{\psi_0}||^2 \left[1 - \left(\frac{\sum_{k=1}^{K_{klip}} < I_{\psi_0}, Z_k^{KL} >_S}{||I_{\psi_0}||} \right)^2 \right] \simeq \\ ||I_{\psi_0}||^2 \left(1 - \frac{\sum_{k=1}^{K_{klip}} \Lambda_k}{\sum_{k=1}^{K} \Lambda_k} \right) \end{aligned} \tag{2.43}$$

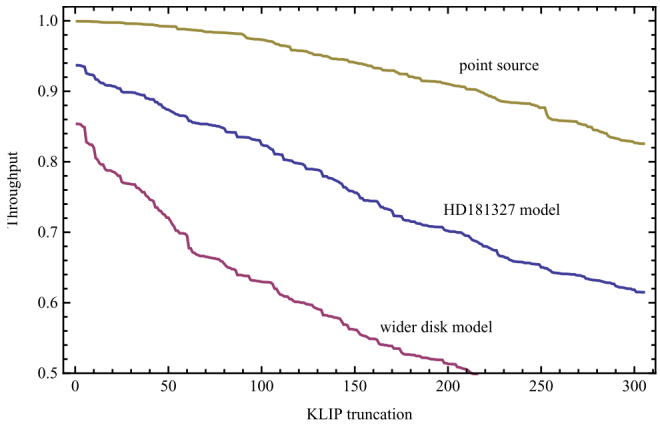

FIGURE 2.15— KLIP throughput based on eq. 2.15 from the projection of the astrophysical signal A onto the KL basis $< A, Z_k^{KL} >_S$. The green line represent the throughput of a planet located 1.5 arcsec from the host star, while blue line and puple line refer to more extended sources: a simple geometrical model corresponding to HD 181327 disk and an hypothetical ring-like disk about three time wider than that. From: Soummer et al. (2012)

that is a decreasing function of K_{klip}. Figure 2.16 shows the comparison between the theoretical expectation of the variance after subtraction is obtained from eq. 2.43 and several residual variances obtained from *HST* NICMOS archive's isolated stars after PSF subtraction has been performed. Eq. 2.43 can be then used to estimate with a semi-analytical approach the expected residual after subtraction. If KLIP is applied in small regions (similar to LOCI), eq. 2.43 can be used to estimate the noise locally around a putative source in the target image.

Given an a prior knowledge on the shape of the astrophysical source (i.e. planet position and flux, disk model, etc.) it is possible to obtain an estimate of the expected Signal to Noise Ratio (SNR) as a function of K_{klip} if S is small enough so that eq. 2.43 represents the local noise close to the source. In this way it is possible to chose K_{klip} a priori with the aim of optimizing the SNR for a given candidate source in the image.

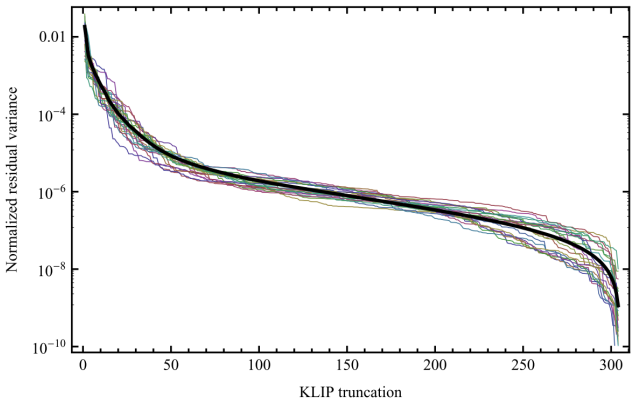

FIGURE 2.16— Normalized total residual variance over the entire image after PSF subtraction. The black curve shows the expected value of $\sigma^2/||I_{\psi_0}||$ based on eq. 2.43. The colored curves correspond to the total residual variance after subtraction for different target stars from *HST* NICMOS archive with no astronomical source around it. From: Soummer et al. (2012)

2.8.4 KLIP vs LOCI

The cost function associated with KLIP (eq. 2.38) is similar to the one associated with LOCI (Lafrenière et al. 2007). The differences though are remarkable, while LOCI minimizes the distance between the target image and the reference PSFs, KLIP minimizes in a statistical sense the difference between *any* PSFs of the references library and the K_{klip}-dimensional orthonormal basis-set $\{Z_k(n)\}_{k=1,..,K_{klip}}$ (Soummer et al. 2012).

The biggest difference between the two algorithms (and the biggest advantage of KLIP over LOCI) is the fact that the $\{R_k\}_{k=1,...,N}$ is not an orthonormal basis, so LOCI requires the inversion of the covariance matrix which is generally an ill-conditioned problem. On the other hand, KLIP regularization is implicit in the truncation of the KL basis. Even though many regularization approaches have been developed (Marois et al. 2010; Pueyo et al. 2012; Soummer et al. 2011) to solve this problem, a great advantage of KLIP remains the fact that it reduces the dimentionality of the problem reducing the number of references and therefore improves the overall speed of the algorithm.

Moreover, KLIP provides a linear framework that enables forward modeling

of astrophysical sources by fitting directly an astrophysical model $A_\xi(n)$ to the PSF-subtracted data $F(n)$, where ξ represent the model parameters. ξ can be evaluated (assuming a noiseless image) minimizing the following cost function:

$$\min_{\{\xi\}} \left\{ \sum_{n=1}^{N_S} \left(F(n) - \sum_{k=1}^{K_{klip}} < A_\xi, Z_k^{KL} >_S Z_k^{KL}(n) \right)^2 \right\} \tag{2.44}$$

A similar approach has been proposed in LOCI (Marois et al. 2010) but it may present degeneracy because the LOCI parameters are not guaranteed to be independent form I_{ψ_0} or A. The same degeneracy is not present in KLIP because the effect of the algorithm on the astrophysical source is completely determined from Eq. 2.44 and because the $\{Z_k(n)\}_{k=1,..,K_{klip}}$ is independent of the science image.

3

Part 2: Original Research

The main outcome of this research project has been summarized in three research papers.

Strampelli et al. 2020a, presents the novel *Stra*KLIP pipeline developed at the Space Telescope Science Institute (STScI) (USA) in collaboration with University of La Laguna (ULL) (Spain) and the Johns Hopkins University (JHU) (USA). The pipeline is designed to detect and characterize faint close-in sources around bright primaries taking advantage of the Karhunen-Loéve Image Processing (KLIP) algorithm introduced in Part I.

A key characteristic of the new pipeline is that it is designed to work with sets of wide-field imaging observations not specifically designed for HCI analysis. From this point of view, it represents a new tools that can be applied to virtually any large image dataset, either from space (HST, JWST, WFIRST-Nancy Grace Roman Telescope) or from the ground (e.g. LSST-Vera Rubin Observatory). To validate the algorithm on existing datasets taken with different instruments, it has been tested on the large *HST*/WFC3-IR survey (Strampelli et al. 2020b; presented hereafter in Chapter 5) and on a similarly large *HST*/ACS survey (Strampelli et al. 2020c; presented hereafter in Chapter 6). Both datasets have been acquired for two *HST* Treasury Programs on the Orion Nebula Cluster (ONC) with completely different goals than the one presented in this thesis, showing that the novel *Stra*KLIP pipeline can be readily applied to a broad variety of surveys, not only the one acquired with the primary goal of detecting candidates companions.

Strampelli et al. 2020b presents a first scientific application of the *Stra*KLIP

pipeline described Strampelli et al. 2020a, based on *HST*/WFC3-IR data from the Cycle 22 HST Treasury Program "The Orion Nebula Cluster as a Paradigm of Star Formation" (GO-13826, P.I. M.Robberto) in the F130N and F139M filters, with a relatively undersampled PSF. The ONC is a relatively near ($\sim$ 402 pc; Kuhn et al. 2019) young star forming region ($\sim$ 2 Myr; Jeffries et al. 2011; Reggiani et al. 2011; Jerabkova et al. 2019) where we mostly observe Class II targets. Starting with a sample of 1392 bonafide unsaturated cluster members, we detect 39 close-in cluster candidates pairs with separation $0.16'' - 0.77''$ (or $\sim 65 - 310$ AU, using the distance of the ONC) and mass range of the primary M_p $0.015 - 1.27$ $M_\odot$ and companion M_c $0.004 - 0.54$ $M_\odot$. Of these 39 binary systems, 21 are bona-fide new candidate detections. Correcting for completeness and combining this new catalog with previously detected ONC binaries, a binary fraction of $11.5\% \pm 0.9\%$ have been evaluated for the cluster for M_p $0.015 - 1.27$ $M_\odot$ and M_c $0.004 - 1.04$ $M_\odot$ and separations $0.16'' - 1.77''$ (or $\sim$ $65 - 695$ AU). Compared to other star-forming regions, this multiplicity function is ~ 2 times smaller than, for example, Taurus, while it is comparable to the field. The mass ratio (q) evaluated from this new sample of binaries shows a bottom-heavy distribution with median value ~ 0.25. Overall, this results hint to the fact that ONC binaries may represent a template for the general population of field binaries, supporting the hypothesis that the ONC may be regarded as the closest typical star-forming region in the Milky Way (MW).

Strampelli et al. 2020c presents the application of the *Stra*KLIP pipeline on *HST*/ACS data from HST Tresuary program (GO-10246, P.I. M. Robberto) on the same Orion Nebula Cluster in five different filters: F435W, F555W, F658N, F775W and F850LP, with better sampling of the PSF. The aim of this new paper is both to confirm companions detected in WFC3-IR data (where there is overlap) and to provide consistent and more accurate multi-band photometry using the novel *Stra*KLIP pipepline for the entire cluster. Combining for the first time two HST Treasury program on the ONC and exploiting the richness of this new multi-band dataset, a Spectral Energy Distribution (SED) fitter have been applied to each sources to infer three fundamental parameters (mass, extinction and age) through a Goodman & Weare's affine invariant Markov Chain Monte Carlo (MCMC) ensemble sampler (Foreman-Mackey et al. 2013). Three different Initial Mass Function (IMF) (Kroupa, Chabrier single and system) and two different reddening laws ($R_v = 3.1$ and 5) have been tested. Overall, we observe that changing the IMF, as well as changing the reddening laws, does not strongly impact the outcoming parameter distributions, even though $R_v = 5$ seems to produce more shallow distributions compared to $R_v = 3.1$ in

both the mass and A_V parameters. As representative values for this cluster we find: a median mass between $0.15-0.21$ $M_\odot$, a median extinction A_V between $1.64-2.42$ magnitudes and a median age between $1.6-1.8$ Myr.

In particular, a more in-depth analysis of the age distribution for stars in the cluster unveiled the presence of at least two different populations with an average age of ~ 0.85 and 1.6 Myr, strongly supporting the idea that star formation in the ONC was neither just one singular event or a continuous process diluted over a prolonged period of time, but instead is best described by at least two discrete and sequential episodes of star formation over a range of ~ 5 Myr.

Taking advantage of the available F658N filter in the survey, accretion luminosity (L_{acc}) and mass accretion rate ($\dot{M}_{acc}$) have been estimated for a sample of ~ 700 bonafide cluster sources, providing one of the most extend catalog of mass accretion rates in the ONC up to-date. The $\dot{M}_{acc}-M_\star$ relationship exhibit two different regimes. On one side, we observe that more massive stars ($M_\star > 0.3$ $M_\odot$) display a rather shallow linear relation that agrees with that predicted in the context of centrally irradiated accretion disks around solar-mass stars with an active accretion layer (Mohanty et al. (2005); Hartmann et al. 2006). On the other, lower mass stars ($M_\star \lesssim 0.3$ $M_\odot$) can be in turn divided in two different populations as well. If we extend the line fitting the higher mass stars, we see that it nicely matches a population of low mass objects with high accretion rates. There is, on the other hand, a second branch, departing at $M_\star \sim 0.3$ $M_\odot$, displaying a steeper relation between $\dot{M}_{acc}$ and $M_\star$. These two low mass populations also display differences in age: one appear younger with higher accretion rate, the other more evolved with a lower mass accretion rate. A decay of the mass accretion rate vs. age is not surprising, but in this case it suggests the coexistance in the ONC of two different young populations. Moreover, an analysis of the extinction of these objects suggest that the older sources typically lie in regions less embedded, i.e. more evolved having been exposed for longer time to the ionizing flux from the OB stars.

A new catalog of 119 binaries is presented with separations $0.12'' - 1.95''$ (or $\sim 48-785$ AU), where most of the pairs are corss-matched with WFC3-IR measurements, and a new binary fraction of $13.0\% \pm 1.0\%$ is established for the cluster for M_p $0.015-1.93$ $M_\odot$ and companion M_c $0.004-1.$ $M_\odot$. Even though higher than the one evaluated in Strampelli et al. 2020b with WFC3-IR data alone, the difference can be entirely explained in term of cluster membership selection, where in the latest paper we applied a more stringent selection than in the former for both the stars in the cluster and binaries, leading to a slightly higher result (applying the same stringent selection to Strampelli et al. 2020b sample provide a MF of $12.9\% \pm 1.1\%$). The ratio of wide binaries (i.e. binaries with separation $\gtrsim 0.5$) and close is analyzed in the paper showing the presence

of dynamical evolution on the population fo binaries in the cluster.

Draft version December 18, 2020
Typeset using LaTeX **twocolumn** style in AASTeX63

*Stra*KLIP: A novel pipeline for detection and characterization of close-in faint companions though Karhunen-Loève Image Processing algorithm

Giovanni M. Strampelli,[1,2,3] Laurent Pueyo,[2] Jonathan Aguilar,[1] Antonio Aparicio,[3,4] and Massimo Robberto[5,2]

[1] *Johns Hopkins University, 3400 N. Charles Street, Baltimore, MD 21218, USA*
[2] *Space Telescope Science Institute, 3700 San Martin Dr, Baltimore, MD 21218, USA*
[3] *Department of Astrophysics, University of La Laguna, Av. Astrofísico Francisco Sánchez, 38200 San Cristóbal de La Laguna, Tenerife, Canary Islands, Spain*
[4] *Instituto de Astrofísica de Canarias, C. Vía Láctea, 38200, San Cristóbal de La Laguna, Tenerife, Canary Islands, Spain*
[5] *Johns Hopkins University 3400 N. Charles Street Baltimore, MD 21218, USA*

ABSTRACT

We present a new pipeline developed to detect and characterize faint astronomical companions at small angular separation from the host star using sets of wide-field imaging observations not specifically designed for High Contrast Imaging analysis. The core of the pipeline relies on Karhunen-Loève truncated transformation of the reference PSF library to perform PSF subtraction and indenting candidates. Test of reliability of detections and characterization of companions are made through simulation of binaries and Receiver Operating Characteristic curves through false positive/true positive analysis. The algorithm has been successfully tested on large *HST*/ACS and WFC3 datasets acquired for two HST Treasury Programs on the Orion Nebula Cluster.

Keywords: software — binaries — stars: pre-main sequence — stars: low-mass

1. INTRODUCTION

The ability to detect and analyse companions in binaries and multiple systems is essential to characterize the frequency and parameters of those systems. Linking their parameters to models of dynamical evolution from their original molecular cloud can provide insight on the physics at play during the earliest stages of star formation. For this purpose, the multiplicity of pre-main sequence stars has been investigated over a broad range of environments: dense stellar cluster (e.g. Petr et al. 1998; Köhler et al. 2006; Reipurth et al. 2007; Luhman et al. 2005), young OB associations (e.g. Brown & Verschueren 1997; Shatsky & Tokovinin 2002; Kouwenhoven et al. 2007), T associations (e.g. Kraus et al. 2008, 2011). Speckle interferometry, adaptive optics, aperture masking and Hubble Space Telescope (HST) high-contrast imaging (HCI) or direct imaging (DI) are just some of the techniques that have been applied to obtain rich datasets.

Corresponding author: Giovanni M. Strampelli
strampelligiovanni@jhu.edu

In principle HCI is a most promising technique. However, even when the primary star can be masked out (coronography), the detection of faint close-in companions is heavily hampered by the dominating presence of bright quasi-static speckles mainly caused by imperfections in the optics (Schneider & Silverstone 2003; Biller et al. 2004; Marois et al. 2005; Masciadri et al. 2005). To deal with this problem, and possibly take advantage of the quasi-static nature of the speckles, two main classes of algorithms have been developed: LOCI (Locally Optimized Combination of Images algorithm; Lafrenière et al. 2007) and KLIP (Karhunen-Loève Image Processing algorithm; Soummer et al. 2012). The latest will be used in the following of this paper.

In this paper we present a full pipeline developed to detect faint astrophysical companions at small angular separation in regular wide-field imaging observations, not specifically designed for HCI analysis. In Section §2 will provide a general overview of the pipeline, while in Sections §3 to §8 we describe more in depth each individual steps. The conclusions are presented in §9. Two appendices comprise all the major figures produced during the simulations explained in §8 (Appendix A) and the relative tables (Appendix B) for reference.

2. OVERVIEW OF THE PIPELINE

The core of the pipeline consists of nine steps, mostly coded in Python 3.7 (Van Rossum and Drake 2009) unless otherwise specified, that will be briefly reviewed here and addressed more in detail later in the following sections. Steps 2 and 3 have been developed as Jupyter notebooks[1] (from here after simply Jbooks) because of the highly interactive nature of the analysis.

In order to achieve the KLIP PSF subtraction (Step 6), our pipeline requires two specific inputs:

- a set of *initial _flt HST* images;
- an *initial input catalog* of primary targets to be searched for companions (even though this is a *soft* requirement - see point 2 later in this Chapter).

During the following discussion, the *initial input catalog* of potential target sources refers to the source list preliminary extracted using standard image-analysis tools, while the *actual input catalog* is the derived list required for the pipeline to work. The same distinction applies to the images, where the prefix *initial* refers to the initial *_flt HST images* calibrated by the standard WFC3 pipeline and downloaded from the Space Telescope Science Institute (STScI) MAST archive, different from the *input _flt HST images* needed by the pipeline. The generic term *image* will be often used as an abbreviation for *_flt HST image*. The term *postage-stamp* and *tile* will be intended as interchangeable, both referring to a small *FITS* image cut around a target source that will define the searching region $\mathcal{S}$ for companions.

1. **Image load:** a preliminary step needed to adapt the *initial input images* to the format expected by the pipeline. The pipeline require a set of *input _flt images* in electrons/sec, already multiplied by the pixel area map (PAM[2][3]): an image where each pixel value describes that pixel's area on the sky relative to the native plate scale and allow to account for differences between on-sky pixel size across the field of view. The pipeline rearrange these images as a multi-dimension *datacube* with the following layers: 1) the *SCI* labeled image that will contain the actual data, 2) the *DQ* labeled image containing the data quality flags and 3) the *ERR* labeled image containing the uncertainties related to the *SCI* image;

2. **Source Catalog:** if the *initial input catalog* is not provided, a collection of routines have been developed to create it matching *HST* images with Gaia catalogue (Gaia Collaboration et al. 2018). This allows the pipeline to work even if only the *initial input images* have provided out of the MAST pipeline, without further analysis. This step is handled as a Jbook;

3. **Input Catalog:** the *initial input catalog* of target sources is modified and reassembled in order to produce an *input catalog* for the pipeline in a suitable format. Also this step is handled as a Jbook;

4. **Postage stamps:** small *postage-stamp* images are created for each entry of the *input catalog*, trimmed so that the centroid of each star coincides with the center of its *tile* and setting-up a search region $\mathcal{S}$ for each target;

5. **Groups:** the *tiles* are grouped according to their position in the field of view (FOV) of the instrument, creating a set of *tiles datacubes* to be processed to determine suitable field-dependent PSF stars;

6. **KLIP analysis:** PSF subtraction is performed on each *tile* using KLIP algorithm (Soummer et al. 2012);

7. **Residual survey:** the residual *tiles* produced by the previous step are analyzed looking for the presence of a previously undetected astronomical source;

8. **Candidates:** an output catalog of candidate detections with a preliminary photometry is produced.

9. **Analysis:** tools needed to assess the reliability of the detections are provided, based on a statistical analysis of simulated injected companion and false positive detections. During this step, the pipeline records the output of the photometry performed on simulated binaries and isolated stars to build ROC curves and perform false positive rejections

[1] The Jupyter Notebook is an open-source web application that allows to create and share documents that contain live code, equations, visualizations and narrative text. https://jupyter.org/index.html

[2] *HST*/WFC3-IR and UVIS:https://www.stsci.edu/hst/instrumentation/wfc3/data-analysis/pixel-area-maps

[3] ACS:https://www.stsci.edu/hst/instrumentation/acs/data-analysis/pixel-area-maps.

The final product of the pipeline is represented by a hierarchical data format (HDF5) *pandas*[4] dataframe, which includes different layers related to the different steps of the pipeline. A library of Jbooks allows to analyze the output of the pipeline and produce the results shown in Strampelli et al. (2020a,b). As in the case of steps 2 and 3, the Jbook format has been chosen because of the highly interactive nature of the final analysis. They provide examples of the ancillary routines developed to analyze and interpret the output catalog, providing warnings or eventually excluding false positive detections.

Hereafter we provide more details on the major steps.

3. ACS/WFC3 IMAGE READER (STEP: 1)

In order for the rest of the pipeline to work, the *initial input images* need to be read and transformed in a suitable format. The *input images* expected by the pipeline are *flt HST* images in the format delivered by the STScI MAST archive. In the case of WFC3-IR, these are *single-chip* image datacubes composed by 5 layers. Of these, the important ones are:

- a science image where the actual data reside with the extension *SCI*;
- a data quality image with all the information about bad pixel, saturated pixel, cosmic ray etc., with the extension *DQ*;
- an error image where the variance of the science image is store with the extension *ERR*;

The pipeline looks only for these three specific labels and ignores the others.

The *split_chip.py* routine has been developed to take advantage of *ACSmask/WFC3mask* from DOLPHOT package (Dolphin 2000)[5] to mask out all pixels flagged as bad in the data quality image (so that a flagged pixel will be avoided in future sky determination, photometry, etc.) and multiply the *initial input image* by the PAM. In the case of *ACS/WFC3-UVIS*, the routine splits the *initial input images* in two *.chipN* new *FITS* datacubes (where *N* represent the chip number 1 or 2), each with it's unique *SCI* corrected image, *DQ* and *ERR* sublayers stored into it. In the case of *WFC3-IR* images, the routine will just store the new *SCI* corrected image along with the linked *DQ* and *ERR*. Before running this step it is usually best practice to backup all the *initial input images* because this task will alter them.

[4] https://pandas.pydata.org/docs/index.html

[5] See the packages handbook at http://americano.dolphinsim.com/dolphot/ for more details

4. STANDARD INPUT CATALOG (STEP: 3)

In this step the pipeline converts the input catalog into three *pandas* dataframes with standard labels, filling the entries needed by the pipeline to run:

- a *header* dataframe storing all the fundamental static information the pipeline will need in order to work and provide final results (i.e. specific project-dependent column labels, selected pipeline input options, information about the detector such has the pixel-scale, the detector dimensions etc.). This header also covers a 'recovery mode' role and can be used to trace back the many options selected during the different steps of the pipeline, if there is the need to go back and repeat;
- a *unique* dataframe which holds data about the physical position on the *initial input image* and photometry of each sources in the *initial input catalog* with relative uncertainties. If a source has been detected multiples times, one entry for each detection will be stored in the dataframe. Two different IDs label uniquely each source (*MainID*) and link together different detections (*UniqueID*) of the same source. This dataframe also stores miscellaneous information regarding each detection such as the *visit*, *CCD*, *PA_V3*, *saturation*, *image name* and more;
- a *mean* dataframe holds the averaged photometry for each *unique* entry as well as the celestial coordinates. The ID of this dataframe is the same *UniqueID* as in the *unique* dataframe.

Following a convention similar to the one adopted by Robberto et al. (2013), a *type* (f) is provided with the *initial input catalog* to help during some crucial decision-making points along the pipeline, and it is added to the *unique* dataframe. *type 0* sources are stars that are not detected in the specific filter under study and are generally ignored in this filter. *type 1* labeled sources instead are the "standard" sources accepted by the pipeline. Sources may appear as *type 0* in some filter and *type 1* in others, both depending on their brightness in different passbands. *type 2* and *type 3* label close pairs, the main difference being the presence of combined (in the former) or individual (in the latter) photometry in the *initial input catalog* (see Figure 2 for an example of a *type 2* source).

Type 2 sources turn out to be crucial to test the overall performance of the pipeline because they provide a first batch of targets to use during the fine tuning of the many options available in each step of the pipeline: one should at least be able to recover most - if not all - of

type	Explanation
0	undetected in the filter
1	detected in at least one filter
2	unresolved double
3	resolved double
n	user defined flag

Table 1. *type* flag entry adopted by the pipeline. Only source with a *type 1* will be selected as possible PSF reference. Sources with *type 1,2* or *n* (where $n \notin [0, 1, 2, 3]$) will be processed by the pipeline in search for a companion while *type 0* or *3* sources will be skipped.

the 'suspected', but not fully resolved, binary systems in the catalog. On the other hand, resolved pairs can pose a problem for the creation of a good PSF. Any target with a resolved companion within a given distance will then be labeled as *type 3*. The pipeline will ignore these sources, as their fluxes can be derived using more conventional PSF photometry techniques.

If the *type* flag is not provided with the *initial input catalog*, the star is initially considered *type 1*.

A new flag is added to each entry of the *unique* dataframe indicating the source as either a *good/bad candidate* for PSF subtraction, a *good PSF* star or a *wide-double*. Both good candidates and PSF stars are analyzed by the pipeline, the difference between them being that the "good candidate" star are not selected for the PSF library. To be selected as a PSF star, a source must be bright and well isolated (*type 1* in essence), but not saturated. This selection can be made parsing a maximum number of saturated pixel in the tile, as well as a user-defined range of magnitudes and errors. *Good candidates* are selected by a user-defined range of magnitudes and errors with *type* $\neq 0$ or 3. This means that that any kind of *type* flag can be introduced in the pipeline by the user to process particular sources including galaxies, stars with disk, photoionization, Herbig-Haro objects etc. The pipeline will still run on them and the residuals can easily be retrieved at the end calling the right *type* flag.

Bad candidate, either because saturated, not detected in the filter or too faints, as well as *wide doubles* (*type 3*) will be instead ignored by most of the steps of the pipeline.

A last flag is added to the *unique* dataframe indicating the *quadrant* (or *cell*) where the source appears in the field of view of the instrument. Each *cell* (all of equal size) is constructed to be large enough to contain enough PSF stars so that different *KLIP-modes* can be investigated during the PSF subtraction step. The number of the *KLIP-modes* chosen to truncate the Karhunen-Loève transformation is in fact strictly related to number of references in the *PSF reference library*. On the other hand, the size of the *cells* must be small enough so that variations of the PSF with the position on the chip do not affect the local PSF model. The WFC3/IR channel has a $\simeq 10\%$ difference between the diagonals, corresponding to a field of view of 136×123 arcsec. To maintain the PSF asymmetry within a nominal 1% variation we have divided the field of view in a 10×10 cells, with about 50 sources per cell. In Figure 1 we show the density of good candidates (gray dots), PSF reference stars (yellow dots) and wide doubles (blue dots).

An output HDF5 dataframe composed by the three compiled *header*, *mean* and *unique* dataframe is saved as a product of this step. This HDF5 dataframe will generally represent the *input catalog* required by the pipeline to perform the following steps.

5. TILE DATACUBES (STEPS: 4 AND 5)

During this step the pipeline runs through any entry in the *input catalog* that is not labeled as *wide double* and creates a *tile* (with a user defined side, the default being 1.5 arcsec) centered on the coordinates of the source on the *input image*. To create a tile, the routine first creates a temporary tile centered on the source using one of the following options:

- *input coordinates*: the coordinate from the *input catalog* is used as default to create the temporary tile for the source;
- *reference filter*: the routine takes into account all the other available filter (for the specific entry) not flagged as *bad* and selects the coordinate from the filter with the smaller magnitude error as new input coordinate for the tile. This can be used for example when different exposures are taken back to back without changing the telescope pointing;
- *reference ID*: similar to *reference filter*, but instead it selects the coordinate from all the other detections of the target in the *same* filter. This comes in handy when the pointings between two visits are very close due to a small dither.

In general, the second and third options are used when for any reason the input coordinates for a target are not reliable and there is the need to acquire the starting position of the tile from elsewhere.

The presence of cosmic ray (CR) in the temporary tile can heavily affect the alignment process (as well as the identification of a future candidate companions in the *residual tile* - see Sec. 6) driving the alignment to pixels that do not belong to the target star. Therefore, before

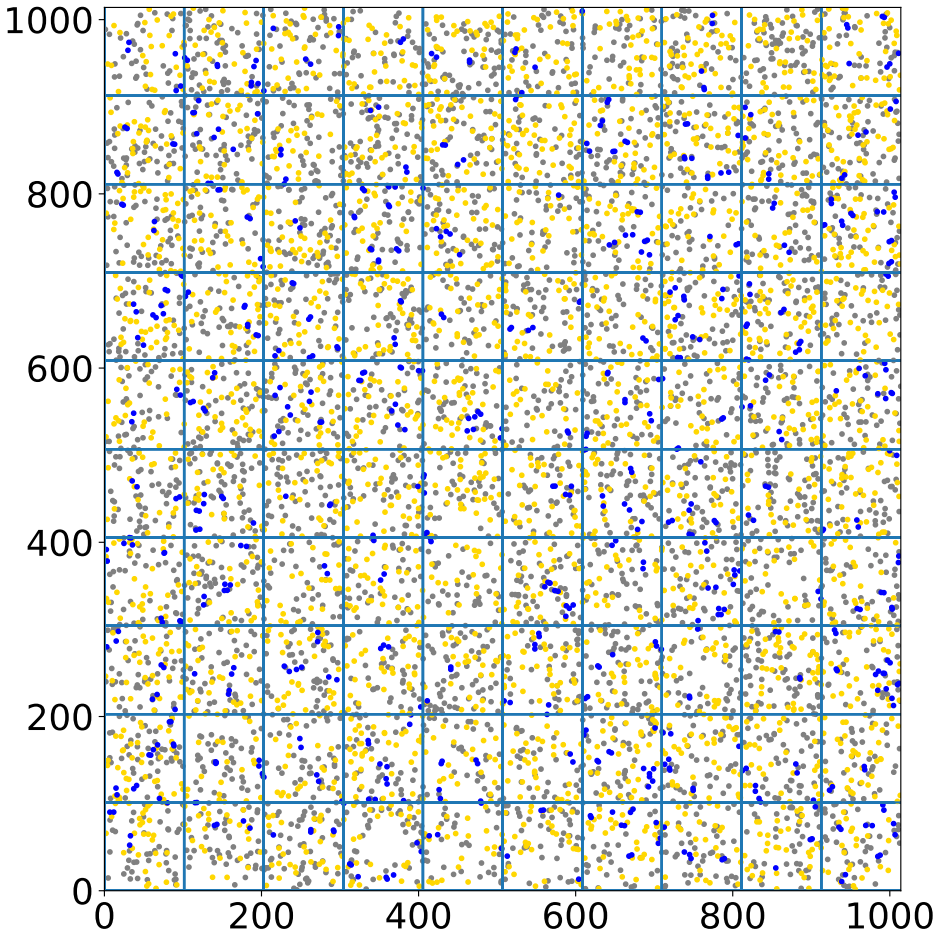

Figure 1. *WFC3-IR* FOV (1014x1014 pixels). Each gray dots marks the position on the instrument of a selected *good candidate*, while yellow dots marks *PSF* stars. Blue dots marks the position of identified *wide doubles* In this example we settled on one hundred *quadrants* with a averaged number of isolated targets (*good candidates*) of ~ 44 and averaged number of *PSF* stars of ~ 32.

performing the alignment, two options are available to mask any pixel suspected to be affected by a CR:

- *DQ mask*: if the position of CR are recorded in the DQ image layer of the *input image*, then they can be corrected in the temporary tile applying a median filter. For each CR-flagged pixel in the temporary tile, the median value of the counts in a 2 by 2 pixel mask will be evaluated (ignoring any CR-flagged pixel in the mask) and attributed to the pixel to be corrected.
- *L.A. cosmic ray removal*: cosmic rays (CR) can be identified and removed using the *Astro-SCRAPPY*[6] python module (McCully et al. (2018) - based on the L.A. Cosmic algorithm from

[6] available at https://github.com/astropy/astroscrappy

van Dokkum (2001)). Figure 2 show an application of this module in the pipeline where the CR is identified and removed from the tile without affecting the central unresolved binary (labeled *type 2*)

After CR-cleaning, the temporary tile can be shifted to align its center with the estimated center of the source. Three possibilities are provided to estimate the new center:

- *maximum*: the brightest pixel within 2 pixel (default) from the center of the temporary tile is selected as the new center of the tile;
- *PSF matching*: the routine matches a user-provided PSF to find the position where the PSF is optimally aligned with the data; this uses the *matched filter* technique explained hereafter in Section 7.
- *no corrections*: the initial input coordinates are taken as the new center of the tile with no further corrections applied.

The default behaviour is to use the *input coordinate* along with the *maximum* option, but this can be changed. Any other options can be selected for all entries in the *input catalog* or can be forced and applied (parsing the *UniqueID* to specific targets when their behaviour is different from the global set). In this way, for example, it is possible to change the basic behaviour to *reference filter* for all but some of the sources, and to align the tile using the *maximum* for some and the *PSF fitting* for other entries of the *input catalog*.

When the final tile is created, after the centering step, the routine evaluates the new coordinates (if any correction has been made) moving the center of the tile to the new positions in the *input image* and updating the position-labeled columns in the *unique* dataframe accordingly. The original sub-pixel position of the source is preserved during this process. The output at this stage is a new FITS datacube, one for each entry in the *input catalog*, containing the following four layers:

- the newly created tile labeled as *Data*;
- a tile cut from the *ERR* layer of the *input image* and labeled as *eData*;
- a tile obtained from the *DQ* layer of the *input image* labeled *DQ* as well;
- if the option to remove CR has been enabled, then the CR free data tile is also recorded with label *CR_Clean*

Once a *tile* datacube for each selected entry of the *input catalog* has been made, two *FITS* datacubes are created, one with all the selected *PSF* stars and another with all the targets for the upcoming PSF subtraction. Both datacubes can be made of either *Data* tiles or *CR_Clean* tiles, depending on the user's preference. It is advised to carefully inspect each newly created tile using any application able to read and visualize *FITS* files (i.e. DS9; Joye & Mandel 2003). It should be noted though that as part of this pipeline, routines have been developed to visually inspect the new tiles and extract useful information at glance, instead of inspecting them one at the time through DS9 for example. These routines can be easily accessed through a Jbooks. Those routines comes particularly handily to check for:

- the presence of any bad entry in the catalog, like e.g. the repetition of the same source under different *UniqueIDs*
- a poisoned list of PSF stars due to wrongly labeled sources (for example a *type 2* source labeled as *type 1*)
- CR heavily affected tiles or by other prominent structures.

because any of those (but not only) problems could hamper the following PSF subtraction step and the overall final outcome of the pipeline.

At the end of this stage of the pipeline, a new dataframe is added to the HDF5 general dataframe labeled as *counts*. This new dataframe, similar in nature to the *unique* dataframe, is organized as a *pandas multi-index* dataframe where each entry is split and grouped according to the different filters. This new dataframe records all the data that will be created in the next steps and are fundamental for the pipeline to run, but that are not needed to be shown at *higher-level*. They are kept in this dataframe to avoid cluttering the *unique* and *main* dataframe.

6. PSF SUBTRACTION AND CANDIDATE DETECTION (STEPS: 6 AND 7)

During this step the pipeline performs the PSF subtraction using pyKLIP[7] (Wang et al. 2015). The pyKLIP module implements the KLIP algorithm to achieve accurate PSF subtraction through the following operation (for more details see Soummer et al. 2012):

$$T(n) - \hat{I}_{\psi_0} = \epsilon A(n). \quad (1)$$

[7] https://pyklip.readthedocs.io/en/latest/

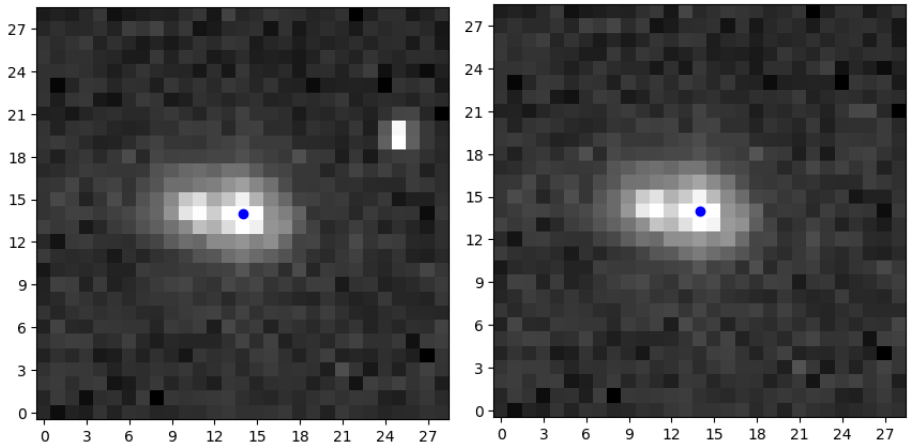

Figure 2. *HST*/ACS *type 2* star tile before (left) and after (right) L.A. CR removal, in the filter F580LP. The blue dot mark the central pixel of the tile. The base of each tile is 1.5 arcsec.

Here $T(n)$ represents the $n-th$ input tile (either with *Data* label or *CR_Clean* label) of the datacube; $\hat{I}_{\psi_0}$ is the best representation of I_{ψ_0} (the model of the *isolated* source with no other astronomical signal in the search area $\mathcal{S}$); $\epsilon A(n)$ is the extra astronomical source that may ($\epsilon = 1$) or may not ($\epsilon = 0$) be present in the input tile $T(n)$.

The typical output of this process is thus a new tile, having the same size as the input tile, containing the residual of the subtraction process with overall mean equal to zero. Any additional astronomical signal possibly present in $T(n)$ will be apparent in this *residual's tile*. In other words, the $\epsilon A(n)$ is nearly orthogonal to the main telescope's PSF representations and therefore minimally affected by the subtraction process. Depending on its brightness, it will appear as an extended PSF (see Figure 3) or just as a few bight pixels (see Figure 4). For each input tile, the PSF subtraction process is repeated iterating over different values of the KLIPmode K_{klip}, the number of modes where to truncate the Karhunen-Loève transformation. Different KLIPmode values allow to better sample different portions of the search area $\mathcal{S}$, with smaller value allowing to better retrieve signal very close to the target source than higher one. A user-defined list of KLIPmodes can be investigated and for each of them, a new *KLIPmodeN* layer (where N is the number of KLIPmode investigated) is appended to the *tile* datacube containing the residual of the KLIP subtraction operation just performed.

To select a candidate detection, the routine inspects all *KLIPmode* layers relative to the same source (observed over different visits and filters) and compares the position of the brightest pixel in each tile. A candidate will be flagged if:

- the brightest pixel is detected with counts above a user-defined multiple value of standard deviation, calculated after a 3σ cut of all values in the *residual tile* to eliminate outliers;
- the brightest pixel is detected in the same position over all the filters and visits;
- the brightest pixel is present in at least 2 different KLIPmodes.

To determine spatial coincidence between different visits, the routine factors in the eventual telescope rotation and small misalignment, allowing for a pre-defined number pixels, typically 1, of discrepancy. To choose the best KLIPmode, the routine then compares the signal to noise (SNR) for the KLIPmodes that result in a detection, choosing the one with the higher possible SNR and the lower possible KLIPmode. The output of this routines is recorded in the *counts* layer of the HDF5 dataframe for future analysis.

7. PHOTOMETRY (STEP: 8)

The last step of the pipeline is the creation of a catalog recording the averaged properties of every binary system detected using the KLIP algorithm. Photometry is performed at this stage, and the pipeline offers three different approaches: aperture photometry, matched filter photometry and PSF photometry. While aperture

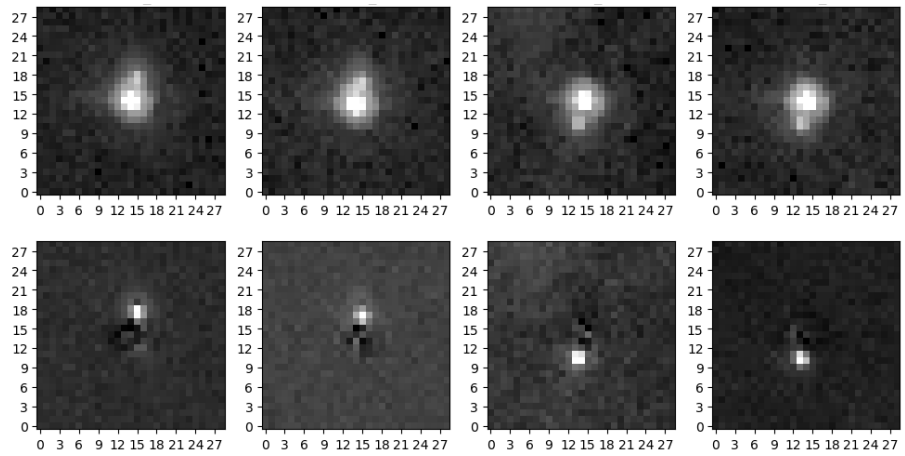

Figure 3. Top row: *HST*/ACS F850LP input tiles of same target observed in 4 different visits with 2 different orientation angle of the telescope. Lower row: PSF subtraction output (*residual's tile*). The additional astronomical signal in the input tile is perfectly clear (once we remove the central star) and it appear as an extended PSF.

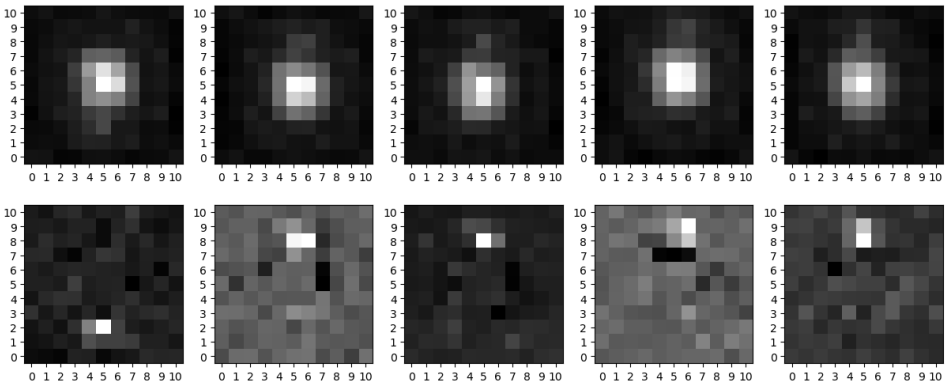

Figure 4. Same as Figure 3. Top row: *HST*/WFC3-IR F130M input tiles. Lower row: PSF subtraction output. In this case the additional astronomical signal in the input tile appears as just a few bright pixels in the *residual's tile*.

photometry always provides an accurate value, in particular when the stars are well isolated and there is no companion present, the other two methods can provide a more precise estimate of the flux of a star, if the Point Spread Function is well sample. This is typically the case for ACS and the visible channel of WFC3, but not of WFC3/IR. Hereafter we illustrate each method and their application to ACS simulations, to underline the strengths and flaws and the strategy adopted by our pipeline to deal with these limitations.

7.1. *Aperture photometry*

To perform aperture photometry the pipeline uses the $photometry_{AP}$ routine which integrates some of the *photutils*[8] feature to perform aperture photometry. Figure 5 shows the two tiles required by this routine, as well as a sample of the grow curves created to determine the

[8] photutils is a python module affiliated to Astropy that provides tools for detecting and performing photometry of astronomical sources. https://photutils.readthedocs.io/en/stable/index.html

optimal sky value. First, the routine uses the *CircularAnnulus* module of *photutils* to evaluate the median sky background (C_{sk}). Specifically, it takes a 3σ cut median of the sky in an annulus between two chosen radii (r_a and r_b) (*Sky* tile in Figure 5). This sky estimate is then subtracted from the data tile creating a *sky-subtracted* tile. Using the *CircularAperture* module of *photutils*, the routine then sets to zero all pixels outside a circular area of radius r_i centered on the star, creating a final *sky-subtracted aperture* tile (or simply *Aperture* tile in Figure 5), that immediately provides the total counts (C'_{ap}) of the source inside the mask. To check the accuracy of sky estimate, many *curves of growth* are created (last tile in Figure 5) correcting the sky value by small amounts and performing multi-aperture photometry at different radii to enhance the systematic errors on the sky estimate. Indeed, when the sky is correctly estimated then the curve will remain flat over the full range of selected radii. Otherwise, the multi-aperture photomery will show a parabolic shape due to the fact that the sky error grows quadratically with the number of pixels in the aperture, i.e. $\propto r_i^2$. If the sky has been overestimated, too much flux will be removed as the radius increases and the counts will show a parabolic decrease vs. radius; viceversa, if he sky has been underestimated. So, by making different grow curves, the routine looks for the flattest curve in the sample (black curve in Figure 5) and returns the correct sky estimate.

To evaluate the photometric uncertainty we use the following formula:

$$\Delta C_{ap} = \sqrt{var_1 + var_2 + var_3} \tag{2}$$

where var_1,var_2 and var_3 are the three main source of errors added in quadrature.

The first term,

$$var_1 = N_{ap}\, std(C_{sk})^2, \tag{3}$$

represents the random noise floor in the aperture, including readout noise and contamination from neighbouring stars. This term is given by the variance of the sky values, multiplied by the number of pixels in the aperture. The second term

$$var_2 = C_{ap} \tag{4}$$

where C_{ap} represent the photoelectrons counted inside the aperture and var_2 is the Poisson noise associated to the brightness of the target star.

$$var_3 = N_{ap}^2 \left(\frac{std(C_{sk})^2}{N_{sky}} \right), \tag{5}$$

is the uncertainty in the estimate of the sky brightness, not accounted for by the variance of source counts but affecting the actual measure.

Once the final counts in the aperture and the uncertainties on their estimate are evaluated, they are converted in magnitude, m and its relative uncertainty, dm using the formulae:

$$m = -2.5\, log_{10}\left(\frac{C_{ap}}{ExpTime} \right) + ZPT \tag{6}$$

$$dm = 1.0857 \left(\frac{\Delta C_{ap}}{C_{ap}} \right) \tag{7}$$

where *ExpTime* is the exposure time used when the data was acquired and ZPT is the zero point related to the *input tile*'s filter.

7.2. *WFC3 KLIP Companion's Aperture photometry*

As already noted in Strampelli et al. (2020a), due to the fact that WFC3/IR PSF is highly undersampled, after PSF subtraction, the majority of the flux from a faint candidate companion is contained within just a few pixels of the residual tile. Thus, to derive its total flux, one has to apply a large and rather uncertain aperture correction. To mitigate this problem, the routine performs photometry of the companion using a 4-pixel aperture and uses the already processed data to establish the relative aperture correction. To this purpose, for each isolated source in the input catalog the routine determines a 2×2 square pixel area including the brightest pixel of the original image. After probing the 4 possible mask positions, the routine considers the one providing the highest total counts, C_{4p}. The known magnitude of each primary is then related to the four pixel counts through the equation:

$$m_{4p} = -2.5 log_{10}(C_{4p}) + \Delta \tag{8}$$

where Δ is the zero point relating the 4-pixel counts to the previously known photometry. Having multiple "standard" stars, the final Δ value is determined as the 3σ cut median of the full set, with an uncertainty $sigma_\Delta$ given by the associated standard deviation:

Once the final Δ have been determined, a similar procedure is applied to the residual tile and the counts in the 4-pixel aperture are recorded for the companion. Equations 8, with the newly evaluate C_{4p} counts for the companion and the final Δ value, provide the final magnitudes of the candidate companions. The associated uncertainties are similar to those evaluated for a generic aperture photometry (see paragraph 7.1) but now they take into account also the uncertainty on the aperture correction, i.e.

$$\Delta C_{ap} = \sqrt{var_1 + var_2 + var_3 + e\Delta^2} \tag{9}$$

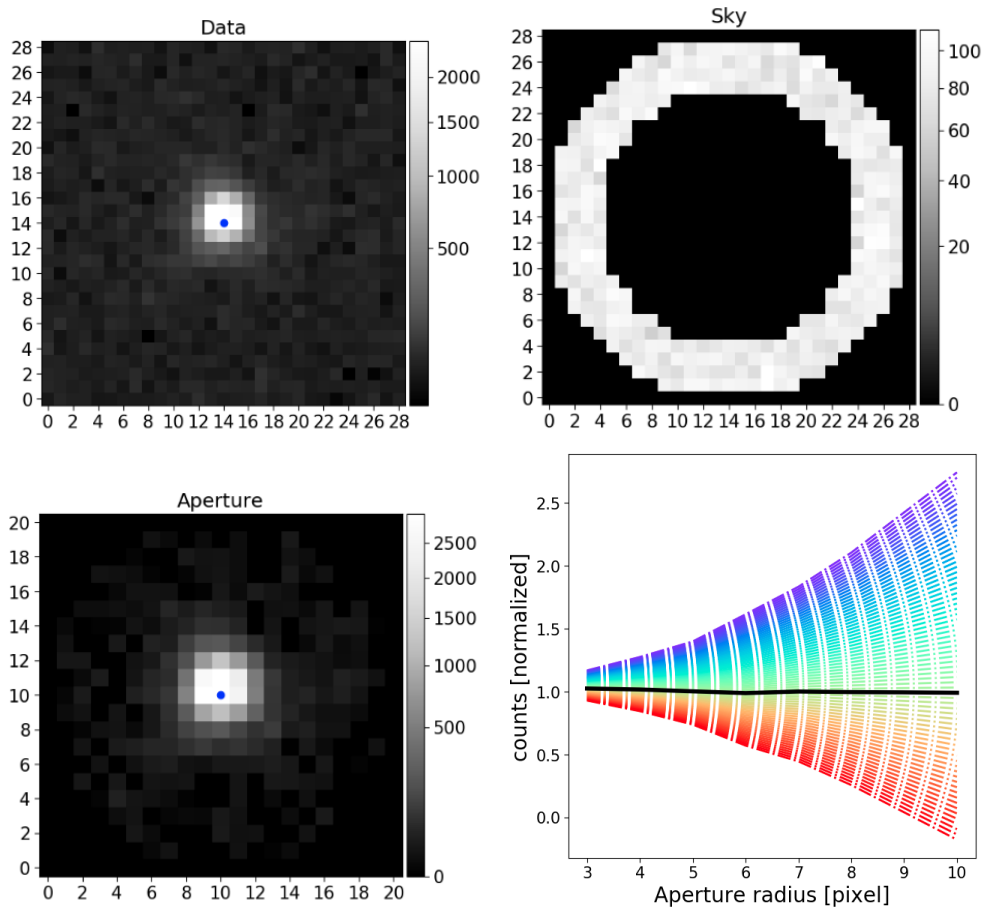

Figure 5. Top row: input data tile (left) and sky annulus (right). The blue point marks the center of the tile. Bottom row: Sky-subtracted aperture-selected data tile (left) and grow curves (rigth). Each different curve in this last plot is calculated correcting the estimation of the sky by a step of ±1% to a maximum of ±30% (blu/red). The black line correspond to the "flattest" curve across all the radii and correspond to the curve with a sky correction of −1%. Each curve in this example has been normalized to the average counts of the black curve for radii bigger than 5

In the case of the 4-pixel aperture photometry for companions, the *sky* refers to background in the residual tile after PSF subtraction has been performed.

7.3. *Matched filter photometry*

For well sampled data, the pipeline offers a second method to extract photometry, *matched filter photometry* (Rothstein (1954); Turin (1960)). In general, *matched filter* (MF) solves the problem of detecting with the highest signal-to-noise a signal of known shape in noisy data. The solution is given by the cross-correlation between a known signal template (the reference PSF in this case) and an unknown noisy signal (the target). The pipeline uses the $photometry_{MF}$ routine that takes advantage of the MF routines present in *pyKLIP* package, based on the scipy signals processing library of Fast Fourier Transformations (FFT) to perform the convolution of the template with an image.

Figure 6 shows the different tiles used by the $photometry_{MF}$ routine. First, the sky is evaluated us-

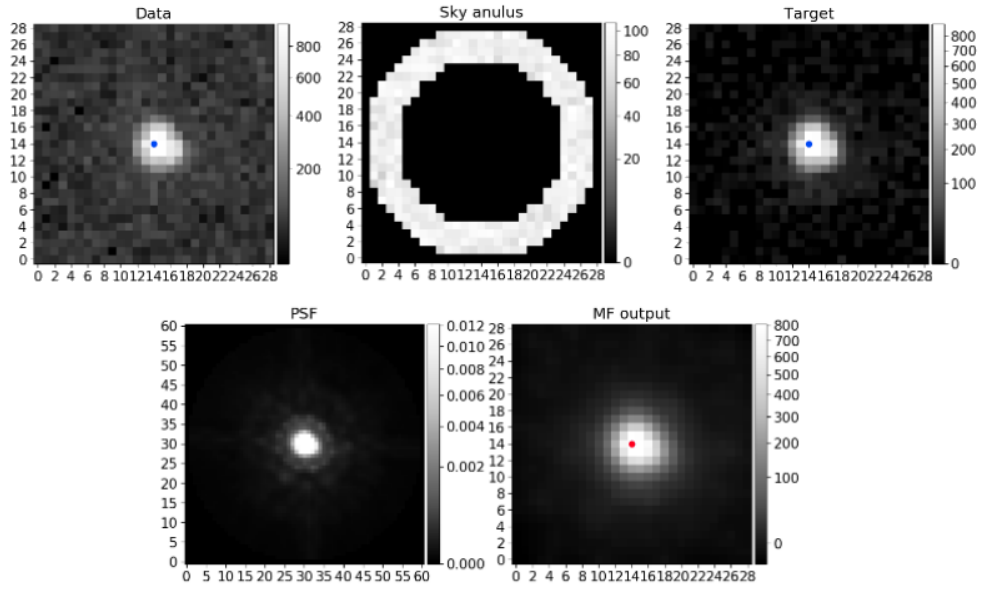

Figure 6. Top row: input data tile (left), sky annulus (center) and sky subtracted target tile (right). Bottom row: PSF reference tile from Tiny Tim (left) and MF output tile (right). The red (blue) dot marks the maximum (center) in tile.

ing an approach similar to the $photometry_{AP}$ routine, adopting an annulus between r_a and r_b (*Sky annuls* tile in Figure 6). Also in this case, the sky estimate can be further refined using the *grow curves* as explained in paragraph 7.1. The background sky is then subtracted from the *Data* tile to produce a *sky-subtracted* target tile (or just *Target* in Figure 6) This tile is convolved with the reference tile, i.e. the *PSF* tile obtained for example from Tiny Tim[9] and the output of this operation is stored in the *MF output* tile.

The counts of the star can then be recovered dividing the brigthest pixel in the MF output by the *troughput* (i.e. the normalization factor that will rescale the counts MF output to the real flux of the star):

$$C_{MF} = \frac{max(MF_{output})}{throughput} \tag{10}$$

$$throughput = |\Sigma_{i,j}\, abs(PSF_{i,j})^2| \tag{11}$$

[9] Tiny Tim is a program that generates simulated Hubble Space Telescope point spread functions (PSFs). https://www.stsci.edu/software/tinytim/

where PSF represents the input template tile. To estimate the uncertainties on C_{MF}, the routine follows the same equations 3 to 5 used for $photometry_{AP}$ with the difference that since no aperture is performed in this photometry, a "noise-equivalent area" needs to be defined from to derive the number of pixels ($\overline{N}_{ap}$) contributing to the uncertainty estimate. Following King (1983), the effect of the background, B, can be computed by adding it over an equivalent area whose dimension depends on the size and shape of the PSF. The pipeline uses King's approximate rule of thumb for the equivalent noise area

$$\sigma_B^2 = 8\pi a^2 B \tag{12}$$

where $a \sim 0.5\lambda/D$ is half the diffraction-limited angular resolution of the telescope at the effective wavelength of the filter in use. Future versions will include the more rigorous results presented by King (1983) in tabular form. Once σ_B^2 is evaluated, it can be combined witht he Poisson noise associated to the brigthness of the star as:

$$\Delta C_{MF} = \sqrt{C_{MF} + \sigma_B^2} \tag{13}$$

Once C_{MF} and ΔC_{MF} are evaluated, the same Eq. 6 and 7 can be applied.

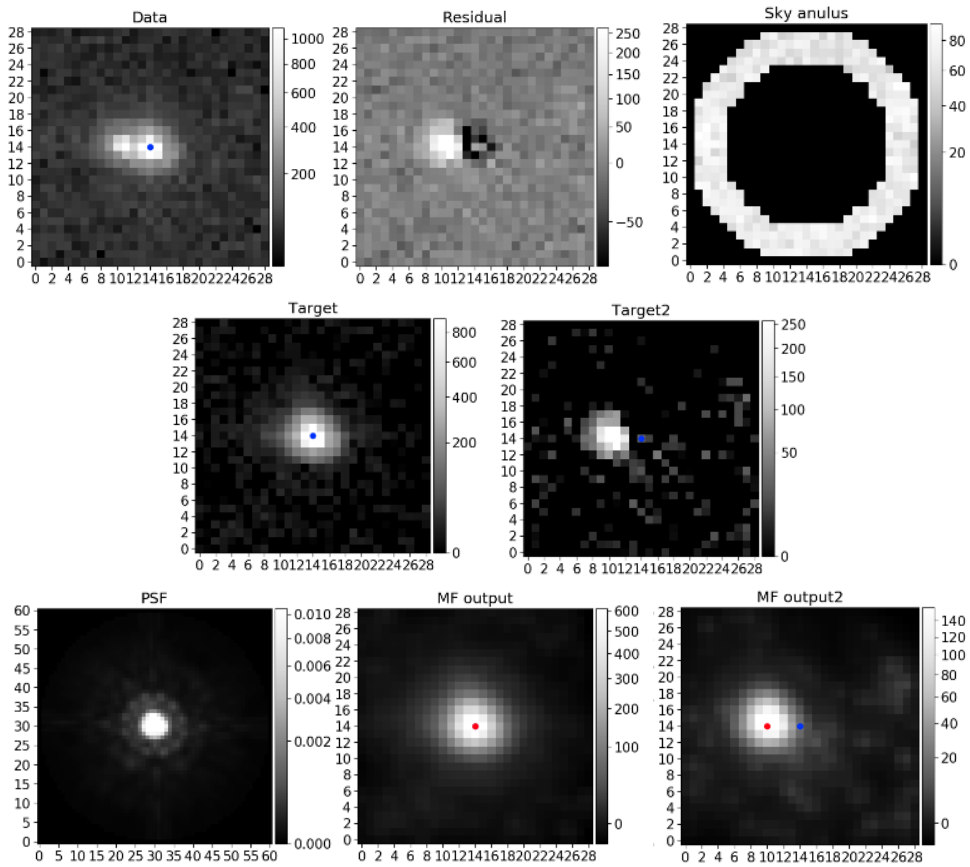

Figure 7. Top row: input data tile (left), residual tile after PSF subtraction (center) and sky annulus (right). Central row: isolated sky-subtracted primary (left) and isolated residual-background-subtracted companion (right). Bottom row: PSF reference tile from TinyTim and MF output tile for primary and companion. The blue (red) dot marks the center (maximum) in the MF output tile.

7.4. *Binary's Matched Filter photometry*

In the case of a close binary system, where aperture photometry fails due to the presence of both stars in the extraction aperture, the MF photometry technique can be easily applied to retrieve the flux of primary and companion apart. With reference to the tiles shown in Figure 7, to retrieve the flux of the primary, the routine subtracts the *residual tile* from the *input tile* (Data) obtaining a new tile (target) where the primary is isolated and the $photometry_{MF}$ routine can work as explained in the previous paragraph. For the companion, instead, the routine evaluates and subtracts the 3σ cut median background in the *residual* tile producing a new tile (target2) for the $photometry_{MF}$.

7.5. *PSF photometry*

The third option to perform photometry of well sample data is PSF photometry. $photometry_{PSF}$ performs PSF fitting making extensive use of the *BasicPSFPhotometry* package from *photutils*[10]. As initial guess for the coordinates and flux, $photometry_{PSF}$ evaluates a centroid on the tile and uses the flux estimated by

[10] https://photutils.readthedocs.io/en/stable/index.html

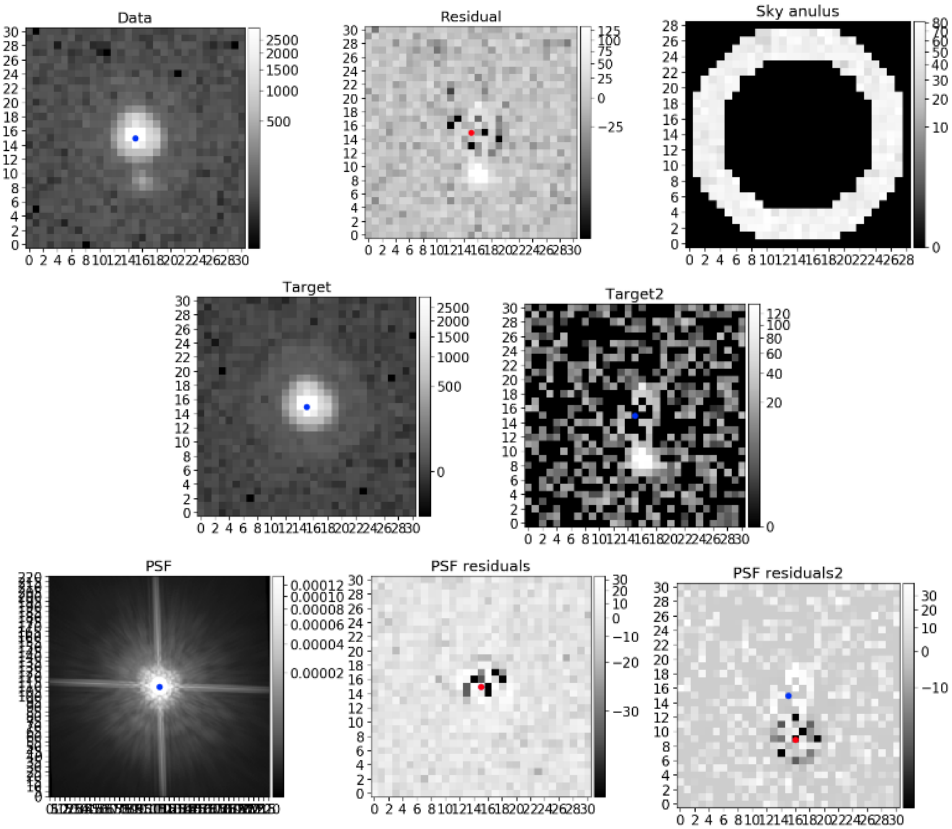

Figure 8. Similar to Fig. 5, top row: input data tile (left), residual tile after PSF subtraction (central) and sky annulus (right). Central row: isolated sky-subtracted primary (left) and isolated residual-background-subtracted companion (right). Bottom row: PSF reference tile from TinyTim and PSF residual tile for primary and companion. The blue (red) dot marks the coordinate for PSF fitting.

$photometry_{AP}$. Once the flux of the star has been evaluated through PSF fitting, $photometry_{PSF}$ takes advantage of equations similar to Eq. 12 and Eq. 13 to estimate the uncertainties on the counts. Then it convert counts and errors to magnitude units using Eq. 6 and 7. Moreover, a reduced χ^2 is evaluated for each performed photometry as:

$$\chi^2 = \frac{1}{m-n}\sum_{i,j}\left(\frac{x_{i,j}-\mu_{i,j}}{\sigma_{i,j}}\right)^2 = \\ = \frac{1}{m-n}\sum_{i,j}\left(\frac{Residual_{i,j}}{eData_{i,j}}\right)^2 \quad (14)$$

where m is the number of number of pixels in the tile, n is the number of free parameter for the fit, i.e. $n = 3$ since we are fitting both the positions i,j and the flux, $x_{i,j} - \mu_{i,j}$ is the difference between the observable ($x_{i,j}$) and the model ($\mu_{i,j}$). A *residual tile* is produced by the $photometry_{PSF}$ while $\sigma_{i,j}$ is a tile comprising the pixel-related uncertainties on the flux of the observable (i.e. the *eData tile* created during the step 4 of the pipeline as explained in section 5 ; see also Figure 8 for a graphical example of the tiles).

As we can see from the "Residual" tile in the example in Figures 7 and 8, the primary component has been over-subtracted (because of the contamination from the

companion during the PSF subtraction), which will now lead to the primary to be too bright in the "Target" tile, and thus the wrong answer when evaluating the photometry. Conversely, the secondary is likely slightly subtracted by the PSF subtraction and so "Target2" is missing some flux that cannot be recovered. This problem will be addressed more specifically in Section 7.7, where we present the corrections we applied to mitigate it when retrieving the photometry of both primaries and companion sources.

7.6. *Binary's PSF photometry*

Like in the case of *matched filter photometry*, the $photometry_{PSF}$ routine can be utilized to estimate the flux of both members of a binary system once it has been split in it's basic component through KLIP. The routine will perform steps very similar to $photometry_{MF}$, as shown in Figure 8 , evaluating the flux for both primary and companion through PSF fitting instead of performing a convolution. As explained before, the *PSF residual* tiles can be utilized to evaluate the goodness of the performed fit for both the primary and companion.

7.7. *Pipeline photometry performance*

The performance of the three built-in photometry suites has been tested for the *HST*/ACS instrument simulating isolated stars and binaries at different separation and magnitudes differences between companions and primaries. Given our primary scientific interest on the Orion Nebula Cluster, we tested the pipeline simulating stars that would be plausible to observe in the ONC. We performed *aperture*, *matched filter* and *PSF photometry* on the sample, and the outputs analyzed to detect possible systematic shifts emerging from the three different methodologies.

Similar test have been conducted also for the branch of the pipeline working with *HST*/WFC3-IR data. Since they have been extensively presented in (Strampelli et al. 2020a), in the following paragraphs we will mainly focus on *HST*/ACS data simulations. Given the better spatial sampling of ACS vs. WFC-IR, our results may provide a more accurate assessment of the advantages and limitations of each method.

7.7.1. *Test I: Isolated stars*

To test the performance of the three photometry routines, thousands of simulated isolated stars have been generated to closely resemble the stars present in the Orion Nebula Cluster both in flux and position on the sky. We created 50 PSF datacubes with 11.05" diameter equally spaced on both chip of the ACS/WFC focal plane, with mutual separation of 400 pixels, using Tiny Tim. Then the magnitudes obtained with these three approaches is compared in five different target filter: F435W, F555W, F658N, F775W and F850LP. Each PSF datacube has been created for temperatures between 2000 and 3000 °K in steps of 250 °K , sampling the lower end of the temperature range of M-dwarfs. Each PSF datacube comprises 25 different sub-pixel shifted PSFs. Each shifted PSF is derived from the standard Tiny Tim PSF created with the *SUB=5* option , splitting each native pixel in 25 sub-pixels. When the *SUB* option is enabled, Tiny Tim does not convolve the PSF with the charge diffusion (CD) kernel. Following Hoffmann & Anderson (2017) we performed the charge diffusion correction by applying the CD kernel to the oversampled PSF, before shifting the PSF by a finite amount of sub pixels and rescaled to the native resolution. This operation consist in applying the CD kernel to subsets of the PSF tile that posses the same pixel phase. Arranging the subsampled pixel in this way places neighboring pixels in an order similar to the order of the natural ACS resolution. Then, each sample of subsampled pixel with the same pixel phase is convolved with the CD kernel. This process is repeated 25 times to cover all the possible pixel phases in the 5x5 subsampled PSF.

Once the subsampled PSF has been convolved by the CD kernel, a subpixel shift is applied to center the PSF in each of the 25 sub-pixels and the PSF is resampled to the native ACS resolution producing 25 slightly different shifted PSF for each temperature, chip ad position on the CCD.

To keep these simulation as close to reality as possible, the stars have been generated covering for each filter a magnitude range matching Robberto et al. (2013) catalog of Orion Nebula Cluster sources, constrained to prevent stars to saturate or being too faint to be detected given the exposure time. The stars have then been divided in bins with width equal to 1 magnitude. Once a magnitude bin is selected, a random magnitude is extracted (we will refer to this reference magnitude as Mag_i) and converted in temperature using a 1 Myr isochrone from the bt-Settl family of models. Then a random subpixel shift is generated for the artificial target and an on-sky source's coordinate is randomly selected from Robberto et al. (2013) catalogue. The coordinates are chosen in a way that, overall, all simulated sources are equally distributed both on sky and on the detector. The CCD and the coordinates of the catalog source, as well as the random pixel phase and the magnitude-dependent temperature are then used to select the closer PSF in the PSF datacubes previously generated. This PSF is rescaled to the selected flux using the standard HST zero points and the background

	F435W	F555W	F658N	F775W	F850LP
b_{ap}	0.003 ± 0.061	-0.006 ± 0.143	-0.007 ± 0.262	-0.010 ± 0.106	-0.004 ± 0.099
b_{mf}	-0.045 ± 0.156	-0.057 ± 0.095	-0.059 ± 0.150	-0.067 ± 0.037	-0.066 ± 0.059
b_{psf}	0.001 ± 0.017	0.001 ± 0.019	-0.000 ± 0.246	-0.000 ± 0.102	0.000 ± 0.095

Table 2. Values of the constants evaluated from each simulation as explained in the text.

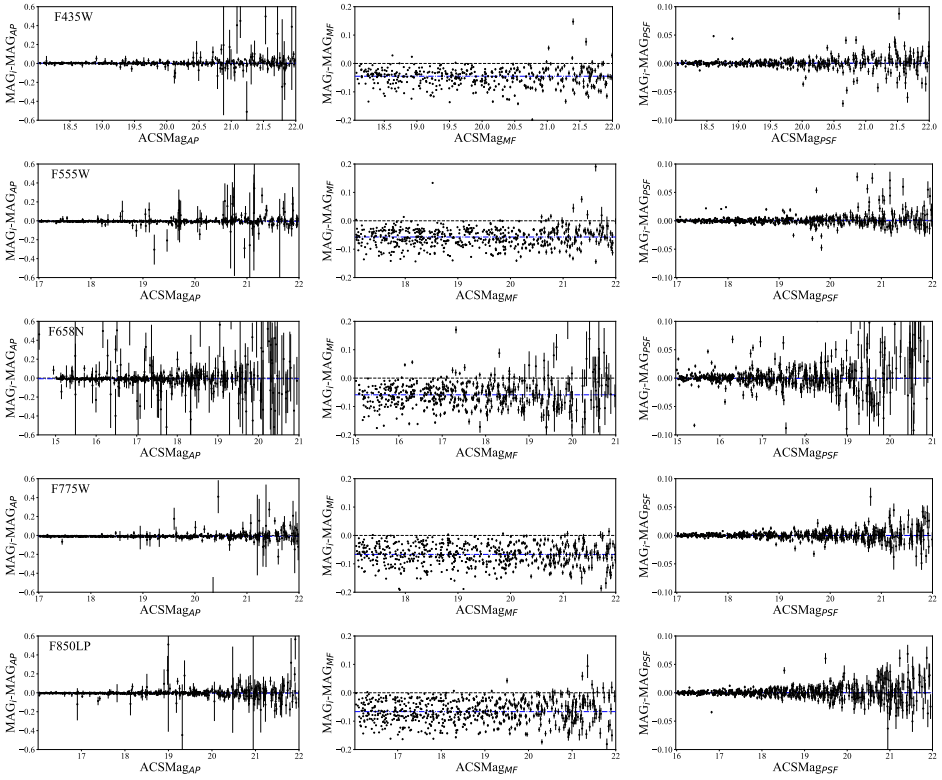

Figure 9. The plot shows the deltas between the known Mag_i and the Mag_x vs Mag_x, where the subscribed Mag_x represent the output of one of the photometric routines applied to isolated stars: *aperture* photometry (left), the *matched filter* photometry (center) and the *PSF* photometry (right). Each row shows the results for each filter (F435W, F555W, F658N, F775W and F850LP) analyzed in this simulation. The constant fit is shown as a blue dash-dotted line while the black dashed line shows the locus of points where Mag_i=Mag_x. Note that the Y-axis range may differ moving from one technique to the other.

is added to each pixel. This last step is performed using the *make_noise_image*[11] from *photutils* that extract each background pixel value from a Gaussian distribution with mean given by the 3σ-cut median of the sky evaluated at the source's real on-sky coordinates and standard deviation given by the corresponding scatter. To conclude this process, Poisson noise is added to the

[11] https://photutils.readthedocs.io/en/stable/api/photutils.datasets.make_noise_image.html

final tile using the *apply_poisson_noise*[12] from *photutils* as well.

The simulated star is than parsed to the three routines for photometry. Because for each position multiple PSF where generated with subpixel shifts, both $photometry_{MF}$ and $photometry_{PSF}$ subtract from the target (normalized by the total flux in the tile) all the subpixel shifted PSFs, choosing the one that minimize the residual of this operation to use as reference PSF.

This process has been repeated for a sample of ~ 1500 artificial stars, for each filters. The output photometry produced by the three methods has been compared to the input magnitude Mag_i of the simulated source. The discrepancies have been analyzed finding the averaged value of the three delta magnitude distributions, i.e., Mag_i - Mag_{AP} vs Mag_{AP}, Mag_i - Mag_{MF} vs Mag_{MF} and Mag_i - Mag_{PSF} vs Mag_{PSF}, to find the presence of systematic shifts in the output of these three routines when compared to the known input. The results of this analysis are shown in Figure 9 and in Table 2 for each filter. The *PSF* photometry (right panel in the figure) offer the right trade-off between accuracy and precision when compared to the other two methods, usually providing the smaller delta with the smaller uncertainties. Overall, the $photometry_{MF}$ is the worst of the three approach when we are corcern in retriving an accurate estimate of the flux of the source, with the $photometry_{AP}$ slightly worst than and $photometry_{PSF}$.

No system is perfect though, so even if the routines try to account for missing flux due to their use of a finite aperture ($aperture_{AP}$) the limited extent of the PSF used for the fit (both $aperture_{MF}$ and $aperture_{PSF}$) and the not perfect estimate of the background (despite having applied for all the tree systems the grow curve correction), cause an offset between the input flux and the measured value. Evaluating these deltas as we have done in our specific test can then help mitigating this problem (see Table 2), providing a insight about when correct or not real data, where the input magnitudes of the sources is unknown. Comparing the results in Table 2, in our simulation we observe that the $photometry_{AP}$ and $photometry_{PSF}$ yields systematic error that overall are smaller than the uncertainties on the *deltas*. So trying to correct for this difference in those two cases might be counterproductive because to account for a small delta we will introduce an even larger uncertainty. Conversely, this is not true for $photometry_{MF}$, where the correction is need to account for the observed larger delta (at the price of including in the estimate an additional source of uncertainties). The correction to the magnitude take the form of:

$$m_{cor,i} = m_i + \Delta i \tag{15}$$

where m_i and $\mathrm{m}_{corr,i}$ are the measured and corrected magnitudes, Δ_i is the averaged shift of the measures from the expected value by the three $photometry_i$ tools. The associated uncertainties can be obtained adding the spread of the simualtions to the magnitude error as:

$$em_{corr,i} = \sqrt{em_i^2 + \sigma_i^2} \tag{16}$$

where σ_i represent the spread of the measures at a given magnitude bin.

In conclusion, the $photometry_{PSF}$ appear as both the most accurate and precise between the three routines, and it's contribution to the uncertainty is the smallest when we apply the correction, and therefore it seems to be most preferable. Moreover, $photometry_{MF}$ appear to systematically underestimates the star photometry. Because MF and PSF photometry are usually thought as strictly equivalent from a mathematical standpoint, this result appears to be odd and it will require further analysis to be able to identify the reason why this is happening.

If the PSF created by Tiny Tim is not deemed an acceptable representation of the real PSF of the instrument, a different PSF can be generated, for example form the data itself, and then parsed to the routine that simulate the stars to produce a new set of fits.

7.7.2. *Test II: Binaries*

Similar to the case of isolated star, the three photometry routines have been tested in the presence of binaries to understand their overall performance. As in the previous case, ~ 1500 pairs have been simulated for each filter and for a range of separation ranging between 3 and 10 pixels from the host star, in step of one pixel. The procedure to generate a binary is in many way similar to the one for isolated star. First two PSF are selected as explained in section 7.7.1 and rescaled to match the flux of the primary and companion we want to simulate (i.e. the flux of the two stars separated, not the whole system). Then, the rescaled companion PSF is injected in the tile of the primary at a given random position (the injection location are randomly selected such as they lie on a circle with radius the selected separation and center the primary star). Once the companion in injected, both background and Poisson noise are added to the common tile as explained in section 7.7.1.

The final tile containing the binary system is then parsed to the routine that performs PSF subtraction as

[12] https://photutils.readthedocs.io/en/stable/api/photutils.datasets.apply_poisson_noise.html

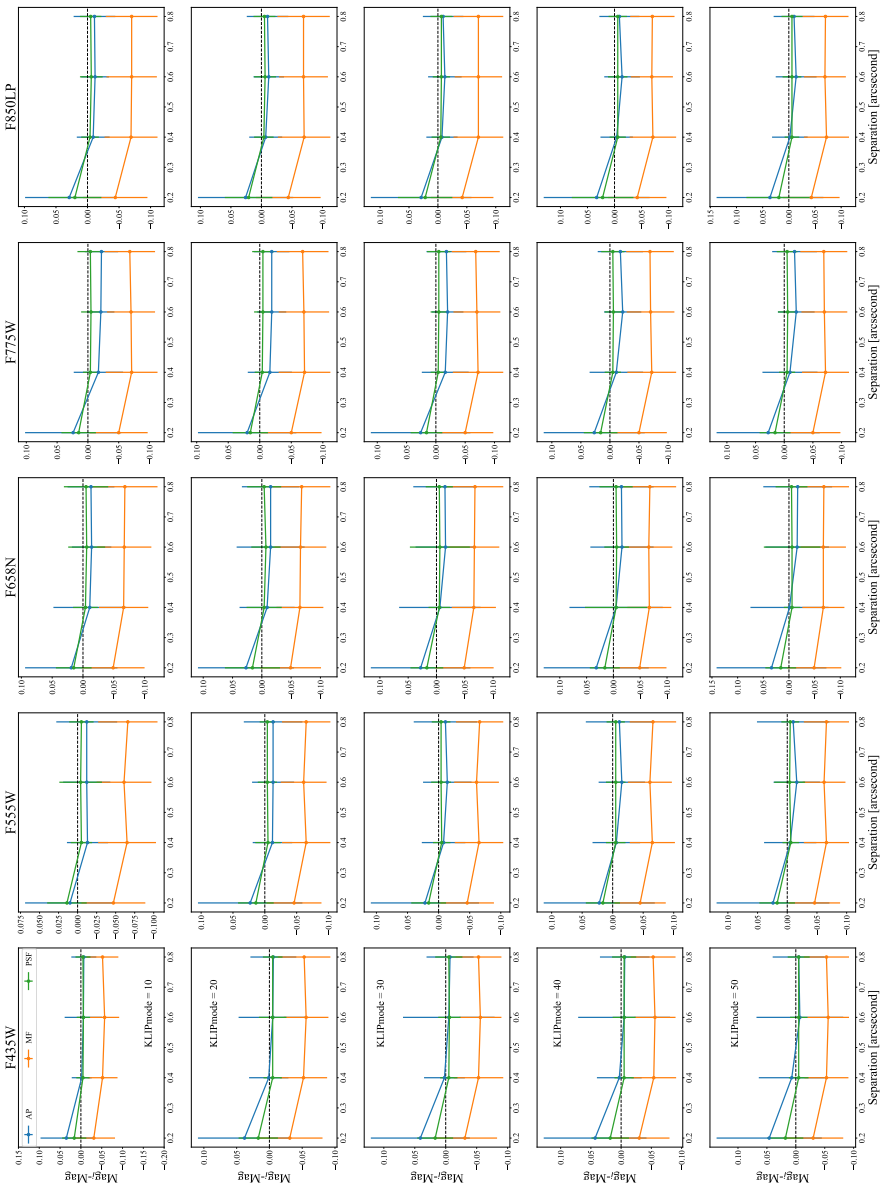

Figure 10. The plot shows the results of the linear fit applied to the distribution of deltas (Mag$_i$ - Mag$_x$) vs the contrast of the binary (Mag$_{comp}$ - Mag$_{prim}$) as a function of the separation between primary and companions, where the Mag$_x$ represent the output of one of the photometric routines applied on the isolated primary stars. Each columns represent a different filter analyzed in the survey while each row refer to a different KLIPmode. The black dashed line shows the locus of points where Mag$_i$=Mag$_x$. Note that the Y-axis range may differ moving from one technique to the other.

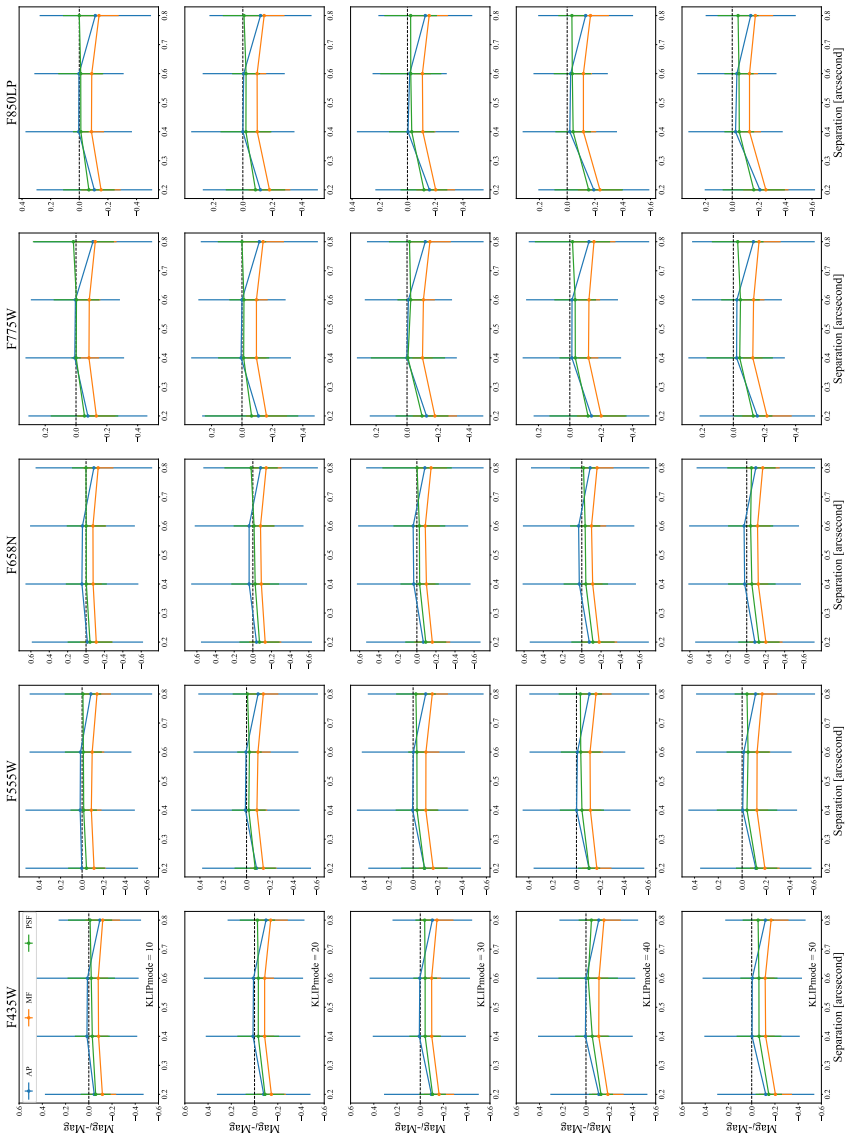

Figure 11. Similar to Figure 10 but for isolated companions

explained 6 and the *residual tile* is retrieved. The *residual tile* is then subtracted from the tile containing the binary to obtain a tile where the primary is isolated (*isolated primary tile*) while the *residual tile* alone is the tile where the companion has been isolated (*isolated companion tile*). The two tiles with isolated primary

and companion are then parsed to the three photometry routines and the output is compared to the original known flux of the primary and companion alone. Even though this is primarily a test for the photometry of the pipeline, it also yields a second interesting result. Since we know a-priori also the position of the injected companion, we can allow the routine to search for the companion in the *isolated companion tile* in a similar way as described by (Soummer et al. 2012), before performing photometry. If the position does not coincide within one pixel with the coordinate of the injection, the photometry is rejected. So analyzing the rate of rejections, one can understand, depending on the configuration of the binary system (i.e. filter, magnitude of the primary, difference in magnitude between companion and primary, separation, KLIPmode selected for the subtraction etc.) the overall performance of pipeline to actually find companions regardless on their real presence. In other words, this analysis can be use to estimate the rate of false positive and true positive detections as a function of the configuration of the binary, and help strengthen any decision about detecting a companion or refusing a candidate. In the next section 8 we will illustrate the last (optional) step of the pipeline where the infrastructure needed for false positive detection is created. For practial applications, the false positive analysis on *HST*/WFC3-IR data is covered by (Strampelli et al. 2020a)) while *HST*/ACS data are addressed in (Strampelli et al. 2020b).

Moving back to the photometry, we performed a study similar to the one previously presented for isolated stars in Figure 9, but in this case we analyzed *isolated primaries* (once the companion has been identified and subtracted), and *isolated companions*. Contrary to the case of isolated stars, the analysis on the binaries depends on a much wider group of variables. Firstly, we need to consider the deltas Mag_i - Mag_x versus the contrast (i.e. the difference in magnitude between companion and primary), where the Mag_x represent the output of one of the photometric routines applied on the isolated primary stars itself. Secondly, each of this distributions can be evaluated for each filter, possible separation of the binary and KLIPmode utilize to truncate the Karhunen-Loève transformation. Similar arguments can be made for the photometry of the companions. Due to this complexity, we summarize the results of these analysis in Figures 10 and 10, where only the outcome of the constant fit applied on each distributions as a function of the separations are shown, with error bars representing the relative uncertainty on each fit. More over, each columns refer to a different filter while each row refer to a different KLIPmode. As expected, when a close companion (separation $\leq 0.2''$) is subtracted from a binary the outcome of the three routines is worst than for wider binaries (separation $> 0.2''$) due to the increasing overlap between the two PSFs. For wide binaries, similar to the case of isolated stars, the $photometry_{MF}$ appear to be less accurate in correctly retrieving the the flux of either the isolate primary or companion, constantly underestimating the flux of both component, while the $photometry_{AP}$ and $photometry_{PSF}$ do a better job. In particular, $photometry_{PSF}$ appear more precise compared to the others. However, both $photometry_{AP}$ and $photometry_{PSF}$ show problems in correctly evaluate the photometry of an isolated primary when a companion is found very close to the hosting star (separation $\leq 0.2''$) due to an uncompleted subtraction of the close-in companion, that in turn brings to an overestimate of the isolated primary. This trend is reflected in the isolated companions where both routine tends to underestimate the flux of close-in companion, bringing to an underestimate of the isolated companion. In this case, smaller KLIPmode are able to achieve better results than bigger KLIPmode, when dealing with close-in companions Moreover, due to the finite dimension of the tiles we used in the simulation, when a companion is very close to the border of the tile (separation $\gtrsim 0.8''$), $photometry_{AP}$ fairly fails to recover the correct flux of the isolated companions, while the $photometry_{PSF}$ is able to correctly reconstruct the flux of the isolated companion.

8. FALSE POSITIVE ANALYSIS (STEP: 9)

In this section we mainly focus on the approach undertaken by the pipeline to build the infrastructure needed to implement the false positive analysis. This final step heavily rely on the simulation of isolated stars and binaries described in section 7.7.1, where we have shown how to inject artificial companions and isolated sources for *HST*/ACS data. A similar approach can be followed for *HST*/WFC3-IR data as well, as fully described in Strampelli et al. (2020a). Once a library of both singles and pairs is created, it can be parsed to the pipeline for analysis. It is important to notice that each binary tile is linked to a corresponding single source tile by the same primary star, i.e. the tiles are created in tandem: one with a single source, and one with the same sources plus an injected companion with random flux and random position i,j on the tile. In this way the pipeline can measure the flux at the injected position i,j both for the isolated source (building the null hypothesis) and for the linked binary (building the test hypothesis). As we shown in Strampelli et al. (2020a), we can build Receiver Operating Curves (ROC) from this analysis and estimate the probability to have false positive in our

sample of candidates as a function of the particular configuration of the binary (i.e. filter under examination, the magnitude of the primary, delta magnitude between companion and primary, KLIPmode utilized to detect the companion and separation between the two). We need to stress that this step does not provide false positive rejection, as it only focuses on the simulated sources and knows nothing about the real one: it does not separate single false positives from true detections in the sample, but only provide an estimate on how probable is that a specific configuration can produce false positive in the simulations. In other words, its only scope is the production of the dataframe with values that can be compared to real detections in order to make an informed decision if a companion is plausibly a false positive or is probably real. A series of ancillary routines has been developed to perform this analysis, as shown in the two scientific application of the pipeline. For a practical application of this analysis, we highly encourage the reader to look at Strampelli et al. (2020a) where this approach is deeply discussed on *HST*/WFC3-IR data.

9. CONCLUSION

A new pipeline have been developed to detect and characterize faint astronomical sources close to their host star. Our *Stra*KLIP relies on Karhunen-Loève truncated transformation theory to perform PSF subtraction. Using a highly adaptable series of routines it provides a catalog of candidate companions starting just from an input catalog of target stars and a series of *initial _flt HST* images, or even simply the sample of *initial _flt HST* if the catalog is not available At the actual stage of the development *STRA*KLIP is able to detect and characterize binaries. If more than two souces are present in the same search area $\mathcal{S}$, then only the brightest one will be considered. The extension to the case of multiple sources is the subject a future version of the pipeline.

REFERENCES

Biller, B. A., Close, L., Lenzen, R., et al. 2004, Proc. SPIE, 389 https://ui.adsabs.harvard.edu/abs/2004SPIE.5490..389B

Brown, A. G. A., & Verschueren, W. 1997, A&A, 319, 811 https://ui.adsabs.harvard.edu/abs/1997A&A...319..811B

Dolphin, A. E. 2000, PASP, 112, 1383 https://ui.adsabs.harvard.edu/abs/2000PASP..112.1383D

Gaia Collaboration, Brown, A. G. A., Vallenari, A., et al. 2018, A&A, 616, A1 https://ui.adsabs.harvard.edu/abs/2018A&A...616A...1G

Hoffmann, S. L., & Anderson, J. 2017, Instrument Science Report ACS 2017-8

Joye, W. A., & Mandel, E. 2003, Astronomical Data Analysis Software and Systems XII, 489 https://ui.adsabs.harvard.edu/abs/2003ASPC..295..489J

King, I. R. 1983, PASP, 95, 163

Kraus, A. L., Ireland, M. J., Martinache, F., et al. 2008, ApJ, 679, 762 https://ui.adsabs.harvard.edu/abs/2008ApJ...679..762K

Kraus, A. L., Ireland, M. J., Martinache, F., et al. 2011, ApJ, 731, 8 https://ui.adsabs.harvard.edu/abs/2011ApJ...731....8K

Köhler, R., Petr-Gotzens, M. G., McCaughrean, M. J., et al. 2006, A&A, 458, 461 https://ui.adsabs.harvard.edu/abs/2006A&A...458..461K

Kouwenhoven, M. B. N., Brown, A. G. A., Portegies Zwart, S. F., et al. 2007, A&A, 474, 77 https://ui.adsabs.harvard.edu/abs/2007A&A...464..581K

Lafrenière, D., Marois, C., Doyon, R., et al. 2007, ApJ, 660, 770 https://ui.adsabs.harvard.edu/abs/2007ApJ...660..770L

Luhman, K. L., McLeod, K. K., & Goldenson, N. 2005, ApJ, 623, 1141 https://ui.adsabs.harvard.edu/abs/2005ApJ...623.1141L

Marois, C., Doyon, R., Racine, R., et al. 2005, JRASC, 99, 130 https://ui.adsabs.harvard.edu/abs/2005JRASC..99..130M

Masciadri, E., Mundt, R., Henning, T., et al. 2005, ApJ, 625, 1004 https://ui.adsabs.harvard.edu/abs/2005ApJ...625.1004M

McCully C., Crawford S., Kovacs G., Tollerud E., Betts E. et al.,*Zenodo , Nov 2018.* *https://doi.org/10.5281/zenodo.1482019*

Petr, M. G., Coudé du Foresto, V., Beckwith, S. V. W., et al. 1998, ApJ, 500, 825 *https://ui.adsabs.harvard.edu/abs/1998ApJ...500..825P*

Reipurth, B., Guimarães, M. M., Connelley, M. S., et al. 2007, AJ, 134, 2272 *http://adsabs.harvard.edu/abs/2007AJ....134.2272R*

Robberto, M., Soderblom, D. R., Bergeron, E., et al. 2013, ApJS, 207, 10 *https://ui.adsabs.harvard.edu/abs/2013ApJS..207...10R*

Rothstein, J. 1954, AAAS, 119, 874 *https://science.sciencemag.org/content/119/3103/874.1*

Shatsky, N., & Tokovinin, A. 2002, A&A, 382, 92 *https://ui.adsabs.harvard.edu/abs/2002A&A...382...92S*

Schneider, G., & Silverstone, M. D. 2003, Proc. SPIE, 1 *https://ui.adsabs.harvard.edu/abs/2003SPIE.4860....1S*

Soummer, R., Pueyo, L., & Larkin, J. 2012, ApJL, 755, L28 *https://ui.adsabs.harvard.edu/abs/2012ApJ...755L..28S*

Strampelli, G. M., Aguilar, J., Pueyo, L., et al. 2020, ApJ, 896, 81 *https://ui.adsabs.harvard.edu/abs/2020ApJ...896...81S*

Strampelli, G. M., Pueyo, L., et al. 2020, under prep.

Turin, G. 1960, IETTAW,6 ,311 https://ieeexplore.ieee.org/document/1057571

van Dokkum, P. G. 2001, PASP, 113, 1420 https://ui.adsabs.harvard.edu/abs/2001PASP..113.1420V

Van Rossum G. and Drake F. L.., *Python 3 Reference Manual*

Wang, J. J., Ruffio, J.-B., De Rosa, R. J., et al. 2015, pyKLIP: PSF Subtraction for Exoplanets and Disks, ascl:1506.001 *https://ui.adsabs.harvard.edu/abs/2015ascl.soft06001W*

The Astrophysical Journal, 896:81 (20pp), 2020 June 10 https://doi.org/10.3847/1538-4357/ab8eb3

HST Survey of the Orion Nebula Cluster in the H_2O 1.4 μm Absorption Band. III. The Population of Substellar Binary Companions

Giovanni M. Strampelli[1,2,3], Jonathan Aguilar[1], Laurent Pueyo[2], Antonio Aparicio[3,4], Mario Gennaro[2], Leonardo Ubeda[2], and Massimo Robberto[1,2]
[1] Johns Hopkins University, 3400 N. Charles Street, Baltimore, MD 21218, USA; strampelligiovanni@jhu.edu
[2] Space Telescope Science Institute, 3700 San Martin Dr, Baltimore, MD 21218, USA
[3] Department of Astrophysics, University of La Laguna, Av. Astrofísico Francisco Sánchez, E-38200 San Cristóbal de La Laguna, Tenerife, Canary Islands, Spain
[4] Instituto de Astrofísica de Canarias, C. Vía Láctea, E-38200, San Cristóbal de La Laguna, Tenerife, Canary Islands, Spain
Received 2020 March 26; revised 2020 April 28; accepted 2020 April 28; published 2020 June 16

Abstract

We present new results concerning the substellar binary population in the Orion Nebula Cluster (ONC). Using the Karhunen–Loève Image Projection algorithm, we have reprocessed images taken with the IR channel of the Wide Field Camera 3 mounted on the Hubble Space Telescope to unveil faint, close companions in the wings of the stellar point-spread functions. Starting with a sample of 1392 bona fide unsaturated cluster members, we detect 39 close-pair cluster candidates with separation 0.″16–0.″77. The primary masses span a range $M_p \sim 0.015$–$1.27\,M_\odot$, whereas for the companions we derive $M_c \sim 0.004$–$0.54\,M_\odot$. Of these 39 binary systems, 18 were already known, while the remaining 21 are new detections. Correcting for completeness and combining our catalog with previously detected ONC binaries, we obtain an overall binary fraction of $11.5\% \pm 0.9\%$. Compared to other star-forming regions, our multiplicity function is ∼2 times smaller than, for example, Taurus, while compared to the binaries in the field we obtain comparable values. We analyze the mass functions of the binaries, finding differences between the mass distributions of binaries and single stars and between primary and companion mass distributions. The mass ratio shows a bottom-heavy distribution with median value $M_c/M_p \sim 0.25$. Overall, our results suggest that ONC binaries may represent a template for the typical population of field binaries, supporting the hypothesis that the ONC may be regarded as a most typical star-forming region in the Milky Way.

Unified Astronomy Thesaurus concepts: Binary stars (154); Star forming regions (1565); Low mass stars (2050); Substellar companion stars (1648); Companion stars (291); Multiple stars (1081); Brown dwarfs (185); M dwarf stars (982)

Supporting material: machine-readable tables

1. Introduction

Binary stars are coeval pairs of stars born in the same environment, with the same metallicity, but with different mass. Understanding their properties provides us with key information on stellar evolution, from the early phases of star formation to the most violent phenomenology that may characterize the final moments of their life. In young systems, knowing the effective temperature and absolute luminosity of a pair can constrain theoretical models developed to predict isochrones and evolutionary tracks on the H-R diagrams during the pre-main-sequence phase (Gennaro et al. 2012; Stassun et al. 2014). Ignoring the presence of binaries, on the other hand, represents a nuisance that may affect the statistical analysis of the same H-R diagrams (Jerabkova et al. 2019).

The distribution and frequency of binary systems with substellar companions have been the object of several studies (see, e.g., Duchêne & Kraus 2013, review and references therein). In principle, very-low-mass companions (down to the deuterium burning limit, Spiegel et al. 2011) might form like stars through early fragmentation and gravitational collapse of a common prestellar core, or like planets in a circumstellar disk, reaching their observed wide orbits through migration or scattering. Characterizing the population of low-mass companions can thus shed light on the mechanism of star and planet formation at the lower and upper boundaries, respectively, of their mass range.

Since substellar objects are unable to sustain hydrogen fusion in their cores and quickly fade away and become undetectable, young stellar clusters in the solar vicinity are ideal for large statistical studies. Using direct imaging techniques, the main observational challenge is that objects potentially resolved may be hidden under the extended point-spread function (PSF) wings of the primary. Nondetections only provide upper limits on the companion frequency within a wide range of mass and semimajor axis (SMA). To probe beyond these limits, image processing techniques that remove the PSF while preserving the flux of the companion have been developed.

The key element in performing PSF subtraction is having an accurate template for the PSF itself. In one-to-one PSF subtraction, also called reference differential imaging, a single reference PSF is directly subtracted from the science image. For the two PSFs to match, reference and target images should be acquired while maintaining the same instrument configuration, in the same part of the sky, and as close in time as possible. This helps to reduce changes in the PSF due to variations resulting from, for example, the unstable thermal environment in a low earth orbit or instrument flexures and variable atmospheric conditions on the ground. In practice, if only one reference PSF is available, the results of the subtraction will always be subject to a variety of systematic and random differences between the reference and science images. To reduce the impact of using a particular realization of

the reference PSF on the subtraction residuals, it is advantageous to combine multiple PSFs. A variety of observing strategies and algorithms have been developed in order to optimally combine multiple reference PSF images (e.g., Marois et al. 2014). Eventually, in the case of a positive detection, finding a faint object in the immediate vicinity of a star does not provide conclusive evidence of a physical association. Complementary information, such as common proper or parallactic motion, is needed to disentangle real pairs from random alignments. Lacking multiple-epoch data, the presence of photospheric features characteristic of young, low-mass objects may provide strong indications for real binary systems.

In this paper, we presents the results of a search for substellar companions in the Orion Nebula Cluster (ONC) based on data obtained with the Hubble Space Telescope (HST). The ONC is ideal for this type of investigation: it is massive enough ($\sim 2000 M_{\odot}$) to provide us with a rich sample of targets and sufficiently nearby ($\simeq$400 pc; Kuhn et al. 2019) that the angular scale of a Wide Field Camera 3 (WFC3)/IR pixel, $0\farcs13$, corresponds to a physical separation of $\simeq$50 au, that is, the distance of Pluto to the Sun at aphelion.

Our strategy is based on reprocessing standard wide-field imaging data with advanced PSF subtraction techniques, namely the Karhunen–Loève Image Projection (KLIP) algorithm (Soummer et al. 2012), fully exploiting the exquisite stability of the HST. In particular, we have used a data set consisting of images obtained with the IR channel of the HST/WFC3 through a pair of filters tailored to measure the depth of the 1.4 μm H_2O absorption feature: F139M (in band) and F130N (adjacent, line-free continuum). In the first paper of this series (Robberto et al. 2020, hereafter Paper I with corresponding catalog of sources: Catalog I), we have shown that the presence of the water absorption feature in the atmosphere of low-luminosity sources can be used to separate the substellar cluster population of the ONC from background stars and galaxies. The flux decrease in the F139M filter relative to the nearby F130N continuum produces a negative (blue) m_{130}–m_{139} color index highly sensitive to the effective temperature down to $T_{\rm eff} \simeq 2800$ K ($\sim 0.06\,M_{\odot}$); below this value, the absorption feature remains strong but with a weaker dependence on the effective temperature, reaching m_{130}–$m_{139} \simeq -0.5$ at temperature $T_{\rm eff} \simeq 2200$ K ($\sim 0.01\,M_{\odot}$).

The possibility of discriminating low-mass objects from the population of reddened field stars has allowed Gennaro & Robberto (2020, hereafter Paper II) to investigate the shape of the initial mass function of "field" cluster members down to planetary masses. Catalog I, however, only reaches separations as small as $0\farcs8$ (320 au), inside of which the search for binary candidates is hampered by PSF blending. By applying the KLIP algorithm and advanced statistical analysis to discard false-positive detections, we are able to provide a new, comprehensive picture of binarity in the ONC from 70 to 310 au.

In Section 2, we summarize the main characteristics of the data set. In Section 3 we present our methodology, and in Section 4 we present the results of our search. We discuss the main properties of our sample in Section 5, while in Section 6 we summarize our findings.

2. Data Set

The Cycle 22 HST Treasury Program "The Orion Nebula Cluster as a Paradigm of Star Formation" (GO-13826, P.I. M. Robberto) aims to reconstruct the low-mass initial mass function (IMF) down to $\sim 5 M_{\rm Jup}$ in the ONC. Paper I presents the survey strategy, sensitivity limits, and completeness analysis, leading to a census of the stellar and substellar population in the ONC down to a few Jupiter masses in the F130N and F139M filters. The 208 images taken in each filter produce wide-field mosaics covering an area of about one-sixth of a square degree. The number of *unique* sources, either ONC members or background stars and galaxies, is 4504, but in this paper we reprocess the full data set of more than $\sim$8700 source detections, because the mosaicking strategy allowed detection of the same sources during multiple visits. Figure 1 shows the color–magnitude diagram (CMD) for all 4504 sources, with the clear separation between the cluster population at the top and left side of the diagram, and the background sources at bottom right, with positive $m_{130}-m_{139}$ color. A 1 Myr isochrone, adapted from the BT-Settl model to correct for the discrepancy between the model and the data, is overplotted in red up to a mass $M \lesssim 0.75 M_{\odot}$ (see Paper I for a description of the models and of their semiempirical calibration). For masses $\geqslant 0.75\,M_{\odot}$ we departed from the BT-Settl model, adopting instead the MESA isochrones and Stellar Tracks for the WFC3 IR channel in our F130N and F139M filters (Choi et al. 2016; Dotter 2016).

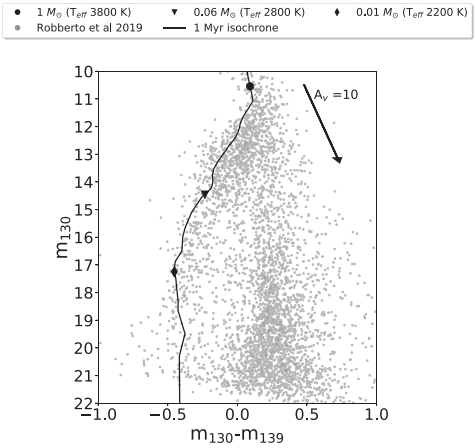

Figure 1. Color–magnitude diagram in filters F130N and F139M for all sources detected in the ONC field. The black line is a 1 Myr isochrone with three characteristic masses, from bottom to top $M_{\odot} = 0.01$, 0.06, and 1.

3. Data Analysis

3.1. Catalogs of Reference and Target Stars

As reported in Paper I, saturation in the F130N filter starts at $m \simeq 10.9$, while the noise floor is at $m \simeq 22$, setting the magnitude limits of the primaries and companions we are able to analyze.

Our input catalog of targets contained 8210 individual detections (of which 4220 are unique) with m_{130} magnitudes in the range 10.9–22; about 50% of them correspond to repeated detections of the same sources.

Our PSF subtraction technique requires a reference catalog of sources uncontaminated by astrophysical or instrumental

noise. We create it from our sample and perform several clean-up steps:

1. *Visual binary removal*. We remove from our catalog 157 unique pairs, for a total of 623 total entries with a neighbor closer than 1.″5 projected distance according to Catalog I. In this way, we avoid contamination from nearby neighbors whose PSF wings may affect the region searched for low-mass companions.
2. *Bad pixel removal*. The data set of full-frame WFC3 images is cleaned from cosmic-ray events in the early stages of standard data processing thanks to the nondestructive sampling of the accumulating signal. Static bad pixels are also flagged by the pipeline. However, we perform an independent check by stacking the images and applying a 10σ threshold to the distribution of median pixel values. We did not find any detection with a flagged pixel closer than $\sim$0.″8 in any visit.
3. *ACS catalog matching*. The HST/ACS survey of Robberto et al. (2013) provides a high-resolution morphological classification of the sources in the ONC. By cross-matching the ACS catalog with our list of WFC3 detections, we discard all objects flagged as nonstellar: silhouette disk, proplyds, sources with evidence of jets or photoionization, Herbig–Haro objects, or resolved galaxies. We discarded a total of 222 unique objects for a total of 458 entries from the catalog.

Applying these selection criteria, we end up with a catalog of 7129 individual sources, counting multiple observations of the same object separately.

The next step is to create "postage stamps" centered on each source and perform the PSF subtraction inside this area. In setting our 11×11 ($1.''5 \times 1.''5$) pixel stamp size, we consider the following factors:

1. The area must be large enough to contain the bright wings of the PSF, for sources matching our assumed range of magnitudes.
2. The area must have enough pixels to provide a meaningful noise calculation. Detections of close companions are affected by small-number statistics, and a correction to the estimated contrast and signal-to-noise ratio (S/N) has to be applied (Mawet et al. 2014). The following argument shows that the correction is very small for an 11×11 stamp. The number of λ/D resolution elements per pixel for WFC3 in the F139M filter is close to 1; that is, WFC3-IR is significantly undersampled. Therefore, an 11×11 pixel stamp contains about the same number of resolution elements. The correction factor to the S/N is given by $(\sqrt{1 + 1/n})^{-1}$, which for $n = 121$ is 0.996. Therefore, the sample size does not represent a significant source of uncertainty versus other noise sources, such as photon or read noise.
3. The area must be small enough that tiles do not overlap; having rejected from our catalog objects with a nearest companion closer than 1.″5, we find this results in a tile half-size of 0.″7. With a WFC3 pixel scale of $0.''13\,\mathrm{pixel}^{-1}$, the tile half-size translates to a radius of approximately 280 au from a point source in the ONC.

3.2. PSF Subtraction

Accurate PSF subtraction depends strongly on the quality of the reference PSF, a task greatly simplified by the stability of the HST, which has enabled the compilation of libraries of PSF models for reference differential imaging (e.g., Choquet et al. 2014). Still, for the most accurate PSF subtraction, one has to deal with the field distortion of WFC3 and the small but nonnegligible time dependence of the HST focus. These effects make the PSF both spatially and time dependent. Our strategy is especially well suited for handling both effects.

The strategy consists of dividing the field of view into 100 equal cells, each cell small enough to neglect local PSF distortion but large enough to build a local PSF library containing enough stars to build an accurate model.

For each cell, PSF subtraction is then performed as follows:

1. The postage stamps for all stars in the cell are stacked together into a single data cube.
2. Iterating through the data cube, each stamp is assumed as the science image.
3. A reference model of the PSF for subtraction is constructed, selecting from the remaining postage stamps those with a photometric error $\sigma_{\mathrm{F130N}} \leqslant 0.01$.
4. The PSF of the target star is then removed using the KLIP algorithm (Soummer et al. 2012).

For each target, we chose the number of modes that simultaneously minimize the standard deviation of the residual image while maximizing the counts of the brightest residual pixel.

To build a preliminary catalog of candidate binaries, we analyze the position of the brightest pixel of the residual images of each target. To be labeled as a candidate detection, at this early stage, we require that

1. the pixels with the highest flux in each residual must be within one pixel in both filters and in all available visits when the source is observed with different telescope orientations, and
2. the candidate must be detected in at least two different KLIP modes.

The one-pixel distance (rather than zero) is needed to take into account possible misalignments of the center of the stars in the reference library, due to the undersampled PSF and lack of dithering in the survey. This is reflected in an accuracy of our separation estimates of about one-half pixel, that is, 0.″07 or 28 au at the distance of the ONC.

3.3. Cluster and Background Candidates

Inspection of the residuals immediately after PSF subtraction reveals a large number of candidate companions, but further down-selection has to be applied to reject sources that presumably do not belong to the ONC. To separate cluster stars from background sources, we use the position of the stars on the CMD. As shown in Paper I, the pair of filters chosen for this survey is sensitive to the depth of the 1.4 μm H_2O absorption band. This temperature-sensitive feature is prominent in the atmosphere of M-type stars and brown dwarfs, down to planetary-mass objects, and can be then used to separate the substellar cluster population of the ONC from background stars and galaxies. Following Paper I, we consider a source to be an ONC member if it lies in the area delimited by

the 1 Myr isochrone introduced in Section 2, reddened by $A_V = 10$ mag. Any companion candidate bluer (redder) than this isochrone is labeled as cluster (background). In Paper I, we found good agreement between this simple approach and a more rigorous Bayesian statistical treatment. At the end of this process, we obtained 2797 multiple-visit cluster sources, with 1392 *unique* targets for our KLIP PSF subtraction algorithm.

3.4. Companion Photometry

Since the WFC3/IR PSF is highly undersampled, after PSF subtraction we expect most of the flux from a faint candidate companion to be contained within a few pixels. Thus, to derive the total flux, one has to apply a large and rather uncertain aperture correction. To evaluate it, we analyze a sample of isolated bright stars in our catalog, comparing their flux around the brightest pixels with their total flux. This analysis shows that about one-third of the flux is contained within the brightest pixel and ∼60% within the four adjacent brightest pixels. The distribution of relative fluxes for the four brightest pixels is narrower than the distribution for the single pixel. Therefore, we perform our photometry of the companions using a four-pixel aperture, deriving the aperture correction to the total flux through comparison with the Catalog I PSF photometry. Specifically, for each isolated source in Catalog I, we built a square 2×2 pixel mask placed so that one pixel always coincides with the brightest pixel of the original image. After probing the four possible mask positions, we record the maximum value of the total counts as c_{4p}. The magnitude for each primary is then calculated as follows:

$$m_{4p} = -2.5 \log_{10}(c_{4p}) + C \quad (1)$$

where C is a normalization factor between the four-pixel photometry and PSF photometry ($C_{m_{130}} = 21.35 \pm 0.049$, $C_{m_{130}-m_{139}} = -0.002 \pm 0.031$). We then determine C as the mean of the difference between the PSF photometry and the four-pixel photometry of each primary:

$$\langle m_{\rm PSF} - m_{4p} \rangle = C. \quad (2)$$

Measuring c_{4p} for each detected companion and using Equation (1) and the value of C from Equation (2), we determine the magnitudes of our candidate companions. Our estimate of the total uncertainty takes into account the uncertainty on the counts of the candidate, on the background counts in the four-pixel aperture, and on the estimated conversion factor between the PSF and the four-pixel system (the standard deviation of the sample we used to evaluate the conversion factor).

Having determined the photometry for each candidate, a new selection is applied while keeping all of the cluster pairs with companion magnitude in the range $10.9 \geqslant {\rm mag}_{130} \geqslant 22$ (following an approach similar to that mentioned in Section 3.3) and with absolute value of the m_{130}–m_{139} color $\leqslant 1$ to reject noisy outliers. This results in a preliminary selection of 145 cluster candidate binaries.

3.5. Real versus False-positive Detections

To assess our ability to separate plausible candidates from instrument-induced false-positive detections, we perform an extensive set of simulations to determine the receiving operating characteristic (ROC) curves (see Appendix A for an explanation of ROC curve construction) for each binary configuration in our preliminary catalog. A configuration is specified by three parameters: (1) brightness of the primary, (2) contrast between primary and companion, and (3) separation and KLIP mode used during the PSF subtraction phase. We use the ROC curves to derive three other quantities we can use to make the following selections on our candidates:

1. Area under the curve (AUC) of the ROC. The AUC provides us with a good indication of how well the distribution of the true-positive rate (TPR, i.e., detection of companions injected in our simulations) is separated from the distribution of the false-positive rate (FPR, i.e., detection of noise peaks that may have been erroneously determined to be companions). An AUC curve of 0.5 indicates that there is no possibility of separating the two distributions, whereas an AUC = 1 represents perfect separation. An analysis of the results provided by the simulations led us to select candidates only when the corresponding configuration provides an AUC $\geqslant 0.7$.
2. False-positive probability and S/N threshold. As explained in Appendix A, for each given configuration, the ROC curve is built by sliding an S/N threshold across the TPR and FPR distributions. We can therefore invert this process: given the ROC curve for a certain configuration and having determined a limit to the probability for a detection to be a false positive, we find the corresponding S/N that we can use as a threshold for the detection. Because each candidate is found using multiple independent detections (different filters and possibly different locations on the detector for each visit), we multiply the false-positive probabilities of each detection (FP′) to obtain an overall false-positive probability for the whole candidate (FP). In particular, if we assume FP′ to be the same for each detection, it is

$$\mathrm{FP} = \mathrm{FP}'^{(N_f \times N_v)}, \quad (3)$$

   where N_f is the number of filters and N_v is the number of visits for the candidate. Inverting this relation, we find FP′ as a function of FP. Having set FP′, we can find the corresponding S/N threshold from the ROC. With 1392 primaries to be searched, assuming an overall false-positive probability FP = 0.2% for each candidate, we expect about three false-positive detections in our final catalog of binaries. We have verified that this probability value represents an optimal trade-off. A further reduction, that is, a more aggressive reduction of false positives, would imply higher detection thresholds, which would lead to rejecting strong, previously known true detections. Vice versa, relaxing the threshold would cause a large increase in the number of false positives beyond the acceptable rate of 50–100 smaller than the expected detection signal (as a point of reference, the expected binary fraction is 10%–20% as per Kraus and Duchene).
3. Ratio of true positives over false positives (R). For each candidate detection, we binned the TPR and FPR distributions in bins of 0.5 S/N, and we evaluate the ratio of true positives over false positives in the same bin corresponding to the candidate S/N detection. This parameter gives us an indication of how common the candidate S/N is in the distribution of false positives and true positives. Because each candidate results from multiple detections, we keep only candidates with an $R_{\rm median} \geqslant 3$.

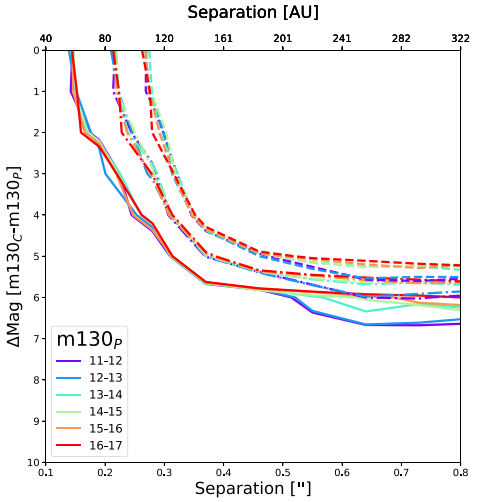

Figure 2. Averaged contrast curve over different visits and KLIP modes for each magnitude bin of the primary star and delta magnitude between companion and primary and projected separation. The three families of curves (solid line, dotted−dashed line, and dashed line) correspond to completeness $\mathcal{C} = 0.1$, 0.3, and 0.5, respectively.

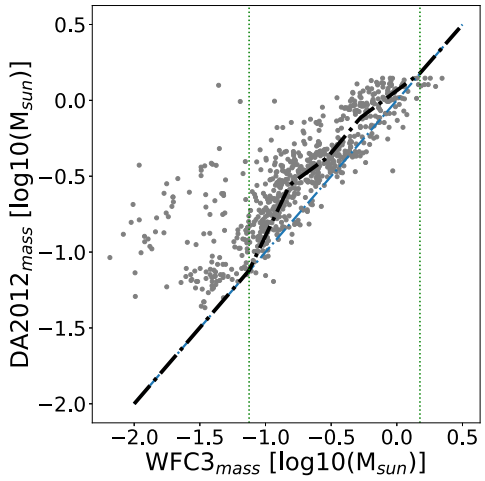

Figure 3. Da Rio et al. DR2012 vs. WFC3 masses (gray points). The two green dotted vertical lines mark the values for $\mathrm{WFC3_{mass}} = 0.075\ M_\odot$ and $1.5 M_\odot$. The blue dotted–dashed line shows the locus of points where $\mathrm{DR2012_{mass}} = \mathrm{WFC3_{mass}}$, while the black dotted–dashed line shows the final spline fit of the data.

As a by-product of our simulations, we also obtain the amount of flux lost to oversubtraction (see Pueyo 2016 and references therein), deriving the correction to apply to the photometry of our candidate companions, with the relative errors. Moreover, from the distributions of TPR and FPR, we can also evaluate the contrast curves as a function of the magnitude of the primary, contrast, and separation. Averaging all data, we obtain the contrast curves shown in Figure 2.

The preceding analysis is not designed to distinguish between true companions and other astrophysical sources of false positives. These include residual contamination from nearby stars and light emitted by circumstellar material. Detector persistence may cause "ghosts" of very bright stars in the subsequent exposures, but they also appear as extended structures that can be easily identified and generally decay within one visit (see Paper I). This is why to conclude this candidate selection we visually inspect all our selected candidates by looking for extended residuals.

3.6. Companion Mass Determination

To estimate the mass of our substellar companions, we start with an analysis of the primaries and isolated ONC stars. Figure 3 shows the comparison between the masses estimated by da Rio et al. (2012) using the Baraffe et al. (1998) evolutionary models ($\mathrm{DR2012_{mass}}$) and the masses obtained from our dereddened WFC3 photometry and the 1 Myr isochrone ($\mathrm{WFC3_{mass}}$, gray points). We use the value of A_V determined by Da Rio et al. when available, otherwise we use the A_V estimate from Paper I, with negative A_V values set to $A_V = 0$. In the range of $\mathrm{WFC3_{mass}}$ between 0.075 and $1.5 M_\odot$ (vertical lines in the plot), we observe good correlation with some systematic differences between the two mass estimates. Below this range, the scatter increases, an indication of the difficulty of the DR2012 optical survey in dealing with the reddest and faintest sources of their sample. To reconcile the two data sets, we use an empirical isochrone, fitting the relation between the $\mathrm{DR2012_{mass}}$ and the $\mathrm{WFC3_{mass}}$ in the 0.075–$1.5 M_\odot$ mass range with a spline function as follows:

1. We bin the distribution of $\mathrm{F130N_{mass}}$ between 0.075 and $1.5 M_\odot$. To have bins perpendicular to the $\mathrm{DR2012_{mass}} = \mathrm{WFC3_{mass}}$ relation (blue line in Figure 3), we apply a rotation matrix to the data by an angle of 45°.
2. We apply a 3σ cut to the distribution of each bin to exclude outliers.
3. We rotate back the data, and we fit a spline matching the 1 Myr isochrone outside the 0.075–$1.5 M_\odot$ $\mathrm{WFC3_{mass}}$ range and the 3-sigma select data otherwise (black dotted line in Figure 3).

In the substellar regime, we decide to rely only on our WFC3 data because of the strong correlation between mass and stellar flux (m_{130}), as evidenced by the color–magnitude diagram (Figure 1).

Finally, to evaluate the mass of our candidate binaries, we assign the same A_V values to both components and then evaluate the mass of the companion using the spline curve.

3.7. Completeness Limit

The completeness of our survey depends on the mass of the primary, the mass ratio of potential candidates, and their separation, that is, the projected SMA. This function, marginalized over the mass of the primaries, can be represented by a set of completeness curves for the mass ratio of the candidate and separation. Completeness as a function of the magnitude of the primary and companion and visual separations can be obtained by direct inspection of the family of ROC curves discussed in Section 3.5. It can then be converted into a

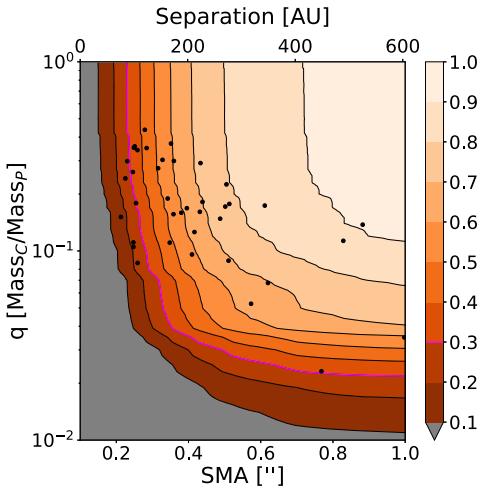

Figure 4. Mass ratio completeness curves estimated as a function SMA with the color coding showing the value of the completeness. The black dot marks the position of each detection on the plot. The magenta line marks the 30% limit, below which we only choose candidates with two or more visits.

completeness as a function of primary mass, mass ratio, and deprojected orbital SMA. This last step is carried out using the following procedure:

1. We interpolate over a finer grid both in mass ratio and separation.
2. Following Brandt et al. (2014), we integrate over all the possible semimajor axes (s) between 0 and 1.8 using a piecewise function $p(s)$:

$$p(s) \simeq \begin{cases} 1.3s & 0 \leqslant s \leqslant 1 \\ -\frac{35}{32}\left(s - \frac{9}{5}\right) & 1 < s < 1.8. \end{cases} \quad (4)$$

We then use this completeness map to apply a final selection to our catalog of candidates to reject any detection with completeness smaller than 10% or between 10% and 30% and with only one visit (i.e., the most likely to be one of the few false positives we expect, since our FP analysis was carried out using single visits). At the end of this selection process, we obtain a final catalog of 39 reliable cluster candidate binaries out of 1392 original cluster targets.

Figure 4 shows the final completeness curves as a function of separation in SMA, where the black dots mark the position of our detections on the completeness map. The magenta line shows the 30% completeness cut we apply to our single-visit detection, while the gray area shows the space of parameters in the plot where we always reject candidates because completeness is smaller than 10%.

4. Results

4.1. Catalog of KLIP-detected Candidate Cluster Binaries

The analysis described in Section 3 provides us with a total of 39 candidate cluster binaries with separation in the range 1.26–5.9 pixels (0.″16–0.″77), corresponding to about 66–309 au projected distance from the primary assuming a distance of 403 pc (Kuhn et al. 2019). The primary masses range between 0.015 $M_\odot$ and 1.27 $M_\odot$, while the companions are in the range 0.004 $M_\odot$–0.54 $M_\odot$.

Table 1 shows the physical and photometric properties of the 39 candidates. Column (1) shows the entry number in the catalog; columns (2) and (3) show the R.A. and decl. for Equinox J2000.0; columns (4) to (11) list the m_{130} magnitude and the $m_{130}-m_{139}$ color with their relative uncertainties for both primary (P) and companion (C); columns (12) to (15) show the estimated mass from F130N photometry, with its uncertainty, for both primary and companion in units of solar mass. The last three columns list the position angle, the separation between primary and companion, and the distance of the system from the core of the cluster (identified by the position of θ^1Ori-C).

In Appendix B we present a gallery of postage stamps (Figures B1–B2) showing the coadded images before and after KLIP subtraction for each candidate; the companions generally appear as bright single pixels in each residual image, due to the WFC3/IR subsampling. Each postage stamp has dimensions 2″ × 2″ and is rotated so that north is up and east is to the left.

In Figure 5 we show the position of each candidate cluster binary projected against the survey area of the WFC3 survey, while Figure 6 shows the color–magnitude diagram for the entire region with the locus of the KLIP candidate cluster binaries.

4.2. Wide Binaries

Previously, binary systems that were well resolved in Catalog I were excluded from our analysis, which was designed to discern close companions hidden under the PSF wings of apparently single stars. We now expand our close-companion catalog by adding the wider pairs from Catalog I: 58 systems with projected separation $d < 1.''8$ (choosing as limit the maximum distance at which we still measure an increase in the number density of stars; see Figure 8 in Section 4.4) and colors compatible with cluster membership for both sources. The brightest star of each pair is generally taken as the primary. Adopting the F130N filter photometry in Catalog I to estimate their masses, we obtain for the primaries values in the range $M_P = 0.02$–$1.08 M_\odot$, while for the companions we find $M_C = 0.01$–$1.04 M_\odot$. Their photometry and resulting physical parameters are listed in Table 2, and a gallery of images is shown in Figure B3 in Appendix B (similar to what we presented for the KLIP pairs).

It should be noted that we did not attempt to find faint substellar companions under the PSF wings of the Paper I binaries, as this goes beyond the current capabilities of our implementation of the KLIP algorithm. Our search strategy, therefore, is generally biased against finding triplets or higher order systems.

4.3. Master Catalog

Hereafter we will refer to the combination of Tables 1 and 2 as our Master Catalog. The Master Catalog contains 97 pairs of stars with separations between 0.″16 and 1.″73 (corresponding to 66–697 au) and masses in the range $M_P = 0.015$–$1.27\,M_\odot$ and $M_C = 0.004$–$1.04\,M_\odot$ for the primary and companion, respectively.

Table 1
Candidate Binaries Catalog (KLIP)

ID (–)	R.A.$_p$ (deg)	Decl.$_p$ (deg)	mag130$_p$ (mag)	color$_p$ (mag)	dmag130$_p$ (mag)	dcolor$_p$ (mag)	mag130$_c$ (mag)	color$_c$ (mag)	dmag130$_c$ (mag)	dcolor$_c$ (mag)	mass$_p$ (solMass)	mass$_c$ (solMass)	emass$_p$ (solMass)	emass$_c$ (solMass)	PA (deg)	Sep (arcsec)	SepOriC (arcsec)
0	83.65873105	−5.461256454	12.7852	0.07241	0.06655	0.00258	14.79325	−0.1649	0.06521	0.10838	0.265761	0.045624	0.007075	0.001164	11.04	0.39	630.53
1	83.75715053	−5.452742454	13.6095	−0.18075	0.01708	0.0045	15.57923	−0.38044	0.03513	0.06504	0.119621	0.031277	0.000737	0.000623	99.61	0.19	316.95
2	83.77675985	−5.451311859	12.7123	−0.27704	0.01868	0.00997	13.52197	−0.55827	0.05769	0.10461	0.280446	0.100214	0.002345	0.002273	280.28	0.19	268.14
3	83.77159336	−5.434358914	13.4775	−0.07256	0.02798	0.0222	16.49632	−0.79747	0.03127	0.04469	0.151852	0.017179	0.001491	0.000305	354.69	0.64	233.43
4	83.78028406	−5.436474308	15.3643	0.10603	0.01405	0.01473	18.24483	−0.16565	0.03714	0.06303	0.183497	0.020358	0.001036	0.000866	9.79	0.19	217.7
5	83.83343099	−5.486611088	13.4015	0.16228	0.17164	0.02449	14.99455	−0.26626	0.04088	0.05973	0.666812	0.115873	0.075648	0.003052	337.9	0.47	353.03
6	83.84672012	−5.476080805	13.6243	−0.17387	0.001	0.00336	19.94556	−0.54334	0.1797	0.2833	0.132205	0.004614	3.5e−05	0.000223	191.76	0.77	327.13
7	83.89252874	−5.455090951	11.8697	0.02297	0.01133	0.03316	15.77574	−0.51272	0.02497	0.04258	0.519625	0.027329	0.003795	0.000757	134.19	0.44	355.41
8	83.61902968	−5.509038831	14.4798	−0.12672	0.01402	0.0054	20.09559	−0.55557	0.09975	0.28998	0.064618	0.004378	0.000643	0.000124	263.09	0.48	837.1
9	83.82263551	−5.537828912	15.0015	−0.00517	0.00923	0.00788	16.19856	−0.36395	0.0304	0.05199	0.138769	0.048765	0.000325	0.000543	8.86	0.19	533.54
10	83.88307815	−5.52992167	14.6918	−0.21926	0.01524	0.00222	19.26116	−0.3466	0.0438	0.08264	0.047936	0.005304	0.000267	5.2e−05	52.26	0.27	555.71
11	83.95476263	−5.559047659	16.8017	−0.0107	0.01704	0.01693	19.66101	−0.37798	0.04246	0.07579	0.014534	0.005086	0.000129	5e−05	183.71	0.22	782.38
12	83.89670965	−5.448594714	12.1409	0.0594	0.00886	0.01629	14.04119	0.12296	0.03058	0.05044	0.495625	0.088725	0.002556	0.001455	276.57	0.2	352.27
13	83.84242884	−5.443706152	11.295	0.19391	0.00395	0.00074	12.32212	0.30177	0.06507	0.13168	1.237085	0.540864	0.002806	0.030071	283.37	0.21	212.6
14	83.87796088	−5.408648543	12.6713	−0.1118	0.03893	0.02001	14.95313	−0.5236	0.0352	0.05679	0.286316	0.042394	0.004905	0.000628	302.46	0.38	224.4
15	83.82474913	−5.426100713	12.2306	0.04893	0.03399	9e−05	14.11821	−0.0027	0.05342	0.08013	0.406357	0.076947	0.009162	0.003184	348.93	0.26	132.99
16	83.72936023	−5.424836418	12.1775	0.04272	0.00146	0.00087	14.31968	−0.24743	0.04968	0.07978	0.472033	0.073861	0.000417	0.001101	51.6	0.28	345.24
17	83.72843059	−5.420142975	12.872	−0.1633	0.04357	0.00869	14.36475	0.15954	0.05711	0.08939	0.235225	0.064372	0.003889	0.00266	325.05	0.24	342.58
18	83.76287689	−5.37716716	11.7742	−0.00565	0.00886	0.01562	14.66854	0.06643	0.03497	0.05352	0.54935	0.047472	0.002964	0.000624	192.6	0.2	205.54
19	83.8540066	−5.400418165	12.8879	0.2529	0.02858	0.02178	14.59045	−0.08418	0.03732	0.06801	0.888352	0.141468	0.016308	0.003351	255.61	0.29	133.26
20	83.85195641	−5.400290404	13.1041	−0.08161	0.05475	0.01808	14.50296	−0.34182	0.03761	0.06597	0.222372	0.066542	0.004893	0.001752	293.64	0.28	126.07
21	83.82696282	−5.401934612	11.734	0.17088	0.01441	0.00394	16.60982	−0.55286	0.04746	0.08143	0.664391	0.015354	0.006383	0.000452	218.71	0.59	53.45
22	83.82851021	−5.373045614	13.4312	0.09716	0.07249	0.00778	14.3886	−0.3652	0.03982	0.07265	0.386487	0.117198	0.019113	0.002972	321.23	0.25	69.73
23	83.85038408	−5.359054015	12.4144	0.05594	0.16081	0.02832	13.75559	−0.08395	0.03971	0.05803	0.502218	0.112976	0.051514	0.002964	279.68	0.39	158.94
24	83.80338979	−5.345419412	11.3224	0.17154	0.08285	0.03132	13.0126	0.00255	0.03685	0.06362	0.910202	0.146558	0.045441	0.003309	84.52	0.33	168.46
25	83.94418968	−5.373398132	12.3236	−0.01377	0.01082	0.00836	13.83882	0.10386	0.04147	0.06897	0.358728	0.086737	0.002629	0.001984	283.55	0.17	455.97
26	83.9590678	−5.354670298	12.9224	0.0274	0.00393	0.00013	15.56152	−0.21944	0.04992	0.08604	0.279615	0.035214	0.000489	0.000885	263.01	0.32	521.21
27	83.91659751	−5.37407979	14.8903	0.19968	0.00154	0.00207	16.45456	−0.23877	0.04946	0.08087	0.147277	0.043943	5.4e−05	0.000883	276.93	0.18	357.29

(This table is available in its entirety in machine-readable form.)

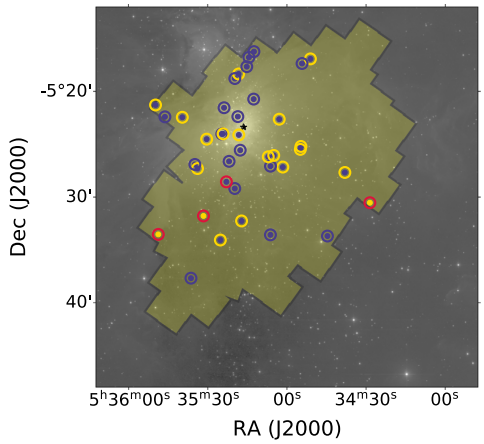

Figure 5. Large-scale view of ONC. The shaded yellow area indicates the field covered by the WFC3 observations, overlaid on the 2MASS *J*-band image of the region (in gray scale). The black star marks the position of θ^1Ori-C. Colored open circles and dots mark the positions of new candidate binary systems, where the dots refer to primary stars and the open circles refer to candidate companions. The colors encode the mass of the object: blue = stellar-mass object, yellow = brown dwarf, red = planetary-mass object.

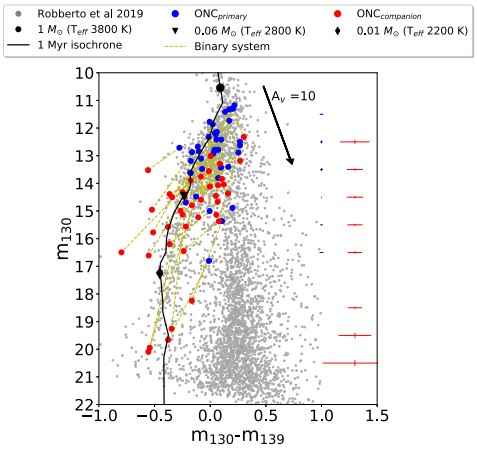

Figure 6. Recreation of the CMD from Figure 1, now including the candidate binary systems. The black line is the 1 Myr isochrone of Paper I, with three characteristic masses marked ($M_\odot$ = 0.01, 0.06, and 1). The blue (red) crosses to the right show the average uncertainties for the primaries (companions) in each magnitude bin. The yellow dotted lines join the components of each candidate binary system.

Figure 7 shows the relation between primary and companion masses for all sources in the Master Catalog, with relative error bars and colors identifying the KLIP binaries (black) versus Catalog I binaries (blue). The diagonal lines mark the loci of systems with primary mass equal to 1, 10, and 100 times the mass of the companion, whereas the horizontal and vertical lines indicate the boundaries between stellar, brown dwarfs, and planetary-mass objects. The number of systems in the areas delimited by these lines is given in Table 3. Overall, we observe a primary star-to-brown-dwarf ratio (SBdR) $N(0.1\text{–}1.27\ M_\odot)/N(0.014\text{–}0.07\ M_\odot) = 15.16$, while the same ratio for isolated stars in the ONC ($\sim$3.8 evaluated from Catalog I or $3.3^{+0.8}_{-0.7}$ from Slesnick et al. 2004; Andersen et al. 2008) and in the field (5.2 or 6 from Bihain & Scholz 2016 and Kirkpatrick et al. 2012, respectively) is much smaller. Because the two SBdRs are different from each other (binaries versus singles in ONC/field), this may suggest a preference for companions to form around stellar-mass primaries instead of brown dwarfs in the ONC. This discrepancy may be due to the intrinsic difficulty in detecting companions around fainter primaries, so we evaluated the SBdR from our *completed* catalog of binaries, obtaining $\sim 10.6 \pm 0.3$. Even if we consider the *completed* distribution of binaries, we still observe a preference for companions to form around primaries in the stellar-mass regime compared to brown dwarf mass.

4.4. Crowding and Apparent Pairs

Given the increasing stellar density toward the inner regions of the cluster, one may expect to find apparent pairs that are due to chance alignments, that is, cluster members that have small projected separation but are physically unrelated. Assuming a random distribution, one can use estimators like a two-point correlation function to evaluate the probability of observing a pair at a particular separation. Departures from random probability may indicate the presence of really close binaries.

To perform this analysis, we follow Jerabkova et al. (2019), building the so-called elbow plot (Gladwin et al. 1999; Larson 1995), showing the number density of detected targets (Σ) as a function of the separation on-sky (θ). As shown by Gladwin et al. (1999), the presence of an elbow in this distribution graphically indicates the presence of resolved binaries.

Figure 8 shows the elbow plot derived from the cluster selected isolated sources of Catalog I (black dashed–dotted histogram) and the same data where we also add the *completed* distribution of binaries obtained from the Master Catalog (black solid histogram). To investigate how the excess of binaries varies with the radial distance from the cluster center, the figure also shows the results for four different rings centered around the position of θ^1Ori-C. Overall, the different distributions agree with each other, all showing a clear overabundance of multiple systems starting at $\sim 10^3$ au (black vertical line). This result is in agreement with Scally et al. (1999), who suggested, based on a common proper motion study, that there should be no binaries wider than 1000 au. Using GAIA DR2 data in combination with ground-based visible images, Jerabkova et al. (2019) finds for the ONC that the overabundance of multiple systems starts at $\sim$3000 au. Our data, reaching fainter objects with the diagnostic power to separate cluster members from background sources, lend support to Scally's findings. Moreover, fitting the elbow part of the global $\Sigma(\theta)$ distribution, we find a slope -1.85 ± 0.32 (red line), in excellent agreement with typical values for young clusters (Gladwin et al. 1999), as well as for early studies of the ONC in particular (Bate et al. 1998). These results indicate that the true population of binaries in the ONC has been reliably assessed, and that no overestimate is introduced by our completeness correction.

Table 2
Candidate Binaries Catalog (Paper I)

ID (–)	R.A.$_p$ (deg)	Decl.$_p$ (deg)	mag130$_p$ (mag)	color$_p$ (mag)	dmag130$_p$ (mag)	dcolor$_p$ (mag)	mag130$_i$ (mag)	color$_i$ (mag)	dmag130$_i$ (mag)	dcolor$_i$ (mag)	mass$_p$ (solMass)	mass$_i$ (solMass)	emass$_p$ (solMass)	emass$_i$ (solMass)	PA (deg)	Sep (arcsec)	SepOriC (arcsec)
39	83.67010811	−5.469291606	12.4762	−0.1028	0.0105	0.02419	12.6109	−0.0753	0.17544	0.01007	0.31939	0.294837	0.002017	0.026015	52.49	0.23	606.5
40	83.7861492	−5.483746113	12.5467	0.25674	0.0203	0.00317	13.2935	0.2766	0.03924	0.01055	0.304773	0.148041	0.003707	0.001391	100.11	1.73	358.21
41	83.75904395	−5.486073354	12.2413	0.13568	0.00245	0.00819	12.9594	0.1272	0.03694	0.02989	0.472413	0.288703	0.000702	0.004652	91.1	1.1	407.88
42	83.7648425	−5.490518796	12.4288	0.08384	0.017	0.01154	12.8926	0.20911	0.33596	0.04195	0.392846	0.291612	0.004566	0.051289	161.56	0.57	411.36
43	83.8069495	−5.479491472	12.0332	0.09606	0.23364	0.06372	12.5605	0.10666	0.20579	0.03443	0.746202	0.450407	0.136334	0.060834	70.46	0.37	326.03
44	83.67804089	−5.477043065	11.8368	−0.01121	0.01237	0.0096	12.9269	0.09626	0.70721	0.06328	0.970304	0.420492	0.00626	0.325515	147.16	0.51	595.74
45	83.71943096	−5.495858274	12.1265	0.09143	0.13229	0.01538	12.7255	0.01296	0.01626	0.02557	0.620919	0.373322	0.054193	0.00396	6.01	0.39	523.0
46	83.78686627	−5.530307995	11.5871	0.17012	0.19642	0.0366	11.7648	0.11608	0.67489	0.06516	0.933022	0.847697	0.13524	0.461341	37.83	0.29	518.98
47	83.85699037	−5.505832787	11.2803	0.1473	0.00951	0.02309	12.6551	0.06466	0.0217	0.0111	0.828948	0.288616	0.004103	0.002726	316.07	1.67	440.42
48	83.84501338	−5.527000855	12.2636	0.15405	0.01354	0.01051	14.4277	0.0801	0.063	0.00569	0.457653	0.073295	0.003914	0.001426	291.03	0.79	503.44
49	83.85831779	−5.429934619	11.3567	0.25637	0.0281	0.01127	14.955	0.0025	0.02352	0.00545	0.798198	0.042626	0.012866	0.000412	285.94	1.03	203.63
50	83.81740099	−5.415657407	12.3663	0.144	0.01447	0.02249	12.9353	0.07994	0.01686	0.02084	0.344818	0.218099	0.003521	0.001498	41.43	0.54	93.62
51	83.82657047	−5.407414011	12.9546	0.03889	0.02408	0.03683	13.3095	−0.0916	0.08866	0.03445	0.212993	0.146618	0.002143	0.003701	254.0	0.42	70.03
52	83.81419875	−5.433193235	13.5574	−0.18268	0.01932	0.00492	17.1937	−0.31123	0.03401	0.03388	0.128238	0.010471	0.000738	0.000182	91.71	1.57	157.45
53	83.81199692	−5.403242771	12.2095	0.03668	0.01502	0.00801	12.254	0.06378	0.00146	0.00032	0.439431	0.42074	0.004345	0.000387	336.22	1.34	54.29
54	83.81573332	−5.406840395	13.1448	0.08197	0.11398	0.00834	14.1365	−0.1525	0.21425	0.00495	0.172171	0.073254	0.0083	0.008503	84.78	0.25	62.63
55	83.80571344	−5.398079905	13.7532	−0.40305	0.00883	0.03132	14.3648	−0.36328	0.00074	0.00117	0.10579	0.064912	0.000391	3.3e−05	280.12	0.98	55.33
56	83.80291343	−5.452961783	12.5712	−0.0486	0.00591	0.0051	12.5777	−0.05039	0.01511	0.00762	0.300361	0.299461	0.000737	0.001895	21.52	0.27	234.7
57	83.71669487	−5.411941851	12.6526	0.07137	0.13295	0.02342	12.7138	0.16735	0.14902	0.02458	0.361068	0.346167	0.03348	0.034895	254.17	0.5	375.45
58	83.76820899	−5.387204813	11.3141	0.18785	0.07296	0.02795	12.2152	−0.18174	0.09618	0.00477	0.828116	0.389445	0.033476	0.025407	318.89	1.03	181.57
59	83.75430427	−5.402825758	11.9109	0.066	0.00149	0.00187	12.209	0.10544	0.00297	0.0015	0.483427	0.382948	0.000425	0.00079	247.41	1.05	236.2
60	83.74711256	−5.392456476	13.2541	−0.03134	0.01629	0.00829	13.8071	−0.03113	0.04928	0.03227	0.151572	0.100371	0.000789	0.002337	350.7	0.6	257.49
61	83.75085224	−5.402563056	14.8182	0.1399	0.01151	0.004	16.5954	−0.322	0.01252	0.01322	0.070804	0.019725	0.000326	0.000119	10.76	1.49	248.2
62	83.69329687	−5.408822911	11.6392	0.12523	0.01411	0.01518	13.1086	0.04691	0.01475	0.01212	0.68968	0.199359	0.006249	0.001087	274.14	1.48	456.27
63	83.6789671	−5.335279829	11.0598	0.12879	0.01307	0.02797	11.164	0.07703	0.11576	0.01705	1.085792	1.043077	0.007172	0.060041	351.92	0.27	539.42
64	83.73318716	−5.36862182	14.1939	−0.04466	0.02008	0.00515	14.3152	−0.0748	0.10923	0.06099	0.071881	0.067254	0.000491	0.004651	329.48	0.28	316.63
65	83.71736831	−5.375495097	11.0921	0.14235	0.26149	0.00092	11.4305	0.0573	0.27645	0.02362	0.917212	0.766359	0.214105	0.197388	213.64	0.41	367.93
66	83.71579716	−5.360911408	13.1125	0.00998	0.00071	0.01474	13.1251	−0.00467	0.14355	0.01523	0.218997	0.215652	6.2e−05	0.012077	12.53	0.44	384.25

(This table is available in its entirety in machine-readable form.)

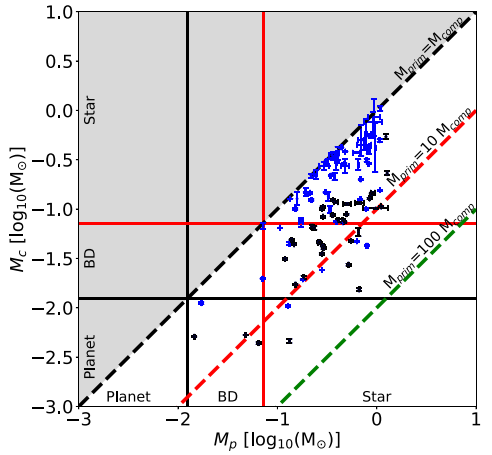

Figure 7. Relation between the mass of the companion and the primary for each candidate binary system, with blue indicating pairs found in Catalog I and black indicating pairs found in this work. The three dotted lines mark where $M_P = M_C$ (black dashed line), $M_P = 10\,M_C$ (red dashed line), and $M_P = 100\,M_C$ (green dashed line). The planetary-mass objects are separated from the brown dwarf mass objects with a black solid line, while the brown dwarf mass objects and stellar mass objects are divided by a red solid line.

Table 3
Summary of Detections in Master Catalog

		Primary		
		Star	Brown Dwarf	Planet
Companion	Star	63	⋯	⋯
	Brown dwarf	26	2	⋯
	Planet	2	4	0

4.5. Comparison with Previous HST Surveys

Reipurth et al. (2007), using HST/ACS Hα images from GO-9825 with 50 mas pixel size (corresponding to about 20 au, 2.5 times smaller than our WFC3-IR data), performed a major survey for visual binaries in the ONC, probing a range of separations similar to ours. More recently, de Furio et al. (2019) used PSF fitting to find close pairs in HST/ACS F555W (V-band) images from GO-10246 to probe separations smaller than 160 au. These surveys, like those performed using ground-based adaptive optics systems, in particular Duchêne et al. (2018), are complementary to our study as they target brighter and bluer (i.e., typically more massive) sources at smaller separations. Comparing the systems in our Master Catalog with those reported in the three aforementioned surveys, we obtain the results listed in Table 4. The columns list the number of targets we identify as cluster members ("Cluster"), those having at least one component classified as background source ("Background"), those appearing unresolved in our data even after KLIP processing ("Unresolved"), and those that do not match any source in our catalog ("Not matched"). If we exclude the binaries that were previously identified in Reipurth et al. (2007) and de Furio et al. (2019) and those identified in Paper I, we are left with 21 new candidate binaries uncovered by the KLIP algorithm. These new candidate detections span a range of primary masses between 0.014 and 0.127 $M_\odot$, companion masses 0.004–0.23 $M_\odot$, separations 0.″16–0.″76, and completeness between 17% and 87% with 49% as median value.

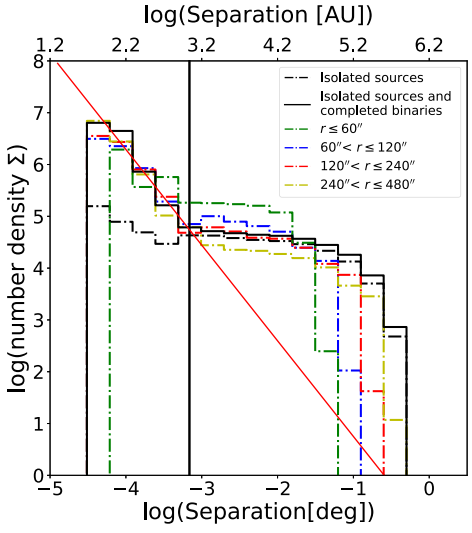

Figure 8. Elbow plot showing the number density of stars $\Sigma(\theta)$ as a function of the on-sky separation θ. The dashed–dotted black histogram shows data from the cluster selected isolated sources from Catalog I (no binaries), while the solid black histogram shows the same data where we added the *completed* distribution of binaries obtained from the Master Catalog (isolated sources plus binaries). The colored dashed–dotted histograms show the distribution obtained from the isolated sources plus binaries data cuts at different distances (r, in the legend) from the position of θ^1Ori-C. The strong gap between the elbow of the isolated sources and the other ones shows that our binaries have to be bound. The vertical black line shows the transition point between the flat portion of the $\Sigma(\theta)$ and the start of the elbow in our plot ($\sim 10^3$ au). The red line shows the fit of the elbow for the completeness-corrected Master Catalog (slope: -1.85 ± 0.32).

Figure 9 shows a comparison between the separations reported in our Master Catalog versus those given by Reipurth et al. (black) and De Furio et al. (red). Overall, there is excellent agreement between our values and those reported by these surveys, with only one major discrepancy against the Reipurth et al. catalog: their source JW 638 is listed as having a companion at $\sim 1''$ separation, whereas our IR images (as well as the ACS visible images of Robberto et al. 2013) show a closer companion at separation $\sim 0.''4$ (see Figure B1, ID 7). If we exclude this detection, the average scatter of separations between our catalog and the others is $\sim 0.''05$, less than one-half WFC3 pixel.

5. Discussion

5.1. Binary Frequency

The multiplicity fraction (MF) of multiple systems is defined as

$$\mathrm{MF} = \frac{N_{\mathrm{mult}}}{N_{\mathrm{mult}} + N_{\mathrm{single}}} \quad (5)$$

where N_{mult} and N_{single} are the number of multiple- and single-star systems in the sample. In Table 5 we report the MF values

Table 4
Number of Matched Binaries between Our Catalog and Previous Surveys

	Cluster	Background	Unresolved	Not Matched
Reipurth et al. (2007)	53	16	8	14
Duchêne et al. (2018)	0	0	7	7
de Furio et al. (2019)	3	3	5	3

Note. Columns show the number of binaries matched to our Master Catalog (Cluster) or detected and rejected because a component was assigned to the background (Background), and the number of binaries matched to a single star in Catalog I but not present in the Master Catalog (Unresolved) or not matched at all (Not Matched).

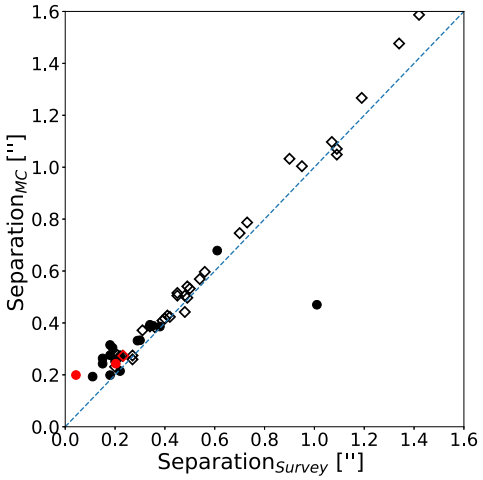

Figure 9. Comparison of separation between Reipurth et al. (black) and De Furio et al. catalogs (red) vs. our Master Catalog for matched cluster–cluster binaries. The dots mark the position of the matched binaries obtained through KLIP PSF subtraction, while the hollow diamonds mark the matched binaries obtained from Paper I. The blue dotted line shows the locus of points where $\text{Separation}_{\text{ONC}} = \text{Separation}_{\text{Survey}}$.

for (1) the Master Catalog ("all"), (2) the Master Catalog split into two different bins of primary mass ("star" or "BD"), and (3) three different primary mass bins (B0, B1, and B2) having the same number of systems in each bin. Table 5 shows that the fraction of binaries among stellar-mass objects is three times larger than among substellar-mass objects for the separation range we are considering. The deficit of very-low-mass binary systems remains regardless of how the limits are defined, as shown by the bottom half of the table.

A variety of MF values have been previously reported in the literature for the ONC. Petr et al. (1998) looked for binaries in the inner $40'' \times 40''$ around the Trapezium, finding MF = 5.9% ± 4.0% in the separation range 0.″14–0.″5 (63–225 au). In a similar separation range, we obtain MF = 8.1% ± 0.8%. Köhler et al. (2006) performed a survey of the periphery of the ONC at 5′–15′ (0.65–2 pc) from the cluster center, probing separations from 0.″1 to 1.″2 and primary masses from 0.1 to $2M_{\odot}$, finding MF = 5.1% ± 2.7%; for a similar range of mass and separation, we find MF = 13.0 ± 1.1. Reipurth et al. (2007) report MF = 8.8% ± 1.1% in the range of separations 0.″17–1.″69 (67.5–675 au), while we find 10.8% ± 0.9%. In general, we obtain larger MF values than previous ONC studies because the combination of HST/WFC3 and KLIP allows us to

Table 5
Multiplicity Fraction for the Complete Sample and Different Subsamples of Primary Masses in the Separation Range 0.″16–1.″73

Label	Primary Mass ($M_{\odot}$)	MF (%)
All	0.01–1.27	11.5 ± 0.9
Star	0.08–1.27	14.6 ± 1.1
BD	0.01–0.08	4.6 ± 1.3
B0	0.50–1.27	21.6 ± 2.9
B1	0.28–0.50	14.5 ± 1.9
B2	0.01–0.28	6.8 ± 1.0

unveil a larger number of faint companions at low angular separations. Still, in comparison with other star-forming regions, our multiplicity function is ∼2 times smaller than, for example, Taurus over a similar separation range (Duchêne & Kraus 2013). On the other hand, comparing our result with the binary frequency in the field obtained by Duquennoy & Mayor (1991) for a similar range of separations, we find approximately the same binary frequency between the field and the ONC. This result is also in agreement with de Furio et al. (2019), where the authors find that the low-mass star binary population of ONC is consistent with that of the Galactic Field over mass ratio 0.6–1 and separation 30–160 au.

5.2. Binary Separation

The left panel of Figure 10 shows the distribution of projected separations in the Master Catalog in bins of 0.″3 before and after completeness correction. The right panel shows histograms of the separations for the three equally populated mass intervals B0, B1, and B2 introduced in Section 5.1. Overall, the separation distribution is peaked toward small values $\lesssim$0.″6, or 240 au. At larger distances, the distribution shows a plateau; both results are consistent with what has been already reported by Reipurth et al. (2007).

Spurzem et al. (2009) have analyzed the disruption of planetary systems in the ONC. Their numerical simulations indicate that moderately close stellar encounters can cause the disruption of planetary systems. They find that the ejected planets have typically low velocity dispersion and in young clusters can be retained by the cluster potential and appear as free floaters. Table 6, based on Spurzem et al. (2009) Equations (36) and (37), shows the typical timescale to get a free floater (τ_{ff}) for the "close" (0.″1–0.″6) and "wide" (0.″6–1.″5) populations of binaries assuming our typical values for the primary and companion mass and system separation. Considering the total number of systems that may harbor a companion, disruptions can be expected, in particular for the wide binary population in the central region of the cluster, which statistically had enough time to undergo at least one

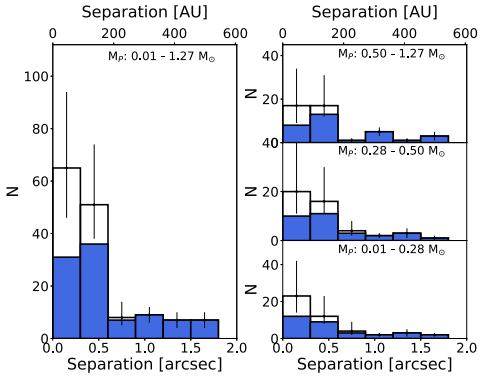

Figure 10. Separation distribution for our full sample (left) and different subsamples of primary masses as in Table 5, in bins of 0.″3. The number of observed companions in each bin is given by the blue histogram; the hollow black histogram—as before—indicates the completeness-corrected value. Error bars are determined according to Poisson statistics.

Table 6
Typical Timescale for Free Floaters for the Close and Wide Binary Populations

	Primary Mass ($M_\odot$)	Companion Mass ($M_\odot$)	Separation (″)	$\tau_{\rm ff}$ (Myr)
Close	0.45	0.22	0.32	111
Wide	0.36	0.17	1.13	37

strong gravitational encounter. The observed spectrum of binary separations, in particular the discontinuity between close and wide binaries at 0.″6 (240 au), can thus be attributed to stellar encounters, as anticipated by Reipurth et al. (2007).

5.3. Binary Separation versus Distance from the Cluster Center

In this section, we examine if the close and wide binaries, separated at 240 au, can be isolated as two distinct populations depending on the distance from the cluster core.

To perform this analysis, we study the completeness-corrected cumulative distributions of close and wide binaries, but instead of simply applying a completeness correction to our observations, we estimate the "true" number of underlying objects required to observe an object given the estimated completeness $\mathcal{C}$. The number of missed detections for each successful detection at completeness $\mathcal{C}$ is modeled as a negative binomial distribution representing the number of failures f occurring before a number of successes s are observed, assuming a probability p of a single success. We define the specific shape of the negative binomial distribution (for each detection) by using the value $p = \mathcal{C}$ for the individual trial success probability, and $s = 1$. Using this negative binomial distribution, we extract a random number of "failures," that is, undetected companions, that were not observed due to noise or incompleteness. We then assign to each of these systems a distance from the center similar to that of the actually observed systems. Finally, we iterate over the sample of observed binaries to obtain a single realization of a "complete" binary population and repeat this procedure 1000 times to obtain the *completed* cumulative distributions shown in Figure 11 for close (green) and wide (blue) binaries. For each

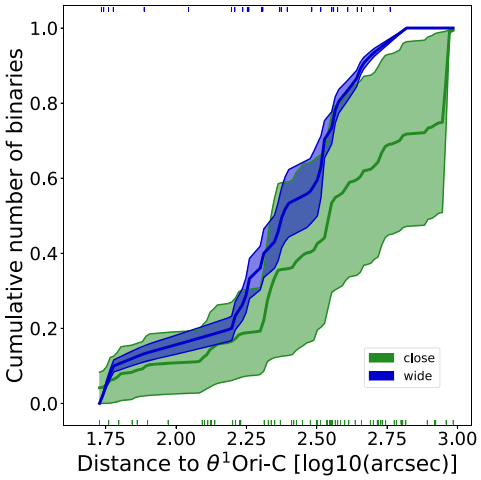

Figure 11. The green (blue) area shows the family of curves obtained through the simulations of *completed* (see text) cumulative distributions for close (wide) binaries as a function of the distance from θ^1Ori. The green (blue) vertical ticks at the bottom (top) of the plot show the distance from the core for each system used to generate the synthetic populations.

iteration, we perform a two-sample Kolmogorov–Smirnov test (K-S test) on the *completed* populations of close and wide binaries as a function of the distance from the core of the cluster. For ∼48% of the K-S tests we obtain a p-value below 0.01. At this level of confidence, we cannot safely reject the hypothesis that the two samples are drawn from the same distribution. This suggests that the two populations may not be different with respect to their spatial distribution.

5.4. Mass Distribution

In order to probe the initial mass functions of multiple systems, in Figure 12 we show the histograms of the primary and companion masses. We fit the histograms using broken power laws (i.e., $\sim m^{-\Gamma_i}$), adopting the peak of each specific sample as the breaking point, and we obtain the results shown in Table 7. Even though the values of Γ_1 are compatible within the errors, both the Γ_2 and the peak of the two populations are not compatible within 1σ. To further characterize the possible differences between the mass distributions of primaries and companions and how they compare to the mass distribution of single stars in the ONC, we show in Figure 13 a set of cumulative mass distributions obtained following the same procedure introduced in Section 5.3. The top left panel shows the comparison between single systems, primaries, and companions. The top right panel shows the comparison between single systems and the full set of masses, both primaries and companions taken individually (we refer to this joint set of mass values as "union"). The bottom panel shows the same comparison where we coadded the mass of the two components of each pair (we refer to this set of mass values as "sum"). In each plot, we also show the cumulative distribution obtained from a Kroupa IMF (Kroupa 2001), a Chabrier IMF for single objects (Chabrier a: Equation (17) in Chabrier 2003),

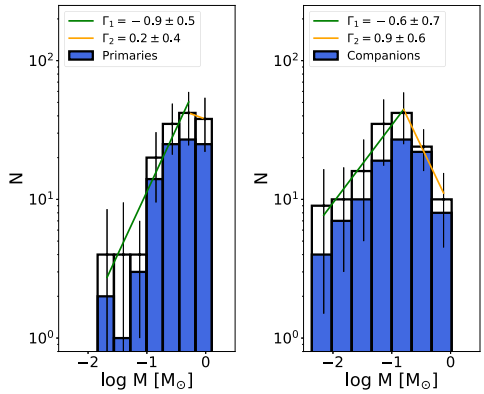

Figure 12. Histogram of masses for primaries and companions. The blue histogram shows the number of companions, while the hollow histogram is corrected for completeness. To bin the two distributions, we used Scott's method (Scott 1979), where the optimal histogram bin width takes into account data variability and data size by asymptotically minimizing the integrated mean square error.

Table 7
Fitted Values for Γ in the Broken Power Law in the Mass Range 0.015–1.27 $M_\odot$

Group	Γ_1	Γ_2	log M
Primaries	-0.9 ± 0.5	0.2 ± 0.4	-0.3 ± 0.1
Companions	-0.6 ± 0.7	0.9 ± 0.6	-0.8 ± 0.2

and a Chabrier IMF with unresolved binaries (Chabrier b: Equation (17) in Chabrier 2003). To avoid introducing biases that are due to the saturation limit of our survey, we cut the mass distributions at 1 $M_\odot$. As explained in Section 5.3, we generate 1000 *complete* samples for each population. For each combination, we perform a two-sample K-S test. The results, summarized in Table 8, are characterized by the ratio $n = \frac{n_i}{n_{\rm tot}}$, where n_i is the number of times the K-S test provides a p-value $\leqslant 0.01$ (corresponding to a confidence level >99% that the two populations are distinct) and $n_{\rm tot}$ is the total number of simulations. As the ratio increases, it is safer to reject the hypothesis that the two samples are drawn from the same population. The results suggest that the populations are generally different, in particular (1) the mass distribution of the binaries is different from the mass distribution of single stars, (2) both are different from the Kroupa/Chabrier IMFs, and (3) the primary and companion mass distributions are different from each other (as already noted in Figure 12). The "union" mass distribution is compatible with a Chabrier IMF with unresolved binaries in ∼31% of the tests. The "sum" mass distribution is always incompatible with any Kroupa/Chabrier IMFs.

We interpret these inconsistencies as a result of a systematic deficiency of companion detections below 100 au. Regardless of our best efforts and of our advanced detection techniques, the technical limit of 1–2 pixels for the closest resolvable pairs is basically insurmountable.

Although in this simple exercise we try to enhance the number of binaries by making use of our completeness tests, it must be remarked that the enhancement is only partial. For every detected binary, we can compute the chance for that binary to be detected at exactly the separation and magnitude contrast at which it is detected, and we can enhance our sample by one minus that chance. However, we cannot account for the truly undetected binaries (i.e., the truly close pairs and those with high flux contrast). A demonstration of this is that our "Single" star sample (blue line in the top left panel of Figure 13) follows the distribution of stellar systems (including unresolved binaries) by Chabrier (2003), an obvious sign that many binaries are actually hiding within our singles.

For the same reason, even the conclusions on dissimilarities of the mass distributions of primaries and companions in detected pairs can only be partial, due to biases affecting which systems are preferentially detected as such.

A more complete exercise, involving modeling the a priori binary mass distribution, SMA, inclinations, eccentricity, and spatial distribution within the cluster, will be the focus of an upcoming paper in this series (L. Pueyo et al. 2020, in preparation).

5.5. Mass Ratio

In this final section, we analyze the mass ratio distribution $q = \frac{M_C}{M_P}$, grouping binaries in different bins according to the mass of the primary and following the classification adopted to produce Table 5. The results are shown as violin plots (a method for graphically depicting groups of numerical data similar to a box plot with a marker for the median of the data and the addition of a rotated kernel density plot on each side). Overall, we obtain a median value for the mass ratios $q \sim 0.25$, indicating a deficiency of similar-mass binaries (which would have $q \sim 1$). This result is in agreement with that reported by Duchêne et al. (2018) for smaller separations (10–60 au). To compare our results with other work, we characterize the distribution of mass ratio as a power law $f(q) \propto q^\gamma$. Fitting the completeness-corrected histogram, we determine the median values of q and γ reported in Table 9 for the different mass bins. From a theoretical point of view, we would expect that binaries with separation $\lesssim$100 au most likely have formed through fragmentation of the protostellar disk, while wider systems formed via freefall fragmentation during early collapse. Because these two processes occur at different times and through different mechanics, it is reasonable to expect them to produce companions with different mass functions and in turn different distributions of mass ratios. We tested this hypothesis and obtained $\gamma_{\lesssim 100\ \rm au} = -1.1 \pm 0.5$ and $\gamma_{\gtrsim 100\ \rm au} = -0.6 \pm 0.2$, finding that the distribution with separation $\gtrsim$100 au (with a bigger and better constrained sample) is incompatible at 2.5σ with the population of binaries with separation $\lesssim$100 au.

Correia et al. (2013) studied eight adaptive optics spatially-resolved binaries in the ONC (along with seven binaries from the literature) in the separation range 85–560 au and primary mass 0.15–0.8, finding $\gamma = 1.03 \pm 0.66$, $\gamma = 1.11 \pm 0.37$, and $\gamma = 0.57 \pm 0.38$ for the B98, PS99, and S00 pre-main-sequence tracks, respectively. The authors find good agreement between their results in the ONC and other star-forming regions (e.g., Taurus-Auriga), while our results seem to disagree with both (see below for our comparison with Taurus-Auriga). We think this discrepancy can be explained by the small number of candidates adopted in their survey and by the large number of

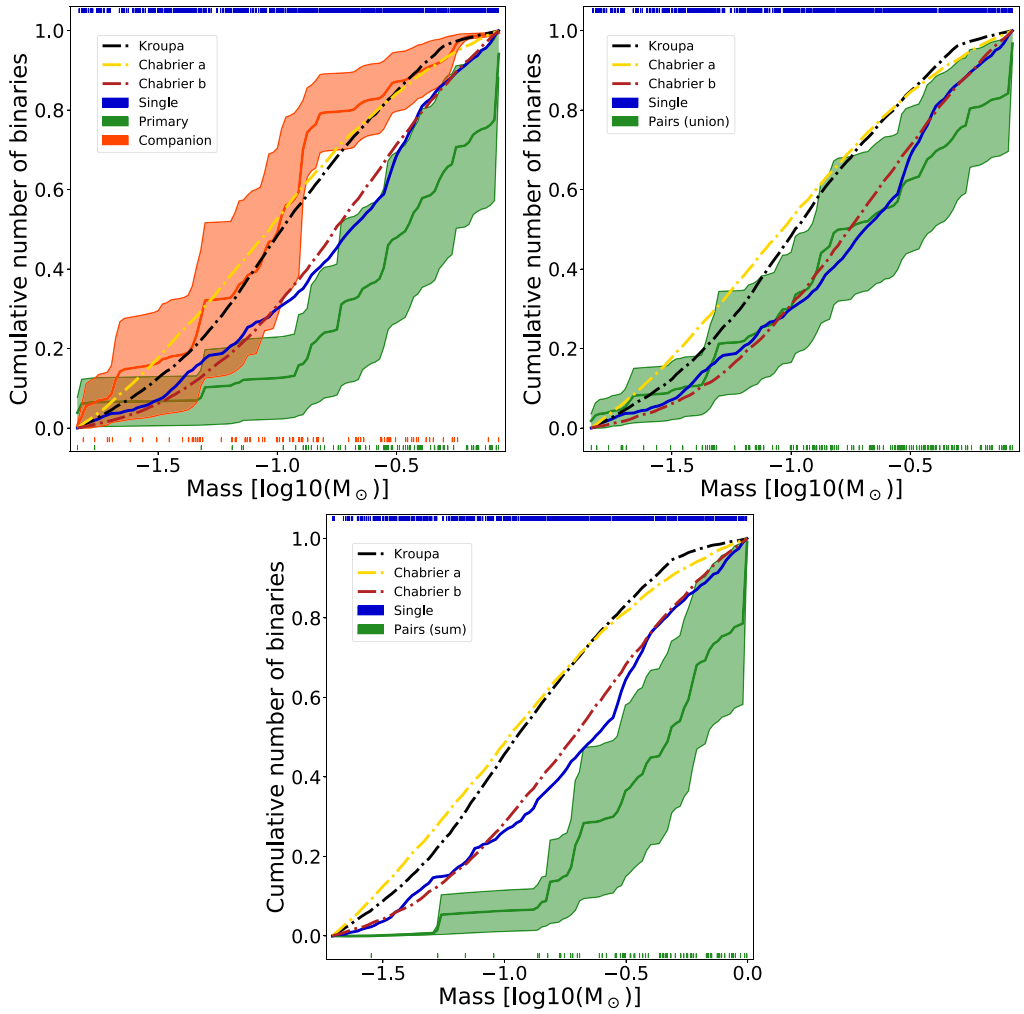

Figure 13. Families of curves obtained through the simulations of *completed* cumulative distributions, as explained in the text. Also shown for reference are the cumulative distributions obtained from a Kroupa IMF (dashed–dotted black line), a Chabrier IMF for single systems (Chabrier a: dashed–dotted yellow line), and a Chabrier IMF with unresolved binaries (Chabrier b: dashed–dotted brown). The colored vertical ticks at the top and bottom of the plot show the total mass of each system used to generate the synthetic populations.

close-in, small-mass companions detected in ours. We decided to test this assumption by down-sampling the number of candidates in our catalog, randomly extracting the same number as in Correia et al. in a similar range of masses and separation $\gtrsim$100 au. We repeated this operation 100 times, finding that in 88%/78%/38% of the cases we agree within 2σ with the results from the PS99/S00/B98 tracks. Note that the candidates we exclude for this test have an average completeness value of 76%, and any candidate with completeness smaller than 30% has been detected through multiple visits. So we conclude that the discrepancy can be attributed to the presence of close-in, small-mass candidate companions we detected through KLIP analysis in our work.

Kraus et al. (2011) conducted a high-resolution imaging survey of the Taurus-Auriga star-forming region by probing the range of separations between 15 and 5000 au for primary and companion masses in the range 0.25–2.5$M_{\odot}$ and 0.01–1.17 $M_{\odot}$, respectively, obtaining $\gamma = 0.2 \pm 0.2$ at separation $\lesssim$100 and 0.08 ± 0.2 at separations $\gtrsim$100, that is, finding an almost flat distribution of q with at most a slight excess of similar-mass binaries. Instead, we find an overabundance of low-q binaries. This result still holds even if we consider a range of overlapping

Table 8
Comparison between Different Samples

	Kroupa	Chabrier a	Chabrier b	Singles	Companions
Primaries	1	1	1	1	1
Companions	0.94	0.92	1	1	⋯
Pairs (Union)	1	1	0.69	0.79	⋯
Pairs (Sum)	1	1	1	1	⋯

Note. The table shows the ratio n of the K-S two-sample test providing a p-value below 0.01 over the total number of simulations. A bigger n allows us to safely reject the hypothesis that the two samples of each test are drawn from the same population.

Table 9
Median Value of q and Power-law Index γ Obtained for Different Ranges of Mass of the Primary

Label	q-median	γ
All	0.25	-0.7 ± 0.2
Star	0.25	-0.7 ± 0.2
BD	0.15	-0.9 ± 0.8
B0	0.15	-0.8 ± 0.4
B1	0.25	-0.5 ± 0.3
B2	0.30	-0.6 ± 0.3

primary and companion masses and separations between the two surveys (0.28–1.27$M_\odot$ and 0.01–1.04 $M_\odot$ and 66–680 au, respectively), obtaining $\gamma_{\rm Kraus} = 0.3 \pm 0.3$ and our $\gamma = -0.4 \pm 0.2$. If instead we limit both data sets at separation $\gtrsim$100 au and companion masses $\gtrsim$0.05 $M_\odot$, the gammas obtained from the two surveys are now compatible within $\sim 1\sigma$, reconciling the difference. Kraus et al. (2011) also remark that their mass-ratio distribution is in stark contrast with Duquennoy & Mayor (1991), who studied field binaries with spectral type between F7 and G9 ($\sim$0.8–1.4 $M_\odot$) and found a mass-ratio distribution peaked toward low masses ($q \sim 0.3$) with few similar-mass companions, a finding very close to our result, $q \sim 0.25$. They derived the γ from the Duquennoy & Mayor (1991) data set, obtaining $\gamma_{q:0\text{–}1.1} = -0.36 \pm 0.07$ and $\gamma_{q:0.2\text{–}1.1} = -1.2 \pm 0.2$. This last value, obtained with a stronger fit ($\chi_\nu = 0.7$ with seven degrees of freedom), is in good agreement with the γ we obtain primary masses of 0.5–1.27 $M_\odot$ (labeled B0 in Table 9). These results, together with the results about the multiplicity fraction presented in Section 5.1, suggest that ONC binaries may represent a template for the typical population of field binaries, upholding the hypothesis that the ONC may be regarded as a most typical star-forming region in the Milky Way.

Figure 15 shows the mass ratio of each pair versus the mass of the primary, that is, the detailed distribution of the data points used to create Figure 14. The shape of each point indicates the mass of the primary (circle = star; hollow diamond = brown dwarf). The limits for substellar and planetary-mass companions are shown as dashed lines. The gray area represents the region of parameter space inaccessible because of our detection limits. Figure 15 shows an over-abundance of companions around stellar versus brown dwarf primaries, consistent with the general trend for star-forming regions and young associations (Duchêne & Kraus 2013). When detected, very-low-mass companions tend to have $q \leqslant 0.4$. If present, very-low-mass binary systems with nearly equal mass must have remained unresolved, with a projected SMA smaller than our inner separation limit at the distance of the Orion Nebula. In fact, Winters et al. (2019) find the

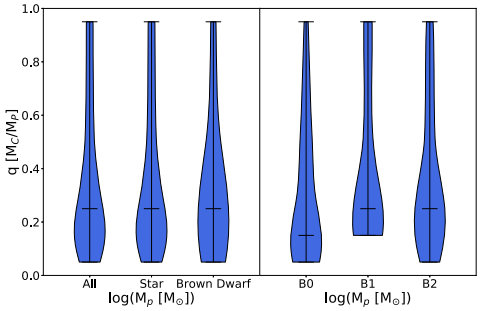

Figure 14. Left panel: violin plots of the mass ratio distribution for all candidates and candidates with primaries in the stellar/brown dwarf mass regime. Right panel: same as left panel for different bins of mass of the primary (see Table 9 for more details). The shape of each distribution shows the probability density of the data smoothed by a kernel density estimator, while the horizontal black lines mark their median values.

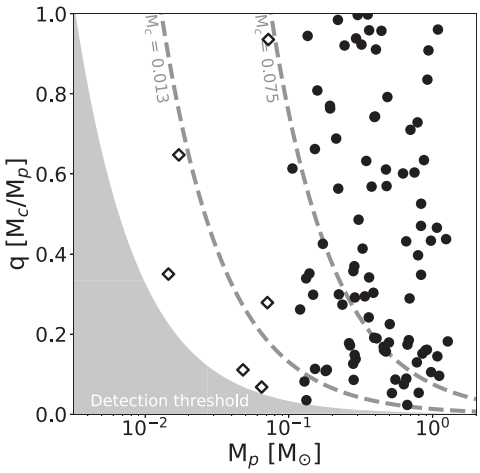

Figure 15. Distribution of mass ratio as a function of mass of the primary for the *ONC candidate binary catalog* objects. The primary masses for each candidate are shown by their shape (circle = star; hollow diamond = brown dwarf). The two gray dashed lines show the values of q for which $M_c = 0.075$ and $M_c = 0.013$ as a function of M_p.

majority of very-low-mass objects in a local volume with 25 pc radius have $q \gtrsim 0.4$, and their separation peaks at $\sim$20 au. As a comparison, the smallest separation we resolve is $\simeq$50 au with

low completeness $\mathcal{C} \sim 0.1$. On the other hand, our data seem to suggest that very-low-mass binary systems with nearly equal mass and wide separation are exceptionally rare, a possible indication that core fragmentation at the lowest masses favors the formation of asymmetrical systems.

6. Conclusion

We performed a new analysis of HST WFC3/IR images of the Orion Nebula Cluster using the KLIP algorithm to find faint companions around low-mass primaries. Starting from a sample of 1392 unique, bona fide cluster targets, we find the following:

1. We find 39 candidate binary systems within separation $0\farcs16$–$0\farcs77$ and mass range $M_p \sim 0.015$–$1.27\,M_\odot$ for the primary and $M_c \sim 0.004$–$0.54\,M_\odot$ for the companion. Of these, 21 are detected for the first time ever. The detection of the H_2O absorption feature allows us to assess with high confidence the membership of these sources in the ONC, although final confirmation of their nature as gravitationally bound systems will require future proper motion studies.
2. The overall multiplicity fraction for the ONC determined from the HST/WFC3-IR data is $11.5\% \pm 0.9\%$. In comparison with other star-forming regions, this value is ∼2 times smaller than, for example, Taurus over a similar separation range (Duchêne & Kraus 2013). We find approximately the same binary frequency in the field and in ONC (Duquennoy & Mayor 1991).
3. The mass distribution of the sources belonging to a binary system (either primaries, companions, or combined) is different from the mass distribution of single stars; the primary and companion mass distributions are also different from each other.
4. The mass ratio distribution is compatible with what is expected from a scenario where close-in binaries formed through fragmentation of the protostellar disk while wider systems formed via freefall fragmentation.
5. We find an almost complete absence of brown dwarfs and very-low-mass M-dwarf pairs with similar mass (high-q systems), and a steep distribution of mass ratios peaked toward small q-values (median values $q \simeq 0.25$).

Overall, our results suggest that ONC binaries may represent a template for the typical population of field binaries, supporting the hypothesis that the ONC may be regarded as a most typical star-forming region in the Milky Way.

The authors thank the anonymous referees for the interesting suggestions and comments. G.M.S. wants to thank the Instituto de Astrofísica de Canarias for hospitality. The authors thank Bo Reipurth for useful comments on the manuscript. Support for program No. GO-13826 was provided by NASA through a grant from the Space Telescope Science Institute, which is operated by the Association of Universities for Research in Astronomy, Incorporated, under NASA contract NASS-26555. C.F.M. acknowledges an ESO fellowship. J.A. was supported in part by a grant from the National Physical Science Consortium. G.M.S. and A.A. are supported by the Ministerio de Ciencia, Innovación y Universidades of Spain (grant AYA2017-89841-P) and by the Instituto de Astrofísica de Canarias. This research has made use of the VizieR catalog access tool, CDS, Strasbourg, France. The original description of the VizieR service was published in Ochsenbein et al. (2000).

Facilities: HST (ACS, WFC3).

Software: Numpy (van der Walt et al. 2011), Astropy (Astropy Collaboration et al. 2013; Price-Whelan et al. 2018), Scipy (Virtanen et al. 2020), Matplotlib (Hunter 2007), PyKLIP (Wang et al. 2015), Pandas (McKinney 2010; Reback et al. 2020).

Appendix A
Receiver Operating Characteristic Curves

An ROC curve is a plot that shows the diagnostic ability of a binary classifier system as the discrimination threshold (T) varies. The ROC curve is created by plotting the true-positive rate (or TPR) versus the false-positive rate (FPR) at various threshold T values. When T is set low enough, we accept the whole distribution of TP, but we also accept the whole distribution of FP, so in the ROC curve plot we are at the point (1,1). When we increase T, we will lose some TP as well as some FP (the exact rate and so the shape of the ROC curve depend on the exact distribution of the two populations) until we reach the point (0,0), where the selected threshold excludes all of the TP and FP.

To build ROC curves for our detection, we first need to simulate the TPR and FPR populations representative of each of our candidates. Our sensitivity strongly depends on the magnitude of the primary ($m_{\rm F130M}$), the contrast (Δmag) achieved by PSF subtraction, and the distance of the companion from the primary (separation). We therefore sorted our targets into magnitude bins of the primary from 10 to 22, Δmag from 0 to 10 (both with a width equal to 1), and separation from $0''$ to $1''$ in steps of $0\farcs1$. To build the TPR distribution and the FPR distribution for each of these configurations, we do the following:

1. We created 1000 fake binaries. To simulate both the primary and the companion components, we first simulated an isolated star using the model of the PSF obtained from KLIP, rescaled to match the flux of the object we want to simulate. To perturb the PSF model, we created a local model of the noise by combining WFC3 error maps from all of the stars of the survey in the same magnitude bin of the simulated star. To take into account different pixel phases, we add a small shift ($\leqslant$0.5 pixel) to the position of the star. Then we inject the simulated companion into the tile of the simulated primary and add the sky to the final combined tile. During this procedure, we also saved the tile of the isolated primary for future analysis.
2. For each simulation (either the binary or the isolated primary), we perform the same PSF subtraction process illustrated in Section 3.2, retrieving the value of the (positive) S/N in the pixel where we injected (building the TPR) or did not inject the companion (building the FPR). We decided to use only the positive values to build the ROC curves because by definition the signal from a candidate detection has to be positive.

To encapsulate in a single number the performance of our model to distinguish between classifiers, we evaluate the area under the curve (AUC) of an ROC. The higher the AUC, the better the model is at distinguishing between the true-positive population and the false-positive population.

Figure A1 shows examples of the TP (blue) and FP (orange) histograms for a given binary configuration and the corresponding ROC curves. Also provided for each ROC curve is the value of the corresponding AUC.

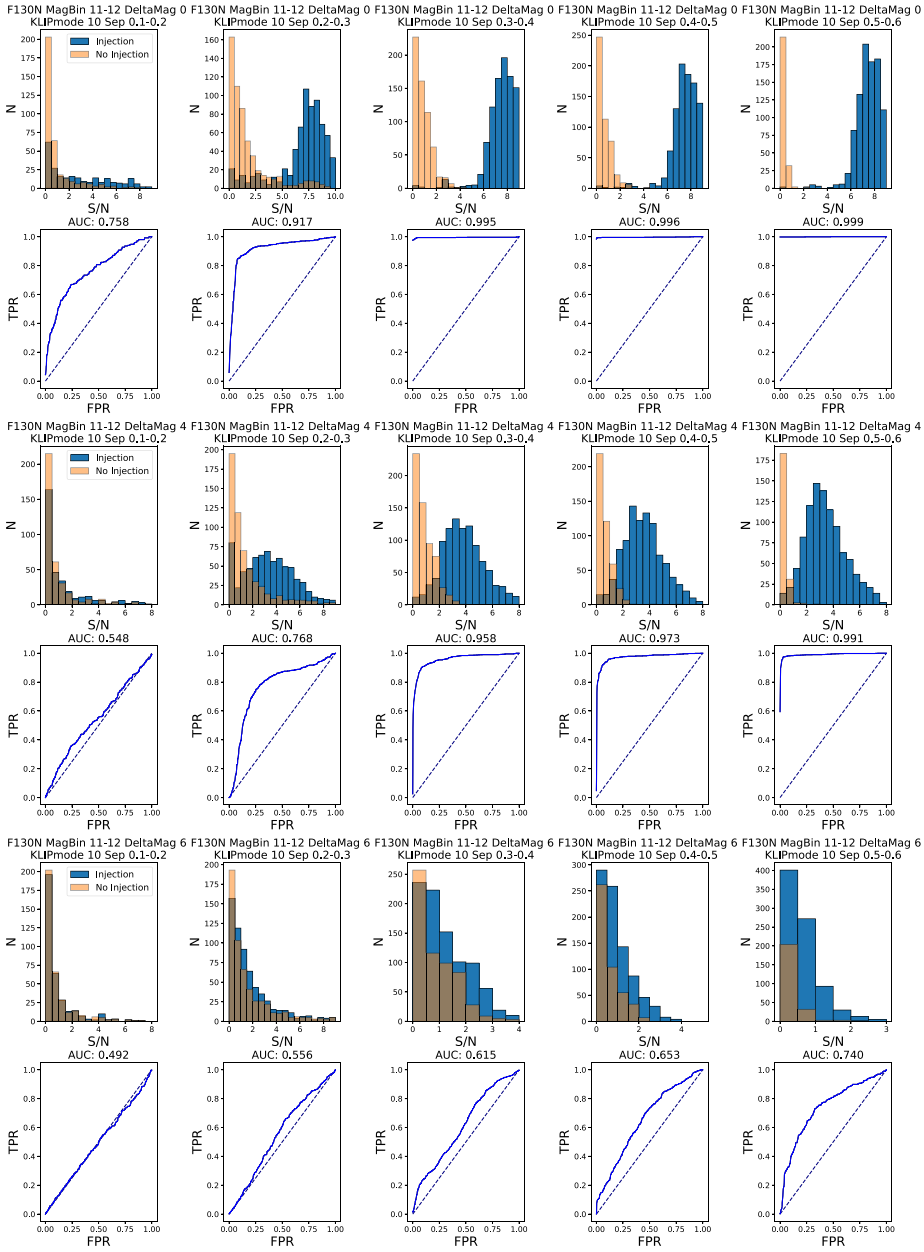

Figure A1. Distributions of S/N and derived ROC curves for filter F130N, magnitude bin of the primary 11–12, Δmag 0, 4, and 6, and different distances from the center of the tile.

Appendix B
Gallery of Binaries

Figures B1–B2 show the coadded images pre- and postsubtraction for each of the candidate cluster binaries presented in Table 1. Each stamp has dimensions of 2″ × 2″. Figure B3 shows the postage stamp for the candidate binary from Table 2. Each stamp has dimensions of 2″ × 2″. Each postage stamp has been rotated and aligned to have north up and east to the left.

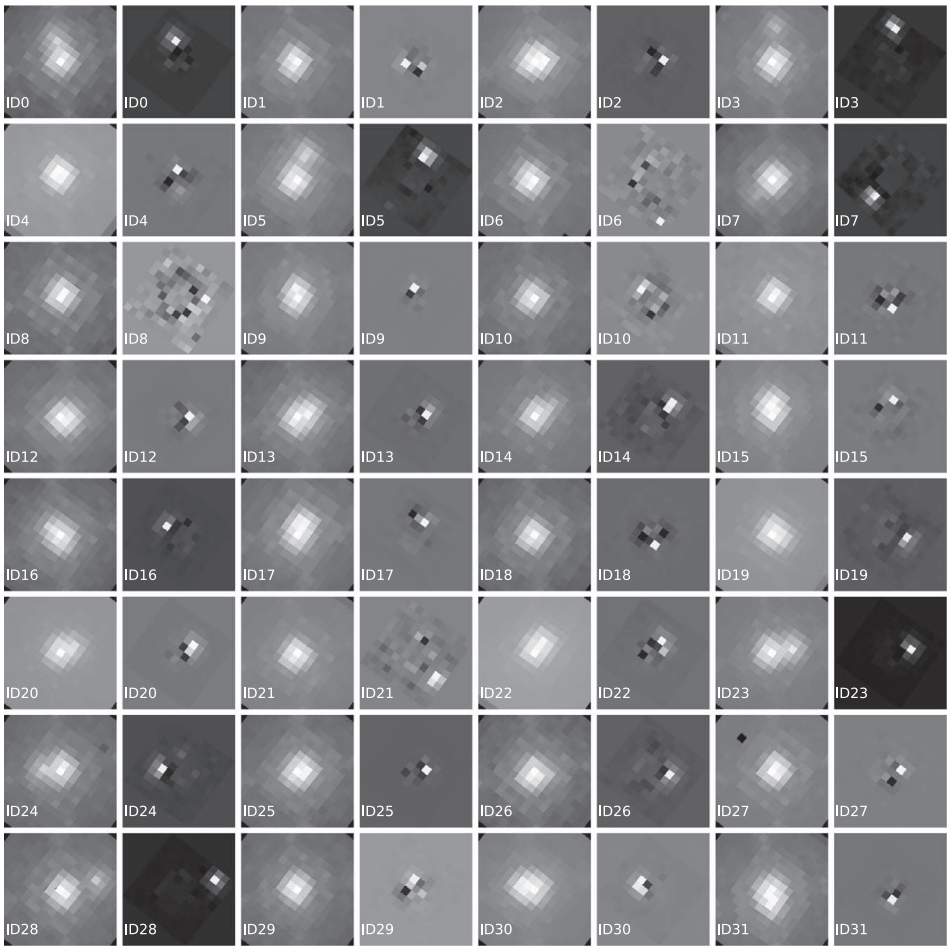

Figure B1. Each tile shows the residual image after running KLIP for each primary target for which we detect a companion (brighter pixel in the tile). Each stamp has dimensions of 2″ × 2″. North is up and east is on the left.

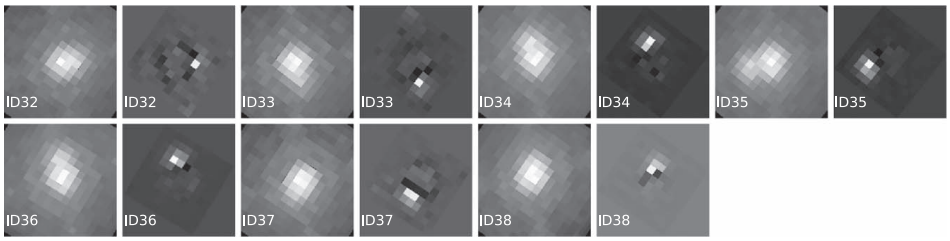

Figure B2. Each tile shows the residual image after running KLIP for each primary target for which we detect a companion (brighter pixel in the tile). Each stamp has dimensions of $2'' \times 2''$. North is up and east is on the left.

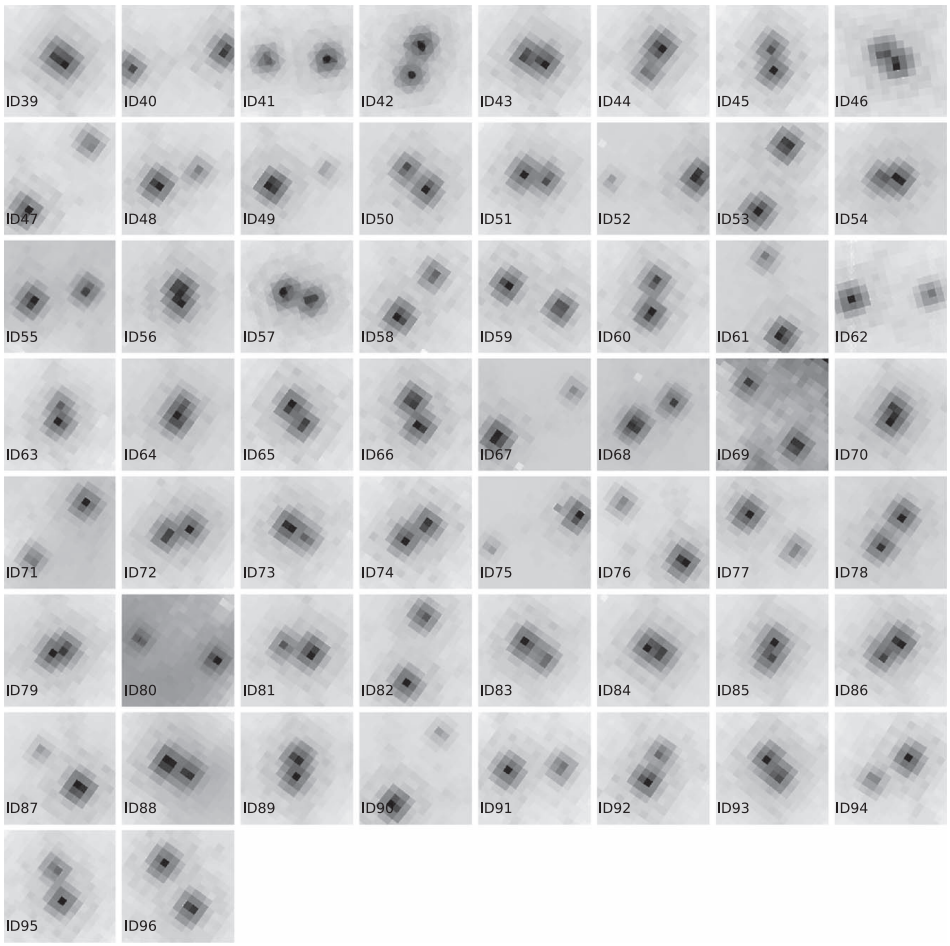

Figure B3. WFC3 binaries identified from Catalog I up to separation $\leqslant 1\farcs5$. Each stamp has dimensions of $2'' \times 2''$. North is up and east is on the left.

ORCID iDs

Giovanni M. Strampelli https://orcid.org/0000-0002-1652-420X
Jonathan Aguilar https://orcid.org/0000-0003-3184-0873
Antonio Aparicio https://orcid.org/0000-0002-6054-0004
Mario Gennaro https://orcid.org/0000-0002-5581-2896
Massimo Robberto https://orcid.org/0000-0002-9573-3199

References

Andersen, M., Meyer, M. R., Greissl, J., & Aversa, A. 2008, ApJL, 683, L183
Astropy Collaboration, Robitaille, T. P., Tollerud, E. J., et al. 2013, A&A, 558, A33
Baraffe, I., Chabrier, G., Allard, F., & Hauschildt, P. H. 1998, A&A, 337, 403
Bate, M. R., Clarke, C. J., & McCaughrean, M. J. 1998, MNRAS, 297, 1163
Bihain, G., & Scholz, R. D. 2016, A&A, 589, A26
Brandt, T. D., McElwain, M. W., Turner, E. L., et al. 2014, ApJ, 794, 159
Chabrier, G. 2003, PASP, 115, 763
Choi, J., Dotter, A., Conroy, C., et al. 2016, ApJ, 823, 102
Choquet, É, Pueyo, L., Hagan, J. B., et al. 2014, Proc. SPIE, 9143, 914357
Correia, S., Duchêne, G., Reipurth, B., et al. 2013, A&A, 557, 63
da Rio, N., Robberto, M., Hillenbrand, L. A., Henning, T., & Stassun, K. G. 2012, ApJ, 748, 14
de Furio, M., Reiter, M., Meyer, M. R., et al. 2019, ApJ, 886, 95
Dotter, A. 2016, ApJS, 222, 8
Duchêne, G., & Kraus, A. 2013, ARA&A, 51, 269
Duchêne, G., Lacour, S., Moraux, E., Goodwin, S., & Bouvier, J. 2018, MNRAS, 478, 1825
Duquennoy, A., & Mayor, M. 1991, A&A, 500, 337
Gennaro, M., Prada Moroni, P. G., & Tognelli, E. 2012, MNRAS, 420, 986
Gennaro, M., & Robberto, M. 2020, ApJ, 896, 80
Gladwin, P. P., Kitsionas, S., Boffin, H. M., & Whitworth, A. P. 1999, MNRAS, 302, 305
Hunter, J. D. 2007, CSE, 9, 90
Jerabkova, T., Beccari, G., Boffin, H. M. J., et al. 2019, A&A, 627, A57
Kirkpatrick, J. D., Gelino, C. R., Cushing, M. C., et al. 2012, ApJ, 753, 156
Köhler, R., Petr-Gotzens, M. G., McCaughrean, M. J., et al. 2006, in Proc. IAU Symp. 240, Binary Stars as Critical Tools & Tests in Contemporary Astrophysics, ed. W. I. Hartkopf, E. F. Guinan, & P. Harmanec (Cambridge: Cambridge Univ. Press), 114
Kraus, A. L., Ireland, M. J., Martinache, F., & Hillenbrand, L. A. 2011, ApJ, 731, 8
Kroupa, P. 2001, MNRAS, 322, 231
Kuhn, M. A., Hillenbrand, L. A., Sills, A., Feigelson, E. D., & Getman, K. V. 2019, ApJ, 870, 32
Larson, R. B. 1995, MNRAS, 272, 213
Marois, C., Correia, C., Galicher, R., et al. 2014, Proc. SPIE, 9148, 91480U
Mawet, D., Milli, J., Wahhaj, Z., et al. 2014, ApJ, 792, 97
McKinney, W. 2010, in Proc. 9th Python in Science Conf., ed. S. van der Walt & J. Millman (Austin, TX: SciPy), 56
Ochsenbein, F., Bauer, P., & Marcout, J. 2000, A&AS, 143, 23
Petr, M. G., Coude du Foresto, V., Beckwith, S. V. W., Richichi, A., & McCaughrean, M. J. 1998, ApJ, 500, 825
Price-Whelan, A. M., Sipőcz, B. M., Günther, H. M., et al. 2018, AJ, 156, 123
Pueyo, L. 2016, ApJ, 824, 117
Reback, J., McKinney, W., jbrockmendel, et al. 2020, pandas-dev/pandas: Pandas v1.0.3, Zenodo, doi:10.5281/zenodo.3715232
Reipurth, B., Guimarães, M. M., Connelley, M. S., & Bally, J. 2007, AJ, 134, 2272
Robberto, M., Gennaro, M., & Gabellini, M. G. U. 2020, ApJ, 896, 79
Robberto, M., Soderblom, D. R., Bergeron, E., et al. 2013, ApJS, 207, 10
Scally, A., Clarke, C., & McCaughrean, M. J. 1999, MNRAS, 306, 253
Scott, D. W. 1979, Biometrika, 66, 605
Slesnick, C. L., Hillenbrand, L. A., & Carpenter, J. M. 2004, ApJ, 610, 1045
Soummer, R., Pueyo, L., & Larkin, J. 2012, ApJL, 755, 28
Spiegel, D. S., Burrows, A., & Milsom, J. A. 2011, ApJ, 727, 57
Spurzem, R., Giersz, M., Heggie, D. C., & Lin, D. N. 2009, ApJ, 697, 458
Stassun, K. G., Feiden, G. A., & Torres, G. 2014, NewAR, 60–61, 1
van der Walt, S., Colbert, S. C., & Varoquaux, G. 2011, CSE, 13, 22
Virtanen, P., Gommers, R., Oliphant, T. E., et al. 2020, Natur Meth., 17, 261
Wang, J. J., Ruffio, J.-B., de Rosa, R. J., et al. 2015, pyKLIP: PSF Subtraction for Exoplanets and Disks, Astrophysics Source Code Library, ascl:1506.001
Winters, J. G., Henry, T. J., Jao, W.-C., et al. 2019, AJ, 157, 216

Draft version January 5, 2021
Typeset using LaTeX **twocolumn** style in AASTeX63

HST Survey of the Orion Nebula Cluster ACS/Visible Bands. IV. Star formation and dynamical evolution in the ONC

Giovanni M. Strampelli,[1,2] Massimo Robberto,[1,3] Laurent Pueyo,[3] and Antonio Aparicio[2,4]

[1] *Johns Hopkins University, 3400 N. Charles Street, Baltimore, MD 21218, USA*
[2] *Department of Astrophysics, University of La Laguna, Av. Astrofísico Francisco Sánchez, 38200 San Cristóbal de La Laguna, Tenerife, Canary Islands, Spain*
[3] *Space Telescope Science Institute, 3700 San Martin Dr, Baltimore, MD 21218, USA*
[4] *Instituto de Astrofísica de Canarias, C. Vía Láctea, 38200, San Cristóbal de La Laguna, Tenerife, Canary Islands, Spain*

ABSTRACT

We provide the results of a comprehensive study based on two *HST* Treasury program on the Orion Nebula Cluster and newly performed PSF photometry. Thanks to the wide variety of filters available in the surveys, we perform MCMC simulations to estimate mass, age and extinction for each sources in the cluster. An analysis of the age distribution strongly support the idea that star formation in the ONC is best described by at least two discrete and sequential episodes over a few Myrs. We evaluated the mass accretion rate ($\dot{M}_{acc}$) for a sample of ~ 700 bonafide cluster sources, providing one of the most extend catalog of mass accretion rates in the ONC up to-date. The $\dot{M}_{acc} - M_{\star}$ relation clearly show the presence of two distinct population, one made up of bright accretor that follow a relation $\dot{M}_{acc} \propto M_{\star}{}^{1.26\pm0.11}$ and a second one that, departing at $M_{\star} \sim 0.3\ M_{\odot}$ follow a much steeper relation $\dot{M}_{acc} \propto M_{\star}{}^{6.23\pm2.38}$. To address binarity in the cluster, we coupled together the results from two Treasury programs obtaining a catalog of 119 binary systems, 5 of which obtained from this new study. When we take into account completeness correction and chance-alignment arguments, we find a binary fraction of $13.0\% \pm 1.0\%$ in the range of separations $0.15 - 1.95''$ and clear sign of dynamical evolution in the history of the cluster.

Keywords: software — binaries — stars: pre-main sequence — stars: low-mass

1. INTRODUCTION

The Orion Nebula Cluster (ONC) is one of the richest ($\sim$ 2000 cluster members), youngest ($\sim$ 2 Myr; Jeffries et al. 2011; Reggiani et al. 2011; Jerabkova et al. 2019) and relatively near star forming region ($\sim$ 402 pc; Kuhn et al. 2019) within 2 kpc from the sun (Lada & Lada 2003; Portegies Zwart et al. 2010). Thanks to its close proximity to the Sun and its modest foreground extinction ($A_V \sim 1$ Scandariato et al. 2011), the ONC as a whole (Herbig & Terndrup 1986; Hillenbrand 1997; Getman et al. 2005; Da Rio et al. 2012; Robberto et al. 2013, 2020) as well as its population of multiple systems (Petr et al. 1998; Simon 1997; Scally et al. 1999; Köhler et al. 2006; Reipurth et al. 2007; De Furio et al. 2019; Strampelli et al. 2020a) have been thoroughly investigated in the past at different wavelength, making of the ONC the excellent laboratory where to investigate critical aspect of star an planetary formation such as dynamical interactions, star formation rate, initial mass function and protoplanetary disk evolution.

In this work we combine for the first time the results from two *HST* Treasury programs on the Orion Nebula Cluster (ONC; GO-10246 and GO-13826, P.I. M. Robberto) executed almost 15 years apart. We concentrate on the ACS/WFC and WFC3-IR datasets, obtained in seven different filters (F435W, F555W, F658N, F775W, and F850LP with ACS, F130N and F139M with WFC3), providing a revised photometric catalog for the five visible bands, with the aim of contributing to the general understanding of the evolution history of this cluster and star formation in general.

Taking advantage of the wide selection of filters with the most accurate photometric data, and adopting a Bayesian approach with Markov Chain Monte Carlo (MCMC) strategy, we estimate the main properties of each component of the cluster (e.g. mass, extinction and

Corresponding author: Giovanni M. Strampelli
strampelligiovanni@jhu.edu

age). The HST photometry also allow us to measure the $H\alpha$-line luminosity, $L_{H\alpha}$, and the total accretion luminosity, L_{acc}, that in turn allow us to derive an estimate of the mass accretion rate, $\dot{M}_{acc}$, for ~ 700 cluster sources. In the second part of this paper we exploit the *Stra*KLIP pipeline (Strampelli et al. 2020b) to search for faint substellar companions in the ACS data and combine the results with the binaries recently detected with the same method in the WFC3-IR data (Strampelli et al. 2020a). This produces a comprehensive HST catalog of 119 binaries in the ONC.

The paper is organized as follows: the observations and the new ACS photometric catalog is presented in §2, together with the new ACS binary catalog created using *Stra*KLIP. In §3 we introduce our Bayesian strategy to perform Spectral Energy Distribution fitting and our final catalog of bona-fide cluster members. In Section §4 we present the MCMC derived parameters, the mass accretion luminosities and rate. We also present the stellar parameters, with their distributions, of the combined ACS+WFC3 binary catalog. In Section §5 we discuss the implication of our findings for both samples of isolated and binary stars. Our conclusion are summarized in §6.

2. OBSERVATIONS AND DATA REDUCTION

In this work we reanalyze the *HST*/ACS observations obtained for the *HST* Treasury Program on the Orion Nebula Cluster (GO-10246) carried out between October 2004 and March 2005 in the filters F435W, F555W, F658N, F775W and F850LP. The original data reduction strategy led to the detection of 3398 unique sources (Robberto et al. 2013), most of them observed two or more times in different *HST* visits. The ACS source catalog of Robberto et al. (2013) only lists individual detection, for a grand total of 8185 different multi-color observations, and serves as a starting point for our new analysis. Our new analysis has been motivated by the advances in the ACS instrument calibration, by the desire of performing more accurate PSF photometry instead of the original aperture photometry, by the search for close and faint binary companions, and by the goal of vetting and averaging the individual measures obtained in different visits to increase the reliability of the derived stellar parameters.

Table 1 reports the most recent photometric zero points of each filter, relative to the epoch of observations, as provided by the *ACS Zeropoints Calculator*[1]. Compared to the original zero points implemented by the Robberto et al. (2013), the *ACS Zeropoints Calculator* provide a difference between -0.002 and 0.019 magnitudes in the zero points, where the smaller difference refer to the F555W filter and the higher to both in F775W and F850LP filters.

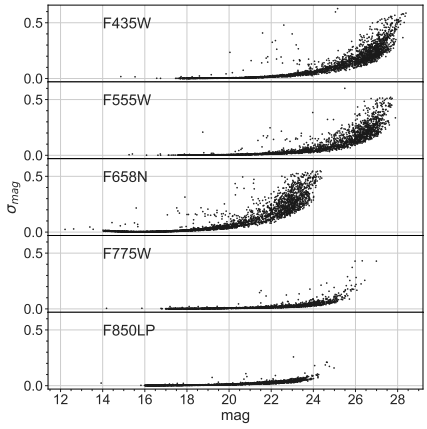

Figure 1. Photometric errors as a function of magnitude for the five ACS filters.

To perform PSF photometry we used the *BasicPSFPhotometry* package from *photutils*[2] implemented in the *Stra*KLIP pipeline (Strampelli et al. 2020b). Reference PSFs have been taken from Tiny Tim[3] for each filter. For sources observed multiple times we averaged the PSF photometry obtained in different visits , corresponding also to different positions on the focal plane, obtaining a new master catalog for 3296 isolated stars. Sources with with poor PSF fit, as indicated by a parameter $\chi^2 < 3$, as well as sources that show substantial saturation (i.e. 3 or more pixel saturated) are kept in the catalog listing their aperture photometry according to the prescriptions presented in (Strampelli et al. 2020b). Table A1 (in the Appendix) shows a sample of our final catalog.

In Figure 1 we plot the averaged magnitudes versus their estimated uncertainties in the five ACS filters. The 5σ sensitivity limit ($\sigma_{mag} \simeq 0.2$) are about m435 = 25.3, m555= 25.2, m658 = 22.2, m775 = 24.7 and m850 = 23.8 in the Vega system.

[1] https://acszeropoints.stsci.edu/

[2] https://photutils.readthedocs.io/en/stable/index.html

[3] https://www.stsci.edu/hst/instrumentation/focus-and-pointing/focus/tiny-tim-hst-psf-modeling

FILTER (–)	PHOTPLAM $\AA$	PHOTFLAM erg$\AA^{-1}$cm^{-2}s^{-1}	Ground Equivalent (–)	Exposure (–)	Integration time (s)	VEGAmag mag
F435W	4329.2	3.113e-19	Johnson B	6	420	25.776
F555W	5360.2	1.948e-19	Johnson V	9	385	25.722
F658N	6584.0	1.977e-18	Broad $H\alpha$	1	340	22.378
F775W	7693.9	9.928e-20	Sloan i	8	385	25.275
F850LP	9034.6	1.503e-19	Sloan z	7	385	24.345

Table 1. List of zeropoints for each filter as obtained from the STScI *ACS Zeropoints Calculator*.

2.1. *Binary detection*

In order to use the KLIP algorithm, some preliminary cleaning of the source catalog has do performed. Starting from the sample of 3398 unique sources listed Robberto et al. (2013), we discard 598 *bad* sources that appear either saturated (in 3 or more pixels in three or more filters) or too faint (compared to sensitivity limit provided above) in order to down-select sources with at least one color. We also reject 291 sources having a well resolved neighbour with separation smaller than $\sim 2''$, specifically 144 pairs and possible 3 ternary systems, generally referred hereafter as *wide multiples*). This produced a KLIP master catalog of 2509 sources, nicely isolated and with signal-to-noise high enough, in two filters, to search for faint companions. To detect and characterize faint astronomical signals blended with the PSF of the target source we use *Stra*KLIP Strampelli et al. (2020b). Here we provide a brief summary of the main elements of *Stra*KLIP, pointing the reader to the paper for the details. The five fundamental steps in the pipeline are:

1. **Postage stamp creation:** small *postage-stamp* images (also referred as *tiles*) are constructed for each source of the *input catalog*. These images represent the search regions $\mathcal{S}$ that will be inspected for each target. $\mathcal{S}$ must be large enough to include the bright wings of the PSF, and be small enough to avoid contamination from the wing of other catalog sources in the vicinity;

2. **Groups:** a grid of 10×5 cells is created on the detector and the *tile* are grouped accordingly, under the assumption that the sources falling in each cell share the same systematic image distortion. The sources belonging to each cell are analyzed to determine the local, field-dependent PSF reference, creating a PSF library;

3. **KLIP analysis:** PSF subtraction is performed on each source of each *tile* using the local PSF and KLIP algorithm (Soummer et al. 2012);

4. **Residual detection:** the *residual tiles* from the precedent step are inspected for the presence of any previously undetected astronomical signal, at the appropriate significance level. After analyzing a few *residual tiles*, we decide to exclude filter F658N from the search for companions due the high residual noise left *tile* after the PSF subtraction step was performed;

5. **Candidates extraction:** a preliminary catalog of candidates with relative photometry is produced.

The result of this analysis resulted in a list 59 candidate binary systems and one ternary or, if we count the ternary as a system of two binaries (as used by Kuiper 1942, e.g. AB and AC), 61 multiple systems in total.

3. ANALYSIS

3.1. *Bayesian analysis*

One of the main goals of this work is to determine the principal parameters that characterize each sources in the catalog: mass, extinction and age. To this purpose, we perform Spectral Energy Distribution (SED) fitting comparing the observed photometry to synthetic photometry derived from theoretical models (see Section 3.1.1). Since young PMS sources are known to be variable, instead of fitting the actual magnitudes we use the colors , i.e. for ACS m435-m555, m555-m775, and m775-m850, neglecting the m658 filter centered on the H_α line that may be dominated by accretion, mass loss or other circumstellar emission. Using colors makes our results rather insensitive to the distance of the sources, and of the ONC in general. When the WFC3 m130-m139 colors from Robberto et al. (2020) are available, we include them in our fitting procedure, counting again on the fact that colors are rather insensitive to stellar variability. We do not consider, however a combined ACS-WFC3 color like e.g. m850-m130, since the observations have been taken years apart and variability in this case can be a limiting factor.

Our fitting procedure follows a Bayesian approach in order to obtain a probability distribution for the parameters under study. Our implementation is based on a MCMC algorithm, represented schematically in Figure 2, based on the following main steps:

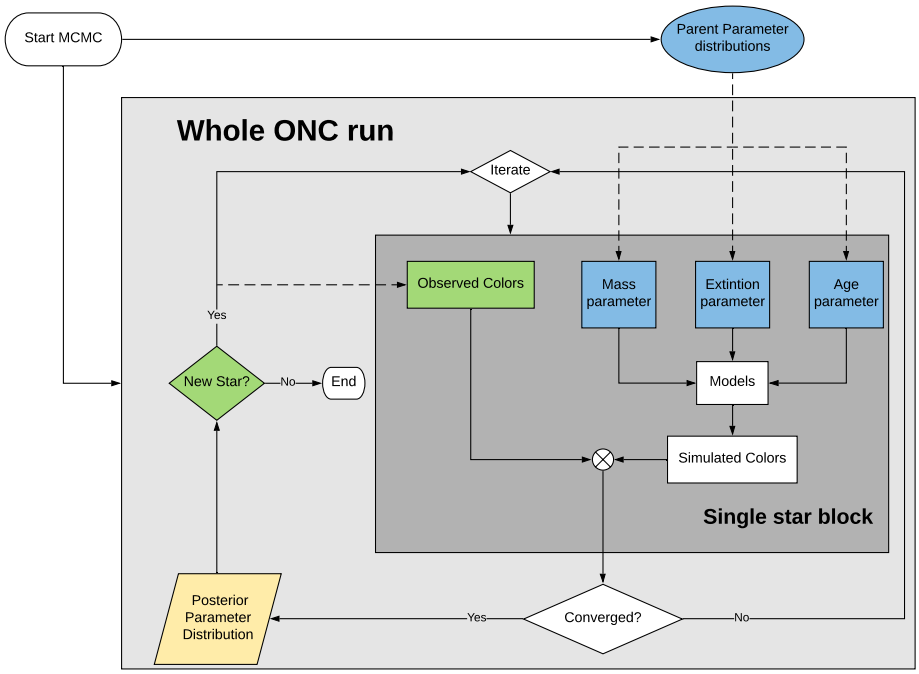

Figure 2. Flowchart for the ONC sources parameter estimations. The light grey area represent the whole ONC run while the dark one represent the simulation of a single star. The green colored blocks represent fixed ingredient for the simulation while in blue are shown the MCMC fitting parameters. The yellow block shows the stored final output of each iterations

- at the start of the MCMC run, three parent uniform distributions spanning the whole parameter space are generated. From them, each parameter will be extracted during each iteration of the MCMC run;

- for each star in the sample, a user's defined number of *walkers* is generated, limied in this work to a maximum of 100. Then the following loop is iterated for each walker:

  – the *observed color* m443-m555, m555-m775, m775-m850 and m130-m139 are pulled from the catalog for the star under consideration. We adopt the Cardelli et al. (1989) reddening law has to de-redden the observed colors, parameterized with two different value $R_V = 3.1$ and $R_V = 5$. The de-reddened colors are then parsed to the fitting routine as fixed ingredient for the simulation.

  – the three parameters (mass, extinction and age) are randomly extracted from their parent distributions and combined with the model (see Section 3.1.1) to obtain simulated color. The simulated and observed color are then compared with the aim at finding the set of parameters that better reproduce the input observations for the star. In order to do that, we need the following ingredient: 1) a knowledge of the priors on the fitting parameters (see Section 3.1.2), 2) a definition of a likelihood function to compare observations and simulations (see Section 3.1.3), 3) an algorithm for sampling the posterior distribution of the fit parameters (see Section 3.1.4);

  – this process is iterated until convergence is found or a predefined number of steps are elapsed, then the posterior distribution of the

parameters is saved for future analysis and the routine moves to the following source;

3.1.1. *Models*

Theoretical models of the *BT-Settl* family[4] spanning a range between 1 and 100 Myr have been selected for this work. They take advantage of the stellar interior calculations made by Baraffe et al. (2015), and the PHOENIX atmospheric model. The BT-Settl models, in particular, integrate cloud formation and dust sedimentation in the atmospheres of BDs.

3.1.2. *Priors*

We define three class of prior for our test:

- The prior on the mass is provided by the selected IMF for the run Three different IMF have been implemented: *Chabrier singles* and *Chabrier systems* IMFs (Chabrier 2003) and *Kroupa* IMF (Kroupa 2001). For all cases we require that all masses are enclosed in the interval [0.001,2] $M_{\odot}$.

- The prior on the age is parameterized as a log-normal distribution with mean = 2 and variance = 1. This is in accordance with previous work focused on the distribution of ages in this cluster (Jeffries et al. 2011; Reggiani et al. 2011; Jerabkova et al. 2019). The accepted ages span a range of values of [0.5,100] Myr. To obtain a less coarse grid than the one provide by the single isochrones, we perform a 3D interpolation over the available parameter space.

- The prior on the extinction is evaluated through a kernel-density estimate of the distribution of extinctions obtained from Da Rio et al. (2012) , where the authors present a comprehensive census of the ONC stars in I band and two medium-filter bands ($\lambda \sim 753$ and 770 nm), deriving mass, age and in particular the extinction A_V for $\sim$ 1700 stars in this cluster. The possible range of values accepted for the A_V is [-1,15] magnitudes. We decide to allow negative A_V to provide a little more flexibility to the fitting routine due to the presence of uncertainties in the estimate of the observed color. Any source whose output resulted in a negative A_V has been carefully handled and inspected to ensure the goodness of these results ($\sim$ 60 sources).

[4] https://phoenix.ens-lyon.fr/Grids/BT-Settl

3.1.3. *Likelihood*

To be able to compare observations and simulations we utilize the different colors available in our joined catalog. In our case the likelihood is simply defined as:

$$\mathcal{L}(obs|\theta) = \prod_{i=0}^{N_{col}} e^{-0.5\times\left(\frac{col_{i,obs}-col_{i,mod}(\theta)}{ecol_{i,obs}}\right)^2} \quad (1)$$

where i runs through the different color of our survey (m435-m555, m555-m775,m775-m850 and m130-m139) and the labels *obs* and *mod* represent the observed and simulated colors (col) and errors (ecol). θ instead represent the whole set of fitting parameters (i.e. mass, extinction and age) that combined with the models provide the different $col_{i,mod}$.

3.1.4. *MCMC and posterior probabilities*

In order to derive the parameters that best describe our observations, we use *emcee*, the Foreman-Mackey (2016) Python implementation of the Goodman & Weare (2010) affine-invariant sampler. For a given set of parameters θ, we evaluate the corresponding value of the colors from the models and we than use the likelihood and prior discussed above to obtain the posterior probability distribution for θ. We ensure that the individual chains are properly converged and thinned to retain uncorrelated samples. The following convergence criteria is checked every 100 iterations:

- we ask the chain to be longer than 50 times the estimated auto-correlation time (τ_f, i.e. the number of steps needed before the chain loose information about it's starting properties);

- and that the estimate of τ_f changed by less than 1% since the previous check.

When this criteria are met, the routine exit the single star iteration loop and save the posterior distribution of the three parameters to a file. Then it moves to the next source, if present. Over all we perform a total of six different MCMC run, one for each combination of the 3 IMFs and 2 different reddening law summarized as follow:

- Kroupa, $R_v = 3.1$;
- Chabries singles, $R_v = 3.1$;
- Chabrier systems, $R_v = 3.1$;
- Kroupa, $R_v = 5$;
- Chabries singles, $R_v = 5$;
- Chabrier systems, $R_v = 5$;

For each of them, we obtained a different estimate for each of the three parameter (mass, A_V and age).

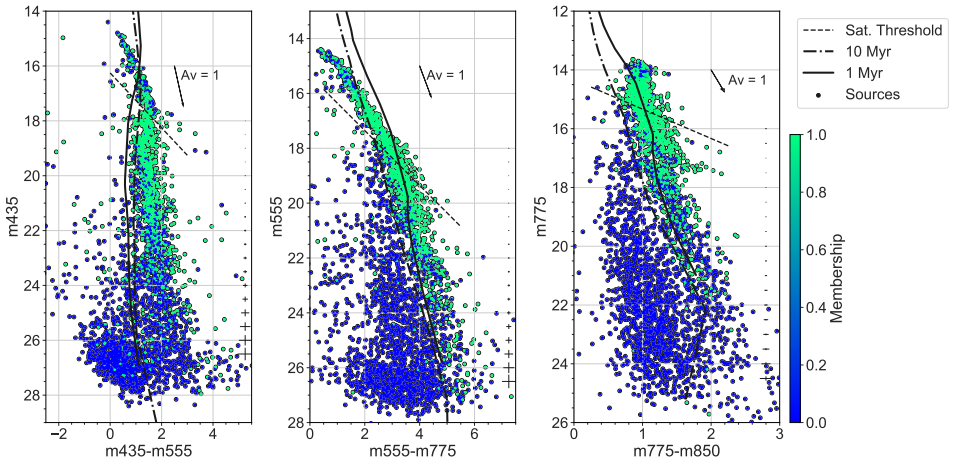

Figure 3. CMDs for filters F435W, F555W, F775W and F850LP construct from the new PSF photometry for the whole sample of the 3300 unique sources. The color code the membership of each source to the cluster (green) or background (blue). The diagonal black dashed line shows the locus of point where stars star to be dominated by saturated pixels as explained in the text, while the the black continuous and dash dotted line show the 1 and 10 Myr isochrone for each CMD. Typical error bars averaged for bin of magnitude are shown on the right of each plot.

3.2. *Membership selection*

The top plane of Figure 3 shows the (m435, m435-m555), (m555, m555-m775) and (m775, m775-m850) color magnitude diagrams (CMD) for all sources in the catalog, together with two BT-settl isochrones (1 Myr - continuous line; 10 Myr - dash dotted line) as well as the $A_V = 1$ vector, for comparison. The dashed diagonal line show the saturation threshold above which we consider a source saturated. The colors adopted in in this plot represent the membership (green) to the cluster, determined as follows:

- we matched the input ACS catalog with the WFC3 ONC catalogs from (Robberto et al. 2020). Taking advantage of the analysis performed there to select bona-fide cluster member (i.e. $log(BF) > 1$), we find in total 863 stellar-object matches;

- sources that are not matched are then labeled as cluster members if they posses a color redder than the 10 Myr isochrones in the two redder CMDs, if the source is detected in all of them. Otherwise, we consider only the single redder CMD.

This selection provides us with a total of 1078 bona-fide cluster members (isolated in the lower planes of Figure 3), or 2646 multiple detections in different visits.

Similar criteria have been adopted to the catalog of 57 candidate binaries, trimming them to just 15 cluster-cluster member pairs identified by KLIP.

3.3. *Binary chance alignment*

Once we establish a membership criteria, we can estimate the number of cluster-cluster chance alignment in our sample of binaries. To do so, we randomly extract from a uniform distribution positions inside a circular area around the center of the cluster (identified as the location of θ^1 Ori C) of radius $R \lesssim 100''$, where we expect the majority of chance alignment to happen due to the increase of density of stars toward the center of the cluster. Than, we count the number pairs having a "companion" closer than $2''$. Because these objects are randomly placed, their binarity is given only by chance. From this simple toy model we expect $\sim 6\%$ of chance alignments in this inner region ($R \lesssim 100''$) for wide binaries in the range of separation $0.5 - 2''$ and $\lesssim 0.5\%$ for close-in binaries ($\lesssim 0.5''$).

4. RESULTS

Building on the estimate of the three main parameters for each source detected in the catalog, we will discuss our results following the two main topics addressed in this work: isolated star (4.1) and binaries (4.2).

In the first part we will explore the estimated distributions of mass, extinction and age, outcome of our

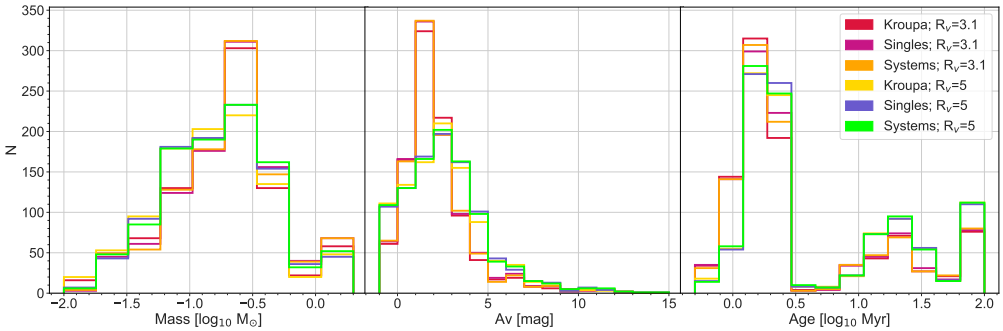

Figure 4. Cluster members mass (left), extinction (center) and age (right) histograms obtained through the Bayesian analysis described in Section 3.1. Each colored line refer to a different MCMC run performed changing either the IMF or the extinction law.

	Mass ($M_\odot$)	A_v (mag)	Age (Myr)
Kroupa; R_v=3.1	0.18 ± 0.13	1.67 ± 1.21	1.6 ± 0.53
Singles; R_v=3.1	0.21 ± 0.14	1.64 ± 1.27	1.68 ± 0.56
Systems; R_v=3.1	0.2 ± 0.13	1.65 ± 1.26	1.66 ± 0.56
Kroupa; R_v=5	0.15 ± 0.13	2.35 ± 1.92	1.78 ± 0.61
Singles; R_v=5	0.16 ± 0.14	2.41 ± 1.94	1.8 ± 0.63
Systems; R_v=5	0.16 ± 0.14	2.42 ± 1.94	1.79 ± 0.62

Table 2. Median values and standard deviations for the three histograms in Figures 4, after a 3σ cut selection has been performed on the samples.

Bayesian analysis for isolated cluster members only. Taking advantage of the multiple filters available in this survey, and in particular the F658N filter, we will also investigate the $H\alpha$ excess and mass accretion rate for these sources.

In the second part instead, we will focus on the 15 binaries detected through KLIP. After discussing the proprietaries of this small sample of binaries, we will combine them with well resolved binaries already present in the input catalog and with the binaries presented in Strampelli et al. (2020a) from WFC3-IR data to compare results and establish more general trends for the population of binaries in the ONC.

The implication of those results will be addressed in more details in Section 5 instead.

4.1. *Isolated stars*

4.1.1. *Mass, extinction and age distribution*

The derived mass, extinction and age for each cluster member are provided in Table A2 (in the Appendix), along with the accretion properties of each sources (see later Section 4.1.5).

Having derived mass, extinction and age for each cluster member, we can start our analysis by assessing their average values and general distributions. Figure 4 shows the histograms of the three parameter distributions, whereas Table 2 lists the median and standard deviation of each sample after a 3σ cut have been applied. Overall there is good agreement in each family of distribution (mass, A_V, Age) over the different parameters for our Bayesian analysis (IMFs and reddening laws). Changing the IMF as well as the extinction laws does not strongly impact the overall distributions, even though $R_v = 5$ seems to produce more shallow distributions compared to $R_v = 3.1$ in both the mass and A_v parameter. In summary, the parameters that characterize the main properties of the ONC depend on the assumed IMF and reddening law. For each of them we therefore have a range of values, i.e. a median mass between $0.15 - 0.21\ M_\odot$, a median extinction A_V between $1.64 - 2.42$ magnitudes and a median age between $1.6 - 1.8$ Myr. These values are all in good agreement with previous estimates (e.g. Da Rio et al. 2012). In view of these results we can not make any claim of a real difference between choosing a different reddening law or IMFs (at least at this level of detail). We will then consider the mass, A_V and ages resulting from the Chabrier *singles* IMF, $R_v = 3.1$, as study case for the rest of the paper.

As introduced in Section 3.1.2, we allow the extinction to probe negative values during the MCMC run to better fit the observables to the model and allow some degree of uncertainties in the process (both from our measurement and the models). For our selection of cluster members, between $\sim 2 - 3\%$ sources (depending on the selected MCMC run) resulted at the end with an estimated $Av < 0$. Even though statistically insignifi-

cant if compared to the whole sample, we decide to reject those sources from the rest of the analysis.

The age distribution shows the expected peak around a few Myr (~ 2). There are, however, two detectable secondary peaks at ~ 22 Myr and 90 Myr. Overall, we can associate to these peaks $\sim 62\%$ of our sources with an age below ~ 5 Myr, $\sim 26\%$ between the $\sim 5-50$ Myr and only $\sim 12\%$ above this value. An age estimate of many tenths of Myrs is suspicious for bonafide ONC cluster members. Even though previous work on the ONC (e.g. Prosser et al. 1994; Hillenbrand 1997; Slesnick et al. 2004) highlighted the existence of a apparently older populations, some of them could probalby belong to a miss-labeled foreground population laying somewhere on the line of sight toward the ONC (Alves & Bouy 2012; Bouy et al. 2014). Bouy et al. (2014), for example, found the presence of a large foreground population towards the Orion A cloud, with an age spread between $5-10$ Myr. This population contains several distinct subgroups and stretches across several degrees in front of the Orion A cloud. On the other hand, Robberto et al. (2020) demonstrate that the expected contamination from those foreground populations in his WFC3-IR field of view is almost negligible. Due to the similarity in the footprint of the ACS and WFC3 surveys in the two Treasury program we are considering in this work, we also expect contamination from those sources in our data to be small. On the other hand, uncertainties in the measurements, presence and orientation of disk, variability, extinction, atmospheric spots etc. can all contribute to a spread in luminosity and in turn the observed spread of ages (Reggiani et al. 2011). Due to all these uncertainties, we decide to reject any sources whose estimated age is $\gtrsim 5Myr$ from any future analysis concerning masses, ages and derived quantities (i.e. L_{acc} e $\dot{M}_{acc}$, see Section 4.1.4). We will come back again to this point of the age spread later on in Section 5.1, but more work is clearly required to unveil the true nature of those sources.

4.1.2. *Hertzsprung–Russell Diagram*

Having derived through Bayesian fitting the mass, extinction and age of each source, we can now determine the star luminosity ($L_\star$) and effective temperature ($T_{\rm eff}$). Because the best fit for mass, extinction and age has been performed comparing the measured vs. model magnitude differences (colors) and not the magnitudes themselves, our results are independent on the assumed distance of the cluster, besides being generally immune to photospheric variability that may compromise the estimates derived using non-simultaneous observations.

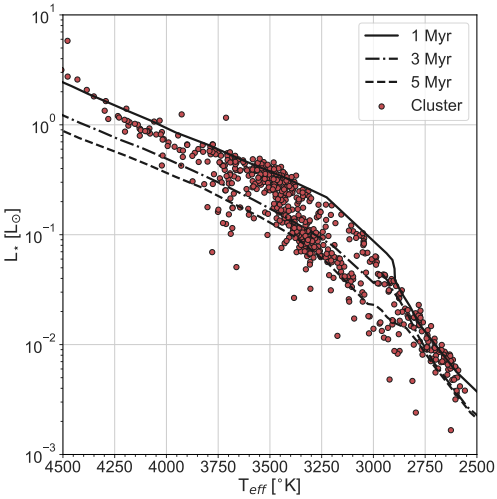

Figure 5. HRD of the ONC sources (red). Luminosity and temperature are derived from the best fit of the models. Three isochrones (1, 10, 50 Myr) are shown for comparison.

When we determine $L_\star$, we observed a discrepancy between the stellar magnitudes provided by the models (associate to the best-fit colors) and the actual magnitudes that one would obtain just dereddening the measured magnitudes for the star. We converted this magnitude difference directly into a correction to the luminosity provided by the best-fit model. In this way, the colors provide us with an estimate of the stellar parameter, in particular $T_{\rm eff}$, but the magnitudes and the reddening provide us with $L_\star$. This mimics the standard process of determining $T_{\rm eff}$ from spectroscopy and $L_\star$ from photometry (e.g. Hillenbrand 1997).

The results of this procedure are shown in Figure 5, where we present the Hertzsprung–Russell Diagram (HRD) for the selected cluster sources. Three isochrones of 1, 3 and 5 Myr are also shown for comparison (see Section 3.1.1). The most striking feature of this HRD is the different distribution above and below $T \sim 3500°K$. Below this value we observe a large spread in luminosity ($T_{\rm eff} \lesssim 3500$ °K, $\sigma log(L_\star/L_\odot) \sim 0.1$) that is not present in sources of higher temperature ($T_{\rm eff} > 3500$ °K, $\sigma log(L_\star/L_\odot) \sim 0.25$).

The cause of this luminosity spread can be most probably found in the fact that at $T \sim 3500°K$ the H_2O water vapor starts to appear in absorption, i.e. we record a negative value for the WFC3-IR color m130-m139. The presence of H_2O provides a strong constraint on the ef-

fective temperature of the star, and therefore plays a significative role controlling the age estimate provided by our Bayesian fit. Conversely, the age estimate for sources with $T \gtrsim 3500°K$ is less constrained and therefore mostly driven by the prior on the age that we have set as a log-normal distribution with $\mu = 2$ Myr.

As anticipated earlier, in Section 5.1 we will discuss in more details the implications of this luminosity spread.

4.1.3. *Hα luminosity*

The continuum excess emission in young stellar objects (YSOs) is easily detected as Balmer continuum emission (see for example Gullbring et al. 1998; Herczeg & Hillenbrand 2008; Rigliaco et al. 2012; Alcalá et al. 2014; Manara et al. 2016a, and reference there in). To measure the excess in $H\alpha$ we followed a similar approach to De Marchi et al. (2010), but profiting on the multiple bands available in the survey. We define the excess in $H\alpha$ emission as follow:

$$\Delta H\alpha = m658^{obs} - m658^{mod} - \Delta \tag{2}$$

where the superscript *obs* refer to the de-reddened observed magnitudes in filter F658N, while the *mod* refer to the corresponding magnitudes from the models once mass, and age are established for the source and a distance of $\simeq 400$ pc (Kuhn et al. 2019) have been assumed for the cluster. Any uncertainties in the estimate of the distance of the cluster, as well as on the model's parameters, are factored in the Δ as follow. The Δ represent the best rigid translation one has to apply to the photometry of the specific source to match *observed* magnitudes and the models. We evaluate it as the weighed average of the differences between each filter magnitude and corresponding value from the model:

$$\Delta = \frac{\sum_i w_i x_i}{\sum_i w_i} \tag{3}$$

where $x_i = mag_i^{obs} - mag_i^{mod}$ and $w_i = (\sigma_i^{obs})^{-2}$ for i in [F435W, F555W, F775W, F850LP]. This operation brings the *observed* magnitudes to match the *references* in average and in turn to the recognition of any excess in F658N measurements compare to the model. We decide to apply a threshold to the $\Delta H\alpha$ excess and consider only the sources whose $\Delta H\alpha \geq 4\sigma$. Moreover, this excess in $H\alpha$ can be translated in $H\alpha$ equivalent width ($W_{eq}(H\alpha)$) through the following relationship (see eq. 3 and 4, De Marchi et al. 2010):

$$W_{eq}(H\alpha) = RW \times \left[1 - 10^{-0.4\times(H\alpha - H\alpha^c)}\right] \tag{4}$$

where RW=74.96 is the rectangular width of the filter (see De Marchi et al. 2010, Table 4). We exploit the W_{eq} as an additional layer of selection, discarding any sources whose $W_{eq} \lesssim 10$ Å. The $H\alpha$ excess for the selected sources is then converted in $H\alpha$ emission line luminosity ($L_{H\alpha}$) thought the photometric zero-point and the inverse sensitivity (PHOTLAM; see Table 1).

4.1.4. *Accretion luminosity and mass accretion rate*

The mass accretion rate is a fundamental parameter to study pre-main sequence (PMS) stellar evolution and planet formation as well as to track and understand the evolution of accretion disks around young low-mass stellar ($M \simeq 0.2\ M_\odot$) and young substellar objects (YSOs). $\dot{M}_{acc}$ also set important constrains on disk evolution models (Hartmann et al. 1998). From an observational point of view, $\dot{M}_{acc}$ can be evaluated by measuring the excess of flux, compared to the phosphoric level, due to the release of accretion energy in the form of continuum and lines emission and stellar properties (Gullbring et al. 1998; Hartmann et al. 1998). L_{acc} can be easily obtain from the empirical relation L_{line} vs L_{acc} (e.g. Natta et al. 2006; Rigliaco et al. 2011; Fang et al. 2013; Herczeg & Hillenbrand 2015; Manara et al. 2015, 2016b; Alcalá et al. 2017).

The energy released by magnetospheric accretion process (i.e. the energy loss per unit of time of the accretion energy, or accretion luminosity; L_{acc}) contribute to the ionization and heating of the circumstellar gas (Hartmann et al. 1998, 2016). The measured $H\alpha$ luminosity that is produced during this process can than be related to the L_{acc} through the following relation:

$$logL_{acc} = a \times log(L_{H\alpha}/L_\odot) + b \tag{5}$$

where the two coefficients are the revised $L_{acc} - L_{H\alpha}$ coefficients a= 1.13±0.41 and b= 1.74±0.19 from Alcalá et al. (2017) (Table B.1). The final mass accretion rate ($\dot{M}_{acc}$) can be estimated from the accretion luminosity, inverting the free-fall equation that links the luminosity feedback released in the impact of the accretion flow with the rate of mass accretion:

$$L_{acc} \simeq \frac{GM_\star \dot{M}_{acc}}{R_\star}\left(1 - \frac{R_\star}{R_{in}}\right) \tag{6}$$

where $R_\star$ and $R_{in} = 5\ R_\star$ are the star and inner-disc radius (Gullbring et al. 1998; Hartmann et al. 1998). Combining equation 5 and 6 and rearranging the terms we obtain:

$$\begin{aligned} log\frac{\dot{M}_{acc}}{M_\odot yr^{-1}} &= -7.39 + log\frac{L_{acc}}{L_\odot} + log\frac{R_\star}{R_\odot} - log\frac{M_\star}{M_\odot} \\ &\simeq (-6.26 \pm 0.05) + log\frac{L_{H\alpha}}{L_\odot} + log\frac{R_\star}{R_\odot} - log\frac{M_\star}{M_\odot} \end{aligned} \tag{7}$$

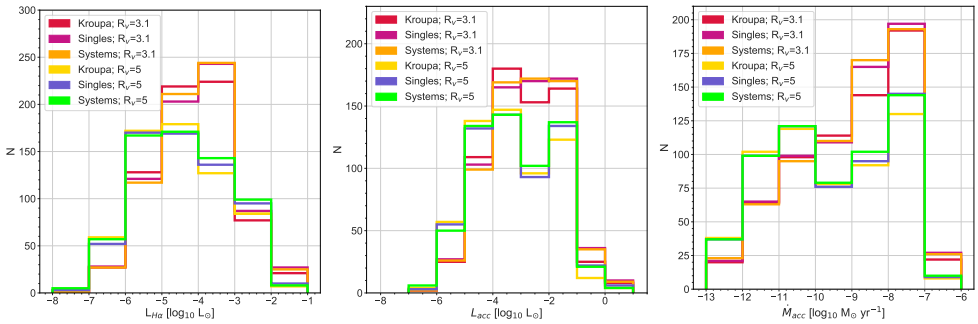

Figure 6. Histograms of the $H\alpha$ luminosity (left), accretion luminosity L_{acc} (center) and mass accretion rate $\dot{M}_{acc}$ (left) for the different parameters employed in our Bayesian analysis

4.1.5. *General accretion properties of the whole sample*

As introduced above in Section 4.1.1, the estimated accretion properties of the sample are provided in Table A2. Figure 6 shows the histograms for $L_{H\alpha}$, L_{acc} and $\dot{M}_{acc}$ discussed in the precedents paragraphs. Because each of them ultimately depends on the estimate of the continuum in F658N, and in turns this depends on on the assumed model parameters, six histograms are shown in each figure, one for each combination of IMF and reddening law employed in the precedent Bayesian analysis. The 3σ cut median value and standard deviation for each one of these collection of histograms is summarized in Table 3 instead.

Overall, there is a slight preference for these estimates to cluster around similar median values for similar reddening law (i.e. $R_V = 3.1$ or 5), even though they remain also perfectly compatibles with each others. Similar to the cases of mass, extinction and age we described in Section 4.1.1, we can not make any claim of a real difference between choosing a different reddening law or IMF (at least at this level of detail) for what concern the $L_{H\alpha}$, L_{acc} and $\dot{M}_{acc}$ distributions. We will then consider the results from the Chabrier *singles* IMF, $R_v = 3.1$, as study case for the rest of the paper.

Figure 7 shows the relation between L_{acc} and $L_\star$ for our selected sample. The majority of ONC sources in our sample fall below the $L_{acc} = 10^{-1} \times L_\star$ gray dashed line, with very few of them within this and the $L_{acc} = L_\star$ boundary, and only a couple above it. There is no evidence either of strong accreting sources at low stellar luminosity (the majority of sources with $0.01 \lesssim L_\star \lesssim 1$ fall behind the line $L_{acc} = 0.1\ L_\star$). The 3σ cut average estimated uncertainties on the $logL_{acc}$ is ~ 0.31. A linear fit to the data using RANSAC (Fischler & Bolles 1981) *scikit-learn* python module (Pedregosa et al. 2011) as been applied to the data. The fit have been performed a thousand of time, where during each iteration ten thousand trials where performed by the RANSAC routine to establish the best fit parameters, and a final median and standard deviation have been extracted from the overall output distributions of parameters, providing the following relation:

$$logL_{acc} = (2.07 \pm 0.29)\, logL_\star - (0.95 \pm 0.13) \qquad (8)$$

Compared to other star forming regions, the results obtain for the ONC appear to be steeper than the $\rho-$Ophiuchi (Manara et al. 2015), $\sigma-$Orionis (Rigliaco et al. 2011), Chamaeleon I (Manara et al. 2016b) or Lupus (Alcalá et al. 2017), but still compatible within 3σ. Even though the best fit derived from our data for this cluster is the one provided by Eq. 8, in the low-L_{acc} low-$L_\star$ portion of the plot, the data seem to suggest the presence of a small group of stars that depart from this general trend. This second population appears systematically brighter than the fit for the main ONC population, but in very good agreement with the trend found in Chamaeleon I (Manara et al. 2016b, purple dashed line in Figure 7).

	$logL_{H\alpha}$ ($logL_\odot$)	$logL_{acc}$ ($logL_\odot$)	$log\dot{M}_{acc}$ ($logM_\odot\ yr^{-1}$)
Kroupa; R$_v$=3.1	-3.53 ± 0.91	-2.25 ± 1.03	-8.06 ± 0.87
Singles; R$_v$=3.1	-3.4 ± 0.85	-2.1 ± 0.96	-8.05 ± 0.78
Systems; R$_v$=3.1	-3.44 ± 0.86	-2.15 ± 0.98	-8.09 ± 0.8
Kroupa; R$_v$=5	-4.08 ± 1.19	-2.87 ± 1.34	-8.77 ± 1.46
Singles; R$_v$=5	-3.89 ± 1.19	-2.65 ± 1.35	-8.7 ± 1.44
Systems; R$_v$=5	-3.87 ± 1.2	-2.64 ± 1.36	-8.71 ± 1.44

Table 3. Median values and standard deviations oh the $logL_{H\alpha}$, $logL_{acc}$ and $\log(\dot{M}_{acc})$ histograms (Figure 6). N represent the number of sources after applying a 3σ cut selection to the specific sample.

	N	M_p	M_c	A_V	Age	Separation
	(–)	($M_\odot$)	($M_\odot$)	(mag)	(Myr)	(arcsec)
KLIP	15	0.032-1.39	0.006-1.00	-0.9-11.5	0.7-100	0.12-0.34
WIDE	67	0.026-1.93	0.014-0.55	-0.9-13.7	0.7-100	0.23-1.71
All	82	0.026-1.93	0.006-1.00	-0.9-13.7	0.7-100	0.23-1.71

Table 4. Break down the ACS Master catalog.

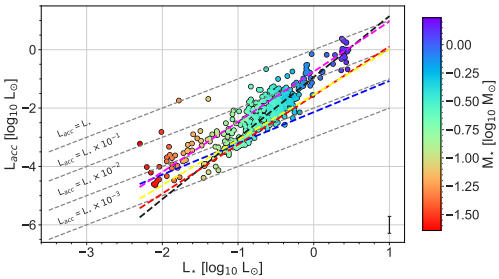

Figure 7. Accretion luminosity (L_{acc}) as a function of stellar luminosity ($L_\star$) for ONC sources, color-coded by their estimated mass assuming a Chabrier *singles* IMF and a reddening law $R_v = 3.1$. The thick black diagonal dashed line represent the best fit obtained from the data (equation 8). As comparison, the best fits for different star forming region are shown: $\rho-$Ophiuchi (Natta et al. 2006) and $\sigma-$Orionis (Rigliaco et al. 2011) as dashed red and blue lines, while Chamaeleon I (Manara et al. 2016b) and Lupus (Alcalá et al. 2017) are drawn as magenta and yellow dashed line. The overall 3σ cut average error bars are shown in the bottom right portion of the plot for comparison.

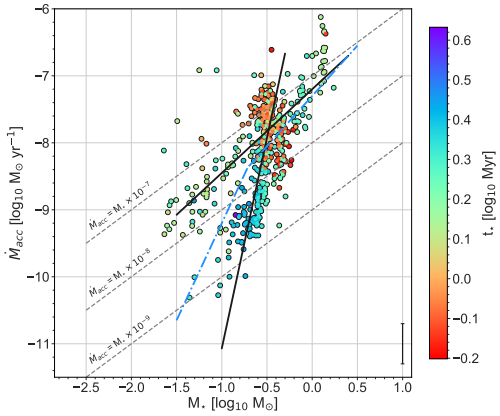

Figure 8. Mass accretion rate ($\dot{M}_{acc}$) as a function of stellar mass ($L_\star$) for ONC sources. The thick black diagonals line shows the two portion of the broken power-law fit obtained for this population with the dashed portion of it showing the ideal extension of each line. As comparison, the blue dash-dotted line represent the power-law theoretically predicted by Vorobyov & Basu (2009). The color code the best fit for the Age of each single sources from our Bayesian analysis. The overall 3σ cut average error bars are shown in the bottom right portion of the plot for comparison.

Figure 8 shows instead the $\dot{M}_{acc} - M_\star$ relation for our selected sample. The 3σ cut averaged estimated uncertainty on $log\dot{M}_{acc}$ is ~ 0.31. Similar to Figure 7, two populations emerge from this plot: 1) one almost parallel to the $\dot{M}_{acc} \sim M_\star \times 10^{-7}$, 2) and a second one, far more steeper, departing from the precedent at $M_\star \lesssim 0.3\ M_\odot$ and covering ~ 3 dex in $\dot{M}_{acc}$, down to $\sim M_\star \times 10^{-10}$. The best fit describing those populations are, for population 1):

$$log\dot{M}_{acc} = (1.26 \pm 0.0.15)\, logM_\star - (7.2 \pm 0.11) \quad (9)$$

and for population 2):

$$log\dot{M}_{acc} = (6.23 \pm 2.38)\, logM_\star - (4.77 \pm 0.11) \quad (10)$$

These fits are shown in the plot as two continuous thick black lines with their intercept point at $\sim 0.3\ M_\odot$. As a comparison, the theoretical relationships predicted by Vorobyov & Basu (2009) are overplotted as a broken blue dash-dotted line. Overall, for $M_\star \gtrsim 0.3\ M_\odot$, our best fit slope for population 1) agrees very well with Vorobyov & Basu (2009) theoretical predictions , while below this mass limit there is an evident discrepancy. We also compare our fits with the results provided by Natta et al. (2006); Rigliaco et al. (2011); Manara et al. (2016b) for $\rho-$Ophiuchi, $\sigma-$Orionis and Chamaeleon I, finding again compatible slopes only for the fit obtained for the population 1).

4.2. *ONC ACS Master Binary Catalog*

Understanding the properties of binary systems (i.e. coeval stars born in the same environment and metallicity, but generally different mass) provide a different tool to unveil fundamental insight on the evolution and origin of stars. Low mass companion, for example, may form like stars through an early fragmentation and gravitational collapse or like planets in a cirumstellar disk, moving to wider orbits through migration or scattering (Spiegel et al. 2011; Duchêne & Kraus 2013).

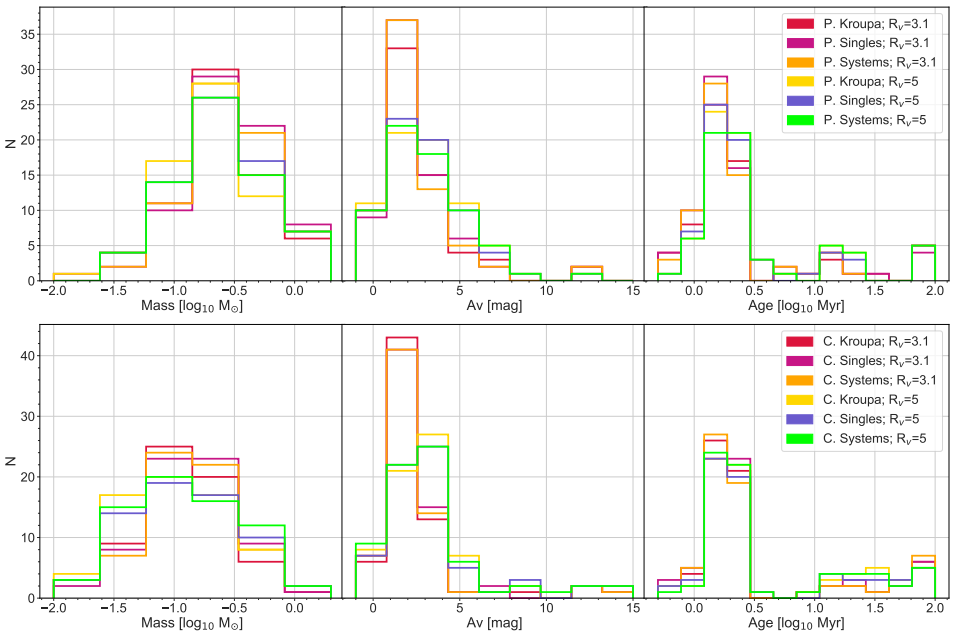

Figure 9. Mass (left), extinction (center) and age (right) histograms for cluster's members binaries. Each colored line refer to a different MCMC run performed changing either the IMF or the extinction law.

	WC	KC	SC	WB	KB	SB
Reipurth et al. (2007)	34	11	4	31	5	1
De Furio et al. (2019)	2	1	8	1	2	0
Strampelli et al. (2020a)	41	13	32	0	0	0

Table 5. Match between the ONC Master catalogue and other ONC binary catalogs from literature. The matches with our Wide: W, KLIP: K and Singles:S, for both Cluster: C and Background: B selection, are listed for each authors

Here, we introduce the ONC ACS Master catalog of binaries as the combination of the binaries obtain through KLIP analysis (often simply referred to as KLIP binaries - K) and the well resolved multiples already present in Robberto et al. (2013) catalog (or simply WIDE binaries - W). A break down of the ONC ACS Master catalogue is shown in Table 4, where the total number of pairs available, the range of masses (i.e. primary mass M_p and companion mass M_c), extinctions (A_V), ages and separations are printed for the two main component of the catalog (KLIP and WIDE) and for the catalog as whole. In Table 5 we show the match between the ACS Master catalogue and a few of previously known catalogs of binaries in the ONC in similar ranges of mass and separations (Reipurth et al. 2007; De Furio et al. 2019; Strampelli et al. 2020a), detected from similar *HST*/ACS and *HST/WFC3-IR* data. Once we subtract from our Master catalogue the binaries already known in the literature in similar ranges of masses and separations (i.e. Reipurth et al. 2007; Robberto et al. 2013; De Furio et al. 2019; Strampelli et al. 2020a) we end up with 5 new bona-fide cluster binaries obtain from our KLIP analysis

Table A3 and A4 in the appendix, shows a small sample of the photometry obtained for the ONC ACS Master catalog, where the only ternary detected (already present in the input catalog) is listed as two separate binary system with a common hosting star. The complete gallery of KLIP and WIDE binaries are presented in Figures 10 and 11.

Table A5 instead, shows the outcome of the Bayesian analysis for our primary stars (same outcome as the isolated star) and the derived parameters for the candidate companions (i.e. mass, extinction, age, temperature and luminosity) as explained below. Because of the uncertainties related to the photometry performed on KLIP residual, we decide to not perform MCMC simulation

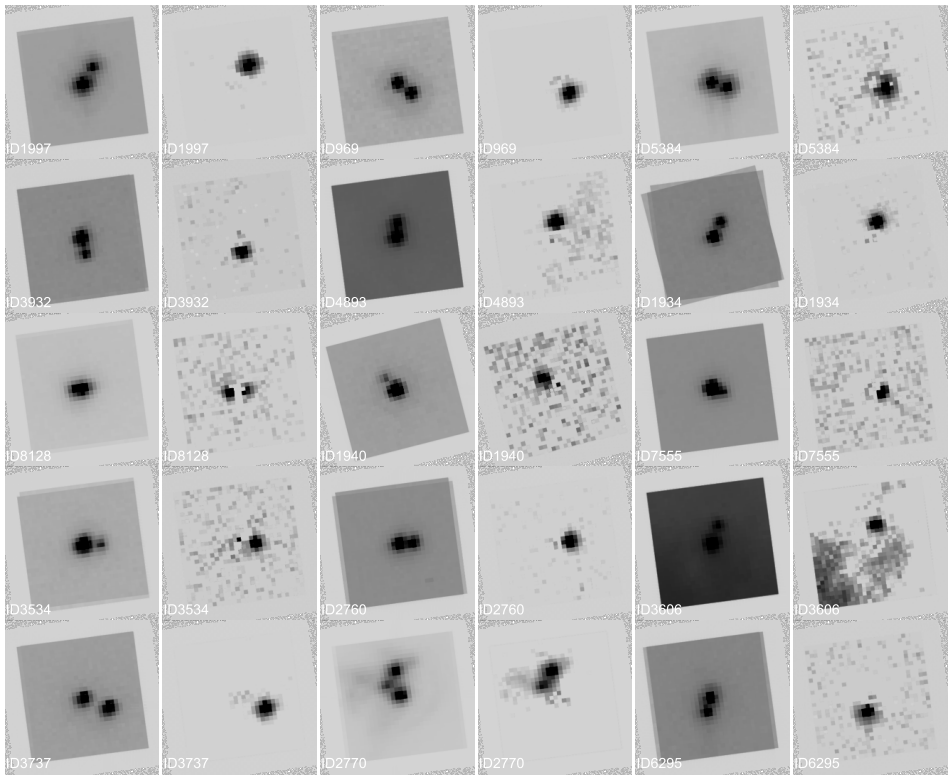

Figure 10. ONC KLIP cluster binaries. The columns alternate the tile as appear in the *HST*/ACS data and the residual tile after KLIP analysis have been performed. North is up, east is left. The base of each tile is $\sim 2''$.

and Bayesian analysis on the sample of candidate companions, instead we evaluate the delta magnitude in each filter where the putative companion have been detected, and from this delta and the primary mass, temperature and luminosity, we derive the filter-related corresponding quantities for the companion

Similar to Section 4.1.1 about isolated stars, we present in Figure 9 the histograms of the three parameters (mass, extinction and age) for primaries (top panel) and companions (bottom panel) estimated as explain above. The median value of each parameter and the corresponding 1-σ uncertainty are summarized in Table 6.

4.2.1. *ACS/WFC3-IR Union Master catalog*

From this point forward, we will complement the ACS Master catalog of binaries with the binaries previously detected in Strampelli et al. (2020a), where for binaries detected in both surveys, we will keep the detection from the ACS Master catalog where possible, given the larger wavelength coverage provided by the ACS survey compared to the WFC3IR one to estimate the mass, age and extinction. We will refer to this new catalog simply the *union* master catalog, comprising a total of 119 cluster binaries, covering an overall range of separations $0.12 - 1.95''$. Due to the small variations between the different MCMC simulations, we will follow the example set for the isolated stars, assuming the output of the Chabrier Singles, R_v=3.1 estimates for these systems. 11 pairs in this sample are missing an estimate of the mass for either the primary or the companion, mainly due to problem with producing a photometry reliable enough to correctly estimate the star parameters. Luckily, 3 out of these 11 pairs where also detected in the WFC3-IR survey, so we kept, for those objects, the measurements provided in the WFC3-IR master catalog,

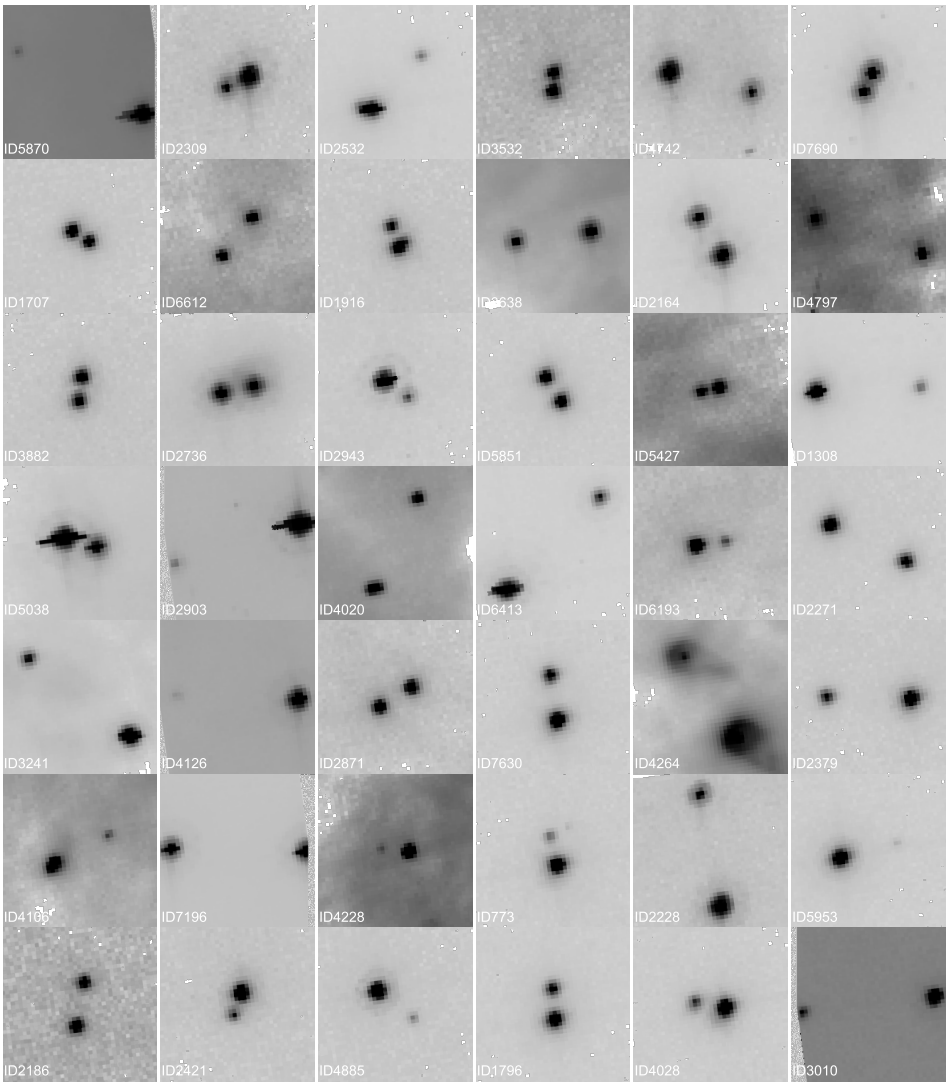

Figure 11. ONC WIDE cluster binaries. Each columns show in *HST*/ACS data for binaries already presented in Robberto et al. (2013). North is up, east is left. The base of each tile is ~ 2".

leaving only 8 detected binaries without a mass estimation.

Similar to the case of isolated star, we inspected the extinction and age distributions for all the binaries in our sample, selecting only the pairs for which we obtain a reliable enough estimate of their stellar parameters. We will limit the overall sample to only these systems for any analysis concerning the mass, age and derived quantities (such as L_{acc} and $\dot{M}_{acc}$). This selected sample, covering a range of masses $M_p = 0.015 - 1.6\ M_\odot$ and $M_c =$

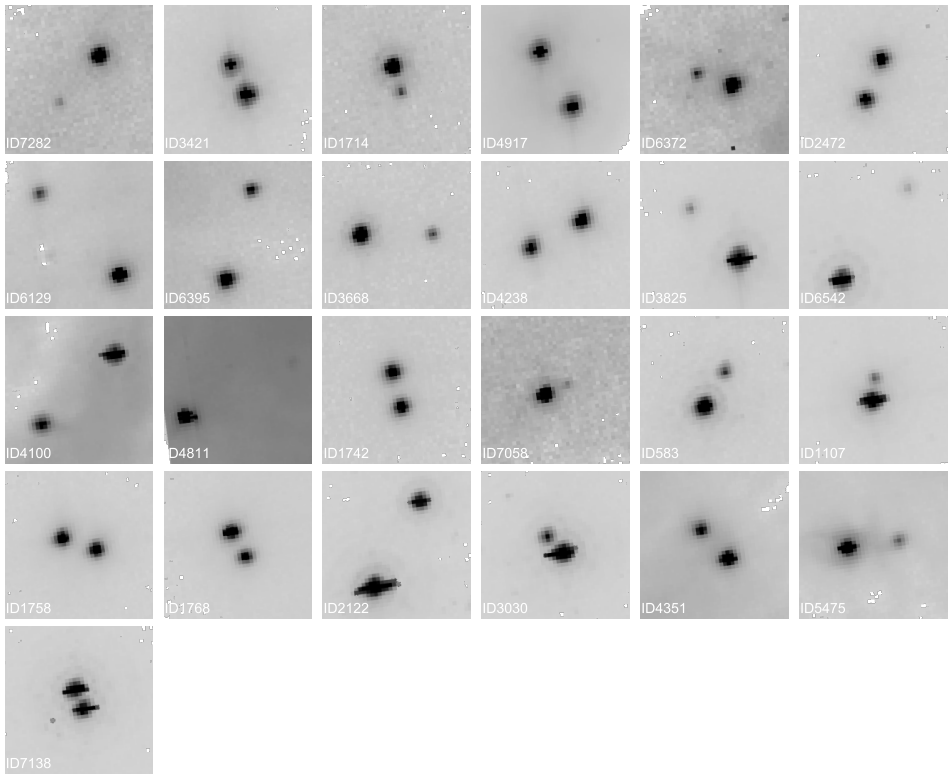

Figure 12. Same as 11

$0.004 - 1\ M_{\odot}$, is shown in Table 7 binned by both mass of the primary and companion (stellar, brown dwarf or BD and planetary mass).

In the range of masses and separations ($0.12 - 1.95''$) inspected by this work, our data seem to suggest a very high frequency of BD companions, i.e. $\sim 35\%$ of the detected companions are classified as BD from our Bayesian Analysis. For field objects, an almost complete absence of close-in (< 3 AU) BD companions is well documented (e.g. the "brown dwarf desert"; Marcy & Butler 2000; Grether & Lineweaver 2006; Triaud et al. 2017), whereas Gizis et al. (2001) found evidence for a larger fraction ($\gtrsim 5\%$) of BD companions at wide separations (> 1000 AU). Our survey probes an intermediate distance range and a much earlier stage. Indeed, the high frequency we find could be ephemeral if the majority of wide binary systems is not going to survive future encounters and the dynamical evolution of the cluster.

In Figures B1, B2, B3 and B4 we show the cross match between the *HST*/WFC3-IR ONC Master catalogue (Strampelli et al. 2020a) and the *HST*/ACS one. Each row alternate binaries from ACS with the matched binary as observed in WFC3-IR. Each columns instead, alternate the original input data and the residual after KLIP analysis (if performed). Over all we confirm a total of 12 binaries we previously detected in WFC3-IR filters through KLIP (over a total of 39 detections)

4.2.2. *Completeness correction*

Thanks to the completeness analysis provided in Strampelli et al. (2020a) for the WFC3-IR data, we computed the underlying distribution of separations by evaluating the fraction of missing binaries. This provided us with an estimate for the completeness of the *union* Master catalog, comparing the detections in the ACS master catalog to the WFC3 *completed* master catalog over similar ranges of separations. We estimate a com-

	Mass ($M_\odot$)	A_v (mag)	Age (Myr)
P. Kroupa; R_v=3.1	0.21 ± 0.15	1.76 ± 1.24	1.63 ± 0.51
P. Singles; R_v=3.1	0.26 ± 0.17	1.61 ± 1.36	1.62 ± 0.55
P. Systems; R_v=3.1	0.26 ± 0.17	1.55 ± 1.3	1.63 ± 0.54
P. Kroupa; R_v=5	0.17 ± 0.13	2.68 ± 2.12	1.75 ± 0.6
P. Singles; R_v=5	0.22 ± 0.15	2.66 ± 2.12	1.77 ± 0.64
P. Systems; R_v=5	0.18 ± 0.14	2.67 ± 2.21	1.77 ± 0.64
C. Kroupa; R_v=3.1	0.11 ± 0.11	1.81 ± 0.87	1.7 ± 0.43
C. Singles; R_v=3.1	0.13 ± 0.13	1.79 ± 0.9	1.73 ± 0.51
C. Systems; R_v=3.1	0.12 ± 0.13	1.72 ± 0.91	1.73 ± 0.49
C. Kroupa; R_v=5	0.08 ± 0.09	2.71 ± 1.56	1.87 ± 0.51
C. Singles; R_v=5	0.08 ± 0.12	2.68 ± 1.42	1.73 ± 0.55
C. Systems; R_v=5	0.1 ± 0.14	2.67 ± 1.59	1.81 ± 0.52

Table 6. Median values and standard deviations for the three histograms in Figures 9, after a 3σ cut selection has been performed on the samples.

		Primary	
		Star	BD
$Companion_{Union}$	Star	44	-
	BD	25	2
	Planet	1	3

Table 7. Summary of detections in the *union* master catalog.

pleteness of $\sim 28\%$ for separation $\lesssim 0.2''$, 78% between $\sim 0.2'' - 0.4''$ and 1 otherwise.

4.3. *Separation distribution*

Figure 13 show the separation distribution function for both ACS/WFC3-IR samples and their joined catalog, where the top panel show a comparison between the two samples (blue/red) while the bottom panel shows the overall distribution for the *union* Master catalogs (purple) and the completeness correction we estimated for this catalog as a dashed cyan histogram. This plot (as already reported by Reipurth et al. 2007; Strampelli et al. 2020a), show two clearly separated populations: one large population with separation $\lesssim 0.5''$, and one minor but much wider

Taking into account the considerations made in Section 3.3, we estimate a number of chance alignment in the *union* Master catalog as ~ 13 within a distance from the center of the cluster of $\lesssim 100''$. The large majority of them are expected to posses separation bigger than $\sim 0.5''$, with a negligible contribution from close-in binaries. When we inspect our sample of binaries within that distance, we find 17 binaries with separation $\gtrsim 0.5''$. We decide than to select even more our catalog, rejecting these binaries as most probable chance alignment between cluster stars.

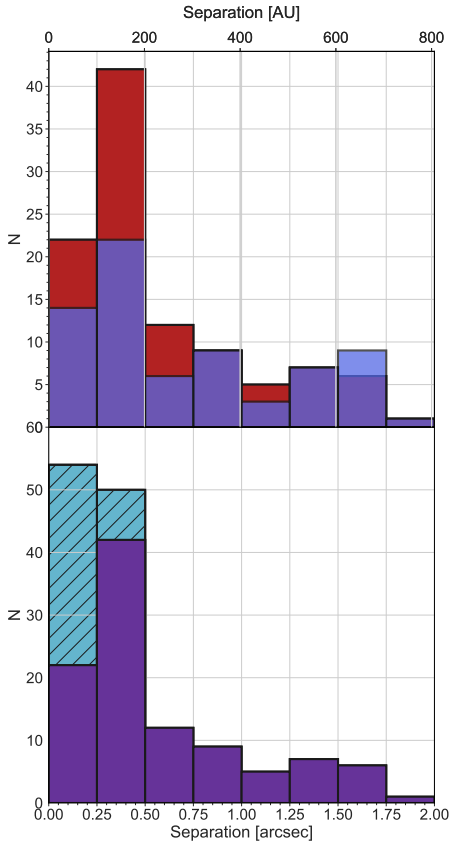

Figure 13. Top: Separation distribution for our two full samples of candidates (blue: ACS, red:WFC3-IR) in bins of 0.25". Bottom: Separation distribution for the selected *union* master catalog. The dashed cyan portion of the histogram shows the expected completeness correction for the sample.

Figure 14 shows the cumulative distribution, from this selected *union* master catalog, for wide (blue) and close (red) binaries as a function of their distance from the center of the cluster and their ratio (wide over close, panel on the right). As already shown in the past (e.g. Reipurth et al. 2007), the plot on the left in Figure

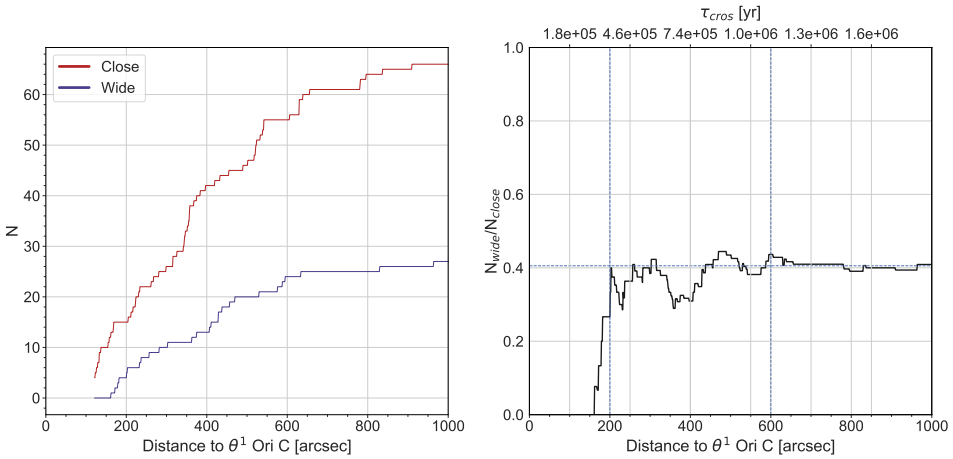

Figure 14. Left: Distance distribution from θ^1 Ori C from the *Union* Master catalog for Wide (blue) and close (red) binaries. Right: Same as left where we show the ratio of wide over close binaries. The top axis in this panel shows approximately the cluster crossing time τ_{cross} from specific distances. The two vertical lines shows approximately the point past which the ratio start becomes flat (at $\sim 200''$) and when it truly flatten out (at $\sim 600''$), while the horizontal one shows the average value of the ratio past this point (~ 0.4).

14 shows some very interesting trends. For separations from the center from the cluster $\lesssim 200''$ we observe a steep rise in the ratio of wide over close binaries, at which point it becomes almost flat (with an average ratio of ~ 0.4). Interesting, our selected cluster-cluster chance-alignment free sample of binaries suggest this transition to happen at about half the distance than the one obtained by Reipurth et al. (2007) (i.e. $\sim 460''$). We will come back later to this plots and on his implication on the history of the cluster.

4.4. *Mass ratio distribution*

Figure 15 shows the mass ratio vs primary mass for ONC selected *union* binary master catalogs. Overall, we are able to populate almost homogeneously the star-star as well as the star-BD parameter space of this plot both for high and low mass ratios. Figure 16 instead, shows violin plots for the mass ratio distributions of both our ACS (blue) and WFC3 (red) Master catalogs apart (left) and the selected *union* master catalog (purple pipes, on the right). We see a general tendency of ACS detection to supply mostly high mass-ratio binaries while the WFC3-IR detection contribute to the total sample principally through low mass-ratio binaries (as expected by saturation/detection threshold arguments). The selected *union* distributions on the right has a median $q \sim 0.45$ (both for the overall sample and the star-like primaries) and ~ 0.35 for BD mass primaries, still pointing toward a slight trend towards low-mass companions.

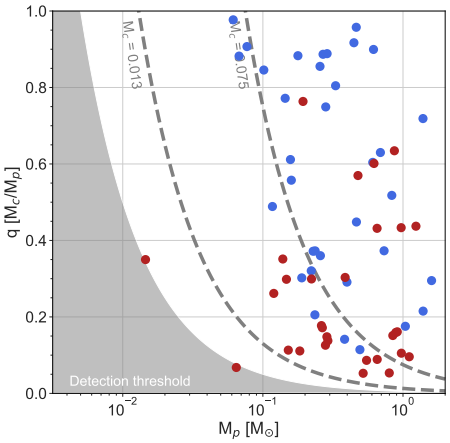

Figure 15. Mass ratio distribution as a function of primary mass objects for the *Union* Master catalog. The sources are color-coded by their original catalog (blue: ACS - this work, red: WFC3-IR - Strampelli et al. (2020a)). The two grey dashed and dot dashed lines show the values of q for which $M_c = 0.075$ and $M_c = 0.013$ as a function of M_p.

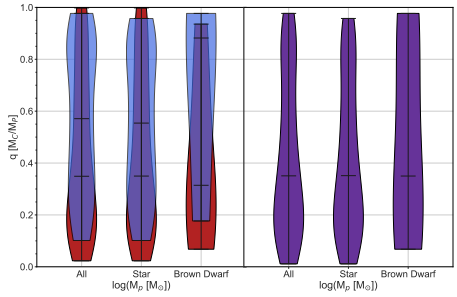

Figure 16. Left panel: mass ratio distribution violin plots for our two full sample of candidates (blue: ACS, red:WFC3-IR) and candidates with primaries in the stellar/BD mass regime. Right panel: same as left panel for the selected *union* master catalog.

4.5. *The multiplicity fraction in the ONC*

After apply a stringent selection, discarding the possible 17 chance alignment pairs, we evaluate the multiplicity fraction (MF) for different configurations of our sample of binaries. First we provide the MF of our *uncompleted* ACS samples in the range of separations $0.12 - 1.95''$ as:

$$MF = 6.9\% \pm 0.8\% \tag{11}$$

finding it compatible within 3σ with Reipurth et al. estimation for the ONC of $MF = 8.8\% \pm 1.1\%$. We then compare the WFC3-IR and ACS *uncompleted* master catalogs over similar ranges of masses ($0.1 - 1\ M_\odot$), separations ($0.15 - 1.5''$), finding:

$$\begin{aligned} MF_{ACS} &= 5.1\% \pm 0.9\% \\ MF_{WFC3} &= 5.5\% \pm 0.8\% \end{aligned} \tag{12}$$

Both results are in very good agreement and well with 1σ one from the other. With the completeness assessed for the *union* master catalog, we also evaluate the multiply fraction for the *complete union* master catalog as:

$$MF_{union} = 13.0\% \pm 1.0\% \tag{13}$$

Because there is a small difference in the way we evaluate cluster membership in Strampelli et al. (2020a) and in this work, we reevaluated the the MF for WFC3-IR data with the new rules presented in Section 3.2 and after discarding chance alignments, obtaining a new MF estimate of 12.9 ± 1.1 for this sample. These result from WFC3-IR alone is in remarkable good agreement with our actual results from both the Treasury program joined together, supporting very well all the conclusion presented in our previous work.

5. DISCUSSION

In this last section we address the implications that our findings may have on our understanding of star formation and evolution of the ONC, considering first the results obtained for isolated stars before discussing the binary systems.

5.1. *Age and luminosity spread*

The right panel of Figure 4 shows a wide distribution of ages (according to our study case Chabrier single, $R_V = 3.1$) for bona-fide ONC members with three distinguishable peaks. In this Section we return to these data, selecting it even further and rejecting any sources that show saturation in any of the three CMDs presented earlier (i.e. any source laying above even just one of the saturation diagonal line shown in Figure 3). This leaves us with 347 well detected, non saturated stars. Moreover, as anticipated earlier, we will focus only on those sources with an age estimate $\lesssim 5$ Myr. The data presented in Figure 17 reveal the presence of two distinct populations. We fit each one of them with a log-normal distribution, finding the following averages:

- $0.5 - 1.2$ Myr: $< Age >= 0.848 \pm 0.001$ Myr;
- $1.2 - 5$ Myr: $< Age >= 1.569 \pm 0.004$ Myr;

It is intriguing to notice that our results suggest the presence of two populations (red and green) with about 1 Myr average age difference spanning the age range up to ~ 5 Myr. This supports the idea that star formation in the ONC was not a continuous process diluted over a prolonged period of time, but instead is best described by at least two discrete and sequential episodes of star formation over the same range of time, similar to the results obtained by Beccari et al. (2017).

In Section 4.1.2 we have already discussed the spread in term of star luminosity through the HRD, see Figure 5. Together with a real age effect, star spots can also have an impact on the luminosity of a star (Gully-Santiago et al. 2017). Indeed, it is well known that low mass young stars usually present large spot coverage along with strong magnetic field (Johns-Krull & Valenti 1996). This may produce a luminosity spread specifically for this type of objects. Theoretical models show that stars in the mass range $0.1 - 1.12\ M_\odot$, covered by spots for at least $\gtrsim 50\%$ of their surface, have in general radii inflated by a factor of 10% during the PMS stage (Somers & Pinsonneault 2015). This in turn, translates in a difference of about 2 in the luminosity between heavily spotted and spotted-free models. Even though those predictions suggest the possible presence of a luminosity spread in young stellar clusters, they do not seem suffi-

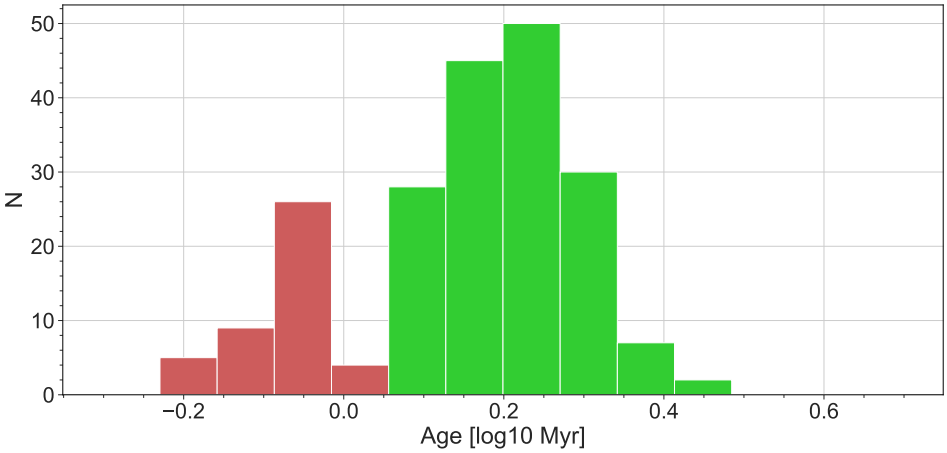

Figure 17. Histograms obtained for the age distribution from the Chabrier single, $R_V = 3.1$ fit, after selections to avoid saturated stars have been applied. Four different populations are shown: $0.5-1.1$ Myr (green), $1.1-5Myr$ (green), $5-50$ Myr (blue) and $50-100$ (purple).

cient to justify the larger spread we observe in our HRD diagram for stars cooler than $\sim 3500°K$.

5.2. *Mass accretion rates*

The $log\dot{M}_{acc}$- $logM_\star$ relation shows some peculiar results. Two regimes can be identified (black thick lines in Figure 8) with different slopes that intercept at about 0.3 $M_\odot$. The more massive stars, $M_\star \gtrsim 0.3\ M_\odot$, display a linear relation that agrees with that predicted in the context of centrally irradiated accretion disks around solar-mass stars with an active accretion layer (Mohanty et al. 2005; Hartmann et al. 2006).

In what concerns the stars with lower mass, two regimes can be identified. If we extend the line fitting the higher mass stars, described by equation 9, we see that it nicely matches a population of low mass objects with high accretion rates. There is, on the other hand, a second branch with a steeper relation between $\dot{M}_{acc}$ and $M_\star$. Various explanations for this bi-modal distribution have been provided. For example, it has been suggested that the disk accretion timescale depends on the stellar mass, with disks around stars with $M_\star \lesssim 0.3\ M_\odot$ evolving more rapidly towards lower value of $\dot{M}_{acc}$. In support of this idea, Vorobyov & Basu (2009) advocate the presence of two different accretion regimes at different stellar masses to explain this bi-modality. They modeled the evolution of disks through the gravitational torques they generate, which drive accretion toward the central source for object of $\sim 1\ M_\odot$. In order to model the accretion in very low-mass stars, they implemented turbulence in their models, to supplement the effort of a weak disk self-gravity. This scenario though, does not completely explain the high-accretion low-mass population observe in Figure 8. In any case, all these models assume a nearly coeval system, whereas our data seem to indicate that the bimodality is largely an age effect. To further investigate the difference between the two populations with $M_\star \lesssim 0.3\ M_\odot$, we analyze their spatial and photometric properties. We find that both populations are evenly distributed on the CMDs, an indication that any systematic displacement due to their different age is suppressed by the differential extinction toward the region. Also, their projected positions in the field do not show any peculiar clustering or other preferences. If we analyze their extinction distribution we find that the sample of sources with high mass-accretion rate has an average value $<A_V> = 2.08 \pm 0.01$ while the population of lower mass accretion rates has an average of $<A_V> = 1.368 \pm 0.003$, suggesting that the older sources typically lie in regions less embedded, i.e. more evolved having been exposed for longer time to the ionizing flux from the OB stars. We must underline that previous studies of other star forming regions, e.g. $\sigma-$Ori (Rigliaco et al. 2011), L1641 (Fang et al. 2013), Chamaeleon Manara et al. (2017), as well as the same ONC (Manara et al. 2012), do not show evidence of a dual population of low mass objects (even though in this particular last case, the effect we observe may be hidden in their large spread of observed $\dot{M}_{acc}$). Rigliaco et al. (2011) results in σ Ori find a dependence of $\dot{M}_{acc}$ with the mass of

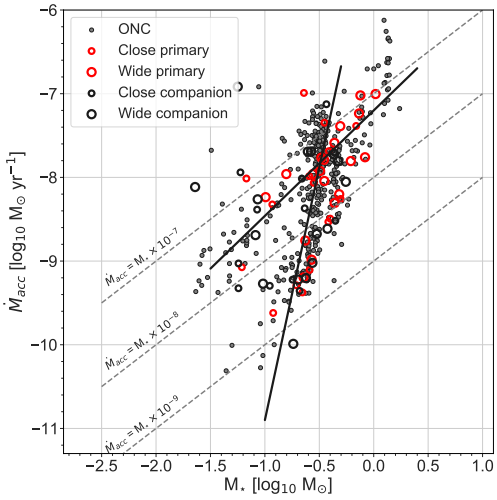

Figure 18. Similar to Figure 8 where the $\dot{M}_{acc}$ vs $L_\star$ values are shown for binaries component (red: primaries, black companions) superimposed to the the ONC values (gray). Small circles represent a member of a close binary (separation $\leq 0.5''$) while a wider one correspond to a wide binary component (separation $> 0.5''$).

		All	Close	Wide
High $\dot{M}_{acc}$	Primaries	0.079	0.034	0.045
	Companions	0.064	0.030	0.034
Low $\dot{M}_{acc}$	Primaries	0.058	0.035	0.023
	Companions	0.058	0.020	0.038

Table 8. Comparison between ratios R (as in Eq. 14) for high and low $\dot{M}_{acc}$, divided by primary and companion components . All: sum of all components (close and wide together); Close/Wide: sum of the members grouped by this class.

the central object, which is stronger for low-mass stars and flattens out for masses larger than $\sim 0.3\ M_\odot$. Manara et al. (2012), in the ONC, find $\dot{M}_{acc}$ to increase with stellar mass and decrease over evolutionary time. Manara et al. (2017), in Chamaeleon instead, find that a broken power-law fit, with a steeper slope for stellar masses lower than $0.3\ M_\odot$ is preferred (similar to our results in the ONC), but still they can not completely rule out the single power-law model.

To conclude this Section about mass accretion rate in the ONC, we analyze the $\dot{M}_{acc}$ vs $M_\star$ relation for binaries in this cluster. Figure 18 shows the results of this analysis, where we overplotted to the data proposed in Figure 8 for isolated stars, the data obtained for the binaries from the ACS/WFC3-IR *union* master catalog. From this plot we observe a slight preference for binaries to populate the high $\dot{M}_{acc}$ ($\gtrsim 10^{-8} M_\star$) portion of the plot. We define the ratio between the number of binaries and the total number of stars for each population as:

$$R = \frac{\sum_i N_i}{N_\star} \tag{14}$$

where N_i represent different grouping of binaries as explained in the following, while $N_\star$ represent the total number of stars in the cluster for the given population. The results for different grouping i are given in Table 8, where we consider the different components grouped by separation classification criteria (Close/Wide) or together (All). Overall, we observe a preference for wide binaries to dominate the high $\dot{M}_{acc}$ population, with primaries more common accretor than companions (even though in the close-in population is more close to even split). On the contrary, the low $\dot{M}_{acc}$ population of binaries shows a different trend, with primaries still dominating the close-in population, wile companion appear more abundant in the wide one. The fact that primaries are more common accretor than companions, in particular in close-in binaries is somewhat expected. In fact, the disc lifetime is regulated by the initial mass of the disc and its viscous evolution timescale, as well as by the rate of photo-evaporation. In binaries, disks around secondaries are supposed to clear more rapidly on average because of their smaller size (Rosotti & Clarke 2018) due to the dependence of the disc outer radius from the mass ratio q and the separation a (Armitage et al. 1999). Why appear that wide low $\dot{M}_{acc}$ companion accretor are more common than primaries is not clear though. Probably, this is not related to a selection effect due to the mass of the components. The column labeled "All" in Table 8 shows that in the low $\dot{M}_{acc}$ population, primaries and companions are split evenly, so we do not have an overall overabundance of companion over primaries that can explain this feature. Moreover, there are a few caveats around these findings that need to be pointed out. More over, there are two different completeness argument that must be taken into account. First, there is an "un-completeness" in our data due to detections, where low mass close-in companies are less likely to be detected (even through KLIP). Second, there is an "un-completeness" due to $\dot{M}_{acc}$ measurements, because the companions detected through KLIP lack $\dot{M}_{acc}$ estimates due to our detection strategy that excluded

the filter F658N from the search of companions. While the first one will affect primary and companion alike (if we don't detect the companion there is no binary to record), the second one will mostly deprive the close-in low-mass companion population. In this case we do detect a companion, but we lack the $\dot{M}_{acc}$ measurement while we still have the record for the primary. So the "un-completeness" of our data can not justify this feature either.

5.3. *Structure and evolution of cluster binaries*

In the range of mass of the primary $0.015 - 1.93\ M_{\odot}$ and separations $0.12 - 1.95''$, we observe from figures 15 and 16 a preference of star-like hosting primaries compared to BDs. Looking at the numbers recorded in Table 7, the stellar mass primaries detected in this work are ~ 17 times more common compared to brown-dwarf mass primaries (we detect only 6 BD mass primaries compared to 104 star mass primaries). Indeed, the peak of the separation distribution of BD is $\lesssim 20$ AU for BD and VLM objects in general (Allers 2012; Winters et al. 2019). Translated to our instrument, the peak would be observed at separation of $\sim 0.05''$ at the distance of the ONC of ~ 402 pc (Kuhn et al. 2019). That is ~ 2.4 times smaller the minimum separation we detect in our cluster. Moreover, compared to the minimum separation where we expect to achieve a completeness $\gtrsim 30\%$, it is ~ 4 times smaller and ~ 5.5 times smaller when compared to the median separation we observe for brown-dwarf pairs in our sample. It is clear than, that we are just observing the end-tail of the brown-dwarf binary distribution in our sample, hence the lack of detections for brown-dwarfs primaries. On the other hand, brown-dwarfs and sub-stellar companions in general, are commonly detected throughout allover the survey (the BDs comprise $\sim 31\%$ of all detected companions, while the overall total of sub-stellar companions is $\sim 36\%$). , so the staggering absence of BD primaries can not just be explained by a limit in our detection technique. We analyze the distance from θ^1 Ori C and the separation distribution of these detected BD primary pairs, finding that 6 out of 7 have a distance $\gtrsim 200''$ from θ^1 Ori C and are all close systems (with a median separation $\sim 0.27''$). The seventh system instead is very close to center of the cluster (with a distance from θ^1 Ori C $\sim 60''$) and separation $\sim 1.5''$ (most likely to be just a chance alignment). Over all, these numbers are consistent with what we previously observed in Strampelli et al. (2020a) WFC3-IR data alone and the general trends for star forming regions and young associations as shown by Duchêne & Kraus (2013).

For what concern the mass ratio distribution, the detection provided by the ACS analysis alone tend to balance the previously WFC3-IR contributions providing a final $q \sim 0.42$ when all binaries are counted and and $q \sim 0.26$ for BD primaries only. In particular, if we limit our *union* sample to similar rage of masses as inspected by Duquennoy & Mayor (1991) ($\sim 0.8 - 1.4\ M_{\odot}$) we obtain a median mass ratio of ~ 0.31 that is very similar their results for field stars of $q \sim 0.3$.

This enlarged sample coming from two HST Treasury programs joint together, offer a strong parallel between the ONC population of solar mass primary and field binaries, advocating that ONC binaries may be regarded as a template for the typical population of field binaries and the ONC itself for the typical star forming region in the Milky way.

To study the dynamical evolution of the ONC (and better understand the two population of *wide* and *close*) we will take advantage of Figure 14. Following Reipurth et al. (2007) explanation (and reference there in), two basic mechanism can affect the stability of young binary systems: rapid dynamical decay and the passage of the system through a denser region of the cluster (that could have been even much denser in the past; Scally et al. 2005). While the former may not bear an impact on the ONC population, being mostly relevant during Class 0 phase (see for example Reipurth 2000), the latter may help understand the current observations. While a binary system is falling through the potential well of a cluster, it will acquire kinetic energy through encounters, and binaries, in particular the one with weak binding energy (either because of a small mass of the primary or because very wide) will eventually be disrupted (Heggie 1975). If this assumptions are correct, binaries at a distance from the cluster larger than the corresponding crossing time should not display dynamical alterations due to encounters with other members of the cluster. In Figure 14 we evaluate the crossing time for different distances as $\tau_{cros} = 2R/\mu$, where R is the cluster radius and $\mu \sim 2.6\ kms^{-1}$(Kim et al. 2019). If we assume an age for the cluster of ~ 1 Myr, the figure suggest that binaries with $\tau_{cross} \lesssim 0.4$ Myr (or within a distance from the center $\lesssim 200''$) have been heavily processed by dynamical interaction with the rest of the cluster (leading to the probable disruption of the wider pairs and the steep decrease of the ratio of *wide* over close binaries). This is followed by a second region between $\sim 200'' - 600''$ (with a corresponding $\tau_{cross} \lesssim 0.4$ and ~ 1 Myr) where dynamical interaction are partially affecting the two distributions of binaries, showed by the presence of these strong oscillations in the ratio of binaries. Then, we observe an outer region where the ratio appear truly

constant and stable (for separation $\gtrsim 600''$). The average ratio of wide over close binaries in this flatten area is ~ 0.4.

Overall this picture bear clear evidence of dynamical evolution still ongoing in the ONC.

6. CONCLUSION

We reanalyzed Robberto et al. (2013) *HST*/ACS/WFC ONC catalog in filters F435W, F555W, F658N, F775W and F850LP providing a new estimate for the photometry of each of its sources. We also complement our catalog with the recently published *HST*/WFC3-IR measures from Robberto et al. (2020) in filter F130N and F139M, bridging together for the first time two *HST* Treasury programs spanning almost 15 years The wide selection of filters available allowed us to provide reliable estimates of three stellar parameters (mass, extinction and age)

Overall, we find good agreement in each family of distributions (mass, A_V, Age) over the different parameters for our Bayesian analysis (IMFs and reddening laws). Changing the IMF does not strongly impact the overall distributions as well as changing the extinctions law, even though $R_v = 5$ seems to produce more shallow distributions compared to $R_v = 3.1$ in both the mass and A_V parameter. As representative parameters value for this cluster we find: a median mass between $0.15 - 0.21$ $M_\odot$, a median extinction A_V between $1.64 - 2.42$ magnitudes and a median Age between $1.6 - 1.8$ Myr.

In particular, the age distribution for stars in the cluster unveil the presence of at least two different populations with an average age of $< Age >= 0.848 \pm 0.001$ Myr and $< Age >= 1.569 \pm 0.004$ Myr, strongly supporting the idea that star formation in the ONC was neither just one singular event or a process diluted over a prolonged period of time, but instead is best described by at least two discrete and sequential episodes of star formation in the first few Myr.

The presence of the F658N allow us to provide an estimate on the $H\alpha$ luminosity and in turn on the accretion rate for $\sim$ 700 cluster sources in the catalog. This is, up to-date, the most comprehensive catalog concerning mass accretion rate in the Orion Nebula Cluster to our knowledge. We find a relation $L_{acc} \propto L_\star{}^{2.07\pm0.29}$. For what concern the mass accretion rate, we find evidence of two distinct populations, one of high $\dot{M}_{acc}$ sources characterized by a relation $\dot{M}_{acc} \propto M_\star{}^{1.26\pm0.11}$ and one that, detparting at $M_\star \sim 0.3$ $M_\odot$, follow a much steeper relation $\dot{M}_{acc} \propto M_\star{}^{6.23\pm2.38}$. A bimodal relationship can be interpret as an evidence in support of the self-gravity in the early evolution of more massive disks (Vorobyov & Basu 2009) , even though other process (i.e. planet formation and/or photo-evaporation) may lead disk dissipation on different time-scale, depending on the mass of the star. On the other hand, a linear relation as the one we observe for high $\dot{M}_{acc}$ sources is predicted in the context of centrally irradiated accretion disks around solar-mass stars with an active accretion layer.

Moreover, we also analyze the binarity properties of this cluster taking advantage of the *Stra*KLIP pipeline to detect faint companion blended in the bright PSF of the primary and finding 15 cluster-cluster bonafide binaries of which 5 truly new. We combined these detection with the binaries obtained from the Robberto et al. (2013) catalog and the binaries already presented in Strampelli et al. (2020a) obtaining a grand total of 119 cluster-cluster binaries sample. When we complete this sample and correct for chance alignment in the cluster, we obtain a final multiplicity fraction of $13.0\% \pm 1.0\%$. The ratio of the cumulative distributions of wide over close binaries shows a steep increase up to a distance of $\sim 200''$ from the center of the cluster that than becomes almost flat (with some strong oscillation) between $200'' - 600''$ and than flats out past the $\sim 600''$, strongly pointing toward a dynamical evolution happened in the history of the clusters and still on going. We also analyze the mass ratio distribution obtaining a median mass ratio for overall catalog of ~ 0.45 that drops to ~ 0.35 when we consider only BD primaries. If we limit our sample to similar rage of masses as the one proposed by Duquennoy & Mayor (1991) for field star, we find very similar results, pointing again towards a strong similarity between the ONC population and field binaries.

APPENDIX

A. ONC CATALOGS

In Table A1 we present a a short preview of the photometric catalog 1077 bona fide cluster members, organized as follows: column (1) lists an incremental index labeling each source, column (2) reports the index presented by Robberto et al. (2013) for cross-identification, columns (3-4) show R.A. and DEC., columns (5-18) report the average

number of saturated pixels, magnitude and uncertainty for each *HST*/ACS/WFC filter, while columns (19-22) list the corresponding WFC3 magnitudes and uncertainties from Robberto et al. (2020).

The derived mass, extinction and age for each cluster member are listed instead in Table A2, along with the accretion properties of each sources. The break down of the table is as follow: columns (1) shows an incremental list of indexes linking each entry to the photometric catalog presented in Table A1. Columns (2-7) list the values of the parameters Mass, A_V and Age estimated through our Bayesian analysis introduced in Section 3.1, with relative errors. Columns (8-11) show the Temperature and Luminosity estimated from the models given the parameters mass, extinction and age, with relative errors. Columns (12-17) report the excess in $H\alpha$ (D$H\alpha$), equivalent width and $H\alpha$ line luminosity, with relative errors, as explained in Section 4.1.3. Columns (18-21) list the accretion luminosity and mass accretion rate and relative errors for each of our sources as explained in Section 4.1.4.

Table A3 and A4 shows a small sample of the photometry obtained for the ONC ACS Master catalog, where the only ternary detected (already present in the input catalog) is listed as two separate binary system with a common hosting star. The subscripts $_p$ and $_c$ refer to the primary star and candidate companion respectively. Column (1) shows the general ID of the catalog, while columns (2 and 3) list IDs linking this catalog to the original from Robberto et al. (2013) and to the catalog of isolated star shown in Table A1. A -1 in the ONCID$_c$ columns indicate that the companion is detected through KLIP analysis. The remaining columns (4-19) show the photometry in the five filters available in this survey (i.e. F435W, F555W, F658N, F775W and F850LP; columns 4-15) as well as the photometry from the matched sources from Robberto et al. (2020) and Strampelli et al. (2020a) in the WFC3-IR filter (i.e. F130N and F139M; columns 15-19) and relative errors. The last two columns (20-21) shows the position angle and the separation for each system.

Table A1. *Sample of the data available in the ONC catalog included in this work*

ID	ONCID	Ra	Dec	spx435	mag435	dmag435	spx555	mag555	dmag555	spx658	mag658	dmag658	spx775	mag775	dmag775	spx850	mag850	dmag850	mag130	dmag130	mag139	dmag139
(-)	(-)	(deg)	(deg)	(mag)	(mag)	(mag)	(mag)	(mag)	(mag)	(mag)	(mag)	(mag)	(mag)	(mag)	(mag)	(mag)	(mag)	(mag)	(mag)	(mag)	(mag)	(mag)
0	8	83.550104	-5.405411	0	20.8568	0.0112	0	19.0551	0.0045	0	16.9373	0.0078	20	15.6529	0.0115	19	14.5685	0.0245				
1	77	83.572083	-5.379979	0	21.1552	0.0079	0	19.74	0.0034	0	17.5418	0.0074	8	16.4178	0.0033	6.7	15.3536	0.0048	13.96	13.96	0.02	0.02
2	152	83.586653	-5.391405	0	18.8572	0.002	3	17.584	0.0014	0	15.7358	0.0026	41	15.0377	0.0106	30.3	14.2182	0.0204	13.03	13.03	0.02	0.02
3	163	83.587446	-5.41345	0	18.9506	0.0026	2.5	17.6509	0.0018	0	15.8543	0.0032	36.5	15.1409	0.0121	23.5	14.3813	0.0212	13.3	13.3	0.01	0.01
4	209	83.593296	-5.374131	0	20.9719	0.0086	0	19.401	0.0036	0	17.307	0.0076	15	15.8711	0.0068	17.5	14.6745	0.0154	13.17	13.17	0.01	0.01
5	242	83.599458	-5.261178	0	18.8632	0.0025	10	16.7854	0.0009	1	14.733	0.0066	78.5	14.3814	0.0199	87.5	13.2975	0.0538	11.21	11.21	0	0
6	246	83.599842	-5.476314	0	21.2206	0.0142	0	19.868	0.0063	0	17.6521	0.0142	7	16.4624	0.0056	8	15.3416	0.0084	13.85	13.85	0.03	0.03
7	266	83.603212	-5.369553	2.5	17.8037	0.0014	13.5	16.5027	0.0018	0	14.7091	0.0068	66.5	14.5263	0.0183	58.5	13.7184	0.0388	12.58	12.58	0.02	0.02
8	282	83.606912	-5.365983	0	19.8641	0.0044	0	18.9044	0.003	0	16.4237	0.004	14	15.8954	0.0066	14.5	14.8821	0.0119	13.5	13.5	0.01	0.01
9	303	83.609892	-5.442672	4	17.3803	0.005	27	15.7758	0.0104	9	13.1379	0.0258	93	14.0376	0.0344	103	13.0285	0.0919				
10	306	83.610427	-5.38996	0	19.4277	0.0023	1	17.9559	0.0015	0	15.9203	0.0023	50.5	14.8277	0.0107	53	13.7713	0.0264	12.25	12.25	0.03	0.03
11	315	83.611587	-5.328142	0	22.468	0.0224	0	20.8604	0.0182	0	18.755	0.0367	2	17.2304	0.0036	2	16.1724	0.0027	14.42	14.42	0.01	0.01
12	316	83.611617	-5.475611	6	17.2826	0.0053	20	16.1497	0.0057	4	13.8668	0.0143	71	14.4936	0.0263	65	13.5996	0.0604	12.31	12.31	0.02	0.02
13	321	83.612437	-5.300894	0	22.9428	0.0285	0	21.1042	0.0082	0	17.7237	0.0106	2.5	17.122	0.0016	4.5	15.5935	0.0036				
14	325	83.613037	-5.280203	0	20.4044	0.0059	0	18.947	0.003	0	16.9811	0.0057	15.5	15.8349	0.007	14	14.8388	0.0126	13.5	13.5	0.01	0.01
15	338	83.614708	-5.474569	0	18.5671	0.0031	7	17.107	0.0017	0	15.3617	0.0054	66	14.549	0.0255	65	13.5584	0.0624	12.13	12.13	0.01	0.01
16	353	83.616338	-5.442944	9	17.0209	0.0061	32	15.6776	0.012	3	14.1126	0.0162	84	14.1907	0.0316	73	13.3447	0.0734	11.72	11.72	0.01	0.01
17	356	83.616733	-5.226761	0			0	25.2165	0.0652	0	21.4319	0.0831	0	20.1666	0.0061	0	18.4653	0.0048				
18	364	83.617529	-5.444353	0	21.0965	0.0131	0	19.4686	0.0053	0	17.3207	0.0108	12	15.939	0.009	13	14.8246	0.0181	13.38	13.38	0.01	0.01
19	372	83.618829	-5.416053	54.5	15.3239	0.0032	79.5	14.7106	0.0239	22.5	12.5662	0.027	116	13.808	0.0276	119	12.8571	0.0729	11.07	11.07	0.01	0.01
20	374	83.619021	-5.50905	0	21.1257	0.0133	0	20.1027	0.007	0	17.0781	0.0088	3	17.1683	0.0022	3	16.174	0.0023	14.48	14.48	0.01	0.01
21	389	83.620686	-5.396677	0	21.0086	0.0062	0	19.6776	0.0029	0	17.1745	0.0048	9.8	16.2308	0.0035	8.8	15.1833	0.0055	13.82	13.82	0.01	0.01
22	401	83.621842	-5.244542	0	24.3715	0.0609	0	20.5127	0.0081	0	16.9749	0.0057	8	16.1863	0.0073	10	14.6677	0.0162				
23	412	83.622375	-5.431053	0	20.5021	0.0063	0	19.0389	0.0031	0	17.1098	0.0064	12.5	15.9987	0.006	10.5	15.043	0.0096	13.77	13.77	0	0
24	414	83.622702	-5.393709	0	20.3	0.0039	0	18.9422	0.0021	0	16.9483	0.004	12.8	15.9932	0.0043	10.8	15.0841	0.0064	13.81	13.81	0.02	0.02
25	422	83.622917	-5.231986	0	19.2298	0.003	1.5	17.8934	0.002	0	15.6295	0.0034	31	15.3848	0.0102	25.5	14.393	0.0212	12.81	12.81	0.02	0.02

NOTE—*Table A1 is published in its entirety in the machine-readable format. A portion is shown here for guidance regarding its form and content.*

Table A2. *Sample of the data available in the ONC catalog included in this work*

ID	M_{2a}	dM_{2a}	A_{v2a}	dA_{v2a}	A_{2a}	dA_{2a}	T_{2a}	dT_{2a}	L_{2a}	dL_{2a}	$DH\alpha_{2a}$	$dDH\alpha_{2a}$	EWQ_{2a}	$dEWQ_{2a}$	$logLH\alpha_{2a}$	$dlogLH\alpha_{2a}$	$logL_{acc2a}$	$dlogL_{acc2a}$	$logdM_{acc2a}$	$dlogdM_{acc2a}$
(-)	($M_\odot$)	($M_\odot$)	(mag)	(mag)	(Myr)	(Myr)	(°K)	(°K)	($L_\odot$)	($L_\odot$)	(mag)	(mag)	(Å)	(Å)	($\log(L_\odot)$)	($\log(L_\odot)$)	($\log(L_\odot)$)	($\log(L_\odot)$)	($M_\odot$ yr^{-1})	($M_\odot$ yr^{-1})
0	0.3313	0.0027	2.149	0.0232	1.2365	0.0284	3482.2111	4.6402	0.375	0.0018	0.5834	0.0164	31.16	1.1298	-3.1826	0.0167	-1.8564	0.2017	-7.6214	0.2018
1	0.1403	0.002	1.3456	0.0163	20.9567	0.1096	3162.2129	4.5449	0.0091	0.0002	0.5648	0.0314	30.4052	2.1668	-4.8014	0.0315	-3.6856	0.2706	-10.2591	0.2708
2	0.1892	0.0286	1.4907	0.2177	2.5219	0.8238	3188.8569	66.2197	0.0627	0.0017	0.2813	0.1284	17.1066	8.8624	-4.4322	0.2492	-3.2684	1.2875	-9.1918	1.2893
3	0.204	0.0258	1.5675	0.1699	2.5668	0.918	3219.4111	56.6532	0.0735	0.0124	0.2148	0.0683	13.4554	4.7167	-4.4975	0.1591	-3.3422	0.8951	-9.2804	0.8998
4	0.1354	0.002	1.826	0.0178	20.8388	0.1227	3150.8567	4.5774	0.0069	0.0001	0.351	0.0311	20.706	2.1445	-5.087	0.0455	-4.0083	0.3503	-10.6736	0.3504
5	0.5011	0.0733	2.5678	0.3475	1.7391	0.6652	3770.3267	93.243	0.3552	0.0575	0.6001	0.0068	31.8299	0.4709	-2.8372	0.0085	-1.4661	0.1925	-7.8308	0.2148
6	0.0724	0.0001	-0.7336	0.0171	14.951	0.1965	2748.2892	2.9645	0.0028	0	0.6934	0.0192	35.3798	1.3274	-5.7687	0.0172	-4.7786	0.2284	-11.0031	0.2284
7	0.2548	0.0412	1.1763	0.2661	2.2513	0.8753	3329.2308	83.8847	0.0939	0.0173	0.4146	0.1224	23.791	8.4506	-3.9151	0.1614	-2.684	0.7946	-8.7888	0.8017
8	0.2916	0.0015	1.0768	0.0191	0.8619	0.0026	3433.459	2.6742	0.3198	0.0039	0.9703	0.0259	44.2914	1.7879	-3.2153	0.0184	-1.8933	0.2044	-7.5821	0.2045
9	0.4495	0.3491	1.6328	0.7417	1.7641	0.6762	3689.2469	551.1757	0.1019	0.0866										
10	0.104	0.0278	2.5143	0.2641	2.3103	0.6675	2970.0605	98.9753	0.0155	0.0033	0	0.5737	9.324	39.6059	-5.3395		-4.2937	12.5761	-10.1737	12.577
11	0.0688	0.0001	-0.9926	0.0071	14.7978	0.2847	2726.5813	3.2301	0.0029	0	0.4884	0.0388	27.1561	2.6768	-6.0248	0.0433	-5.068	0.3825	-11.2097	0.3825
12	0.3116	0.063	0.5058	0.3503	1.685	0.617	3442.5644	124.9665	0.1967	0.0178										
13	0.2744	0.0066	3.5067	0.0671	0.9381	0.0069	3386.6221	12.2671	0.2643	0.0097	1.4888	0.0799	55.9353	5.5184	-2.8766	0.0433	-1.5106	0.2475	-7.2065	0.2483
14	0.1782	0.0019	0.9568	0.0099	22.2784	0.1071	3242.2391	3.8007	0.0129	0.0002	0.4809	0.0249	26.8253	1.7194	-4.6648	0.0284	-3.5313	0.2543	-10.2185	0.2544
15	0.1665	0.0221	1.7745	0.1974	2.6259	0.7359	3139.6779	53.5437	0.0395	0.0014	0.2498	0.1477	15.4072	10.1996	-4.6235	0.3458	-3.4845	1.7078	-9.4793	1.7089
16	0.874	0.2196	0.675	0.1464	1.7873	0.6983	4234.4905	194.2088	1.2018	0.2158										
17	0.1312	0.1366	4.3677	2.0359	1.882	0.8311	3039.9635	376.6713	0.0675	0.0674										
18	0.1468	0.0036	1.8637	0.0334	21.3934	0.6686	3176.9174	7.8859	0.008	0.0001	0.4146	0.0335	23.7921	2.31	-4.9297	0.0427	-3.8305	0.3282	-10.5209	0.3285

NOTE—*Table A2 is published in its entirety in the machine-readable format. A portion is shown here for guidance regarding its form and content.*

Table A3. *Sample of the data referring to the hosting stars available in the ONC binary catalog included in this work*

ID	ONCID$_p$	ONCID$_c$	Ra$_p$	Dec$_p$	mag435$_p$	dmag435$_p$	mag555$_p$	dmag555$_p$	mag65$_p$	dmag658$_p$	mag775$_p$	dmag775$_p$	mag850$_p$	dmag850$_p$	mag130$_p$	dmag130$_p$	mag139$_p$	dmag139$_p$
(–)	(–)	(–)	(deg)	(deg)	(mag)	(mag)	(mag)	(mag)	(mag)	(mag)	(mag)	(mag)	(mag)	(mag)	(mag)	(mag)	(mag)	(mag)
0	969	-1	83.670121	-5.469264	20.2074	0.0081	19.0275	0.0042	16.3513	0.008	14.9571	0.0138	13.8966	0.0334	12.4762	0.0105	12.579	0.0218
1	1934	-1	83.72845	-5.420167	20.4874	0.0093	19.6703	0.0063	16.2317	0.0102	15.9204	0.0065	14.6485	0.0158	12.872	0.0436	13.0353	0.0427
2	1940	-1	83.729375	-5.424839	18.6224	0.0061	17.088	0.0017	15.3297	0.0025	14.5543	0.0254	13.6046	0.0602	12.1775	0.0015	12.1348	0.0012
3	1997	-1	83.733164	-5.368618	26.0019	0.1376	23.7592	0.0287	21.0648	0.0936	18.6195	0.0035	17.2121	0.0032	14.1939	0.0201	14.2386	0.0194
4	2760	-1	83.776737	-5.451317	19.5605	0.0062	18.8367	0.0038	16.1577	0.0067	15.7176	0.0077	14.4559	0.0196	12.7123	0.0187	12.9893	0.0158
5	2770	-1	83.776846	-5.559789	18.1952	0.0048	15.9917	0.008	14.0323	0.0068	13.9172	0.0368	12.9543	0.0967	11.2943	0.0094	11.0866	0.0078
6	3534	-1	83.802979	-5.270403	19.532	0.0061	17.8501	0.0021	15.8145	0.0044	14.8813	0.0145	13.9121	0.033	12.4198	0.0163	12.3202	0.0051
7	3606	-1	83.804854	-5.372528	19.8733	0.0052	18.2704	0.0026	16.0951	0.0061	15.1785	0.012	14.2483	0.0243	12.5846	0.0668	12.3378	0.0228
8	3737	-1	83.806929	-5.479489	20.2288	0.0067	18.7727	0.0039	16.6007	0.0084	14.7815	0.0155	13.7547	0.0378	12.0332	0.2336	11.9371	0.2248
9	3932	-1	83.810992	-5.279447	22.036	0.017	20.2043	0.0083	16.686	0.0103	15.8967	0.0066	14.6615	0.0156	12.7867	0.0023	12.7489	0.0045
10	4893	-1	83.824769	-5.426109	19.4306	0.0041	18.0018	0.0016	15.5302	0.002	14.6539	0.0119	13.7086	0.0277	12.2306	0.034	12.1817	0.034
11	5384	-1	83.833271	-5.312942	25.113	0.0897	22.9582	0.0245	19.4648	0.0334	18.4334	0.0045	16.9877	0.0038	13.8058	0.0043	13.7345	0.015
12	6295	-1	83.853017	-5.278078	25.4167	0.1217	25.6084	0.1526	23.0163	0.5177	20.5124	0.0111	18.3827	0.0076				
13	7555	-1	83.896733	-5.4486	18.1461	0.005	16.6	0.0014	15.0093	0.0031	14.4584	0.019	13.5222	0.0454	12.1409	0.0089	12.0815	0.0137
14	8128	-1	83.944158	-5.373406	18.4669	0.0058	17.0129	0.0015	15.4535	0.0032	14.5644	0.0252	13.5999	0.0604	12.3236	0.0108	12.3374	0.0069
15	773	769	83.658742	-5.461156	18.1874	0.0018	16.7887	0.0009	15.1136	0.0047	14.5784	0.0177	13.7685	0.0373				
16	1707	1705	83.712504	-5.299017	20.3873	0.0059	18.9189	0.003	17.0517	0.0062	15.0858	0.0126	14.1862	0.0257	13.1034	0.0865	13.2058	0.0766
17	1714	1716	83.713337	-5.282003	23.757	0.0446	18.6261	0.0035	18.6722	0.0215	15.2876	0.0108	14.2205	0.0249				
18	1796	1804	83.719079	-5.496185	18.9118	0.0021	16.872	0.0007	15.8769	0.0025	14.5863	0.0125	13.5803	0.0307				
19	1916	1918	83.726658	-5.289236	19.9448	0.0045	18.4864	0.0025	16.5736	0.0042	15.1058	0.0124	14.1562	0.0264	12.8445	0.0229	12.9481	0.0108
20	2164	2172	83.745554	-5.229367	26.3597	0.1489	21.6581	0.0108	19.0854	0.0269	17.6196	0.0019	16.4189	0.0018				
21	2186	2188	83.747096	-5.3923	22.2797	0.0197	20.3429	0.0057	18.1779	0.0155	16.6769	0.0033	15.4892	0.0045	13.2541	0.0163	13.2854	0.014
22	2228	2234	83.750879	-5.402575	22.2426	0.0193	20.8862	0.0075	18.3943	0.0181	18.4611	0.0028	17.7165	0.0032	14.8182	0.0115	14.6783	0.0108
23	2271	2273	83.75405	-5.402953	19.7472	0.004	17.9936	0.0021	15.8638	0.0032	14.7689	0.0156	13.7592	0.0376	11.9109	0.0015	11.8449	0.0011
24	2309	2307	83.755721	-5.403728	23.729	0.045	23.1375	0.0274	18.9897	0.0271	19.1316	0.0043	17.519	0.0029				
25	2379	2389	83.758967	-5.48605	18.8727	0.0025	17.3867	0.0016	15.2386	0.0042	14.8617	0.0147	13.9601	0.0316	12.2413	0.0024	12.1056	0.0078

NOTE— *Table A3 is published in its entirety in the machine-readable format. A portion is shown here for guidance regarding its form and content.*

Table A4. *Sample of the data referring to the candidate companions available in the ONC binary catalog included in this work*

ID	$ONCID_p$	$ONCID_c$	$mag435_c$	$dmag435_c$	$mag555_c$	$dmag555_c$	$mag65_c$	$dmag658_c$	$mag775_c$	$dmag775_c$	$mag850_c$	$dmag850_c$	$mag130_c$	$dmag130_c$	$mag139_c$	$dmag139_c$
(–)	(–)	(–)	(mag)	(mag)	(mag)	(mag)	(mag)	(mag)	(mag)	(mag)	(mag)	(mag)	(mag)	(mag)	(mag)	(mag)
0	969	-1	20.2709	0.0432			16.649	0.0286					12.6109	0.1754	12.5515	0.1751
1	1934	-1	21.7602	0.0457	20.188	0.0307	17.9998	0.0517					14.3648	0.0571	12.7125	0.0688
2	1940	-1	21.8692	0.0835			17.9173	0.0577					14.3197	0.0497	12.4249	0.0624
3	1997	-1							19.5026	0.0271	17.9497	0.0189	14.3152	0.1092	14.2687	0.0906
4	2760	-1	20.8389	0.0455	19.724	0.0327	16.2583	0.0275					13.522	0.0577	13.2706	0.0873
5	2770	-1	18.107	0.0387			14.5577	0.022					13.2902	0.0447	11.2065	0.0496
6	3534	-1	21.9571	0.0479	20.1748	0.0398	18.3392	0.0475					14.4513	0.0497	12.3692	0.0751
7	3606	-1	21.3055	0.0341	20.1231	0.0543	16.9643	0.0216					12.7295	0.2511	12.4057	0.2379
8	3737	-1	20.0758	0.0272	18.4262	0.0169							12.5605	0.2058	11.9265	0.2029
9	3932	-1	22.5725	0.0448	20.5474	0.0303	18.4051	0.0365					13.5577	0.0399	12.799	0.0562
10	4893	-1	20.3106	0.0316	18.8751	0.0231	16.6103	0.023					14.1182	0.0534	12.2333	0.0597
11	5384	-1							18.683	0.0292	17.1639	0.0138	14.5043	0.0471	14.0348	0.0665
12	6295	-1							21.0586	0.032	18.8975	0.019				
13	7555	-1	20.5772	0.0575			18.2595	0.1093					14.0412	0.0306	12.0179	0.0401
14	8128	-1	20.1688	0.0652			17.2226	0.2809					13.8388	0.0415	12.2197	0.0551
15	773	769	21.3619	0.011	16.8506	0.0011	15.456	0.0062	14.8937	0.0144	13.9484	0.032				
16	1707	1705	20.2363	0.0054	18.7798	0.0028	16.9077	0.0056	15.0867	0.0126	14.1824	0.0258	13.1737	0.2606	13.1884	0.2604
17	1714	1716	20.3991	0.0059	18.542	0.0026	15.9044	0.0032	15.2573	0.0111	14.2059	0.0252				
18	1796	1804	18.3475	0.0014	16.802	0.0007	15.0806	0.0034	14.2916	0.0149	13.355	0.0365				
19	1916	1918	19.9133	0.0044	18.4432	0.0025	16.5873	0.0043	15.1049	0.0124	14.1536	0.0265	14.0675	0.0379	12.7742	0.0539
20	2164	2172	26.3218	0.1573	21.9255	0.0133	20.1367	0.0467	17.8756	0.0022	16.6511	0.002				
21	2186	2188	22.188	0.0186	20.243	0.0054	17.845	0.012	16.2777	0.0047	15.0098	0.01	13.8071	0.0493	13.2852	0.0372
22	2228	2234	25.3371	0.1152	24.9897	0.1161	21.5658	0.1543	20.5372	0.0074	19.1733	0.0082	16.5954	0.0125	15.1402	0.0042
23	2271	2273	18.7623	0.0024	17.0921	0.0013	15.1113	0.0047	14.572	0.0178	13.5472	0.0445	12.209	0.003	11.8055	0.0026
24	2309	2307	23.6046	0.042	22.6979	0.0215	19.517	0.0375	18.837	0.0033	17.522	0.0029				
25	2379	2389	20.6106	0.0068	19.0757	0.0032	16.8092	0.005	15.5803	0.0087	14.597	0.0168	12.9594	0.0369	12.1141	0.0217

NOTE—*Table A4 is published in its entirety in the machine-readable format. A portion is shown here for guidance regarding its form and content.*

Table A5. *Sample of the data available in the ONC binary catalog included in this work*

ID	M_{p2a}	dM_{p2a}	A_{vp2a}	dA_{vp2a}	A_{p2a}	dA_{p2a}	T_{p2a}	dT_{p2a}	L_{p2a}	dL_{p2a}	M_{c2a}	dM_{c2a}	A_{vc2a}	dA_{vc2a}	A_{c2a}	dA_{c2a}	T_{c2a}	dT_{c2a}	L_{c2a}	dL_{c2a}	P.A.	Separation
(-)	$(M_\odot)$	$(M_\odot)$	(mag)	(mag)	(Myr)	(Myr)	(°K)	(°K)	$(L_\odot)$	$(L_\odot)$	$(M_\odot)$	$(M_\odot)$	(mag)	(mag)	(Myr)	(Myr)	(°K)	(°K)	$(L_\odot)$	$(L_\odot)$	(deg)	(arcsec)
0	0.0614	0.003	1.4264	0.1709	1.2102	13.4893	2766.0923	38.7273	0.0132	0.0003	0.06	0.003	1.4264	0.1709	1.2102	13.4893	2760.8743	10.1871	0.0198	0.0018	231	0.21
1	0.1443	0.003	0.9212	0.0362	0.9301	0.0036	3081.2205	7.5078	0.1014	0.0045	0.1113	0.003	0.9212	0.0362	0.9301	0.0036	2990.0144	51.704	0.0678	0.0144	332	0.2
2	0.2214	0.024	1.9878	0.1545	2.416	0.8715	3257.8811	50.7515	0.0643	0.0014	0.071	0.024	1.9878	0.1545	2.416	0.8715	2840.1472	121.296	0.0201	0.0162	51	0.2
3	0.0321	0.0272	1.566	0.4132	1.3108	44.697	2650.7228	134.6149	0.0083	0.0001	0.0057	0.0272	1.566	0.4132	1.3108	44.697	2556.4569	99.2885	0.0054	0.0032		0.27
4	0.2809	0.0022	1.4538	0.0297	0.7507	0.002	3435.2768	3.9006	0.2185	0.0041	0.2105	0.0022	1.4538	0.0297	0.7507	0.002	3285.9343	52.5332	0.1175	0.0989	84	0.15
5	0.3982	0.06	3.2858	0.3963	1.5497	0.5628	3604.6253	97.8138	0.172	0.0075		0.06	3.2858	0.3963	1.5497	0.5628						0.32
6	0.2574	0.055	2.6699	0.2868	2.0768	0.9049	3335.3178	125.8279	0.0864	0.0148	0.0927	0.055	2.6699	0.2868	2.0768	0.9049	2949.9534	143.9742	0.0486	0.0191	280	0.19
7	0.3526	0.0017	1.512	0.0271	1.2129	0.0502	3525.6614	1.4858	0.4262	0.0084	0.2062	0.0017	1.512	0.0271	1.2129	0.0502	3205.2856	2.2847	0.1838	0.042	345	0.24
8	0.3863	0.298	1.317	0.5978	1.7335	0.7423	3583.2819	444.5182	0.3071	0.2276		0.298	1.317	0.5978	1.7335	0.7423					74	0.34
9	0.1088	0.0114	1.7639	0.1061	99.9517	42.7317	3028.3008	104.5039	0.0011	0	0.0957	0.0114	1.7639	0.1061	99.9517	42.7317	2972.5242	46.1549	0.0023	0.0004	190	0.15
10	0.1305	0.0008	1.3771	0.0072	25.7712	0.0787	3125.1893	3.0757	0.0049	0	0.1043	0.0008	1.3771	0.0072	25.7712	0.0787	3019.2956	7.2521	0.0062	0.0001	0	0.18
11	0.077	0.0115	3.0151	0.1239	1.7042	0.3274	2844.9564	35.1763	0.0243	0.0092	0.0698	0.0115	3.0151	0.1239	1.7042	0.3274	2817.8207	103.5453	0.0224	0.0193	71	0.21
12	1.3889	0.0387	11.5216	0.088	1.3129	0.0971	4655.7814	49.0235	6.7196	0.2345	0.9983	0.0387	11.5216	0.088	1.3129	0.0971	4352.8679	26.6916	1.7011	0.222		0.17
13	0.2361	0.0393	2.0057	0.2395	2.2066	0.7987	3289.4214	83.7864	0.0619	0.0107	0.088	0.0393	2.0057	0.2395	2.2066	0.7987	2924.0753	119.2836	0.0359	0.0167		0.15
14	0.1596	0.0249	1.7909	0.2323	2.5044	0.6655	3123.3755	61.8764	0.0348	0.0012	0.089	0.0249	1.7909	0.2323	2.5044	0.6655	2916.1687	108.9655	0.0296	0.0149		0.12
15	0.383	0.4273	0.879	0.7666	1.7977	0.7836	3577.6323	661.6102	0.3029	0.4217	0.0542	0.7993	11.8569	0.1705	2.0728	0.6971	2826.0363	1250.15	0.0192	1.103	21	0.3782
16	0.1192	0.001	2.0718	0.0099	1.3462	0.0041	2952.0075	3.2853	0.055	0.0008	0.1103	0.0008	0.6838	0.0206	99.9906	0.0121	3033.9004	2.9237	0.0028	0		0.2521
17	0.6084	0.2244	12.4223	0.2658	1.6464	0.6303	3926.4277	281.767	0.6459	0.1506	0.3675	0.0015	2.3295	0.0325	1.1181	0.0247	3559.9143	1.4065	0.4335	0.0008	200	0.3478
18	0.4639	0.3479	3.0732	0.7331	1.7408	0.7203	3712.641	583.3233	0.4106	0.3152	0.4442	0.3546	1.4911	0.6446	1.7577	0.753	3680.7554	539.4153	0.3821	0.3191		0.4003
19	0.1466	0.0007	0.9306	0.0139	99.9879	0.0141	3148.8791	1.7791	0.0042	0	0.0679	0.0298	2.6194	0.2465	2.0987	0.8624	2873.5734	157.51	0.0279	0.0132	26	0.289
20	0.1573	0.0038	3.1751	0.0339	1.3623	0.034	3066.9538	10.8632	0.0944	0.0021	0.0962	0.0544	2.1438	1.1756	1.5688	0.2811	2890.2676	176.035	0.0353	0.0348		0.5795
21	0.4367	0.0163	5.3469	0.2167	0.6821	0.0189	3741.7976	22.6278	0.3568	0.0401	0.1262	0.0034	2.371	0.0395	85.0153	2.0004	3125.4195	10.311	0.004	0.0001	355	0.5692
22	0.3977	0.0185	0.6212	0.1204	1.5658	1.3538	3603.7522	8.1783	0.3761	0.1953	0.0403	0.0575	0.3203	0.3792	1.7744	0.8436	2701.6428	384.3007	0.0105	0.0262		1.4762
23	0.2688	0.0424	2.8164	0.2588	2.2558	0.7729	3358.4868	178.0656	0.152	0.0366	0.2384	0.0251	2.3611	0.1586	2.3884	0.8656	3293.5989	50.8728	0.1254	0.0068	246	1.0854
24	0.0676	0.0158	0.2956	0.2832	0.8827	0.0124	2875.6811	48.6233	0.0256	0.01	0.0596	0.0332	0.7586	0.2652	0.9891	0.6497	2862.4953	98.3307	0.0289	0.0156	292	0.3164
25	0.3303	0.0437	1.4308	0.3053	1.5999	0.5581	3478.2486	83.5612	0.2844	0.0076	0.2658	0.0027	1.8512	0.0177	1.3211	0.0332	3341.3659	5.4396	0.2534	0.0046	89	1.0819

NOTE—*Table A5 is published in its entirety in the machine-readable format. A portion is shown here for guidance regarding its form and content.*

B. ACS/WFC3 COMMON BINARIES

cross match between the *HST*/WFC3-IR ONC Master catalogue (Strampelli et al. 2020a) and the *HST*/ACS one. Each row alternate binaries from ACS with the matched binary as observed in WFC3-IR. Each columns instead, alternate the original input data and the residual after KLIP analysis (if performed).

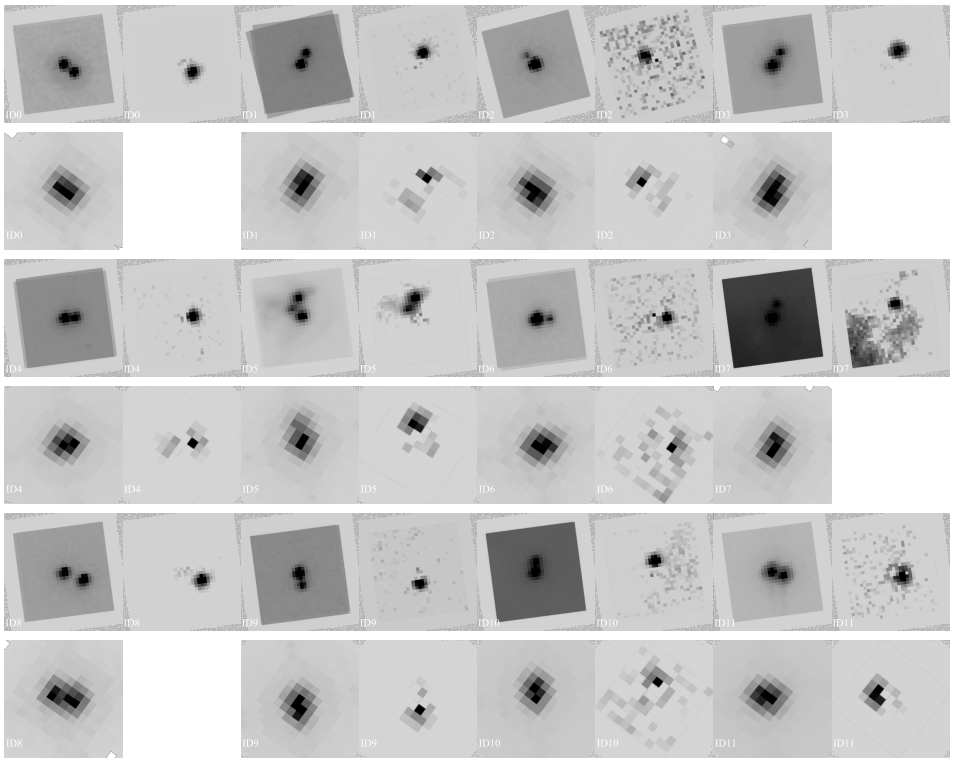

Figure B1. Comparison between the *HST*/WFC3-IR ONC Master catalogue (Strampelli et al. 2020a) and the *HST*/ACS. Each row alternate binaries from ACS with the matched binary as observed in WFC3-IR. Each columns instead, alternate the original input data and the residual after KLIP analysis (if performed).

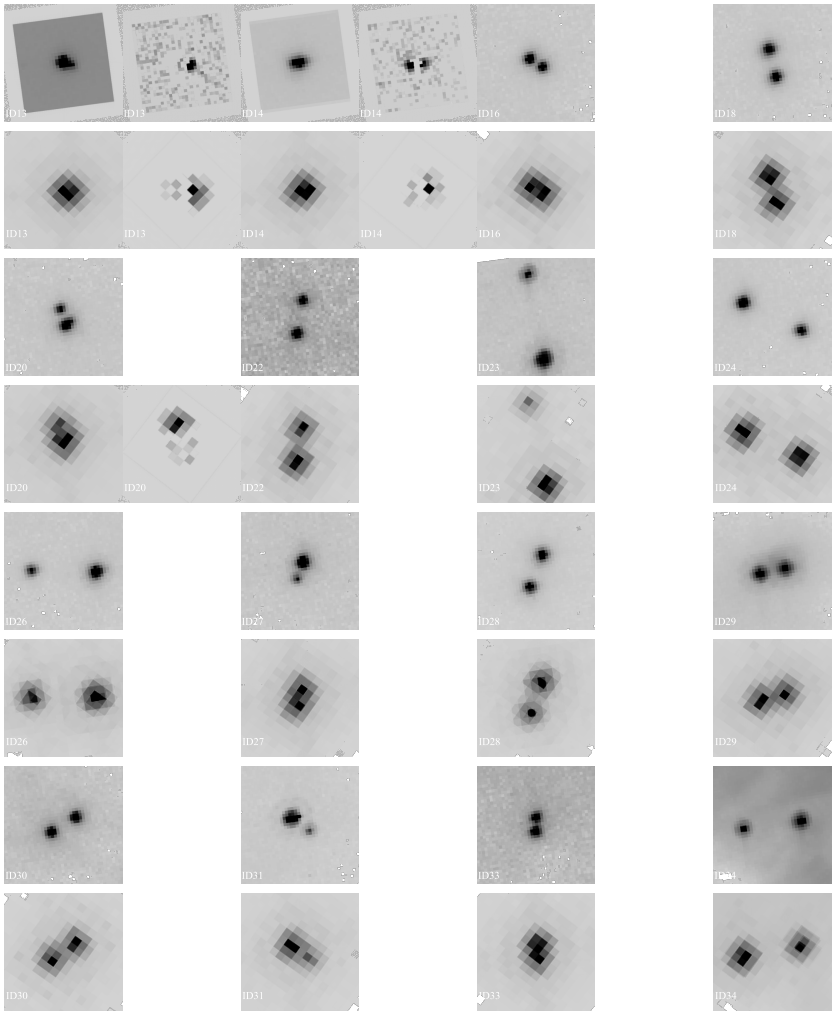

Figure B2. Same as Figure B1

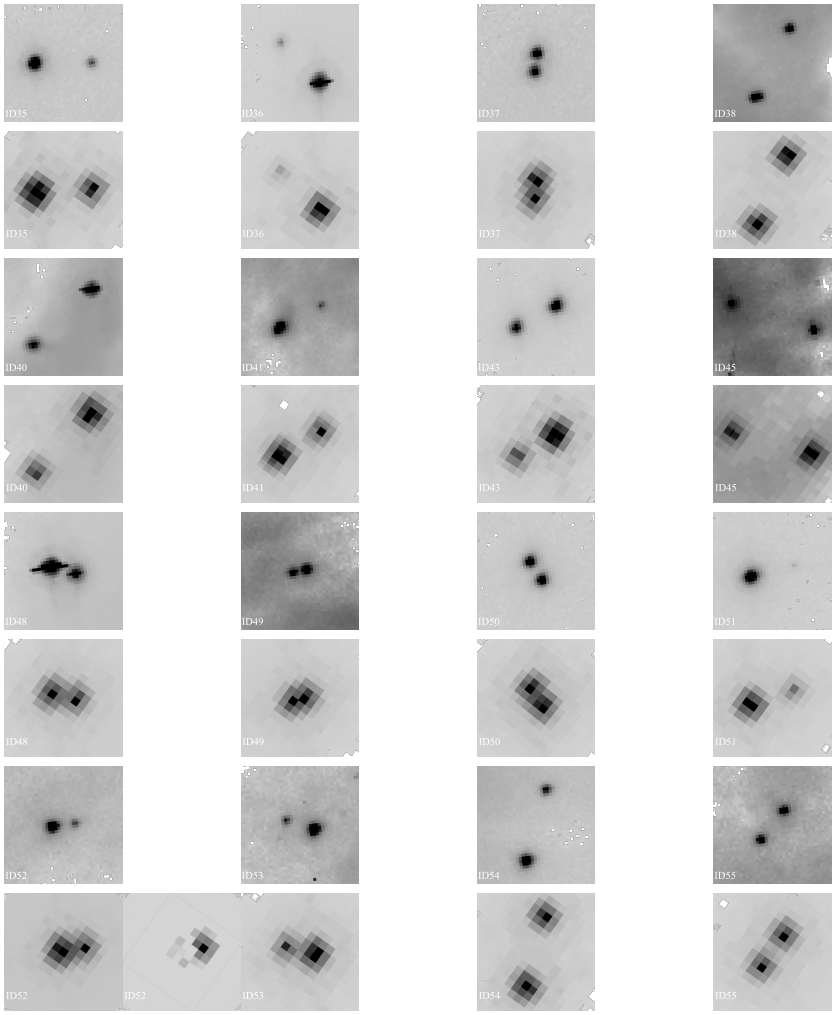

Figure B3. Same as Figure B1

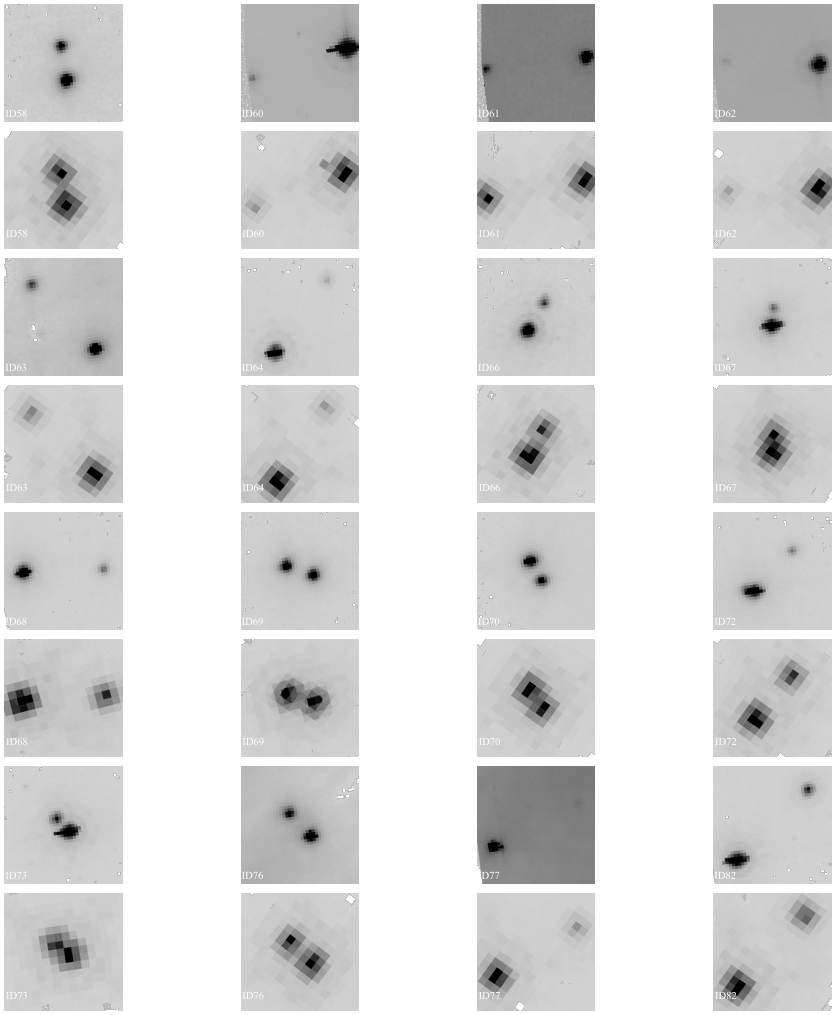

Figure B4. Same as Figure B1

REFERENCES

Alcalá, J. M., Natta, A., Manara, C. F., et al. 2014, A&A, 561, A2, doi: 10.1051/0004-6361/201322254

Alcalá, J. M., Manara, C. F., Natta, A., et al. 2017, A&A, 600, A20, doi: 10.1051/0004-6361/201629929

Allers, K. N. 2012, in From Interacting Binaries to Exoplanets: Essential Modeling Tools, ed. M. T. Richards & I. Hubeny, Vol. 282, 105–110, doi: 10.1017/S1743921311027086

Alves, J., & Bouy, H. 2012, A&A, 547, A97, doi: 10.1051/0004-6361/201220119

Armitage, P. J., Clarke, C. J., & Tout, C. A. 1999, MNRAS, 304, 425, doi: 10.1046/j.1365-8711.1999.02320.x

Baraffe, I., Homeier, D., Allard, F., & Chabrier, G. 2015, A&A, 577, A42, doi: 10.1051/0004-6361/201425481

Beccari, G., Petr-Gotzens, M. G., Boffin, H. M. J., et al. 2017, A&A, 604, A22, doi: 10.1051/0004-6361/201730432

Bouy, H., Alves, J., Bertin, E., Sarro, L. M., & Barrado, D. 2014, A&A, 564, A29, doi: 10.1051/0004-6361/201323191

Cardelli, J. A., Clayton, G. C., & Mathis, J. S. 1989, ApJ, 345, 245, doi: 10.1086/167900

Chabrier, G. 2003, PASP, 115, 763, doi: 10.1086/376392

Da Rio, N., Robberto, M., Hillenbrand, L. A., Henning, T., & Stassun, K. G. 2012, ApJ

De Furio, M., Reiter, M., Meyer, M. R., et al. 2019, ApJ, 886, 95, doi: 10.3847/1538-4357/ab4ae3

De Marchi, G., Panagia, N., & Romaniello, M. 2010, ApJ, 715, 1, doi: 10.1088/0004-637X/715/1/1

Duchêne, G., & Kraus, A. 2013, 1, doi: 10.1146/annurev-astro-081710-102602

Duquennoy, A., & Mayor, M. 1991, A&A, 500, 337

Fang, M., Kim, J. S., van Boekel, R., et al. 2013, ApJS, 207, 5, doi: 10.1088/0067-0049/207/1/5

Fischler, M. A., & Bolles, R. C. 1981, Commun. ACM, 24, 381–395, doi: 10.1145/358669.358692

Foreman-Mackey, D. 2016, corner.py: Scatterplot matrices in Python, doi: 10.21105/joss.00024

Getman, K. V., Flaccomio, E., Broos, P. S., et al. 2005, ApJS, 160, 319, doi: 10.1086/432092

Gizis, J. E., Kirkpatrick, J. D., Burgasser, A., et al. 2001, ApJL, 551, L163, doi: 10.1086/320017

Goodman, J., & Weare, J. 2010, Ensemble samplers with affine invariance, doi: 10.2140/camcos.2010.5.65

Grether, D., & Lineweaver, C. H. 2006, ApJ, 640, 1051, doi: 10.1086/500161

Gullbring, E., Hartmann, L., Briceño, C., & Calvet, N. 1998, ApJ, 492, 323, doi: 10.1086/305032

Gully-Santiago, M. A., Herczeg, G. J., Czekala, I., et al. 2017, ApJ, 836, 200, doi: 10.3847/1538-4357/836/2/200

Hartmann, L., Calvet, N., Gullbring, E., & D'Alessio, P. 1998, ApJ, 495, 385, doi: 10.1086/305277

Hartmann, L., D'Alessio, P., Calvet, N., & Muzerolle, J. 2006, ApJ, 648, 484, doi: 10.1086/505788

Hartmann, L., Herczeg, G., & Calvet, N. 2016, ARA&A, 54, 135, doi: 10.1146/annurev-astro-081915-023347

Heggie, D. C. 1975, MNRAS, 173, 729, doi: 10.1093/mnras/173.3.729

Herbig, G. H., & Terndrup, D. M. 1986, ApJ, 307, 609, doi: 10.1086/164447

Herczeg, G. J., & Hillenbrand, L. A. 2008, ApJ, 681, 594, doi: 10.1086/586728

—. 2015, ApJ, 808, 23, doi: 10.1088/0004-637X/808/1/23

Hillenbrand, L. A. 1997, AJ, 113, 1733, doi: 10.1086/118389

Jeffries, R. D., Littlefair, S. P., Naylor, T., & Mayne, N. J. 2011, MNRAS, 418, 1948, doi: 10.1111/j.1365-2966.2011.19613.x

Jerabkova, T., Beccari, G., Boffin, H. M. J., et al. 2019, A&A, 627, A57, doi: 10.1051/0004-6361/201935016

Johns-Krull, C. M., & Valenti, J. A. 1996, ApJL, 459, L95, doi: 10.1086/309954

Kim, D., Lu, J. R., Konopacky, Q., et al. 2019, AJ, 157, 109, doi: 10.3847/1538-3881/aafb09

Köhler, R., Petr-Gotzens, M. G., McCaughrean, M. J., et al. 2006, Proceedings of the International Astronomical Union, 2, 114, doi: 10.1017/S1743921307003912

Kroupa, P. 2001, MNRAS, 322, 231, doi: 10.1046/j.1365-8711.2001.04022.x

Kuhn, M. A., Hillenbrand, L. A., Sills, A., Feigelson, E. D., & Getman, K. V. 2019, ApJ, 870, 32, doi: 10.3847/1538-4357/aaef8c

Kuiper, G. P. 1942, ApJ, 95, 201, doi: 10.1086/144383

Lada, C. J., & Lada, E. A. 2003, ARA&A, 41, 57, doi: 10.1146/annurev.astro.41.011802.094844

Manara, C. F., Fedele, D., Herczeg, G. J., & Teixeira, P. S. 2016a, A&A, 585, A136, doi: 10.1051/0004-6361/201527224

—. 2016b, A&A, 585, A136, doi: 10.1051/0004-6361/201527224

Manara, C. F., Robberto, M., Da Rio, N., et al. 2012, ApJ, 755, 154, doi: 10.1088/0004-637X/755/2/154

Manara, C. F., Testi, L., Natta, A., & Alcalá, J. M. 2015, A&A, 579, A66, doi: 10.1051/0004-6361/201526169

Manara, C. F., Testi, L., Herczeg, G. J., et al. 2017, A&A, 604, A127, doi: 10.1051/0004-6361/201630147

Marcy, G. W., & Butler, R. P. 2000, PASP, 112, 137, doi: 10.1086/316516

Mohanty, S., Jayawardhana, R., & Basri, G. 2005, ApJ, 626, 498, doi: 10.1086/429794

Natta, A., Testi, L., & Randich, S. 2006, A&A, 452, 245, doi: 10.1051/0004-6361:20054706

Pedregosa, F., Varoquaux, G., Gramfort, A., et al. 2011, Journal of Machine Learning Research, 12, 2825

Petr, M. G., Coude du Foresto, V., Beckwith, S. V. W., Richichi, A., & McCaughrean, M. J. 1998, The Astrophysical Journal, 500, 825, doi: 10.1086/305751

Portegies Zwart, S. F., McMillan, S. L., & Gieles, M. 2010, Annual Review of Astronomy and Astrophysics, 48, 431, doi: 10.1146/annurev-astro-081309-130834

Prosser, C. F., Stauffer, J. R., Hartmann, L., et al. 1994, ApJ, 421, 517, doi: 10.1086/173668

Reggiani, M., Robberto, M., Da Rio, N., et al. 2011, A&A, 534, A83, doi: 10.1051/0004-6361/201116946

Reipurth, B. 2000, AJ, 120, 3177, doi: 10.1086/316865

Reipurth, B., Guimarães, M. M., Connelley, M. S., & Bally, J. 2007, AJ, 134, 2272, doi: 10.1086/523596

Rigliaco, E., Natta, A., Randich, S., Testi, L., & Biazzo, K. 2011, A&A, 525, A47, doi: 10.1051/0004-6361/201015299

Rigliaco, E., Natta, A., Testi, L., et al. 2012, A&A, 548, A56, doi: 10.1051/0004-6361/201219832

Robberto, M., Soderblom, D. R., Bergeron, E., et al. 2013, ApJS, 207, 10, doi: 10.1088/0067-0049/207/1/10

Robberto, M., Gennaro, M., Ubeira Gabellini, M. G., et al. 2020, ApJ, 896, 79, doi: 10.3847/1538-4357/ab911e

Rosotti, G. P., & Clarke, C. J. 2018, MNRAS, 473, 5630, doi: 10.1093/mnras/stx2769

Scally, A., Clarke, C., & McCaughrean, M. J. 1999, Monthly Notices of the Royal Astronomical Society, 306, 253, doi: 10.1046/j.1365-8711.1999.02513.x

Scally, A., Clarke, C., & McCaughrean, M. J. 2005, MNRAS, 358, 742, doi: 10.1111/j.1365-2966.2004.08617.x

Scandariato, G., Robberto, M., Pagano, I., & Hillenbrand, L. A. 2011, A&A, 533, A38, doi: 10.1051/0004-6361/201116554

Simon, M. 1997, ApJL, 482, L81, doi: 10.1086/310678

Slesnick, C. L., Hillenbrand, L. A., & Carpenter, J. M. 2004, ApJ, 610, 1045, doi: 10.1086/421898

Somers, G., & Pinsonneault, M. H. 2015, ApJ, 807, 174, doi: 10.1088/0004-637X/807/2/174

Soummer, R., Pueyo, L., & Larkin, J. 2012, ApJL, 755, L28, doi: 10.1088/2041-8205/755/2/L28

Spiegel, D. S., Burrows, A., & Milsom, J. A. 2011, Astrophysical Journal, 727, 1, doi: 10.1088/0004-637X/727/1/57

Strampelli, G. M., Aguilar, J., Pueyo, L., et al. 2020a, ApJ, 896, 81, doi: 10.3847/1538-4357/ab8eb3

Strampelli, G. M., Pueyo, L., Aguilar, J., et al. 2020b, In prep.

Triaud, A. H. M. J., Martin, D. V., Ségransan, D., et al. 2017, A&A, 608, A129, doi: 10.1051/0004-6361/201730993

Vorobyov, E. I., & Basu, S. 2009, ApJ, 703, 922, doi: 10.1088/0004-637X/703/1/922

Winters, J. G., Henry, T. J., Jao, W.-C., et al. 2019, The Astronomical Journal, 157, 216, doi: 10.3847/1538-3881/ab05dc

7

Conclusion

For the majority of my time as a PhD. student of the University of La Laguna (ULL) (Spain), I had the tremendous opportunity to collaborate with two major institutions in the field of Astrophysics in the United States: the Space Telescope Science Institute (STScI) and the Johns Hopkins University (JHU). Thanks to this outstanding collaboration, I had the chance to work closely with some of the major players in the field of star forming region, binary systems and PSF subtraction techniques, developing my own scientific conscience and analysis method, culminating in the production of a pipeline able to recover faint companions embedded in the host star point spread function in *HST*/ACS and WFC3-IR images.

At the beginning of the project, I focused my attention on the more technical aspects of the work, learning some of the most advanced technique to code in python (i.e. how to efficiently handle and cross-match big amount of data, either catalogs of thousands of stars or hundreds of images, how to parallelize processes to efficiently build a pipeline and take advantage of multiple core CPUs to speed up computationally heavy processes, how to perform optimal PSF subtraction to maximize the SNR of the inquired companion, etc.). The result of this first part of the work produced an highly advanced pipeline named *Stra*KLIP (Strampelli et al. 2020a) that, given a set of *HST*/ACS or WFC3-IR images, is able to identify suitable targets hosting plausible companions and perform its own photometry (aperture, PSF and matched filter) on both components of the systems once they have been identified and properly isolated. This pipeline represents a big step forward in the field of the study of binary systems because it allows, through a plethora of available options, to fully personalize and retain control of each step of the process, to better tailor

the analysis to the single case at hand. A key characteristic of the new pipeline is that it is designed to work with sets of wide-field imaging observations not specifically designed for HCI analysis. From this point of view, it represents a new tool that can be applied to virtually any large image dataset, either from space (HST, JWST, WFIRST-Nancy GraceRoman Telescope) or ground-based facilities (e.g. LSST-Vera Rubin Observatory). Thanks to the *Stra*KLIP pipeline two scientific papers have been produced to date.

In Strampelli et al. (2020b), we show a first application of this pipeline on the *HST*/WFC3-IR Treasury program (GO-13826, P.I. M. Robberto) on the ONC. In this work I studied the population of stellar and substellar objects in the cluster down to a few Jupiter masses in the F130N and F139M filters. Even though the pipeline found more than a few hundreds of candidates astronomical signals, the false positive analysis and vetting process I developed for the WFC3-IR data (through a series of ancillary routine developed along side the pipeline) was able to trim down this list to only 39 bonafide cluster candidate companions of which 18 where already known, leaving 21 plausible candidate cluster companion detections discovered by the pipeline. Once I joined these newly discovered binaries with binaries already known in the input catalog of targets from Robberto et al. (2020), a deep completeness analysis allowed me in the end to asses the full completeness of the sample of 97 binaries in total. This, in turns, granted me the ability to fully asses the MF for the cluster in the range of separation $0.16'' - 1.73''$, $M_p \sim 0.015 - 1.27$ $M_\odot$ and M_c $0.004 - 0.54$ $M_\odot$, finding $MF = 11.5\% \pm 0.5\%$. I also analyzed the mass distribution of primaries and companions apart, and their combined contribution, finding differences between each distribution and between them and the isolated sources. I analyzed in detail the mass ratio (q) distribution, finding a general bottom-heaviness in their trend.

In Strampelli et al. (2020c) instead, we applied the *Stra*KLIP pipeline to *HST*/ACS Treasury program (GO-10246, P.I. M. Robberto) on the same ONC. In this work I focused on two different subjects.

On one side I aimed to produce a new and more accurate PSF photometric catalog for all the isolated sources in the cluster in filters F435W, F555W, F658N, F775W and F850LP. This new photometric catalog has been combined with detections from Robberto et al. (2020) WFC3-IR data in filters F130N and F139M providing an overall catalog of sources in the cluster spanning seven different filters. Thanks to this wide variety of filters available, a Bayesian approach with MCMC strategy have been adopted to estimate three fundamental parameters through SED fitting: mass, age and extinction. Because of the huge computational effort required from those simulations, we partnered

with the Amazon Web Services (AWS)[1] to share the effort. Overall, we find good agreement in each family of distributions (mass, A_V, age) over the different parameters for our Bayesian analysis (IMF and reddening laws). Changing the IMF does not strongly impact the overall distributions as well as changing the extinctions law, even though $R_v = 5$ seems to produce more shallow distributions compared to $R_v = 3.1$ in both the mass and A_V parameter. As representative parameters value for this cluster we find: a median mass between $0.15 - 0.21$ $M_\odot$, a median extinction A_V between $1.64 - 2.42$ magnitudes and a median Age between $1.6 - 1.8$ Myr.

In particular, the age distribution for stars in the cluster unveiled the presence of at least two different populations with an average age of $< Age >= 0.848 \pm 0.001$ and $< Age >= 1.569 \pm 0.004$. This result strongly support the idea that star formation in the ONC was neither just one singular event or a process diluted over a prolonged period of time, but instead is best described by at least two discrete and sequential episodes of star formation over the same range of ~ 5 Myr.

I also provide in the work an estimate of the accretion luminosity (L_{acc}) and mass accretion rate ($\dot{M}_{acc}$) for a sample of ~ 700 bonafide cluster sources, providing one of the most extend catalog of mass accretion rates in the ONC up to-date. Analyzing both $L_{acc}-L_\star$ and $\dot{M}_{acc}-M_\star$ relation, I find that the cluster display a rather linear $L_{acc}-L_\star$ relation $\propto L^{2.07\pm0.29}$, compatible with observation in other star forming regions, e.g. $\rho-$Ophiuchi, $\sigma-$Orionis, Chamaeleon I or Lupus. The $\dot{M}_{acc}-M_\star$ relation clearly show instead the presence of three distinct populations, one made up of high-mass ($M_\star > 0.3 M_\odot$) bright accretor that follow a rather shallow relation $\dot{M}_{acc} \propto M^{1.26\pm0.11}$ and a second one that, departing at $M_\star \sim 0.3$ $M_\odot$ follows a much steeper relation $\dot{M}_{acc} \propto M^{6.23\pm2.38}$. This bimodal relationship can support the idea of self-gravity in the early evolution of more massive disks, even though other process (i.e. planet formation and/or photo-evaporation) may lead to disk dissipation on different time-scale, depending on the mass of the star. The third observed population consists of low-mass high-accretion sources that (within the estimated uncertainties) can not be entirely explained by the spread of the measurements. Ideally, extending the shallow-slope fit (i.e. the one estimated for $M_\star > 0.3 M_\odot$) to lower mass, this fit is able to explain this population as well and is in agreement with predictions in the context of centrally irradiated accretion disks around solar-mass stars with an active accretion layer.

The second part of this work focused on binarity in the ONC again, this time on detections through *Stra*KLIP pipeline on *HST*/ACS data instead. As a

[1] https://aws.amazon.com/what-is-aws/?nc1=f_cc

result of this new run, 19 bonafide cluster member pairs were identified, spanning a range of separation $0.12'' - 0.34''$ and primary mass (M_p) $0.032 - 1.38$ $M_\odot$ and companion mass (M_c) $0.006 - 1.00$ $M_\odot$, of which only 5 truly new detections. Thanks to this new analysis, I was also able to confirm 12 binaries that were previously detected in the WFC3-IR data alone though KLIP. This result per se, shows the strength of the employed technique. Indeed, most of the detections achieved in WFC3-IR data through KLIP are made of just one bright pixel, while in this new ACS analysis appear as a clear and distinct astronomical source thanks to the better sampling of the PSF. This in turn highlights the capability of this technique in recovering buried astronomical signal, in particular in undersampled data as well as the vouching potential of the false positive analysis I employed in the WFC3-IR work that allowed me to trust single pixel detections without any a priori knowledge. Then, I coupled together the results from both Treasury programs, combining the catalogs from both the KLIP analysis and the wide binaries present in both input catalogs, obtaining a final catalog of 119 bonafide cluster binary systems in total, in the range of separations $0.12 - 1.6''$.

Taking into account completeness correction and chance-alignment arguments, in the ranges of $M_p = 0.015 - 1.6$ $M_\odot$, $M_c = 0.004 - 1$ $M_\odot$, I revised the estimate of the multiplicity fraction for the cluster provided in Strampelli et al. (2020b), bringing it to $MF = 13.0\% \pm 1.0\%$, where the difference between the two results can be entirely attributed to the slightly different technique adopted to select cluster membership in the two papers. Even though this value is ~ 2 times smaller than other star forming regions, for example Taurus (Duchêne & Kraus 2013), over a similar separation range, I found good agreement with the binary frequency in the field found by Duquennoy & Mayor (1991) over similar range of masses and separations. Having such a rich catalog of binary available, it allowed me to perform an in-deep analysis of separation distribution of this population. As already mentioned by Reipurth et al. (2007), Strampelli et al. (2020b), this new and enlarged catalog confirms the presence of two distinct populations of binaries in the cluster: one big population of *close*-in pairs (separation $\lesssim 0.6''$), and a second one, less populous group of *wide* binaries (separation $> 0.6''$). Inspecting the trend of *wide* over *close* binaries, shows a clear trend where their ratio has a steep increase up to a distance of $\sim 200''$ from the center of the cluster (identified with the position of θ^1 Ori C) and then becomes flat (still displaying oscillations between $\sim 200'' - 600''$). This result can be associate with a dynamical evolution in the history of the cluster. I also reanalyzed the mass ratio (q) for this new, more complete sample of binaries, mostly confirming previously bottom-heavy observed trend. Limiting the sample to overlapping ranges in masses with field binaries as observed by

Duquennoy & Mayor (1991), my work on the ONC, both on *WFC3*/WFC3-IR and ACS data, strongly suggest similarity between the binaries in the ONC and in the field.

Bibliography

Alexander, R., Pascucci, I., Andrews, S., et al. 2014, Protostars and Planets VI, 475. doi:10.2458/azuuapress9780816531240-ch021 https://ui.adsabs.harvard.edu/abs/2014prpl.conf..475A

Allen, P. R. 2007, ApJ, 668, 492 https://ui.adsabs.harvard.edu/abs/2007ApJ...668..492A

Ambartsumian, V. A. 1937, AZh, 14, 207 https://ui.adsabs.harvard.edu/abs/1937AZh....14..207A

Andre, P., Ward-Thompson, D., & Barsony, M. 1993, ApJ, 406, 122 https://ui.adsabs.harvard.edu/abs/1993ApJ...406..122A

Andre, P., Ward-Thompson, D., & Barsony, M. 2000, Protostars and Planets IV, 59 https://ui.adsabs.harvard.edu/abs/2000prpl.conf...59A

André, P., Basu, S., & Inutsuka, S. 2009, Structure Formation in Astrophysics, 254 https://ui.adsabs.harvard.edu/abs/2009sfa..book..254A

Anosova, J. P. 1986, ApSS, 124, 217 https://ui.adsabs.harvard.edu/abs/1986Ap&SS.124..217A

Bally, J., Ginsburg, A., Forbrich, J., et al. 2020, ApJ, 889, 178 https://ui.adsabs.harvard.edu/abs/2020ApJ...889..178B

Ballesteros-Paredes, J., Klessen, R. S., Mac Low, M.-M., et al. 2007, Protostars and Planets V, 63 https://ui.adsabs.harvard.edu/abs/2007prpl.conf...63B

Basu, S. & Vorobyov, E. I. 2012, ApJ, 750, 30 https://ui.adsabs.harvard.edu/abs/2012ApJ...750...30B

Bate, M. R., Bonnell, I. A., & Bromm, V. 2003, MNRAS, 339, 577 https://ui.adsabs.harvard.edu/abs/2003MNRAS.339..577B

Bate, M. R. 2009, MNRAS, 392, 1363 https://ui.adsabs.harvard.edu/abs/2009MNRAS.392.1363B

Bate, M. R. 2009, MNRAS, 392, 590. doi:10.1111/j.1365-2966.2008.14106.x https://ui.adsabs.harvard.edu/abs/2009MNRAS.392..590B

Batten, A. H. 1973, Binary and multiple systems of stars / by Alan H. Batten. Oxford ; New York : Pergamon Press, [1973] (International series of monographs in natural philosophy ; v. 51) https://ui.adsabs.harvard.edu/abs/1973bmss.book.....B

Beccari, G., Petr-Gotzens, M. G., Boffin, H. M. J., et al. 2017, A&A, 604, A22. doi:10.1051/0004-6361/201730432 https://ui.adsabs.harvard.edu/abs/2017A%26A...604A..22B/

Beck, T. L., Simon, M., & Close, L. M. 2003, ApJ, 583, 358 https://ui.adsabs.harvard.edu/abs/2003ApJ...583..358B

Belloni, D., Kroupa, P., Rocha-Pinto, H. J., et al. 2018, MNRAS, 474, 3740 https://ui.adsabs.harvard.edu/abs/2018MNRAS.474.3740B

Biller, B. A., Close, L., Lenzen, R., et al. 2004, Proc. SPIE, 389 https://ui.adsabs.harvard.edu/abs/2004SPIE.5490..389B

Bloemhof, E. E., Dekany, R. G., Troy, M., et al. 2001, ApJL, 558, L71. doi:10.1086/323494 https://ui.adsabs.harvard.edu/abs/2001ApJ...558L..71B

Bohlin, R. C. 2016, AJ, 152, 60

Bodenheimer, P., Burkert, A., Klein, R. I., et al. 2000, Protostars and Planets IV, 675 https://ui.adsabs.harvard.edu/abs/2000prpl.conf..675B

Boffin, H. M. J., Watkins, S. J., Bhattal, A. S., et al. 1998, MNRAS, 300, 1189 https://ui.adsabs.harvard.edu/abs/1998MNRAS.300.1189B

Bonnell, I. A. 1994, MNRAS, 269, 837. doi:10.1093/mnras/269.3.837 https://ui.adsabs.harvard.edu/abs/1994MNRAS.269..837B

Boss, A. P. & Bodenheimer, P. 1979, ApJ, 234, 289 https://ui.adsabs.harvard.edu/abs/1979ApJ...234..289B

Boss, A. P. 1986, ApJS, 62, 519. doi:10.1086/191150 https://ui.adsabs.harvard.edu/abs/1986ApJS...62..519B

Boss, A. P. 1988, Comments on Astrophysics, 12, 169 https://ui.adsabs.harvard.edu/abs/1988ComAp..12..169B

Boss, A. P. 2002, ApJ, 568, 743 https://ui.adsabs.harvard.edu/abs/2002ApJ...568..743B

Boss, A. P. 2004, MNRAS, 350, L57 https://ui.adsabs.harvard.edu/abs/2004MNRAS.350L..57B

Brown, A. G. A., & Verschueren, W. 1997, A&A, 319, 811 https://ui.adsabs.harvard.edu/abs/1997A&A...319..811B

Carney, B. W., Aguilar, L. A., Latham, D. W., et al. 2005, AJ, 129, 1886 https://ui.adsabs.harvard.edu/abs/2005AJ....129.1886C

Carquillat, J.-M. & Prieur, J.-L. 2007, MNRAS, 380, 1064 https://ui.adsabs.harvard.edu/abs/2007MNRAS.380.1064C

Chabrier, G. 2003, PASP, 115, 763 https://ui.adsabs.harvard.edu/abs/2003PASP..115..763C

Chen, X., Launhardt, R., Bourke, T. L., et al. 2008, ApJ, 683, 862 https://ui.adsabs.harvard.edu/abs/2008ApJ...683..862C

Chen, X., Launhardt, R. and Henning, T. 2009 ApJL, 691(2):1729–1737. https://doi.org/10.1088%2F0004-637x%2F691%2F2%2F1729

Chen X., Arce H. G., Zhang Q., Bourke T. L, Launhardt R. et al. ApJL, 768(2):110 https://doi.org/10.1088%2F0004-637x%2F768%2F2%2F110

Connolly, A. J., Szalay, A. S., Bershady, M. A., et al. 1995, AJ, 110, 1071 https://ui.adsabs.harvard.edu/abs/1995AJ....110.1071C

Connelley, M. S., Reipurth, B., & Tokunaga, A. T. 2008, AJ, 135, 2496 https://ui.adsabs.harvard.edu/abs/2008AJ....135.2496C

Connelley, M. S., Reipurth, B., & Tokunaga, A. T. 2008, AJ, 135, 2526 https://ui.adsabs.harvard.edu/abs/2008AJ....135.2526C

Connelley, M. S., Reipurth, B., & Tokunaga, A. T. 2009, AJ, 138, 1193 https://ui.adsabs.harvard.edu/abs/2009AJ....138.1193C

Cowan, N. B., Agol, E., Meadows, V. S., et al. 2009, ApJ, 700, 915 https://ui.adsabs.harvard.edu/abs/2009ApJ...700..915C

de Jong, T., Boland, W., & Dalgarno, A. 1980, A&A, 91, 68 https://ui.adsabs.harvard.edu/abs/1980A%26A....91...68D

Delfosse, X., Beuzit, J.-L., Marchal, L., et al. 2004, Spectroscopically and Spatially Resolving the Components of the Close Binary Stars, 318, 166 https://ui.adsabs.harvard.edu/abs/2004ASPC..318..166D

Delgado-Donate, E. J., Clarke, C. J., Bate, M. R., et al. 2004, MNRAS, 351, 617 https://ui.adsabs.harvard.edu/abs/2004MNRAS.351..617D

Delgado-Donate, E. J., Clarke, C. J., Bate, M. R., et al. 2004, MNRAS, 351, 617 https://ui.adsabs.harvard.edu/abs/2004MNRAS.351..617D

Delgado-Donate, E. J., Clarke, C. J., & Bate, M. R. 2004, MNRAS, 347, 759

De Rosa, R. J., Patience, J., Wilson, P. A., et al. 2014, MNRAS, 437, 1216. doi:10.1093/mnras/stt1932 https://ui.adsabs.harvard.edu/abs/2014MNRAS.437.1216D

Dieterich, S. B., Henry, T. J., Golimowski, D. A., et al. 2012, AJ, 144, 64 https://ui.adsabs.harvard.edu/abs/2012AJ....144...64D

Dhital, S., West, A. A., Stassun, K. G., et al. 2010, AJ, 139, 2566 https://ui.adsabs.harvard.edu/abs/2010AJ....139.2566D

Duchêne, G. 1999, A&A, 341, 547 https://ui.adsabs.harvard.edu/abs/1999A&A...341..547D

Duchêne, G., Bouvier, J., Bontemps, S., et al. 2004, A&A, 427, 651 https://ui.adsabs.harvard.edu/abs/2004A&A...427..651D

Duchêne, G., Bontemps, S., Bouvier, J., et al. 2007, A&A, 476, 229 https://ui.adsabs.harvard.edu/abs/2007A&A...476..229D

Duchêne, G. & Kraus, A. 2013, ARAA, 51, 269 https://ui.adsabs.harvard.edu/abs/2013ARA%26A..51..269D

Duchêne, G., Lacour, S., Moraux, E., et al. 2018, MNRAS, 478, 1825. doi:10.1093/mnras/sty1180 https://ui.adsabs.harvard.edu/abs/2018MNRAS.478.1825D

Duquennoy, A. & Mayor, M. 1991, A&A, 500, 337 https://ui.adsabs.harvard.edu/abs/1991A&A...248..485D

Enoch, M. L., Corder, S., Duchêne, G., et al. 2011, ApJS, 195, 21. doi:10.1088/0067-0049/195/2/21 https://ui.adsabs.harvard.edu/abs/2011ApJS..195...21E

Fischer, D. A. & Marcy, G. W. 1992, ApJ, 396, 178 https://ui.adsabs.harvard.edu/abs/1992ApJ...396..178F

Fong, W., Laskar, T., Rastinejad, J., et al. 2020, arXiv:2008.08593

Foreman-Mackey, D., Hogg, D. W., Lang, D., et al. 2013, PASP, 125, 306 https://ui.adsabs.harvard.edu/abs/2013PASP..125..306F

Frank, A., Ray, T. P., Cabrit, S., et al. 2014, Protostars and Planets VI, 451 https://ui.adsabs.harvard.edu/abs/2014prpl.conf..451F

Froebrich D., Schmeja S., Smith M. D., Klessen R. S. MNRAS, 368(1):435–446, 03 2006. https://doi.org/10.1111/j.1365-2966.2006.10124.x

Fujii, M. S., Saitoh, T. R., & Portegies Zwart, S. F. 2012, ApJ, 753, 85 https://ui.adsabs.harvard.edu/abs/2012ApJ...753...85F

Fujii, M. S. & Portegies Zwart, S. 2013, MNRAS, 430, 1018 https://ui.adsabs.harvard.edu/abs/2013MNRAS.430.1018F

Gaia Collaboration, Brown, A. G. A., Vallenari, A., et al. 2018, A&A, 616, A1 https://ui.adsabs.harvard.edu/abs/2018A&A...616A...1G

Gennaro, M., Prada Moroni, P. G., & Tognelli, E. 2012, MNRAS, 420, 986. doi:10.1111/j.1365-2966.2011.19945.x https://ui.adsabs.harvard.edu/abs/2012MNRAS.420..986G

Goodwin, S. P., Whitworth, A. P., & Ward-Thompson, D. 2004, A&A, 414, 633. doi:10.1051/0004-6361:20031594 https://ui.adsabs.harvard.edu/abs/2004A&A...414..633G

Goodwin, S. P., Whitworth, A. P., & Ward-Thompson, D. 2004, A&A, 423, 169. doi:10.1051/0004-6361:20040285 https://ui.adsabs.harvard.edu/abs/2004A&A...423..169G

Goodwin, S. P. & Kroupa, P. 2005, A&A, 439, 565. doi:10.1051/0004-6361:20052654 https://ui.adsabs.harvard.edu/abs/2005A&A...439..565G

Goodwin, S. P., Kroupa, P., Goodman, A., et al. 2007, Protostars and Planets V, 133 https://ui.adsabs.harvard.edu/abs/2007prpl.conf..133G

Gorti, U. & Bhatt, H. C. 1996, MNRAS, 283, 566. doi:10.1093/mnras/283.2.566 https://ui.adsabs.harvard.edu/abs/1996MNRAS.283..566G

Gawryszczak, A. J., Goodwin, S. P., Burkert, A., et al. 2005, Protostars and Planets V Posters, 8102 https://ui.adsabs.harvard.edu/abs/2005prpl.conf.8102G

Haisch, K. E., Greene, T. P., Barsony, M., et al. 2004, AJ, 127, 1747 https://ui.adsabs.harvard.edu/abs/2004AJ....127.1747H

Hale, A. 1994, AJ, 107, 306. doi:10.1086/116855 https://ui.adsabs.harvard.edu/abs/1994AJ....107..306H

Hayashi, S. S., Kaifu, N., & Hasegawa, T. 1986, ApSS, 119, 155 https://ui.adsabs.harvard.edu/abs/1986Ap%26SS.119..155H

Hayashi, C. 1981, Fundamental Problems in the Theory of Stellar Evolution, 93, 113 https://ui.adsabs.harvard.edu/abs/1981IAUS...93..113H

Hayashi, C., Narita, S., & Miyama, S. M. 1982, Progress of Theoretical Physics, 68, 1949 https://ui.adsabs.harvard.edu/abs/1982PThPh..68.1949H

Hachisu, I. & Eriguchi, Y. 1985, A&A, 147, 13 https://ui.adsabs.harvard.edu/abs/1985A%26A...147...13H

Hansen, C. J. & Kawaler, S. D. 1994, "Stellar Interiors. Physical Principles, Structure, and Evolution, XIII, 445 pp. 84 figs. 3 1/2" diskette. Springer-Verlag Berlin Heidelberg New York. Also Astronomy and Astrophysics Library", 84. doi:10.1007/978-1-4419-9110-2 https://ui.adsabs.harvard.edu/abs/1994sipp.book.....H

Hansen, C. E., Klein, R. I., McKee, C. F., et al. 2012, ApJ, 747, 22. doi:10.1088/0004-637X/747/1/22 https://ui.adsabs.harvard.edu/abs/2012ApJ...747...22H

Hartigan, P. & Kenyon, S. J. 2003, ApJ, 583, 334. doi:10.1086/345293 https://ui.adsabs.harvard.edu/abs/2003ApJ...583..334H

Hartmann, L., Herczeg, G., & Calvet, N. 2016, ARAA, 54, 135. doi:10.1146/annurev-astro-081915-023347 https://ui.adsabs.harvard.edu/abs/2016ARA%26A..54..135H

Hartmann, L., D'Alessio, P., Calvet, N., et al. 2006, ApJ, 648, 484. doi:10.1086/505788 https://ui.adsabs.harvard.edu/abs/2006ApJ...648..484H

Heggie, D. C. 1975, MNRAS, 173, 729. doi:10.1093/mnras/173.3.729 https://ui.adsabs.harvard.edu/abs/1975MNRAS.173..729H

Herbig, G. H. 1977, ApJ, 217, 693. doi:10.1086/155615 https://ui.adsabs.harvard.edu/abs/1977ApJ...217..693H

Hills, J. G. 1975, AJ, 80, 1075. doi:10.1086/111842 https://ui.adsabs.harvard.edu/abs/1975AJ.....80.1075H

Hinkley, S., Oppenheimer, B. R., Soummer, R., et al. 2007, ApJ, 654, 633. doi:10.1086/509063 https://ui.adsabs.harvard.edu/abs/2007ApJ...654..633H

Hsieh, C.-H., Lai, S.-P., Cheong, P.-I., et al. 2020, ApJ, 894, 23. doi:10.3847/1538-4357/ab7b69 https://ui.adsabs.harvard.edu/abs/2020ApJ...894...23H

Hoffmann, S. L., & Anderson, J. 2017, Instrument Science Report ACS 2017-8

Hopkins, P. F. 2013, MNRAS, 430, 1653. doi:10.1093/mnras/sts704 https://ui.adsabs.harvard.edu/abs/2013MNRAS.430.1653H

Hosking, J. G. & Whitworth, A. P. 2004, MNRAS, 347, 1001. doi:10.1111/j.1365-2966.2004.07274.x https://ui.adsabs.harvard.edu/abs/2004MNRAS.347.1001H

Oppenheimer, B. R. & Hinkley, S. 2009, ARAA, 47, 253. doi:10.1146/annurev-astro-082708-101717 https://ui.adsabs.harvard.edu/abs/2009ARA%26A..47..253O

Harold Hotelling. Relations between two sets of variates. *Biometrika*, 28(3/4):321–377, 1936. http://www.jstor.org/stable/2333955

Jeans, J. H. 1902, Philosophical Transactions of the Royal Society of London Series A, 199, 1

Jeans, J. H. 1919, Cambridge, University press, 1919. https://ui.adsabs.harvard.edu/abs/1919pcsd.book.....J

Jeffries, R. D., Littlefair, S. P., Naylor, T., et al. 2011, MNRAS, 418, 1948. doi:10.1111/j.1365-2966.2011.19613.x https://ui.adsabs.harvard.edu/abs/2011MNRAS.418.1948J

Jerabkova, T., Beccari, G., Boffin, H. M. J., et al. 2019, A&A, 627, A57. doi:10.1051/0004-6361/201935016 https://ui.adsabs.harvard.edu/abs/2019A%26A...627A..57J

Joncour, I., Duchêne, G., & Moraux, E. 2017, A&A, 599, A14. doi:10.1051/0004-6361/201629398 https://ui.adsabs.harvard.edu/abs/2017A%26A...599A..14J

Joye, W. A., & Mandel, E. 2003, Astronomical Data Analysis Software and Systems XII, 489 https://ui.adsabs.harvard.edu/abs/2003ASPC..295..489J

H. Karhunen. *Ann. Acad. Science. Fenn, Ser. A.I. 37*, 1947.

Kauffmann, J., Bertoldi, F., Bourke, T. L., et al. 2008, A&A, 487, 993. doi:10.1051/0004-6361:200809481 https://ui.adsabs.harvard.edu/abs/2008A&A...487..993K

King, I. R. 1983, PASP, 95, 163

Kratter, K. & Lodato, G. 2016, ARAA, 54, 271. doi:10.1146/annurev-astro-081915-023307 https://ui.adsabs.harvard.edu/abs/2016ARA%26A..54..271K

Koch, R. H. & Hrivnak, B. J. 1981, AJ, 86, 438. doi:10.1086/112902 https://ui.adsabs.harvard.edu/abs/1981AJ.....86..438K

Kratter, K. M. 2011, Evolution of Compact Binaries, 447, 47 https://ui.adsabs.harvard.edu/abs/2011ASPC..447...47K

Köhler, R., Petr-Gotzens, M. G., McCaughrean, M. J., et al. 2006, A&A, 458, 461 https://ui.adsabs.harvard.edu/abs/2006A&A...458..461K

Korntreff, C., Kaczmarek, T., & Pfalzner, S. 2012, A&A, 543, A126. doi:10.1051/0004-6361/201118019 https://ui.adsabs.harvard.edu/abs/2012A&A...543A.126K

Kouwenhoven, M. B. N., Brown, A. G. A., & Kaper, L. 2007, A&A, 464, 581 https://ui.adsabs.harvard.edu/abs/2007A&A...464..581K

Kouwenhoven, M. B. N., Brown, A. G. A., Portegies Zwart, S. F., et al. 2007, A&A, 474, 77 https://ui.adsabs.harvard.edu/abs/2007A%26A...474...77K

Kraus, A. L., Ireland, M. J., Martinache, F., et al. 2008, ApJ, 679, 762 https://ui.adsabs.harvard.edu/abs/2008ApJ...679..762K

Kraus, A. L., Ireland, M. J., Martinache, F., et al. 2011, ApJ, 731, 8 https://ui.adsabs.harvard.edu/abs/2011ApJ...731....8K

Kraus, A. L. & Hillenbrand, L. A. 2012, ApJ, 757, 141. doi:10.1088/0004-637X/757/2/141 https://ui.adsabs.harvard.edu/abs/2012ApJ...757..141K

Kroupa, P. 1995, MNRAS, 277, 1491. doi:10.1093/mnras/277.4.1491 https://ui.adsabs.harvard.edu/abs/1995MNRAS.277.1491K

Kroupa, P. 1995, MNRAS, 277, 1507. doi:10.1093/mnras/277.4.1507 https://ui.adsabs.harvard.edu/abs/1995MNRAS.277.1507K

Kroupa, P. & Burkert, A. 2001, ApJ, 555, 945. doi:10.1086/321515 https://ui.adsabs.harvard.edu/abs/2001ApJ...555..945K

Kroupa, P. 2001, MNRAS, 322, 231

Kroupa, P. 2002, Science, 295, 82. doi:10.1126/science.1067524 https://ui.adsabs.harvard.edu/abs/2002Sci...295...82K

Kroupa, P. 2008, The Cambridge N-Body Lectures, 181. doi:10.1007/978-1-4020-8431-78 https://ui.adsabs.harvard.edu/abs/2008LNP...760..181K

Kroupa, P. 2011, Computational Star Formation, 270, 141. doi:10.1017/S1743921311000305 https://ui.adsabs.harvard.edu/abs/2011IAUS..270..141K

Kroupa, P. & Jerabkova, T. 2018, arXiv:1806.10605 https://ui.adsabs.harvard.edu/abs/2018arXiv180610605K

Kuhn, M. A., Hillenbrand, L. A., Sills, A., et al. 2019, ApJ, 870, 32. doi:10.3847/1538-4357/aaef8c https://ui.adsabs.harvard.edu/abs/2019ApJ...870...32K

Kuiper, G. P. 1935, PASP, 47, 15. doi:10.1086/124531 https://ui.adsabs.harvard.edu/abs/1935PASP...47...15K

Kuiper, G. P.˙Problems of Double-Star Astronomy. II. *PASP*, 47(277):121–150, 1935. http://www.jstor.org/stable/40669334

Lada, C. J. & Wilking, B. A. 1984, ApJ, 287, 610 https://ui.adsabs.harvard.edu/abs/1984ApJ...287..610L

Lada, C. J. 1987, Star Forming Regions, 115, 1 https://ui.adsabs.harvard.edu/abs/1987IAUS..115....1L

Lada, C. J. & Kylafis, N. D. 1991, Journal of the British Astronomical Association, 101, 364 https://ui.adsabs.harvard.edu/abs/1991JBAA..101..364L

Lada, C. J. 2006, ApJL, 640, L63. doi:10.1086/503158 https://ui.adsabs.harvard.edu/abs/2006ApJ...640L..63L

Lafrenière, D., Marois, C., Doyon, R., et al. 2007, ApJ, 660, 770 https://ui.adsabs.harvard.edu/abs/2007ApJ...660..770L

Larson, R. B. 2003, Reports on Progress in Physics, 66, 1651. doi:10.1088/0034-4885/66/10/R03 https://ui.adsabs.harvard.edu/abs/1969MNRAS.145..405L

Larson, R. B. 1972, MNRAS, 156, 437 https://ui.adsabs.harvard.edu/abs/1972MNRAS.156..437L

Larson, R. B. 2003, Reports on Progress in Physics, 66, 1651 https://ui.adsabs.harvard.edu/abs/2003RPPh...66.1651L

Launhardt, R., Nutter, D., Ward-Thompson, D., et al. 2010, ApJS, 188, 139 https://ui.adsabs.harvard.edu/abs/2010ApJS..188..139L

Ledoux, P. 1945, ApJ, 102, 143. doi:10.1086/144747 https://ui.adsabs.harvard.edu/abs/1945ApJ...102..143L

Leigh, N. & Geller, A. M. 2012, MNRAS, 425, 2369. doi:10.1111/j.1365-2966.2012.21689.x https://ui.adsabs.harvard.edu/abs/2012MNRAS.425.2369L

M. Loève. *Hermann Paris, France*, 1948.

Looney, L. W., Mundy, L. G., & Welch, W. J. 2000, ApJ, 529, 477. doi:10.1086/308239 https://ui.adsabs.harvard.edu/abs/2000ApJ...529..477L

Luhman, K. L., McLeod, K. K., & Goldenson, N. 2005, ApJ, 623, 1141 https://ui.adsabs.harvard.edu/abs/2005ApJ...623.1141L

Luhman, K. L., Mamajek, E. E., Allen, P. R., et al. 2009, ApJ, 691, 1265 https://ui.adsabs.harvard.edu/abs/2009ApJ...691.1265L

Machida, M. N., Matsumoto, T., Tomisaka, K., et al. 2005, MNRAS, 362, 369. doi:10.1111/j.1365-2966.2005.09297.x https://ui.adsabs.harvard.edu/abs/2005MNRAS.362..369M

Machida, M. N., Matsumoto, T., Hanawa, T., et al. 2005, MNRAS, 362, 382. doi:10.1111/j.1365-2966.2005.09327.x https://ui.adsabs.harvard.edu/abs/2005MNRAS.362..382M

Machida, M. N., Tomisaka, K., Matsumoto, T., et al. 2008, ApJ, 677, 327. doi:10.1086/529133 https://ui.adsabs.harvard.edu/abs/2005MNRAS.362..382M

Machida, M. N., Tomisaka, K., Matsumoto, T., et al. 2008, ApJ, 677, 327. doi:10.1086/529133 https://ui.adsabs.harvard.edu/abs/2008ApJ...677..327M

Myers, P. C. & Benson, P. J. 1983, ApJ, 266, 309 https://ui.adsabs.harvard.edu/abs/1983ApJ...266..309M

Marks, M., Kroupa, P., Dabringhausen, J., et al. 2012, MNRAS, 422, 2246. doi:10.1111/j.1365-2966.2012.20767.x https://ui.adsabs.harvard.edu/abs/2012MNRAS.422.2246M

Marks, M., Janson, M., Kroupa, P., et al. 2015, MNRAS, 452, 1014. doi:10.1093/mnras/stv1361 https://ui.adsabs.harvard.edu/abs/2015MNRAS.452.1014M

Marois, C., Doyon, R., Racine, R., et al. 2000, PASP, 112, 91. doi:10.1086/316492 https://ui.adsabs.harvard.edu/abs/2000PASP..112...91M

Marois, C., Doyon, R., Racine, R., et al. 2005, JRASC, 99, 130 https://ui.adsabs.harvard.edu/abs/2005JRASC..99..130M

Marois, C., Lafrenière, D., Doyon, R., et al. 2006, ApJ, 641, 556. doi:10.1086/500401 https://ui.adsabs.harvard.edu/abs/2006ApJ...641..556M

Marois, C., Phillion, D. W., & Macintosh, B. 2006, Proc. SPIE, 6269, 62693M. doi:10.1117/12.672263 https://ui.adsabs.harvard.edu/abs/2006SPIE.6269E..3MM

Marois, C., Macintosh, B., & Véran, J.-P. 2010, Proc. SPIE, 7736, 77361J. doi:10.1117/12.857225 https://ui.adsabs.harvard.edu/abs/2010SPIE.7736E..1JM

Martín, E. L., Brandner, W., Bouvier, J., et al. 2000, ApJ, 543, 299. doi:10.1086/317089 https://ui.adsabs.harvard.edu/abs/2000ApJ...543..299M

Masciadri, E., Mundt, R., Henning, T., et al. 2005, ApJ, 625, 1004 https://ui.adsabs.harvard.edu/abs/2005ApJ...625.1004M

Massey, P. 2003, ARAA, 41, 15. doi:10.1146/annurev.astro.41.071601.170033 https://ui.adsabs.harvard.edu/abs/2003ARA&A..41...15M

Masunaga, H. & Inutsuka, S.-. ichiro . 2000, ApJ, 531, 350. doi:10.1086/308439 https://ui.adsabs.harvard.edu/abs/2000ApJ...531..350M

Mathieu, R. D. 1994, ARAA, 32, 465. doi:10.1146/annurev.aa.32.090194.002341 https://ui.adsabs.harvard.edu/abs/1994ARA&A..32..465M

Mathieu, R. D., Ghez, A. M., Jensen, E. L. N., et al. 2000, Protostars and Planets IV, 703 https://ui.adsabs.harvard.edu/abs/2000prpl.conf..703M

Maury, A. J., André, P., Hennebelle, P., et al. 2010, A&A, 512, A40 https://ui.adsabs.harvard.edu/abs/2010A&A...512A..40M

Maxted, P. F. L. & Jeffries, R. D. 2005, MNRAS, 362, L45. doi:10.1111/j.1745-3933.2005.00073.x https://ui.adsabs.harvard.edu/abs/2005MNRAS.362L..45M

McCully C., Crawford S., Kovacs G., Tollerud E., Betts E. et al.,*Zenodo , Nov 2018. https://doi.org/10.5281/zenodo.1482019*

Christopher F. McKee and Eve C. Ostriker. Theory of Star Formation. ARAA*, 45(1):565–687, September 2007. https://ui.adsabs.harvard.edu/abs/2007ARA&A..45..565M*

Mitchell, J. 1767, Philos. Trans. R. Soc., 76 , 97

Myers, P. C. & Benson, P. J. 1983, ApJ, 266, 309. doi:10.1086/160780 https://ui.adsabs.harvard.edu/abs/1983ApJ...266..309M

Moeckel, N. & Bate, M. R. 2010, MNRAS, 404, 721. doi:10.1111/j.1365-2966.2010.16347.x https://ui.adsabs.harvard.edu/abs/2010MNRAS.404..721M

Mohanty, S., Jayawardhana, R., & Basri, G. 2005, ApJ, 626, 498. doi:10.1086/429794 https://ui.adsabs.harvard.edu/abs/2005ApJ...626..498M

Mouschovias, T. C. 1991, ApJ, 373, 169 https://ui.adsabs.harvard.edu/abs/1991ApJ...373..169M

Oh, S., Kroupa, P., & Pflamm-Altenburg, J. 2015, ApJ, 805, 92. doi:10.1088/0004-637X/805/2/92 https://ui.adsabs.harvard.edu/abs/2015ApJ...805...92O

Oh, S. & Kroupa, P. 2016, A&A, 590, A107. doi:10.1051/0004-6361/201628233 https://ui.adsabs.harvard.edu/abs/2016A&A...590A.107O

Öpik, E. 1914, Astronomische Nachrichten, 198, 49. doi:10.1002/asna.19141980402 https://ui.adsabs.harvard.edu/abs/1914AN....198...49O

Padoan, P. & Nordlund, Å. 2004, ApJ, 617, 559. doi:10.1086/345413 https://ui.adsabs.harvard.edu/abs/2004ApJ...617..559P

Palla, F. 1996, Disks and Outflows Around Young Stars, 143 https://ui.adsabs.harvard.edu/abs/1996LNP...465..143P/

Patience, J., Ghez, A. M., Reid, I. N., et al. 1998, AJ, 115, 1972 https://ui.adsabs.harvard.edu/abs/1998AJ....115.1972P

Patience, J., Ghez, A. M., Reid, I. N., et al. 2002, AJ, 123, 1570. doi:10.1086/338431 https://ui.adsabs.harvard.edu/abs/2002AJ....123.1570P

Karl F.R.S. Pearson. Liii. on lines and planes of closest fit to systems of points in space. The London, Edinburgh, and Dublin Philosophical Magazine and Journal of Science, *2(11):559–572, 1901.* https://doi.org/10.1080/14786440109462720

Perrin, M. D., Sivaramakrishnan, A., Makidon, R. B., et al. 2003, ApJ, 596, 702. doi:10.1086/377689 https://ui.adsabs.harvard.edu/abs/2003ApJ...596..702P

Petr, M. G., Coudé du Foresto, V., Beckwith, S. V. W., et al. 1998, ApJ, 500, 825 https://ui.adsabs.harvard.edu/abs/1998ApJ...500..825P/exportcitation

Pinfield, D. J., Dobbie, P. D., Jameson, R. F., et al. 2003, MNRAS, 342, 1241. doi:10.1046/j.1365-8711.2003.06630.x https://ui.adsabs.harvard.edu/abs/2003MNRAS.342.1241P

Popovic, G. M., Pavlovic, R., & Ninkovic, S. 2004, Serbian Astronomical Journal, 169, 59 https://ui.adsabs.harvard.edu/abs/2004SerAJ.169...59P

Price, D. J. & Bate, M. R. 2007, MNRAS, 377, 77. doi:10.1111/j.1365-2966.2007.11621.x https://ui.adsabs.harvard.edu/abs/2007MNRAS.377...77P

Pueyo, L., Crepp, J. R., Vasisht, G., et al. 2012, ApJS, 199, 6. doi:10.1088/0067-0049/199/1/6 https://ui.adsabs.harvard.edu/abs/2012ApJS..199....6P

Raghavan, D., McAlister, H. A., Henry, T. J., et al. 2010, ApJS, 190, 1. doi:10.1088/0067-0049/190/1/1 https://ui.adsabs.harvard.edu/abs/2010ApJS..190....1R

Rawiraswattana, K., Lomax, O., & Goodwin, S. P. 2012, MNRAS, 419, 2025. doi:10.1111/j.1365-2966.2011.19864.x https://ui.adsabs.harvard.edu/abs/2012MNRAS.419.2025R

Reggiani, M., Robberto, M., Da Rio, N., et al. 2011, A&A, 534, A83. doi:10.1051/0004-6361/201116946 https://ui.adsabs.harvard.edu/abs/2011A%26A...534A..83R

Reid, I. N. & Gizis, J. E. 1997, AJ, 114, 1992. doi:10.1086/118620 https://ui.adsabs.harvard.edu/abs/1997AJ....114.1992R

Reid, I. N., Gizis, J. E., & Hawley, S. L. 2002, AJ, 124, 2721. doi:10.1086/343777 https://ui.adsabs.harvard.edu/abs/2002AJ....124.2721R

Reipurth, B. & Zinnecker, H. 1993, A&A, 278, 81 https://ui.adsabs.harvard.edu/abs/1993A&A...278...81R

Reipurth, B. 2000, AJ, 120, 3177. doi:10.1086/316865 https://ui.adsabs.harvard.edu/abs/2000AJ....120.3177R

Reipurth, B., & Clarke, C. 2001, AJ, 122, 432 https://ui.adsabs.harvard.edu/abs/2001AJ....122..432R

Reipurth, B., Clarke, C., & Delgado-Donate, E. 2001, astro-ph/0110481 https://ui.adsabs.harvard.edu/abs/2001astro.ph.10481R

Reipurth, B., Rodríguez, L. F., Anglada, G., et al. 2002, AJ, 124, 1045 https://ui.adsabs.harvard.edu/abs/2002AJ....124.1045R

Reipurth, B., Rodríguez, L. F., Anglada, G., et al. 2004, AJ, 127, 1736 https://ui.adsabs.harvard.edu/abs/2004AJ....127.1736R

Reipurth, B., Guimarães, M. M., Connelley, M. S., et al. 2007, AJ, 134, 2272 http://adsabs.harvard.edu/abs/2007AJ....134.2272R

Reipurth, B., Mikkola, S., Connelley, M., et al. 2010, ApJL, 725, L56 https://ui.adsabs.harvard.edu/abs/2010ApJ...725L..56R

Reipurth, B., Clarke, C. J., Boss, A. P., et al. 2014, Protostars and Planets VI, 267. doi:10.2458/azuuapress9780816531240-ch012 https://ui.adsabs.harvard.edu/abs/2014prpl.conf..267R

Reipurth, B. & Mikkola, S. 2015, AJ, 149, 145. doi:10.1088/0004-6256/149/4/145 https://ui.adsabs.harvard.edu/abs/2015AJ...149..145R

Reipurth, B. 2017, , 88, 611 https://ui.adsabs.harvard.edu/abs/2017MmSAI..88..611R

Robberto, M., Soderblom, D. R., Bergeron, E., et al. 2013, ApJS, 207, 10 https://ui.adsabs.harvard.edu/abs/2013ApJS..207...10R

Robberto, M., Gennaro, M., Ubeira Gabellini, M. G., et al. 2020, ApJ, 896, 79. doi:10.3847/1538-4357/ab911e

Rodríguez, L. F., Gómez, Y., & Reipurth, B. 2003, ApJ, 598, 1100 https://ui.adsabs.harvard.edu/abs/2003ApJ...598.1100R

Salpeter, E. E. 1955, ApJ, 121, 161. doi:10.1086/145971 https://ui.adsabs.harvard.edu/abs/1955ApJ...121..161S

Scalo, J. M. 1986, FCP, 11, 1 https://ui.adsabs.harvard.edu/abs/1986FCPh...11....1S

Sadavoy, S. I. & Stahler, S. W. 2017, MNRAS, 469, 3881. doi:10.1093/mnras/stx1061 https://ui.adsabs.harvard.edu/abs/2017MNRAS.469.3881S

Schneider, G., and Silverstone, M. D. 2003, Proc. SPIE, 1 https://ui.adsabs.harvard.edu/abs/2003SPIE.4860....1S

Shatsky, N., & Tokovinin, A. 2002, A&A, 382, 92 https://ui.adsabs.harvard.edu/abs/2002A&A...382...92S

Shu, F. H., Adams, F. C., & Lizano, S. 1987, ARAA, 25, 23. doi:10.1146/annurev.aa.25.090187.000323 https://ui.adsabs.harvard.edu/abs/1987ARA&A..25...23S

Siegler, N., Close, L. M., Cruz, K. L., et al. 2005, ApJ, 621, 1023. doi:10.1086/427743 https://ui.adsabs.harvard.edu/abs/2005ApJ...621.1023S

Simon, M., Ghez, A. M., & Leinert, C. 1993, ApJL, 408, L33 https://ui.adsabs.harvard.edu/abs/1993ApJ...408L..33S

Sparks, W. B. & Ford, H. C. 2002, ApJ, 578, 543. doi:10.1086/342401 https://ui.adsabs.harvard.edu/abs/2002ApJ...578..543S

Spiegel, D. S., Burrows, A., & Milsom, J. A. 2011, ApJ, 727, 57. doi:10.1088/0004-637X/727/1/57 https://ui.adsabs.harvard.edu/abs/2011ApJ...727..57S

Stahler, S. W. 2010, MNRAS, 402, 1758. doi:10.1111/j.1365-2966.2009.15994.x https://ui.adsabs.harvard.edu/abs/2010MNRAS.402.1758S

Stassun, K. G., Feiden, G. A., & Torres, G. 2014, , 60, 1. doi:10.1016/j.newar.2014.06.001 https://ui.adsabs.harvard.edu/abs/2014NewAR..60....1S

Sterzik, M. F. & Durisen, R. H. 1998, A&A, 339, 95 https://ui.adsabs.harvard.edu/abs/1998A&A...339..95S

Sterzik, M. F. & Tokovinin, A. A. 2002, A&A, 384, 1030. doi:10.1051/0004-6361:20020105 https://ui.adsabs.harvard.edu/abs/2002A&A...384.1030S

Strampelli, G. M., Pueyo, L., et al. 2020, under prep.

Strampelli, G. M., Aguilar, J., Pueyo, L., et al. 2020, ApJ, 896, 81 https://ui.adsabs.harvard.edu/abs/2020ApJ...896..81S

Strampelli, G. M., Robberto, M., et al. 2020, under prep.

Soummer, R., Ferrari, A., Aime, C., et al. 2007, ApJ, 669, 642 https://ui.adsabs.harvard.edu/abs/2007ApJ...669..642S

Soummer, R., Hagan, J. B., Pueyo, L., et al. 2011, ApJ, 741, 55. doi:10.1088/0004-637X/741/1/55 https://ui.adsabs.harvard.edu/abs/2011ApJ...741...55S

Soummer, R., Pueyo, L., & Larkin, J. 2012, ApJL, 755, L28 https://ui.adsabs.harvard.edu/abs/2012ApJ...755L..28S

Smartt, S. J., Chen, T.-W., Jerkstrand, A., et al. 2017, , 551, 75. doi:10.1038/nature24303

Thies, I., Kroupa, P., & Theis, C. 2005, MNRAS, 364, 961. doi:10.1111/j.1365-2966.2005.09644.x https://ui.adsabs.harvard.edu/abs/2005MNRAS.364..961T

Thies, I. & Kroupa, P. 2007, ApJ, 671, 767. doi:10.1086/522512 https://ui.adsabs.harvard.edu/abs/2007ApJ...671..767T

Thies, I. & Kroupa, P. 2008, MNRAS, 390, 1200. doi:10.1111/j.1365-2966.2008.13827.x https://ui.adsabs.harvard.edu/abs/2008MNRAS.390.1200T

Thies, I., Pflamm-Altenburg, J., Kroupa, P., et al. 2015, ApJ, 800, 72. doi:10.1088/0004-637X/800/1/72 https://ui.adsabs.harvard.edu/abs/2015ApJ...800..72T

Tobin, J. J., Chandler, C. J., Wilner, D. J., et al. 2013, ApJ, 779, 93 Tinsley, B. M. 1980, FCP, 5, 287 https://ui.adsabs.harvard.edu/abs/1980FCPh....5..287T

Tobin, J. J., Chandler, C. J., Wilner, D. J., et al. 2013, ApJ, 779, 93 https://ui.adsabs.harvard.edu/abs/2013ApJ...779...93T

Tobin, J. J., Looney, L. W., Li, Z.-Y., et al. 2018, ApJ, 867, 43. doi:10.3847/1538-4357/aae1f7 https://ui.adsabs.harvard.edu/abs/2018ApJ...867...43T/exportcita

Tobin, J. J., Kounkel, M., Offner, S., et al. 2019, arXiv:1904.08442 https://ui.adsabs.harvard.edu/abs/2019arXiv190408442T/exportcitation

Tohline, J. E. 1982, FCP, 8, 1 https://ui.adsabs.harvard.edu/abs/1982FCPh....8....1T

Tohline, J. E. 1984, ApJ, 285, 721 https://ui.adsabs.harvard.edu/abs/1984ApJ...285..721T

Tohline, J. E. 2002, ARAA, 40, 349. doi:10.1146/annurev.astro.40.060401.093810 https://ui.adsabs.harvard.edu/abs/2002ARA&A..40..349T

Tokovinin, A. 2018, ApJS, 235, 6. doi:10.3847/1538-4365/aaa1a5 https://ui.adsabs.harvard.edu/abs/2018ApJS..235....6T

Tokovinin, A. & Moe, M. 2020, MNRAS, 491, 5158. doi:10.1093/mnras/stz3299 https://ui.adsabs.harvard.edu/abs/2020MNRAS.491.5158T

Tokovinin, A. 2020, AJ, 160, 69. doi:10.3847/1538-3881/ab9b1e https://ui.adsabs.harvard.edu/abs/2020AJ....160...69T

Tokovinin, A. 2020, Contributions of the Astronomical Observatory Skalnate Pleso, 50, 448. doi:10.31577/caosp.2020.50.2.448 https://ui.adsabs.harvard.edu/abs/2020CoSka..50..448T

Tsuribe, T. & Inutsuka, S.-. ichiro . 1999, ApJL, 523, L155

Umbreit, S., Burkert, A., Henning, T., et al. 2005, ApJ, 623, 940. doi:10.1086/428602 https://ui.adsabs.harvard.edu/abs/2006tbp..book.....V

Valtonen, M. & Karttunen, H. 2006, The Three-Body Problem, by Mauri Valtonen and Hannu Karttunen, pp. . ISBN 0521852242. Cambridge, UK: Cambridge University Press, 2006. https://ui.adsabs.harvard.edu/abs/2006tbp..book.....V

van Albada, T. S. 1968, , 20, 47 https://ui.adsabs.harvard.edu/abs/1968BAN...20..47V

van Dokkum, P. G. 2001, PASP, 113, 1420 https://ui.adsabs.harvard.edu/abs/2001PASP..113.1420V

Van Rossum,G. and Drake F. L. Python 3 Reference Manual. *CreateSpace, Scotts Valley, CA, 2009.*

Vázquez-Semadeni, E., Palau, A., Ballesteros-Paredes, J., et al. 2019, MNRAS, 490, 3061. doi:10.1093/mnras/stz2736 https://ui.adsabs.harvard.edu/abs/2019MNRAS.490.3061V

Vuissoz, C. & Debernardi, Y. 2004, Spectroscopically and Spatially Resolving the Components of the Close Binary Stars, 318, 320 https://ui.adsabs.harvard.edu/abs/2004ASPC..318..320V

Wang, J. J., Ruffio, J.-B., De Rosa, R. J., et al. 2015, pyKLIP: PSF Subtraction for Exoplanets and Disks, ascl:1506.001 https://ui.adsabs.harvard.edu/abs/2015ascl.soft06001W

Ward-Duong, K., Patience, J., De Rosa, R. J., et al. 2015, MNRAS, 449, 2618. doi:10.1093/mnras/stv384 https://ui.adsabs.harvard.edu/abs/2015MNRAS.449.2618W

Watkins, S. J., Bhattal, A. S., Boffin, H. M. J., et al. 1998, MNRAS, 300, 1205. doi:10.1046/j.1365-8711.1998.01987.x https://ui.adsabs.harvard.edu/abs/1998MNRAS.300.1205W

Watkins, S. J., Bhattal, A. S., Boffin, H. M. J., et al. 1998, MNRAS, 300, 1214. doi:10.1046/j.1365-8711.1998.01988.x https://ui.adsabs.harvard.edu/abs/1998MNRAS.300.1214W

White, R. J. & Ghez, A. M. 2001, ApJ, 556, 265. doi:10.1086/321542 https://ui.adsabs.harvard.edu/abs/2001ApJ...556..265W

Whitworth, A. P. & Zinnecker, H. 2004, A&A, 427, 299. doi:10.1051/0004-6361:20041131 https://ui.adsabs.harvard.edu/abs/2004A&A...427..299W

Woitas, J., Leinert, C., & Köhler, R. 2001, A&A, 376, 982. doi:10.1051/0004-6361:20011034 https://ui.adsabs.harvard.edu/abs/2001A&A...376..982W

Zinnecker, H., Bastien, P., Arcoragi, J.-P., et al. 1992, A&A, 265, 726 https://ui.adsabs.harvard.edu/abs/1992A%26A...265..726Z

Zuckerman, B. & Palmer, P. 1974, ARAA, 12, 279 https://ui.adsabs.harvard.edu/abs/1974ARA%26A..12..279Z